Imaging

David K. Jennions, MA, M.Res.

Department of Medical Physics and Bioengineering
University College London

Supervisors:
Dr. Adam Gibson
Prof. Jeremy C. Hebden

Thesis submitted for the degree of Doctor of Philosophy (Ph.D.)
at the University of London

January 2008

ProQuest LLC
789 East Eisenhower Parkway
P.O. Box 1346
Ann Arbor, MI 48106-1346

"When you make the finding yourself - even if you're the last person on Earth to see the light - you'll never forget it."

-Carl Sagan

"There is a single light of science, and to brighten it anywhere is to brighten it everywhere."

-Isaac Asimov

I, David K Jennions, confirm that the work presented in this thesis is my own. Where information has been derived from other sources, it has been indicated as appropriate in the relevant section.

Abstract

Optical Tomography is a medical imaging method for creating three-dimensional images using near infrared light. An instrument, named MONSTIR (Multi-channel Opto-electronic Near-infrared System for Time-resolved Image Reconstruction), has been designed and built to measure the flight times of photons between two positions on the surface of the tissue being imaged. The measurements are used to generate functional images of the newborn infant brain, and to detect and classify breast disease. The aim of my PhD project has been to design a new imaging system, improving on the original design of MONSTIR in order that the images produced from data collected in clinical measurements will lead to improved diagnosis of infant brain trauma and female breast disease, and new functional studies of the neonatal brain.

MONSTIR has been used for conducting fundamental investigations into optical tomography, but has been found to be awkward to use in a clinical environment, inefficient, and has components coming to the end of their useful lifetime. New ultrafast timing electronics have been purchased and tested in conjunction with other new instrumentation intended to reduce measurement errors. The new system's capabilities have been quantified, and improved performance tested in a clinical environment. The data accuracy of MONSTIR whilst in the presence of a large magnetic field has also been quantified, as simultaneous acquisition with magnetic resonance imaging (MRI) could provide useful *a priori* information for reconstruction.

The project has focussed on three major instrumentation changes to MONSTIR: new timing electronics, a new laser calibration method, and updated optical attenuators. First, the original timing electronics required a ~12 s delay between switching source positions to upload data to the control PC. This dead-time is undesirable during clinical studies as the patient must remain still for 12 minutes, whilst collecting only 6 minutes of data. Second, temporal variations have been found in the laser's power output. A new instrument has been designed and tested, resulting in a reduction in intensity errors between repeated measurements over one hour from 40 % to 1 %. Finally, variable optical attenuators are used to compress the dynamic range of the detected signal and protect the detectors from excessive illumination. The original design, using eight apertures of various sizes, does not provide repeatable attenuation, causing a 3 % variation in intensity measurements. A new design has been implemented using x-ray film that has been variably exposed in ten discrete sections, reducing intensity variations to below 1 %.and increasing the maximum attenuation from 2.2 to 3.7 OD.

Implementation of the new instrumentation has improved the system for clinical use. The system is half its original size, takes less than 3 hours to reach thermal stability, and acquires data at 5 s per source containing intensity and meantime uncertainties of 1.9 % and 5.2 ps respectively. The new MONSTIR system requires a delay of 1.5 s between sources, with the result that full 32-channel datasets can be acquired in 3.5 minutes. The increase in acquisition speed allows datasets to be acquired in rapid succession, further reducing data errors in functional imaging. Three dimensional images of breast disease have been produced, and validated using tissue-equivalent phantom studies.

List of figures

List of tables

Acknowledgements

I would firstly like to thank my supervisors, Dr Gibson and Prof. Hebden, for allowing me to continue on from my M.Res. project and delve more deeply into the instrumentation issues that optical imaging presents. The driving force they initially provided, the understanding they had during my recovery, and the patient guidance they have offered over the years are all greatly appreciated.

Special thanks also go to Dr. Nick Everdell and Prof. David Delpy, as their expertise in optical components and instrumentation has been called upon many times during the course of this project. Furthermore, everyone in the Biomedical Optics Research Lab has contributed in some way - be it via complaining about poor data, assisting with the design and road-testing of the new software, sharing their time with me to help rebuild MONSTIR, or simply as competent scientists to bounce question off, I thank you all.

This PhD could not have been possible without the help of five other groups, to whom I am deeply indebted. The Radiation Physics group, specifically Dr. Allesandro Olivio and Dr. Gary Royle, have been beyond accommodating in letting me use their sources for all sorts of odd projects. The reconstruction guys in Computer Science, particularly Dr. Martin Schweiger, have continually tried to explain to the experimentalists in Medical Physics exactly how their code produced images, whilst we have repeatedly attempted to convince them that real data simply doesn't work that way. I hope our conversations have been as useful for you as they have been for me. Dr. John Thornton at the Department of Neurology kindly lent us a few hours with his MRI scanner and managed not to look worried each time I returned with another instrument that could potentially cause his system harm. To all those at CAIS, particularly Dr Mike Dewar, I thank you for the MRes course I started on at UCL. I never would have found the subject area of this PhD if it wasn't for your hard work. Finally the Medical Physics Workshop, most importantly Denzil Booth, have created numerous widgets and plastic oddities, making the new design of the VOAs possible.

Outside UCL my gratitude goes to Dr. Ilkka Nissilä for requesting the data that proved to be what led to the bulk of my research, Dr. Wolfgang Becker for explaining the mysteries of timing electronics to me repeatedly, and the folks at IMRA, Hamamatsu, and DiCon for having a sense of humour with the bizarre data I kept requesting from them about their components.

In addition to those people directly involved in the work for this PhD, I would like to thank all those I have worked with during my time facilitating on the residential courses run by CALT. Most of all I would like to acknowledge Dr. Paul Walker for the guidance and space for reflection that he has built into his courses, especially in the face of tremendous institutional opposition.

Finally to my family for all their challenging, questioning, reassurance, and most of all presence. You are all inspirations.

1 Introduction

1.1 Introduction

The Biomedical Optics Research Laboratory at University College London has developed a time-resolved imaging instrument, using near-infrared light to distinguish between tissues with different optical properties, named MONSTIR (Wells et al. 1997, Schmidt 1999). It has been used to successfully image tissue-equivalent phantoms (Hebden et al. 1998a, Schmidt et al. 2000b, Gibson et al. 2005b), the neonatal head (Hebden et al. 2002, Hebden et al. 2004), forearm (Hillman et al. 2001) and the female breast (Hebden et al. 2005, Yates et al. 2005).

MONSTIR was built in 1997 to record time-resolved measurements of light transmission in order to reconstruct the absolute optical properties of tissues (Schmidt 1999). It was demonstrated that reconstructions of the absorption and scatter could be produced using time-resolved datatypes with MONSTIR (Hebden et al. 1998a). Transmitted intensity measurements are found to be heavily dependent on the coupling between the optical fibres and the surface of the subject (Hebden et al. 1998a, Koizumi et al. 1999). However, intensity can be used if the difference between measurements is used to reconstruct the changes in optical properties. This also removes systematic noise from both data and reconstruction modelling.

It has been proven that unique images of absorption and scatter cannot be derived from intensity measurements alone at a single wavelength (Arridge and Lionheart 1998). It has also been suggested that using two measurements, e.g. intensity and mean flight time, might provide a unique solution (Schweiger et al 1997). MONSTIR was initially designed to measure time-resolved data only and hence needed updating to remove systematic errors in intensity measurements.

In addition, the use of MONSTIR in clinical environments needed to be improved. The original timing electronics extend the time required for acquisitions unnecessarily, as they require a few hundred ms per channel to upload data to the control PC. The electronics and cabling also need more than 12 hours to reach thermal equilibrium, required for accurate timing. MONSTIR was designed to be a portable imaging system, but is cumbersome to move as it occupies two 19" racks, 5' and 6' tall respectively. The time needed to ensure stable measurements and the system's overall size needed to be reduced for MONSTIR to be employed in a clinical environment more readily.

The aim of my PhD was to create an optical tomography system, based on the original MONSTIR, which produces accurate time-resolved and intensity measurements and is more clinical acceptable than the original. First, two main sources of data errors were found by analysing repeated measurements: the power output of MONSTIR's laser source is unstable, and there are repeatability errors in the attenuators protecting the detectors from over-illumination. Second, new instrumentation was designed to monitor variability in laser intensity and a new design for the attenuators was produced in order to improve their reproducibility. Finally, new timing electronics were investigated, purchased, and installed, resolving the clinical problems identified above.

I have implemented these instrumentation advances, resulting in the following improvements:

- Variability in repeated intensity measurements have been reduced from 10 % to 2 %.
- The minimum source-detector separation has been reduced from 5 cm to 3 cm.
- The time taken for MONSTIR to reach thermal stability after transport has been reduced from over 12 hrs to under 3 hrs.
- MONSTIR will now fit in one, smaller rack, as opposed to two.
- Data acquisition time has been more than halved.
- MONSTIR can capture a full 3D dataset in under a minute.

Following the instrumentation improvements, a new MONSTIR system has been constructed. Components, e.g. the laser and source switch, from the original MONSTIR system were shared by the original and new systems, such that an imaging instrument was operational throughout, and comparisons could be made. Instrumentation control, acquisition, and data processing software has been written. Testing has validated and quantified the improved abilities of the new MONSTIR system. This work will lead to production of 3D images of fast haemodynamic responses in the neonatal brain, and improved diagnosis of breast cancer.

To avoid confusion within this thesis, the system as it existed at the onset of my time with the Department of Medical Physics will be labelled MONSTIR-03. Any references to the use of the 'new' system will include updates described in this thesis. References to 'MONSTIR' are therefore generic.

1.2 Aims

The overall aim of this PhD was to build a second-generation optical imaging system to provide the highest data accuracy possible in order that the images produced from data collected in clinical trials will lead to improved diagnosis of infant brain trauma and female breast cancers, and image fast haemodynamic activation in the neonatal brain.

1.2.1 Clinical applications

Optical tomography is a 3D non-invasive and non-ionising imaging technique (Gibson et al. 2005a). Combined with a relatively small size, low cost, and minimal operational requirements, the resulting instrument could be widely used in clinical situations.

Optical tomography of the neonatal brain is being developed to help the diagnosis and treatment of newborn babies suffering from hypoxic-ischaemic brain injury (Wyatt 1993, Volpe 1997). Injury occurs due to breathing difficulties or other problems that prevent the baby from receiving sufficient amounts of oxygenated blood during birth. Hypoxic-ischaema is a major cause of permanent disability in very preterm infants who survive after neonatal intensive care. Currently there is no alternative for measuring blood volume and tissue oxygenation which can be used safely and continuously on infants in intensive care. The reduction of errors in intensity measurements has improved MONSTIR's ability to collect data for absolute imaging, which is the ultimate aim of our work.

Brain activation is currently the subject of many clinical studies (Villringer and Dolan 1995, Siegel et al. 2003, Franceschini and Boas 2004). The new system has been able to image haemodynamic responses in the auditory cortex of the neonatal brain, the first system able to do this in 3D.

In the UK 41,000 women are diagnosed with breast tumours each year, a third of whom will die as a result (Cancer Research UK, 2004). Early detection and treatment can reduce the mortality rate, but the most common method of imaging breast cancer, x-ray mammography, produces a significant number of false positives (Swets JA 1991). X-ray systems have a problem differentiating between malignant and benign carcinomas, as they are structurally similar. Optical tomography offers several advantages (Gibson et al. 2005a), including differentiation of tissues based on functional parameters (e.g. blood volume and oxygenation) as well as structural differences, reducing mammography's confusion over false positives, and requires no compression of the breast, improving the comfort of the patient (Yates et al. 2005). The reduction of the errors in intensity measurements will improve the separation of oxy- and deoxy-haemoglobin and hence the detection of malignant tumours.

1.2.2 Instrumentation

For the purposes of this research, "instrumentation" includes the following:

- All components of MONSTIR, original and new
- Control software
- Calibration theory and practice
- Datatype extraction

The aim of this project was thus to record time-resolved data as accurately and as fast as possible. Research into image reconstruction is published elsewhere (Arridge and Hebden 1997, Arridge 1999, Schweiger et al. 2003).

MONSTIR is intended to be a portable system for use in the diagnosis of neonatal cerebral damage and malignant breast carcinomas. From the point of view of a clinical user, a new MONSTIR would have the following improvements over the original system:

Clinical Impact

- MONSTIR should be no larger than a single, 4' tall, 19" rack.
- The system should be ready to acquire data shortly after moving it.

Data Accuracy

- Meantime measurements must be accurate to within 5 ps.
- Intensity measurements must be accurate to 5 %.

Acquisition Time

- Calibration and setup should occur as quickly as possible.
- Data needs to be acquired in as short a time as possible, in order to capture fast haemodynamic responses.

The ideal clinical application, which exceeds the scope of this research, would involve moving MONSTIR to a patient's bedside, connecting the optical fibres to the patient using an adjustable fibre-holder, switching on, and letting MONSTIR automatically do the rest. Full datasets could be acquired within a few seconds to catch fast haemodynamic invoked responses. Datatypes would be passed to reconstruction software and would notify the user when complete. Specifically, if optical fibre positions had been previously measured, images could be produced in real time using a reconstruction method based on matrix multiplication (§2.3.3.3). After data had been acquired on a patient, MONSTIR could then be immediately moved to perform another acquisition on another patient.

Combining medical images obtained from different modalities is currently one of the most active areas of research in medical physics (Pogue and Paulsen 1998, Ntziachristos et al. 2002). Our main interest is in developing optical tomography to include prior information from other imaging modalities, specifically magnetic resonance imaging (MRI). Combined MRI/optical imaging presents a number of instrumentation issues. The effect of increasing magnetic field on time-resolved data has been investigated, with the result that safe working distances for data acquisition have been found for MONSTIR.

1.3 Published Data

A study performed with Dr. Ilkka Nissilä at Helsinki University of Technology (HUT), comparing the original MONSTIR with their frequency-domain system was published in (Nissilä 2006).

Phantom and speed results from initial testing of the new Becker and Hickl timing electronics was published in (Becker et al. 2005).

Initial results from the new MONSTIR system were presented at OSA 2006 (Jennions et al. 2006) .

1.4 Personal Contribution

The work described in this thesis is the result of my research since September 2003, unless otherwise referenced. This includes:

- Examinations of data accuracy (§3.3).
- The design and testing of new instrumentation (§3.4 and §3.5).
- An investigation into the effects on time-resolved data from a PMT placed in the fringe magnetic field of a magnetic resonance imaging (MRI) system. (§4).
- Quantification of the imaging ability of the improved system (§5).

All results described have been obtained from data taken over the same period.

The work on variable attenuators (§3.5.2) builds on work submitted in my MRes thesis. Background work, error mechanisms, and the basis for the new design are reported in that thesis. The production methods and results obtained for the new attenuators are new to this thesis. This is also noted in §3.5.2.

2 Optical imaging and instrumentation

2.1 Tissue Optics

A coherent, collimated near-infrared beam becomes effectively incoherent and isotropic when passing through tissue (Elwell, C. E. 1995). The principles of photon interactions with tissue, and how these are used in imaging, are described in the following sections.

2.1.1 Photon Interactions

Tissues can be differentiated by their optical properties.

- Refractive index, n, is the ratio of the speed of light in a vacuum to the speed of light in a material. This varies in tissue from 1.33 for water to 1.55 for fat.

- Absorption coefficient, μ_a (mm^{-1}), is a measure of the number of photons absorbed per unit distance. Within a material, this is defined as the change in intensity, dI, with distance, dx:

$$dI = -\mu_a I dx \quad \text{(i)}$$

leading to the Beer-Lambert Law, which describes the exponential decrease of intensity from I_0, to I, with distance, x:

$$I = I_0 e^{-\mu_a x} \quad \text{(ii)}$$

A measure of the attenuation of an object can be given in dB or optical density (OD), as defined by:

$$dB = -10 \times OD = -10 \times \log_{10}\left(I_0 / I\right) \quad \text{(iii)}$$

- Scatter coefficient, μ_s (mm^{-1}), is a measure of the amount of light that is reflected and refracted by a particle. Scatter of light in tissue is due to the chaotic variation in refractive index at a microscopic and macroscopic scale. For a single scattering events, as with μ_a:

$$I = I_0 e^{-\mu_s x} \quad \text{(iv)}$$

- There are two types of scatter anisotropy in tissues, micro- and macro-scopic:

  Tissues have microscopic preferred transmission directions, scattering photons due to intra- and inter-cellular boundaries. For a random medium, the probability of an incoming photon being scattered through an angle θ can be expressed as a function of $\cos(\theta)$, called the scatter phase function.. The anisotropy in the probability distribution is characterised in terms of the scattering anisotropy factor, g:

$$g = \int_{-1}^{1} \cos\theta f(\cos\theta) d\cos\theta \qquad \text{(v)}$$

  A value of $g = 0$ indicates a perfectly isotropically scattering material; $g = 1$ is totally forward directional. Biological tissues scatter light strongly forward and have $0.69 \leq g \leq 0.99$. The transport (or reduced) scattering coefficient is defined as:

$$\mu_s' = \mu_s(1-g) \qquad \text{(vi)}$$

  μ_s' is the reciprocal of the transport scattering length, the distance over which a collimated beam becomes effectively diffuse.

  Macroscopic anisotropy is a variation in scattering coefficient between different axes. This anisotropy occurs in the body mainly due to the fibrous nature of certain tissues, e.g. muscle fibres or white matter in the brain.

- Combining absorption and scatter, the transport attenuation coefficient is:

$$\mu_{tr} = \mu_a + \mu_s(1-g) = \mu_a + \mu_s' \qquad \text{(vii)}$$

  Measured attenuation across tissue at near-infrared wavelengths is governed by μ_{tr}, which is dominated by μ_s' (roughly 1.0 mm^{-1} versus 0.01 mm^{-1} for μ_a). However, only measurements of absorption lead to the separation of the effects of oxy- and deoxygenated haemoglobin, and thus tissue oxygenation level (§2.1.2). The relatively large scattering coefficient allows the transmission of photons through tissue to be modelled as diffusive (§2.3.2), but otherwise leads to cross-talk with the desired absorption measurements.

2.1.2 NIR Imaging

Near-infrared (NIR) imaging has several advantages over other techniques such as magnetic resonance (MR) and x-ray imaging (Gibson et al. 2005a). First, it can be used continuously and repeatedly. NIR absorption in the body is minimal, allowing data to be acquired without causing damage to the patient from heating effects. In addition, NIR radiation is not sufficiently energetic to cause ionisation. Second, the instrumentation used for NIR imaging is relatively inexpensive and compact, which is beneficial in terms of clinical use. Finally, the relative absorption spectra of de-/oxygenated blood are such that small differences in NIR wavelength correspond to measurable differences in absorption coefficient. This allows direct measurements of oxygenation level and haemodynamics. Functional information can be obtained (Hebden et al. 2002) which is vital for brain imaging because it can reveal physiological information before irreversible damage occurs. In addition to brain imaging, this is of relevance to breast imaging (Yates et al. 2005), in which diagnosis can depend on blood volume within the breast.

The selection of wavelengths for imaging is restricted by the relative properties of the tissues' content – water, which makes up 90% of neonatal brain volume (Dittmer DA 1961), absorbs strongly above 1000 nm, while haemoglobin (the oxygen carrier in red blood cells) absorbs strongly below 600 nm.

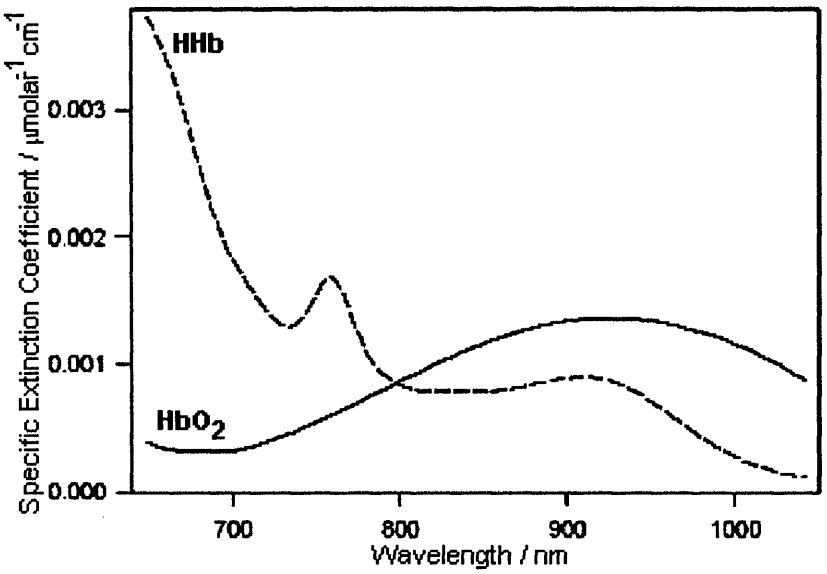

Figure 2-1 Absorption spectrum of Haemoglobin

(Elwell, C. E. 1995)

Figure 2-1 shows the cross-over in absorption spectra of oxygenated haemoglobin (HbO_2) and de-oxygenated haemoglobin (HHb) at roughly 800 nm, called the isobestic point. Using two wavelengths near the cross-over point, absorption data can be used to estimate oxygenation levels (Elwell, C. E. 1995).

2.2 NIR Instrumentation

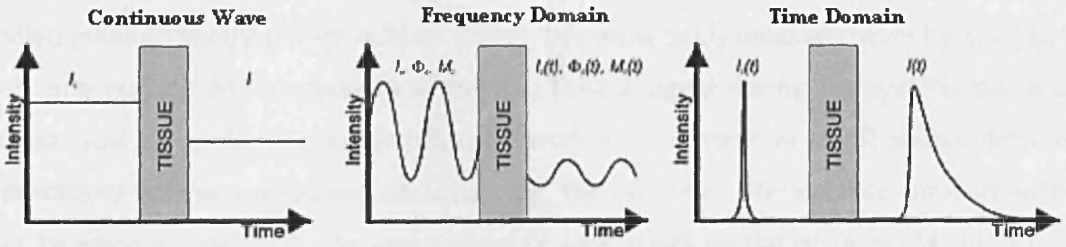

Figure 2-2 Illustrations of the various data sets that can be acquired 1) intensity difference, 2) modulation depth and phase change and 3) time resolved data measurements. (Schmidt 1999)

There are three commonly-used approaches for measuring the optical properties of tissues with near-infrared light. Continuous wave systems, left in Figure 2-2, record the changes in transmitted intensity, whereas frequency-domain (middle) and time-domain systems (right) record additional information. The following sections discuss the instrumentation used for each approach.

2.2.1 Continuous Wave Systems

Optical investigations on the human body, gaining information via transmitted light from a constant source, have been performed for nearly two hundred years (Bright 1831). Continuous wave (CW) systems use a constant or low-frequency modulated source(s) to obtain absorption data, which can be then used to find oxygenation levels (Gibson et al. 2005a).

Oxygen concentration can be measured invasively, but with a time constant of around 30 min (Webster G J 1998). For critically ill patients, continuous monitoring is vital to recognise changes in oxygenation levels in order to take corrective action. Thus, CW techniques for monitoring O_2, CO_2, and overall arterial oxygen saturation, SaO_2, have been developed.

SaO_2 was initially measured non-invasively by passing light through the ear-lobe (Merrick EB and Hayes TJ 1976) using eight wavelengths to discriminate between a variety of absorbers in tissue (e.g. melanin, water, etc.). A two-wavelength method, called pulse oximetry (Yoshiya et al. 1980), performs SaO_2 measurements by analysing the time-varying AC component of the transmitted signal during the systolic phase of blood flow in tissue. Transmission measurements are made at small source-detector separations across a thickness of tissue, e.g. the ear lobe. Reflectance measurements can be made at small (<1 cm) source-detector separations on flat surfaces (Mendelson Y et al. 1983), and can hence be used at various locations on the body (e.g. chest, forehead, limbs). Pulse oximetry systems are commonplace in hospitals and GP surgeries, and are even available for home use on digits or ear lobes.

Near-infrared spectroscopy (NIRS) is a tool for continuously and non-invasively monitoring haemodynamics in human organs (Elwell, C. E. 1995). A multi-wavelength source, e.g.. a pair of laser diodes (§2.2.4.1), is used to continuously illuminate the surface of the subject, with a detector (§2.2.4.3) recording the transmitted light a known distance away. Chromophore (e.g. HbO_2, HHb) changes within the tissue, varying with oxygenation level, can be measured by recording the changes in intensity, and inverting the Beer-Lambert law (Elwell, C. E. 1995). Absolute measurements are not common for this technique, with most measurements taken relative to an arbitrary background, typically at the start of the measurement period.

Optical topography is the two-dimensional (2D) determination of the concentrations of HHb and HbO_2 of tissues on a surface at a given depth (Obrig and Villringer 2003, Koizumi et al. 2003), and can be thought of as making multiple NIRS measurements. The study of haemodynamic changes, e.g. in the cortex, is currently the most common application of CW imaging (Gibson et al. 2005a). Multiple measurements of diffuse reflectance are acquired at small source-detector separations over large tissue areas, with measurements made either sequentially or simultaneously by individually modulating each source.

Images can be reconstructed from CW data using a linear reconstruction methods (§2.3.3.3). A finite-element mesh is created to represent the geometry using estimatations of average optical properties. A matrix of the relationship between fibre positions and measurements is then calculated and inverted. If the inversion is done prior to imaging, images can be produced in real time by multiplying the inverted matrix with the measured changes in the log of the signal amplitude.

One approach for CW topography is frequency multiplexing (Siegel et al. 1999), allowing detection of transmitted light from multiple sources simultaneously. Laser light is used to continuously illuminate multiple positions on a surface via fibre-optics. The light has a different modulation frequency for each wavelength and source channel. Source and detector fibres are held rigidly against the surface by a plastic or aluminium holder, allowing precise measurement of the optical fibre positions. The transmitted light, carried by the detector fibres, is measured by a high-sensitivity photodetector, such as avalanche photodiodes (APDs) or photomultiplier tubes (PMTs), as discussed in §2.2.4.3. The output from each detector is fed into a set of lock-in amplifiers which can discriminate between the different frequencies in the detected signal. This method allows all sources to be illuminated simultaneously, dramatically increasing the speed at which images can be produced.

The commercial Hitachi ETG-100 (Yamashita et al. 1999), typical of current systems, has 20 frequency multiplexed laser diode sources (10 at each of 780 and 830 nm), and 8 APDs. The ETG-100 has been used in a wide variety of investigations (Maki et al. 1995, Watanabe et al. 1998, Watanabe et al. 2000, Takahashi et al. 2000, Yamashita et al. 2001, Watanabe et al. 2002, Koizumi et al. 2003, Obata et al. 2003). A more recent system developed by Hitachi, the ETG-7000, can image the entire adult cortex with 40 pairs of laser diodes and 40 APDs. Other similar systems have also been employed to image the cortex of both newborn babies and adults. (Hintz et al. 2001) used a system with 18 laser diode sources and 16 photodiode detectors for a passive motor activation study in newborn babies. The CW4 system has 16 laser diode sources and 16 APDs, and has been used for motor cortex activation studies in adults (Franceschini et al. 2003).

A new approach to optical topography has been created at University College London (UCL) which involves using software to demultiplex the multiple source signals (Everdell et al. 2004). This allows great flexibility in the number and positioning of sources and detectors. The system currently employs 32 laser diode sources (16 at 785 nm and 16 at 850 nm) and 16 APDs.

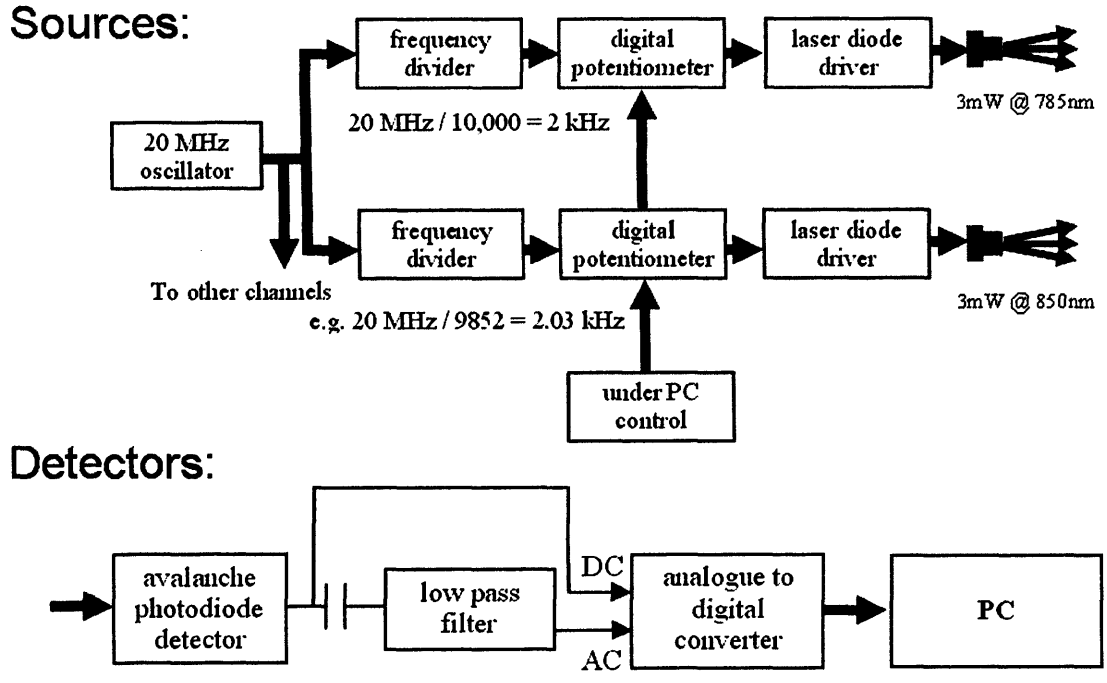

Figure 2-3 Diagram of the UCL frequency modulated CW system. (Everdell et al. 2004)

A diagram of the laser sources and detection system can be found above in Figure 2-3. The multiplexing frequencies are all derived from a single 20 MHz quartz oscillator, which prevents any relative drift in frequency between different sources. A frequency divider is used to create the different frequencies for each source, ranging from 2 kHz to 4 kHz. The frequencies are kept within one octave to prevent any possible interference from harmonics. A digital potentiometer enables the amplitude of the resulting square wave to be adjusted to the required level. The square waves then modulate a laser diode via a driver circuit. The mean power emitted by each laser diode is approximately 2 mW.

The 8 APDs (C5460-01 Hamamatsu, Japan) measure a range of approximately 0 - 100 kHz. The signal from the APDs is AC coupled into a low pass filter, preventing aliasing by keeping the signal below the Nyquist frequency of the analogue to digital converter (ADC), 10 kHz. The signal can be sampled directly from the APD (both DC and AC components) or from the output of the low pass filter (AC component only). A fast Fourier transform (FFT) is subsequently performed in software to separate the different source signals. This represents a novel alternative to the more usual technique of using lock-in amplifiers, reducing the cost of increasing the number of channels and improving the flexibility of the system.

A spatial map of the optical absorption of the tissue under interrogation can be built up from the measurements (Everdell et al. 2004). The system is designed to be able to produce images at 10 Hz with the information from 32 detectors. There is an inverse relationship between the number of detectors being used and the frame rate that can be achieved. Thus a system with just 16 detectors gathering data can operate at a rate of 20 frames per second. Using fewer detectors with a faster acquisition rate would allow the system to investigate fast neuronal signals (Franceschini and Boas 2004). These signals are thought to originate from the changes in refractive index that occur as a result of neuronal depolarisation. The timescale of the changes, however, is much smaller than that of the haemodynamic responses, of the order of 10 - 100 ms.

CW systems have also been constructed to perform tomographic (3D) imaging (Colak et al. 1999, Siegel et al. 1999, Schmitz et al. 2002). A major problem with these systems is that the images produced have relatively low spatial resolutions. However, it has been shown that, due to the fast acquisition rate, using vascular rhythms can improve the accuracy of images and can reveal functional activity (Barbour et al. 2001).

2.2.2 Frequency-Domain systems

Frequency-domain systems use continuous wave light sources (typically laser diodes §2.2.4.1), modulated by a radio-frequency signal (usually 50-500 MHz) (Nissilä et al. 2002). The amplitude and phase of the detected signal from an appropriate high-bandwidth detector (e.g. PMT or APD, depending on the desired sensitivity, §2.2.4.3) are usually derived using lock-in detection, as with frequency multiplexed continuous wave (§2.2.1) measurements. The detected signal is digitized over an appropriate period of time, and phase and amplitude are computed. Images are reconstructed by modelling photon transport through the interrogated volume and iterating the model until convergence with measured data is reached (§2.3.3). Phase measurement for NIRS and imaging is reviewed in (Chance et al. 1998).

Frequency domain source and detector signals appear very similar to those for multiplexed continuous wave. However, multiplexed CW measurements only record the change in intensity, *I*, using the modulation frequency to distinguish between sources. Frequency domain systems measure the resulting change in amplitude, *A*, and also phase, Φ, as shown in Figure 2-4. The additional measurements are required to separate the effects of μ_s' and μ_a (§2.3.3.5)

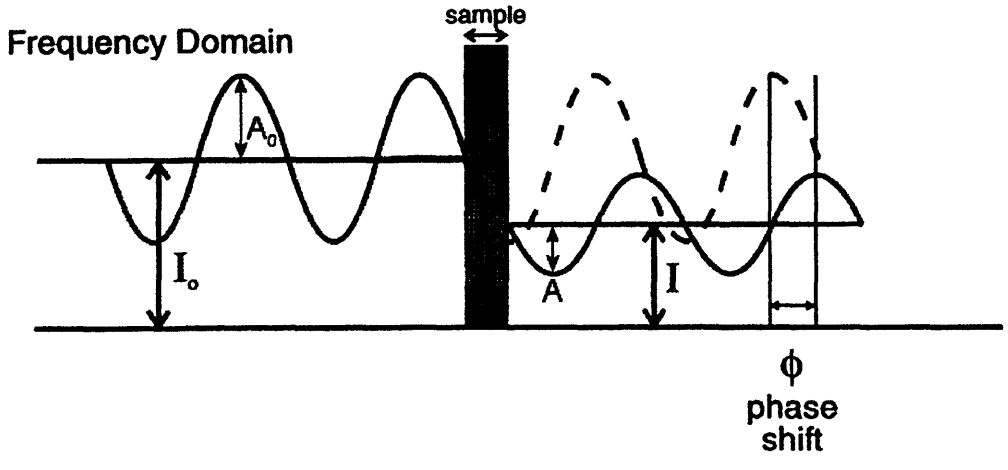

Figure 2-4 Diagram of the datatypes extracted for frequency-domain systems. The input signal has a known DC offset, I_0, amplitude A_0. The phase shift, Φ, and change in amplitude, A/A_0, are measured instead of the change in DC intensity, as recorded by continuous wave measurements.

An example of a frequency-domain instrument is shown in Figure 2-5. The HUT (Helsinki University of Technology) system (Nissilä et al. 2005) has two 5 mW frequency multiplexed laser diodes operating at 760 nm and 830 nm. The 16 source fibres are time-multiplexed using a fibre-optic switch (VX500-16 DiCon, USA) and one of the two wavelengths is selected using a DiCon 1x2 prism switch. The signals from the PMTs are mixed to an intermediate frequency of 5 kHz, and the phase and amplitude are calculated in software from signals digitized using two synchronized PCI-6704E cards (National Instruments, USA). A comparison between the HUT system and MONSTIR-03 is given in (Nissilä 2006).

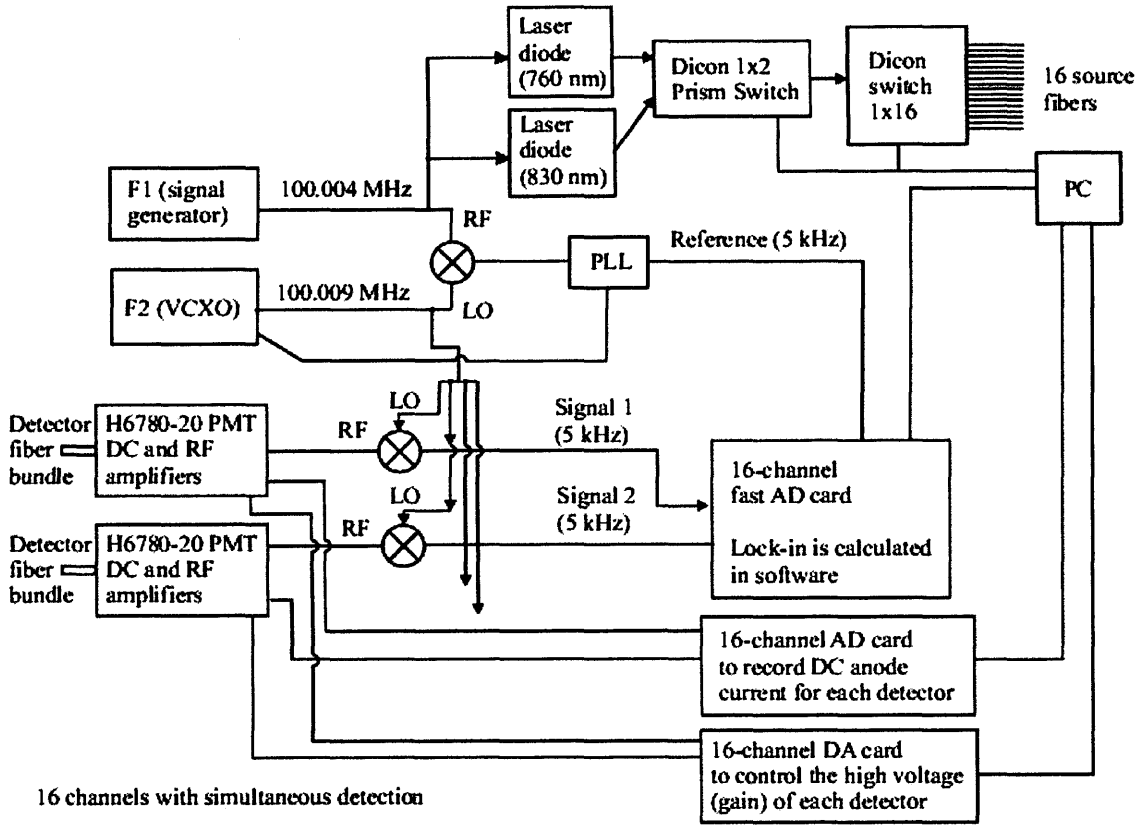

Figure 2-5 Diagram of the HUT frequency-domain system. (Nissilä et al. 2005)

A previously determined look-up table is used to change the gain of the detectors when the active source fibre is switched. This provides a suitable dynamic range, analogous to the variable optical attenuators (VOAs) used in MONSTIR (§2.2.4.1 and §3.5.2). An advantage of this approach is that the signal-to-noise is improved at short source-detector separations, but the actual dynamic range achieved with gain switching is not as large as with MONSTIR's VOAs. The dynamic range of the HUT system, including detector range and switching, is 10^7 as opposed to 10^9 with MONSTIR. Sixteen parallel detection channels pass light to the PMTs, from which the signals are digitised using two synchronized DAC cards.

The use of frequency domain imaging systems has been widely explored, e.g. by Carl Zeiss (Kaschke et al. 1994, Moesta et al. 1996) and by Siemens (Götz et al. 1998). The performance of both systems during quite extensive trials fell below that required of a method of screening for breast cancer, but various improvements to the Carl Zeiss system and their reconstruction method have since been implemented (Franceschini et al. 1997, Fantini et al. 1998).

A variety of frequency domain systems have been developed for both optical topography (Danen et al. 1998, Franceschini et al. 2000) and optical tomography (Pogue et al. 2001a). (Culver et al. 2003) built a hybrid CW / frequency-domain device for optical tomography, combining the benefits of speed and low cost of CW with the separation of scatter and absorption available from the amplitude and phase data.

2.2.3 Time Domain systems

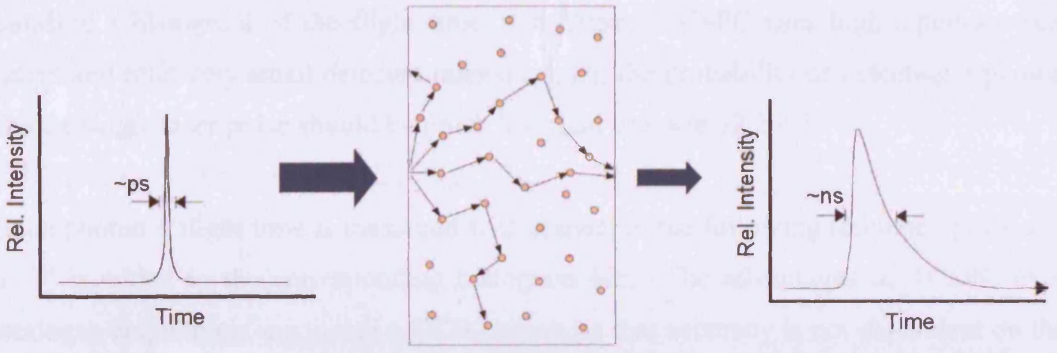

Figure 2-6 Time-domain systems use picosecond pulses (left) to illuminate the surface of an object, recording the resulting temporal distribution (right) of light at a separate point on the surface. The temporal broadening of short pulses is due to multiple scattering events (centre). (Schmidt 1999)

The temporal distribution of photons produced when a short duration (picosecond) pulse of light is transmitted through a highly scattering medium, e.g. tissue, is called a temporal point spread function (TPSF, (Hebden et al. 1997)). After travelling through several centimetres of tissue, the TPSFs will broaden over a few nanoseconds, as shown in Figure 2-6. The shape of the TPSFs can be used to calculate the intensity and mean flight time which provide information about tissue absorption and scatter.

Time domain systems resolve the photon transit time through tissue, as opposed to CW (§2.2.1) techniques which give only intensity measurements of transmitted light. The potential datatypes measured by time-domain systems are expected to give both a better depth sensitivity and spatial resolution, which CW systems can only produce in a limited fashion by using various source-detector separations. Time-domain measurements, e.g. intensity and meantime, are the Fourier equivalent of those recorded with frequency-domain systems, amplitude and phase respectively, but at all frequencies. However other datatypes (§2.3.1.1), possibly more beneficial for reconstructions (Schweiger et al 1997), can be produced from time-resolved data. As with reconstructions of frequency-domain data, images are produced from time-domain data by creating a model of photon transport and iteratively comparing the modelled predictions with measured data (§2.3.3).

Time-domain measurements can be performed using a method called time correlated single photon counting (TCSPC, (Becker 2005b)). TCSPC involves the detection of a single photon from a pulsed input, measuring the flight time of individual photons, and building a histogram of the flight times – a TPSF. TCSPC uses high-repetition rate lasers and relatively small detected intensities, i.e. the probability of detecting a photon from a single laser pulse should be much less than one, see §2.2.4.5.

Each photon's flight time is measured with respect to the following reference pulse and a '1' is added to the corresponding histogram bin. The advantages of TCSPC over analogue acquisition, e.g. using a CCD camera, is that accuracy is not dependent on the size or shape of the detector's pulse height distribution, only the accuracy in counting those pulses.

Recently, time-gated systems have been developed for various applications of optical imaging: optical mammography (Ntziachristos et al. 1998, Grosenick et al. 1999, Hebden et al. 2001), the study of blood oxygenation in the arm during a motor activity (Hillman et al. 2001), neonatal brain imaging (Hintz et al. 1998, Hebden et al. 2002) and adult brain imaging (Ntziachristos et al. 1999, Hoshi et al. 2000, Steinbrink et al. 2001, Liebert A et al. 2003). Different parts of the TPSF give information about different depths inside the tissue. TPSFs from reflectance measurements, for example, contain early photons that have travelled a short path, and thus have probed only superficial layers, and later photons that have probed deeper tissues.

There have been recent applications of time-gated systems to neuroimaging. (Okada et al. 1997) proposed a theoretical study of cerebral imaging with a time domain system, supported by measurements on a phantom. (Eda et al. 1999) described a similar system that they tested on scattering phantoms. (Ntziachristos et al. 1999) used a time-domain system for functional brain imaging during motor cortex activation, and demonstrated the good performance of the system in terms of quantification of absorption changes. (Hoshi et al. 2000) used their time-domain system for cerebral imaging during memory tasks. (Steinbrink et al. 2001) first demonstrated experimentally that time-domain systems enabled depth resolution of brain signals, and were able to distinguish between extra- and intracranial signal during a Valsalva manoeuvre (Steinbrink et al. 2001), a motor activation (Steinbrink et al. 2001), and a visual stimulation (Liebert A et al. 2003).

(Selb et al. 2005) have developed a time domain system based on a pulsed laser and an intensified CCD (ICCD) camera, illustrated in Figure 2-7. The source is a Ti:sapphire pulsed laser (MaiTai Spectra Physics, USA) emitting in the NIR region (750 to 850 nm) with a repetition rate of 80 MHz. The laser is coupled into one of the source fibres (diameter 400 μm), which then delivers the light to the subject's head. Source positions can be selected by scanning the laser beam over an array of source fibre ends with a galvanometer (§2.2.4.2). The diffuse light transmitted by the tissue is detected through optical fibres which deliver the light to an intensifier and the amplified image is in turn recorded on a CCD camera (PicoStar LaVision, Germany). The intensifier acts as a fast shutter, whose opening is triggered relative to the laser pulses. Each camera frame corresponds to one relative delay between the laser pulse and the gate opening, and is the image of all the fibre tips simultaneously. The signal for each fibre is extracted from the ICCD frame by spatially integrating the intensity on all pixels corresponding to this fibre. All camera frames are recorded on a PC for later processing. This system enables a parallel recording of all the detectors, which are imaged simultaneously on the ICCD array. Each detector position consists of seven fibres of different lengths, recording the same TPSF but with a relative delay dependent on their length. To record the TPSF from each fibre, the delay must be scanned electronically, typically from 0 to 4 ns in 50 ps steps. The drawback of this method is the time lost due to the electronic switching of the delay, 0.5 s per step. The time required to record a complete TPSF, which can be up to a few minutes, is also incompatible with functional imaging where behaviours occur on the time scale of seconds.

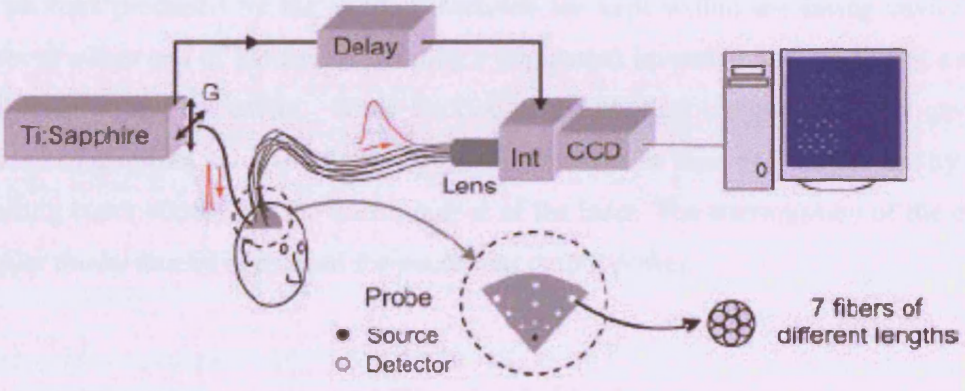

Figure 2-7 Experimental setup for time-gated Time Domain optical measurements. Int, image intensifier; CCD, charge-coupled device camera; G, galvanometer. (Selb et al. 2005)

2.2.4 Opto-electric Instrumentation

2.2.4.1 Source choices

"Laser" is an acronym for "Light Amplification by Stimulated Emission of Radiation". Lasers are at the core of photonics, and hence optical imaging, because laser light has a number of special properties:

- Lasers can emit light as a coherent beam which can propagate over long distances without much divergence and can be focused to very small spots.
- Laser light can be tailored to have a very narrow bandwidth, while most other sources, e.g. filament bulbs, emit light with a very broad spectrum.
- Laser light may be emitted continuously, frequency-modulated, or in the form of short or ultrashort pulses, with durations from microseconds down to a few femtoseconds (10^{-15} s).

The two main choices for NIR sources are solid-state lasers or semiconductor laser-diodes. Both options can be tailored to a desired wavelength, but differ most importantly in power output and size.

Solid-state lasers produce monochromatic, coherent light by amplified stimulated emission. A lasing cavity is a crystalline matrix, doped with selected ions to produce the required wavelength. Electrons from the doped ions are excited within the cavity by an electrical or optical pump. The electrons are kept in excited states by the pump, and the photons produced by the excited electrons are kept within the lasing cavity by a mirror at either end of the cavity, creating a population inversion and producing a stable oscillation within the cavity. Some fraction of the photons circulating in the cavity is usually transmitted by a partially transparent mirror at one end of the cavity. The resulting beam constitutes the useful output of the laser. The transmission of the output coupler mirror can be optimized for maximum output power.

Semiconductor lasers are similar to light emitting diodes (LEDs) at low voltages, with optical gain achieved by stimulated emission at a semiconducting boundary. Most semiconductor lasers are laser diodes, which are pumped by an electrical current in a region where n-doped and p-doped semiconducting materials meet. There are also optically pumped semiconductor lasers, where electrons are excited by absorbed pump light. The emission wavelength depends on the energy levels of the valence and conduction bands in the two materials. Semiconducting materials can therefore be chosen to tailor the wavelength. Laser diodes (LDs) are normally built as edge-emitting lasers, where the laser cavity is formed by cleaved edges of a semiconductor wafer. The typical arrangement (called double heterostructure) restricts the generated carriers to a narrow region and at the same time serves as a waveguide for the optical field. Some modern kinds of LDs are of the surface-emitting type, where the emission direction is perpendicular to the wafer surface, though these tend to generate reduced output power.

Laser efficiencies, the output power emitted as percentage of the input electrical power, are usually of the order of 25 % for optically-pumped solid-state laser systems, though values above 30 % are possible. Laser diodes are the main choice for optically pumping solid-state lasers, as this increases the output efficiency by up to 10 %. Pure laser diode systems can reach the highest efficiencies, above 60 %. Argon-ion lasers generally have efficiencies of a few percent. This efficiency drops to ~0.1 % when an argon-ion laser is used as the pump for titanium-doped sapphire (Ti^{3+}:sapphire) cavities, widely used for femtosecond solid-state lasers (Paschotta R. and Keller U. 2003, Müller D. 2004).

Laser diodes are used directly as sources for many CW systems (§2.2.1) as they are much smaller (~mm diameter) and can be modulated without difficulty (Everdell et al. 2004) in comparison to solid-state lasers. Laser diodes are hence also used frequently in frequency-domain systems. Solid-state lasers require exact alignment of the optical components, and must be re-calibrated after being moved, but have the advantages of better temporal stability and potentially far greater power compared to laser diodes.

MONSTIR's source is a custom-built solid-state laser based on two Type A-70-FC-WS (IMRA America, USA). This uses a coiled optical fibre as a lasing cavity, pumped by laser diodes. Fibre lasers are more compact and do not require time-consuming readjustment after being transported.

Wavelength

Due to the absorption of water above 900 nm and haemoglobin below 600 nm, the 'near-infrared window' used for tissue optics is between 650 and 850 nm. Sources are often chosen either side of the isobestic point of haemoglobin, the point at which the absorption coefficients of oxyhaemoglobin (HbO_2) and deoxyhaemoglobin (HHb) are equal, roughly 800 nm (§2.1.2). A typical pair of wavelengths might be 780 and 830 nm, but the wavelengths used for a given study are often determined in an ad hoc way and usually are dictated by the availability of appropriate light sources (Cope 1991). However, more recently it has been shown (Yamashita et al. 2001, Strangman et al. 2003, Uludag et al. 2004) that using a wavelength between 660 and 760 nm rather than 780 nm provides better differentiation between HHb and HbO_2. (Pifferi et al. 2003) and (Taroni et al. 2004) used four wavelengths (683 nm, 785 nm, 912 nm, and 975 nm) to image the breast. The wavelengths were selected empirically to optimise distinction between HbO_2, HHb, water and lipids. They also found that using four shorter wavelengths (637 nm, 656 nm, 683 nm, and 785 nm) improved the distinction between tumours and cysts.

(Uludag et al. 2004) used both theoretical and experimental methods to investigate cross-talk and the way in which the determination of HHb and HbO_2 concentrations from dual wavelength measurements is affected by noise and error in the measurement. Their results agreed with those of (Yamashita et al. 2001) and (Strangman et al. 2003), i.e. that one of the selected wavelengths should be much shorter than 780 nm.

Laser Safety

The tissues most at risk from any laser irradiation are those in the eye. Absorption in the cornea and lens is very low at NIR wavelengths. They therefore have a low risk of damage. The retina is at highest risk, due to the focusing of the beam through the lens. It should be noted that while the blink reflex, the natural aversion to overly bright light after ~0.25 s (Gerstman et al. 1995), provides some protection against visible light, it cannot be relied upon as a safety mechanism at NIR wavelengths, as NIR is invisible.

The lens focuses parallel light onto a small spot on the retina, strongly increasing the irradiance – especially when staring directly into a collimated laser beam. Moreover, absorption is very strong in the highly pigmented layer underneath the receptor cells. The wavelength region that can cause most damage to the retina is 700 to 1400 nm. The most common type of damage is thermal (burns).

Laser safety requirements in the UK are laid out in the British Standards Institution's (BSI) "Safety of Lasers" (EN 60825-1:1994). The document defines the Maximum Permissible Exposure (MPE), and requires (Section 13.3) the average exposure for a pulse train to not exceed the MPE for a single pulse of equivalent duration. Attenuating glasses / goggles are used in situations where the laser's beam could be transmitted into the eye. In the case of imaging the neonatal brain, where the infant's movement could cause light to enter the eye, the laser's power is reduced beneath the MPE by using neutral density filters in the laser.

In addition to these operational requirements, lasers are classified as follows: (Laser Institute of America 2005)

Class 1 'Lasers which are safe under reasonably foreseeable conditions of operation.'

Class 2 'Lasers emitting visible radiation for which the natural aversion to bright light (blink reflex) prevents retinal injury.'

Class 1M & 2M Same as the above two classifications but adding 'provided the user does not employ concentration optics.'

Class 3R 'Output up to five times the safety limit of classes 1 & 2.'

Class 3B 'Direct intrabeam viewing of these lasers is always hazardous. Viewing diffuse reflections / scattered beam is usually safe.'

Class 4 'Lasers which are also capable of producing hazardous diffuse reflections. They may cause skin injuries and could also constitute a fire hazard. Their use requires extreme caution.'

MONSTIR's IMRA laser is a Class 3B. The power produced by the laser needs to be sufficient to detect photons across the whole head or breast, in order for full 3D datasets to be acquired. The shutters and use of fibre holders ensure that no intrabeam viewing is possible in clinical situations, but safety glasses should always be worn when using MONSTIR in the lab.

2.2.4.2 Optical switches

The light created by a single source typically needs to be switched between various positions on the surface of the subject. Irrespective of number of channels required, the two most common solutions are mirror galvanometers or fibre switches.

Galvanometers originated as current-measuring devices, moving an indicator needle with increased current. However, galvanometers can also be used to precisely position a mirror by computer-controlled currents. Mirror galvanometer systems are used for channel switching by reflecting an incoming beam onto an outgoing fibre end. These are typically high power galvanometer mechanisms with closed loop servo control systems, resulting in frequency responses over 1 kHz. However, galvanometer systems are typically constructed in-house and tend to suffer from optical leakage between source channels as a result of the proximity of all of the output fibre ends.

Fibre switches are more widely available commercially, for example the DiCon fibre switch used in MONSTIR and HUT frequency domain system. The input fibre end is typically mounted on a stepper motor, with the output fibre ends positioned around a circumference. A digital input is accepted to move the motor to a given position, coupling the input fibre to the selected output. Unwanted light leaking into neighbouring channels is typically 10^{-8} times the power transmitted through the selected output fibre. However, fibre switches tend to have much slower switching times, ~100 ms between positions.

2.2.4.3 Photodetectors

Photodetectors are devices used for the detection of light. Applications vary in terms of wavelength, maximum optical power, dynamic range, cost, etc., and there are many types of photodetectors which may be appropriate in a particular case. The two main photodetector types used in optical imaging are:

- **Photodiodes**: semiconductor devices with a p-n junction or p-i-n structure (i stands for "intrinsic material"). Light is absorbed in a depletion region, generating electrical carriers and thus a photocurrent. Such devices can be very compact, fast, highly linear, and exhibit a high quantum efficiency (i.e. generate nearly one electron per incident photon) and a high dynamic range, provided that they are operated in combination with suitable electronics.
- **Photomultipliers**: based on the photoelectric effect and electron multiplication within a vacuum tube; can combine extremely high sensitivity with high speed, but are expensive, bulky, and need a high operating voltage

Specifically for time-resolved measurements, streak cameras are photomultiplier systems which covert the temporal profile of a light pulse into a spatial profile across the front of a detector. Streak cameras can achieve temporal resolutions up to 100 femtoseconds. However, they have minimal detection areas and are typically too bulky and expensive to be included in multi-channel systems.

Very good noise performance can be achieved with photodiodes and photomultipliers. A fundamental limit to this is usually given by shot noise, resulting from the random occurrence of photon absorption events. Other photodetector types that can be used include phototransistors, photoresistors, pyroelectric photodetectors, and thermal detectors (powermeters). Photodetectors are described in more detail below.

Avalanche Photodiodes

Avalanche photodiodes (APDs) are a type of photodiode typically used in continuous wave systems (§2.2.1). These operate with a relatively high reverse voltages, typically tens or even hundreds of volts, and sometimes just below breakdown. In this regime, carriers (electrons and holes) excited by incident photons are rapidly accelerated in a strong internal electric field. The energy of the carriers increases until collisions with the semiconductor lattice generate secondary carriers, which are then picked up by the field and generate further carriers, effectively amplifying the photocurrent. APDs can be used to build very sensitive detectors, which need less electronic signal amplification and are thus less sensitive to electronic noise. However, the avalanche process is subject to high noise, which can offset the mentioned advantages. APDs improve the lowest detection rate by up to ten times compared to standard PDs and have good temporal resolution, but have inferior linearity and reliability, and are much more expensive.

Silicon-based APDs are sensitive in the wavelength region of about 450-1000 nm, with the maximum responsivity occurring around 600-800 nm, ideal for NIR imaging. This peak sensitivity is at somewhat shorter wavelengths than for standard silicon p-i-n diodes. For longer wavelengths, APDs based on germanium or indium gallium arsenide (InGaAs) are used.

APDs can be used for photon counting, e.g. in time-domain systems (§2.2.3), with background count rates below 10^4 counts per second (cps). In that case, the diode is operated slightly above the breakdown threshold voltage, where a single electron-hole pair can trigger a strong avalanche. In case of such an event, electronics are attached to reduce the voltage at the diode below the threshold voltage for a short time. This dead time allows the APD to recover, but reduces the maximum count rate significantly. The requirement for a recovery delay also causes a trade-off between response time and detection area. APDs are more stable over their lifetime and have superior quantum efficiencies compared to photomultiplier tubes, but are unsuitable for MONSTIR due to their longer dead times, low count rates, and minimal detection areas.

Photomultiplier tubes

The basic design of current PMTs has been around since 1939, when Zworykin and Rajchman (Zworykin V.K. 1939) first developed a tube that not only converted an incoming photon into photo-electrons, but also amplified the signal by electrostatically focussing the electron beam onto a number of secondary emissive plates. Material science advances have allowed greater conversion efficiency, and simulations of electron paths through the PMT have allowed refinement of the internal design, but the basic design remains the same.

The internal structure of a typical PMT is shown in Figure 2-8. All PMTs begin with the photoelectric effect: photons are incident on a negatively-charged semiconductor, called the photocathode, from which electrons are excited and emitted into a vacuum, labelled (a) in Figure 2-8. These photo-electrons are accelerated and, in most cases, focussed before colliding with a series of plates called dynodes, Figure 2-8 position (b). The impact with the dynodes causes secondary emission, multiplying the electrons and directing them to the anode, indicated as (c) in Figure 2-8.

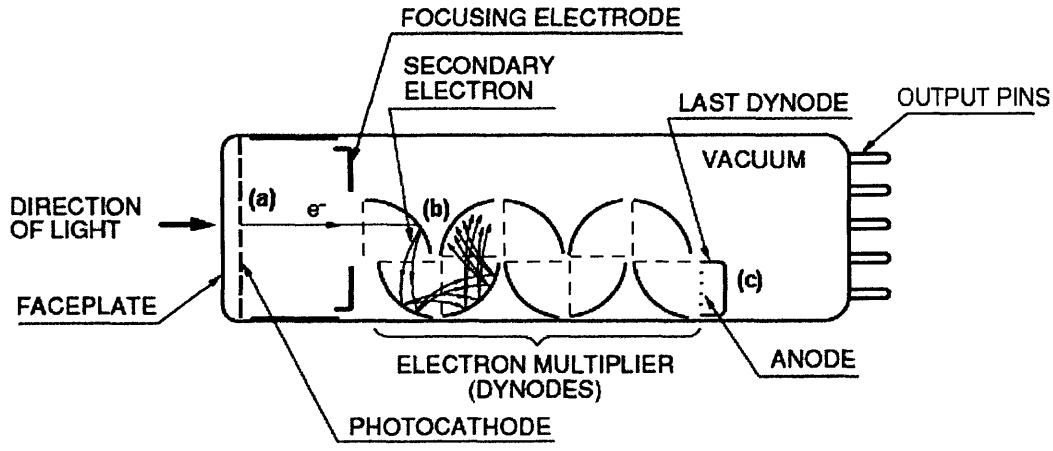

Figure 2-8 Basic PMT design, showing the electron path into dynode section (Hamamatsu, Japan 2006)

Photocathodes can be made from a variety of semiconductors. Each material has a wavelength range over which photons can be converted to photo-electrons, e.g. a multi-alkali for broad-band visible, or InGaAs for near-infrared detection. The quantum efficiency, defined as the ratio of incoming photons to emitted electrons, also differs between photocathode materials.

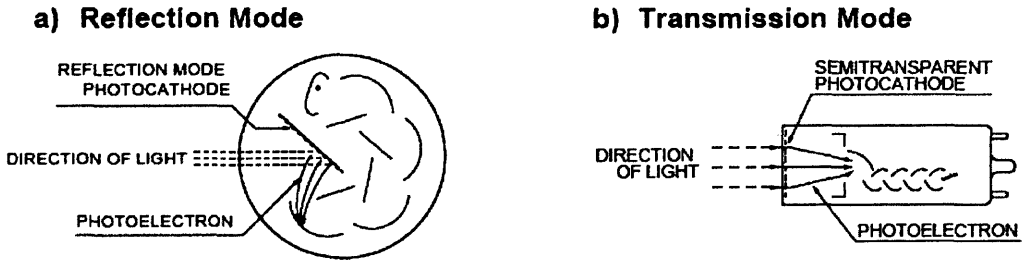

Figure 2-9 Photocathode emission modes (Hamamatsu, Japan 2006)

Photomultiplier tubes operate in reflection- or transmission-mode. For reflection-mode PMTs, Figure 2-9 (a), incoming photons illuminate an opaque photocathode through the side of the body, and photoelectrons are emitted from the same side of the photocathode. This photocathode design is typically used in side-on PMTs, Figure 2-10 (a). Side-on PMTs are generally lower priced and are widely used for spectrophotometers and general photometric systems.

The second PMT type, head-on type Figure 2-10 (b), typically has a semitransparent photocathode deposited upon the inner surface of the entrance window. This type operates in transmission-mode, Figure 2-9 (b), with photoelectrons emitted from the opposite side of the photocathode to the incident photons. The head-on type provides better spatial uniformity than the side-on type and can have a much larger photosensitive area.

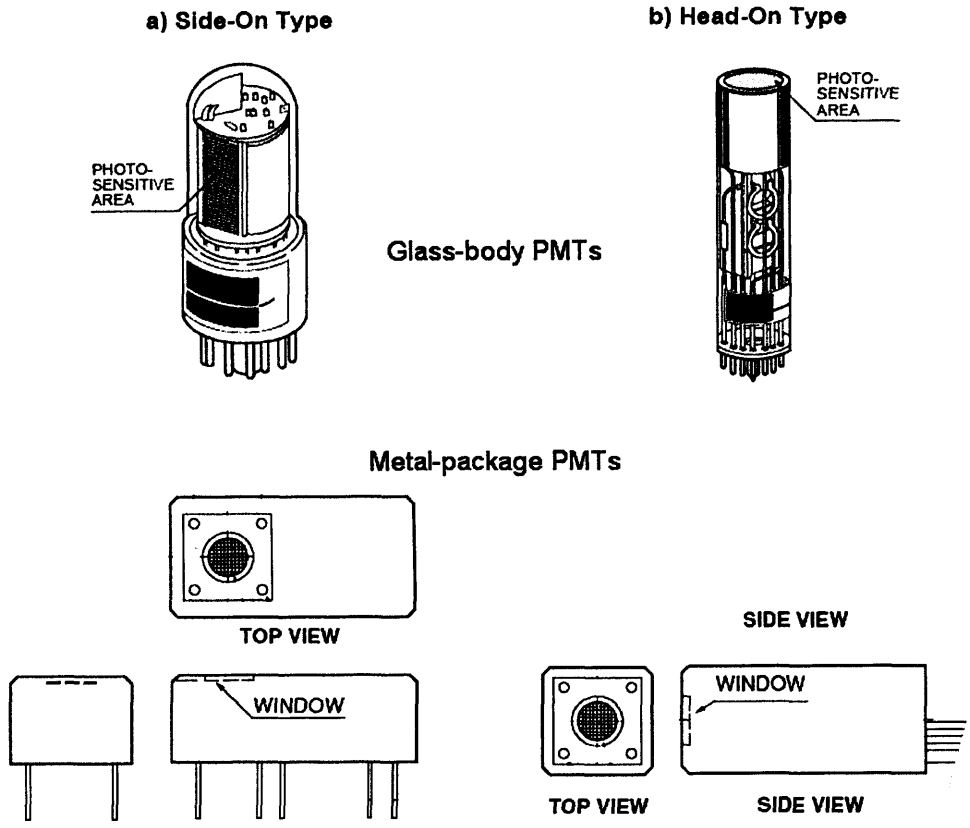

Figure 2-10 The two main PMT types are side-on (left) and head-on (right). Each PMT type can be constructed as glass-type PMTs (upper), or as metal-packages right (lower) (Hamamatsu, Japan 2006).

Metal-package PMTs, shown Figure 2-10 (lower), have been developed more recently. These contain a miniaturised version of a glass-body PMT, with the same possible selections of photocathodes and dynode designs (see below). The package also contains power supply and signal conditioning electronics such that it can be used easily and without additional electronics. Metal package PMTs are used in mainly in applications that have space restrictions, or require fixed coupling to optical fibres.

The dynode construction controls the electron paths through a PMT, label (b) in Figure 2-8. Dynodes are metal electrodes, e.g. nickel or stainless steel, covered with an emissive substrate, e.g. beryllium or magnesium oxide. Dynode sections usually contain up to tens of stages of secondary-emissive electrodes, each having curved surfaces in order to direct electrons.

The electron trajectory through the PMT is primarily determined by the dynode design. A delta-function input of light will be broadened and delayed, producing an analogue pulse, as shown in Figure 2-11, with set timing characteristics for each dynode design. The delay between light input and the resulting pulse peak is called electron transit time (ETT). The time taken for the signal to increase from 10 to 90 % of the peak is the rise time, and fall time is the equivalent for the end of the pulse. In addition, the transit time spread (TTS) is usually expressed as the full-width half-maximum (FWHM) of the output pulse. TTS is a measure of the error in timing accuracy introduced by the PMT.

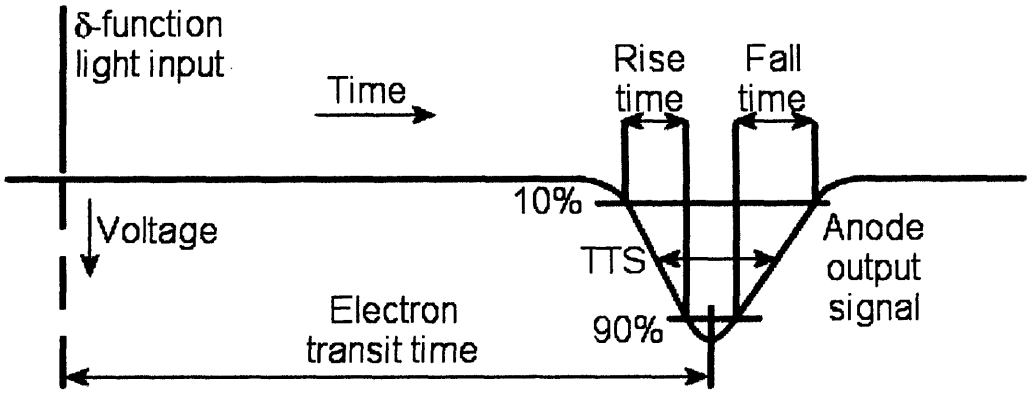

Figure 2-11 Diagram of the PMT output resulting from a delta function photon input. 10% and 90% lines are relative to peak output voltage. TTS: Transit Time Spread

Each dynode construction will have its own response function, temporal responses, and collection efficiencies. Typical dynode constructions currently in use are listed below with the advantages and timing characteristics of each design (Hamamatsu, Japan 2006).

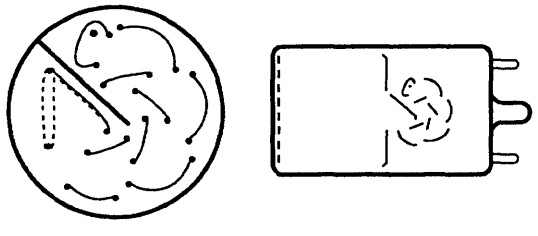

a) **Circular Cage** – Compact and used in all side-on and some head-on PMTs. Fast time response – ETT: 31 ns, TTS: 3.6 ns

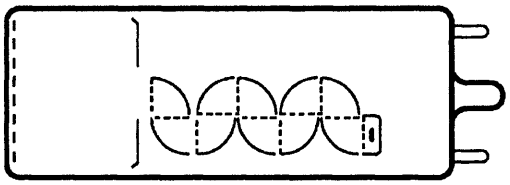

b) **Box-and-grid** – Widely used in head-on PMTs and providing high collection efficiency, resulting in high detection efficiency and uniformity – ETT: 57 - 70 ns, TTS: < 10 ns

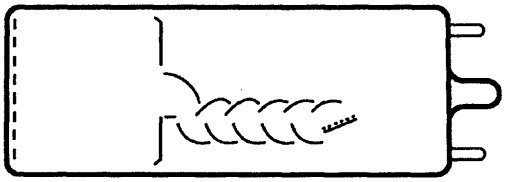

c) **Linear-focussed** – Also widely used in head-on PMTs. Fast temporal response, good time resolution and excellent output pulse linearity – ETT: 16 - 50 ns, TTS: 0.37 - 1.1 ns

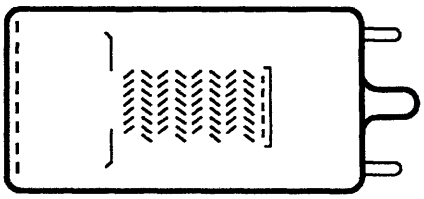

d) **Venetian blind** – Large collection field, hence mainly used in head-on PMTs with large photocathodes – ETT: 60 ns, TTS: < 10 ns

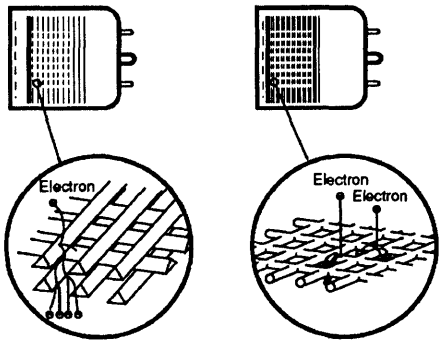

e) **Mesh** – Instead of planar dynodes, these have mesh electrodes stacked in close proximity to each other. Excellent linearity and magnetic immunity. Fine meshes are primarily for detection in high magnetic fields. Meshes also allow position-sensitive measurement – ETT: 15 ns, TTS: < 0.45 ns

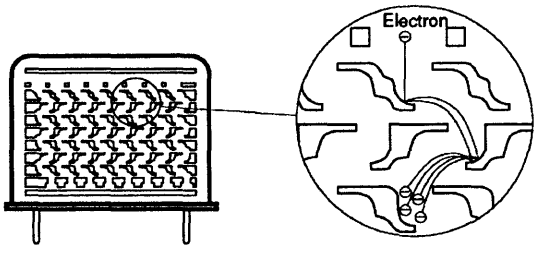

g) **Metal channel** – Micro-machined dynode plates, stacked according to simulated electron trajectories, keep the electron path as short as possible. This ensures excellent linearity, efficiency, and timing characteristics – ETT: 4.7 - 8.8 ns, TTS: 0.4 ns

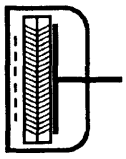

f) **Microchannel Plate (MCP)** – Sub-millimetre dynode channels exhibit dramatically improved timing resolution. As with mesh-type PMTs, MCP-PMTs are stable in high magnetic fields and can be used to provide position-sensitive measurements – ETT: 0.35 - 0.4 ns, TTS: < 0.45 ns

Microchannel plate (MCP) detectors, such as the MCP-PMTs used in MONSTIR (§2.2.5), have excellent time resolution in comparison with standard PMTs. The MCPs consist of a two-dimensional array of a great number of glass capillaries (channels) bundled in parallel and formed into the shape of a thin disk. Each microchannel has an internal diameter on the order of tens of microns with the inner wall processed to have the selected electrical resistance and emissive properties. These channels restrict the photoelectrons' and secondary emissions' motion and minimised the temporal dispersion of the output pulse.

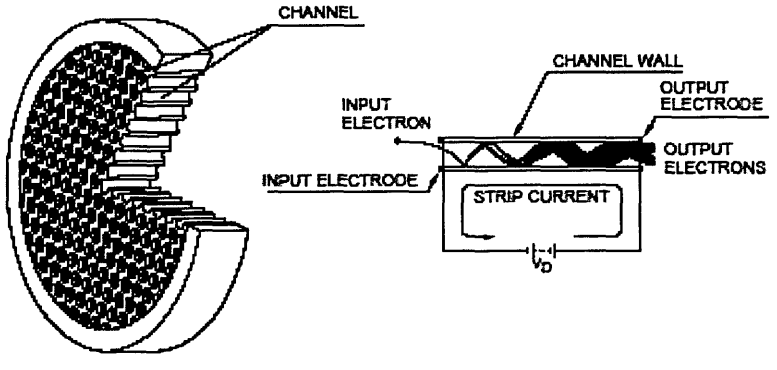

Figure 2-12 Schematic structure of an MCP (left) and secondary emission within the channels (right). (Hamamatsu, Japan 2006)

The TTS of MCP-PMT detectors are typically less than 50 ps whereas standard PMTs have a TTS nearer 300 ps. However, MCP-PMTs tend to have lower efficiencies (~3 %) compared to normal PMTs (~15 %), are much more expensive, and have shorter lifetimes due to faster degradation of the photocathode and micro-channels.

The properties of the PMT tube, as given in Table 2-1, are typically defined by the dynode structure. Magnetic immunity is defined as the maximum field, along the most susceptible PMT axis, at which the output does not deviate from given tolerances. Uniformity refers to the stability of the output signal as the input is scanned across the face of the PMT. Collection efficiency is the probability that photoelectrons emitted from the photocathode land in the effective area of the first dynode. The effective area of the first dynode is where electrons are multiplied without deviation from a favourable trajectory for further dynodes.

	Circular cage	Box-and-grid	Linear-focussed	Venetian blind	Fine mesh	MCP	Metal channel
Magnetic immunity / mT	0.1	0.1	0.1	0.1	500 - 1500*	1500*	5**
Uniformity	Poor	Good	Poor	Good	Good	Good	Good
Collection efficiency	Good	V. good	Good	Poor	Poor	Poor	Good
Rise Time / ns	0.9 – 3.0	6 - 20	0.7 - 3	6 - 18	1.5 - 5.5	0.1 - 0.3	0.65 - 1.5
Electron transit time (ETT) / ns	31	57 - 70	16 - 50	60	15	0.35 - 0.4	4.7 - 8.8
Transit Time Spread (TTS) / ns	3.6	< 10	0.37 - 1.1	< 10	< 0.45	< 0.1	0.4

Table 2-1 Comparison of PMT properties due to dynode construction. *Magnetic field parallel to tube axis, **Metal package PMT. (adapted from (Hamamatsu, Japan 2006))

The output from photomultiplier tubes can be classified as analogue or digital, depending on the incident light intensity and the bandwidth of the detector. Digital mode (also known as photon counting) uses a discriminator (§2.2.4.5) to separate the pulses created by individual photons from the background noise. Photon counting requires the incident light to be of low enough intensity for no more than one photoelectron to be emitted from the photocathode within the time resolution of the detector. If the incident intensity is increased beyond this level, the output pulses overlap and an analogue signal is produced by the detector.

PMTs have two primarily sources of error: dead-time and dark counts. A dead time is required to replace electrons that have been emitted from the photocathode and dynodes. Most PMTs have count rates that are highly linear over many orders of magnitude. However, count rates levels off near a saturation limit set by the dead-time. An estimate of the maximum detectable count rate can be calculated from the maximum continuous anode current, I_{anode}. The number of electrons at the anode, n_{anode}, equals the number of photoelectrons created at the photocathode, $n_{cathode}$, multiplied by the gain, G. The anode current can hence be expressed as (Schmidt 1999):

$$I_{anode} = \frac{n_{anode} e}{\Delta t} = \frac{(n_{cathode} G) e}{\Delta t} = Ge \times \left(\frac{n_{cathode}}{\Delta t} \right) \quad \text{(viii)}$$

The maximum rate at which photoelectrons are created, and hence the maximum detection rate, is therefore:

$$\left(\frac{n_{cathode}}{\Delta t} \right) = \frac{I_{anode}}{Ge} \quad \text{(ix)}$$

A higher maximum count rate would allow smaller source-detector separations to be used, and reduce the dynamic range required from any range compression, such as the VOAs used in MONSTIR (§2.2.4.4).

The photocathodes of the MCP-PMTs in MONSTIR are only illuminated across half of the emissive area for each channel. For a recommended anode current of 50 nA and gain of 10^6, MONSTIR's maximum count rate is ~1.5×10^5 cps. Above this rate the photocathode material is providing the photoelectrons, causing permanent damage to the photocathode and reducing the detector's quantum efficiency.

Dark counts are spontaneous thermal emissions. All detectors need to be combined with heat sinks to dissipate resistive heating due to the high voltage. PMTs can be chilled further to reduce the operating temperature and hence the background noise due to dark counts. For example, solid-state Peltier coolers are used to reduce the temperature of the MCP-PMTs in MONSTIR to about -25°C, reducing dark counts from a few thousand to a few counts per second. Dark counts can be further reduced by increasing the threshold of the discriminators (§2.2.4.5).

2.2.4.4 *Optical range compression*

Light transport in tissue is dominated by scatter and absorption. Beyond a few scatter lengths (~mm) light is effectively diffuse and isotropic. Recorded intensity drops off exponentially with distance from the source. A good approximation is that the measured intensity decreases by a factor of ten for each centimetre between the source and detector.

The right-hand plot in Figure 2-13 shows the range of intensities that were calculated for measurements taken around the circumference of a tissue-equivalent cylindrical phantom, as for the diagram on the left-hand of Figure 2-13. In this simulated example, the recorded intensities vary by up to 10^7 from a minimum directly opposite the source (channel 16) to a maximum for channels neighbouring the source (channels 1 and 32).

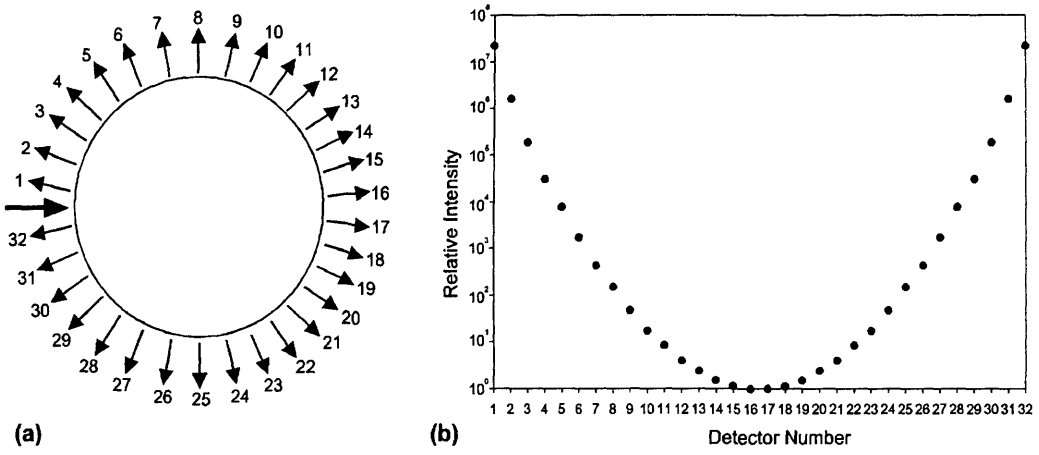

Figure 2-13 An example circular layout for the detectors (a) and the simulated intensity variation between channels (b). (Schmidt 1999)

Optical range compression is typically required in frequency- or time-domain systems because (Schmidt 1999) photodetectors:

- are highly sensitive and can be easily saturated or damaged by excessive illumination
- inherently have a dead time during which no signal can be detected. This imposes a maximum count rate, beyond which counts are lost or signals are distorted.

Cross-talk, the signal from one channel effecting the measurement of the neighbouring channel, also becomes problematic if multi-channel photodetectors are used.

This problem can be overcome in frequency-domain systems by gain-switching the detectors. A pre-determined lookup table is created, matching the appropriate gain for each detector to a given source channel. The gains are then switched by the control PC during acquisition. The advantage of this method is the lack of mechanical components and any optical interference introduced by said components. A settling time is required for most detectors, resulting in an additional delay between switching sources from ~ns to ~ms, depending on photodetector. However, the delay is typically shorter than that introduced with mechanical attenuators.

Another solution is to position optical attenuators in front of each detector channel to reduce the incident intensity. As with gain switching, the settings of the attenuators must be calculated prior to imaging. Discs with variable neutral densities are commercially available. These tend to be expensive and based on reflective attenuation, which causes unwanted reflections. Section §3.5.2, and (Jennions 2003) discusses the solutions of aperture and absorbing-film variable attenuation used in MONSTIR.

2.2.4.5 *Timing electronics*

Time correlated single photon counting (TCSPC, §2.2.3) depends on measuring the time elapsed between a photon being emitted from a source and arriving at a detector. Sources for TCSPC create ultrashort pulses with high repetition rates, and a reference signal must be produced simultaneously. This is achieved by either illuminating a dedicated detector with part of the emitted light or by using the source pump as a reference directly.

Both signal and reference outputs are analogue voltages. For accurate timing, analogue pulses are converted to logic pulses via discriminators. TCSPC hardware uses discriminators on both signal and reference channels (Becker, W 2005). Integral discriminators are the simplest unit that can be used for this conversion, and consists of a device that produces a logic output pulse only if the input pulse exceeds a set amplitude. The logic pulse is created shortly after the leading edge of the input pulse crosses the discrimination level. The discrimination level is normally selected such that dark counts (§2.2.4.3), which tend to have much small pulse heights, are removed. Differential discriminators can also be used, converting pulses which lie in the range between two discrimination levels. Differential discriminators are typically used to select incident radiation with specific energies.

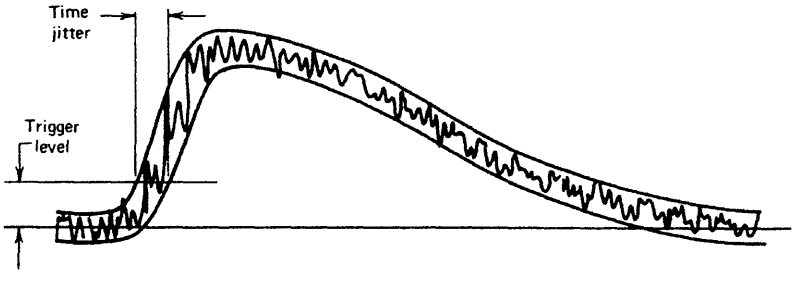

Figure 2-14 An envelope is shown around a noisy pulse. This demonstrates the effect of jitter on timing precision when using discriminators with leading edge triggering. (Knoll, G F 2000)

The analogue pulses produced by a photodetector will have a distribution of pulse-heights, caused by variations in the amplification of the photo-electrons. Due to the pulse variation, uncertainties in timing precision will result from to two sources when using leading edge triggering: time jitter and amplitude walk. The effect of jitter on leading edge timing is shown in Figure 2-14. Random fluctuations within incoming pulse of identical size and shape cause the triggering of the logic pulse at different times with respect to the centre of the pulse. Amplitude walk is associated to pulses of identical shape and timing, but where the difference in amplitude leads to a late arrival of the discriminator trigger level. An example of amplitude walk is shown in Figure 2-15.

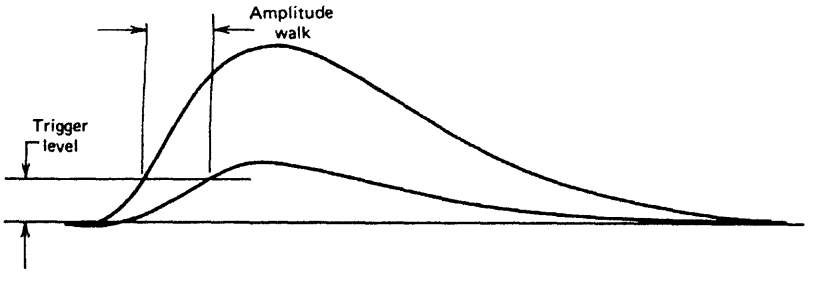

Figure 2-15 Amplitude walk due to leading edge triggering. Two pulses of identical shape, but different amplitude lead to discriminator triggering a different times. (Knoll, G F 2000)

Constant fraction discriminators (CFDs) are designed to produce logic pulses whose characteristics and independent of input amplitude for all pulses of identical shape using a method called crossover triggering. CFDs convert incoming analogue signals into a fast logic pulses with two components, as shown in Figure 2-16. One part is a logic pulse created when the input reaches a pre-set threshold of its maximum, and is hence slightly delayed. The original signal is attenuated down to the same threshold and then added to an inverted form of the delayed pulse. The resultant is a bipolar pulse with a zero crossing at the time that the threshold level was reached. The zero crossing is the final "start" marker for creating the logic pulse used for timing.

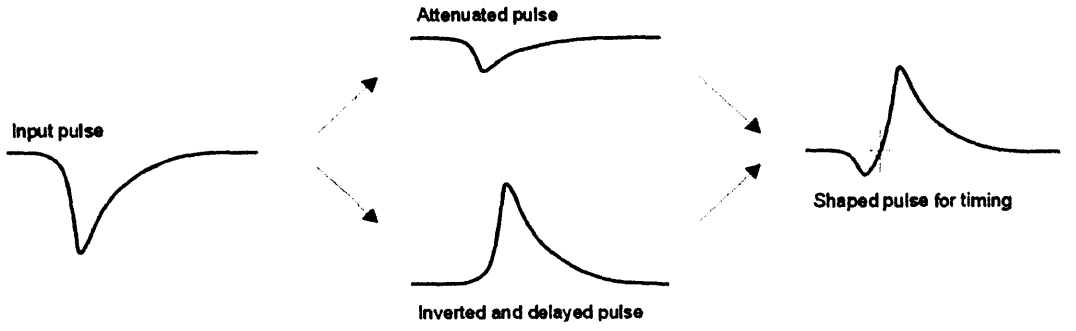

Figure 2-16 The signal processing within the CFDs, allowing accurate flight time measurements (pulses are travelling right to left). (Schmidt 1999)

The time between arrivals of reference and signal pulses can be performed by time-to-digital (TDC) conversion. TDC operates using sine and cosine waves of two frequencies for coarse/fine time interpolation in an electronic vernier arrangement (Lampton M and Raffanti R 1994). This method allows constant readout of timing measurements.

Another method for timing the difference in arrival time of the signal and reference pulses is to use a time-to-amplitude converter (TAC). A TAC starts charging a ramp-generator capacitor upon arrival of the start pulse and provides a constant current until the stop pulse is received. The voltage stored across the capacitor is thus proportional to the time difference between start and stop pulses. The voltage is then measured and stored using an analogue to digital converter (ADC).

The sensitivity of TCSPC (§2.2.3) is mostly limited by dark counts from the detector, and is defined as the intensity at which the signal equals the dark noise (Becker 2005b):

$$S = \left(R_d \, N/T\right)^{1/2} / Q \qquad \text{(x)}$$

where R_d is the dark count rate, N is the number of timing channels, T is the acquisition time, and Q is the quantum efficiency of the detector. The sensitivity of MONSTIR-03 is roughly 17 photons per second.

There are two idealised models for systems that count random events: paralysable or non-paralysable. A dead time is required by timing electronics to process each incoming signal pulse. Non-paralysable systems ignore any count that arrives during the dead time and simply loses the information carried with that count. Paralyzable electronics also lose the information carried with the second count, but the deadtime is extended as if the count was being processed. The two models only differ significantly with high count rates. All TCSPC electronics discussed in this thesis are operated in non-paralysable mode, hence the discussion below only deals with that model.

The recorded count rate, r, for an input count rate, r_0, is (Becker, W 2005):

$$r = r_0 / (1 + r_0 t_d) \qquad \text{(xi)}$$

where t_d is the dead time. At the saturation rate of $r_0 = 1/t_d$ the recorded rate is half of the input rate. This is defined as the "maximum useful count rate" (Becker, W 2005).

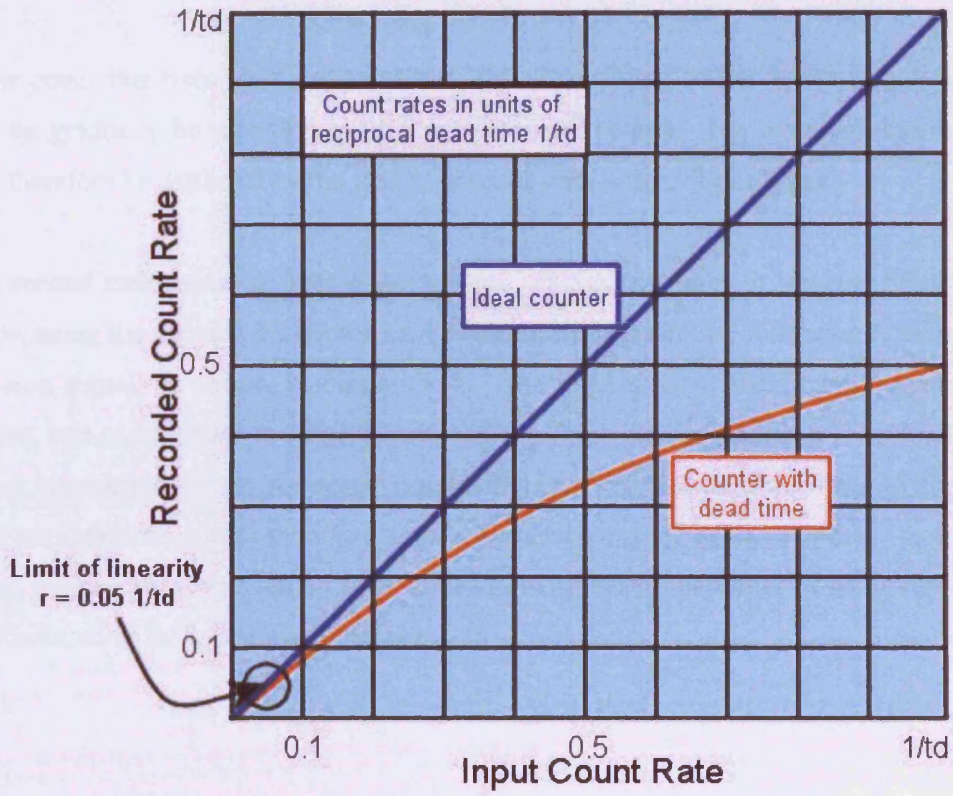

Figure 2-17 Graph showing the relation of ideal and recorded count rate to input count rate. (Becker 2005b)

The limit of linearity between the input and recorded count rate is usually taken as five percent of the saturation rate (Becker, W 2005). Thus the count rate used for comparison between sets of electronics is:

$$r = 0.05(1/t_d) \quad \text{(xii)}$$

The non-linearity is caused by pile-up. Pile-up is the name given to the loss of counts due to the arrival of an initial photon causing a dead time, during which another photon arrives and is ignored.

Pile-up distorts measurements via two mechanisms. The first mechanism is classic pile-up. As the detected count rate, r, reaches a few percent of the laser's repetition rate, l_{rep}, the chance of receiving two start (i.e. detected) pulses in a single timing period increases. The typical rule for non-paralysable TCSPC systems is to limit the number of incident photons such that each channel can only detect a photon for one percent or less of the incident laser pulses. The probability, p, of recording two photons within the same period would hence be 0.01 %:

$$p = (r/l_{rep})^2 \quad \text{(xiii)}$$

If the count rate rises above one percent, photons arriving earlier in the timing period will be gradually be recorded in preference to later counts. The temporal distribution will therefore be distorted by the loss of photons with longer flight-times.

The second mechanism is inter-pulse pile-up. TCSPC operates in 'reverse Start-Stop' mode, using the arrival of a photon as the start of timing, and the following reference as the stop signal, as shown in Figure 2-18. The dead time of the timing engine then begins, and ends t_d later at which point another photon can be recorded. The dead time is not a multiple of the reference repetition time. Photons arriving later in the gap between reference pulses therefore have a greater chance of being recorded. Averaged for an entire acquisition, longer flight-times have higher probabilities of being recorded, as illustrated in the lower plot in Figure 2-18.

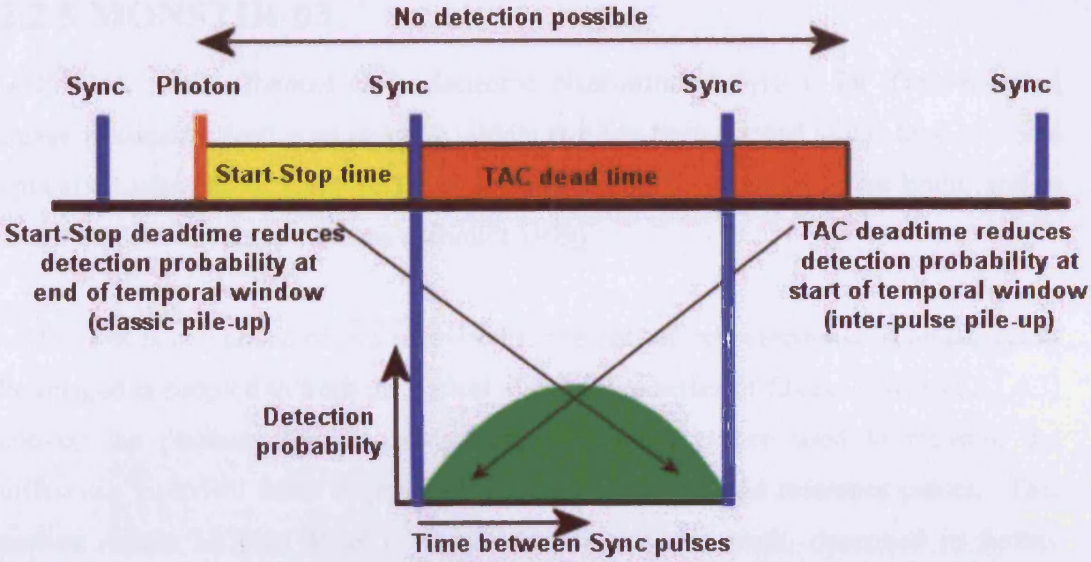

Figure 2-18 An illustration of the effects of two pile-up mechanisms. SYNC is the arrival of the reference pulses. The green area represents the probability of photon detection within a single temporal window, averaged over many cycles and with high count rates, leading to significant pile-up (adapted from Becker 2005b).

Inter-pulse pile-up reduces the probability of recording photons with shorter arrival times by the probability of finding a photon in the previous detection period:

$$p = 1 - \left(r / l_{rep} \right) \qquad \text{(xiv)}$$

This pile-up effect is negligible for a one percent detection rate, but has the opposite effect on recorded TPSFs versus classic pile-up, see Table 2-2.

Classic Pile-up	Loses late photons	Acceptable to 1% detection rate
Inter-Pulse Pile-up	Loses early photons	Acceptable below a few percent

Table 2-2 Summary of the effects of the two main pile-up mechanisms

It is important to note that for MONSTIR a single detection period contains two TPSFs, one from each wavelength. The reference signal can be taken from either wavelength at 40 MHz before the light is interlaced, and the wavelength that appears first in the temporal window is dependent on which reference is used. The effects of the two pile-up mechanisms act across the whole detection window rather than to each wavelength individually, hence classic pile-up would lose photons from the end of the second TPSF and not the first.

2.2.5 MONSTIR-03

MONSTIR (Multi-Channel Opto-electronic Near-infrared System for Time-resolved Image Reconstruction) is an imaging system that has been created to use time-resolved optical tomography to generate functional images of the newborn infant brain, and to detect and classify breast disease (Schmidt 1999).

MONSTIR is comprised of two subsystems: one optical, one electronic. The subject to be imaged is coupled to/from the optical system by a series of fibres. PMTs (§2.2.4.3) convert the photons into electronic signals, which are then used to measure the difference in arrival times between the incoming photons and reference pulses. This section details MONSTIR as it was at the start of this work, described in further sections as MONSTIR-03.

2.2.5.1 Optical System

Photons passing through the subject are scattered and absorbed differently by the various tissues that make up that subject. The optical system of MONSTIR, the components of which are shown in Figure 2-19, has been built to direct the output of a dual-wavelength laser to a specific point on the surface of the subject, and to receive transmitted photons at 31 other points. The intensity at each point is attenuated so as not to saturate the detectors, which convert the optical signal into an electronic signal.

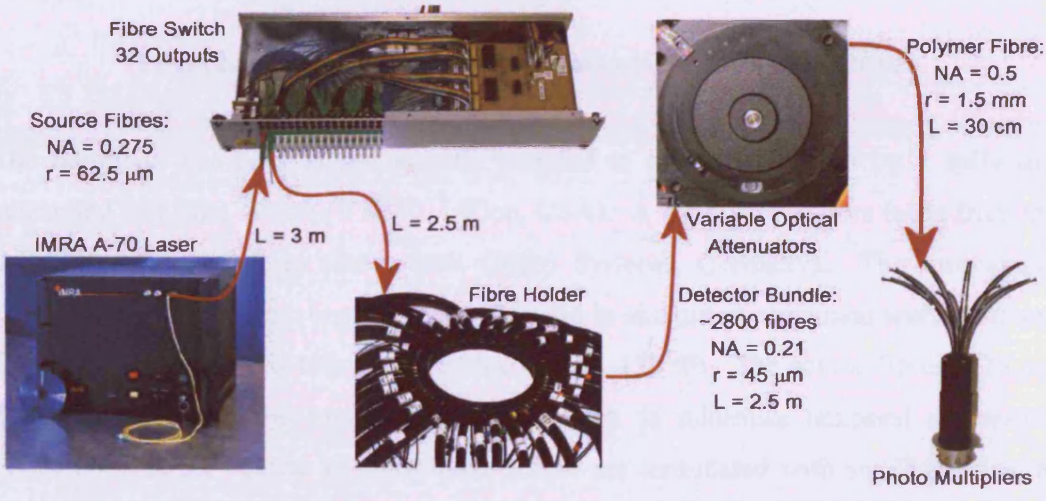

Figure 2-19 Diagram of the optical system in MONSTIR (Jennions 2003)

Laser

MONSTIR uses a custom built portable fibre laser (Type A-70-FC-WS, IMRA America, USA) as a source (Class 3B, §2.2.4.1). The laser's size and low power consumption help keep MONSTIR a portable system. The 19" rack-mount unit produces a single beam of interlaced pulses of 780 nm and 815 nm light. The lasing cavities are Er/Yb fibres, wound in a spiral to conserve space and eliminating the need for re-tuning after movement. The cavities are pumped by a separate fibre oscillator to produce 1560 nm and 1630 nm pulses at 40 MHz. A frequency-doubling crystal is used before the two wavelengths are interlaced, resulting in a single 80 MHz beam of 780 nm and 815 nm.

Reference pulses are also created at 40 MHz by illuminating a photodiode with part of each wavelength's beam, which is split before the two wavelengths are interlaced. The nominal power output is ~55 mW per wavelength, but this can be attenuated using various neutral density filters.

Fibre assembly

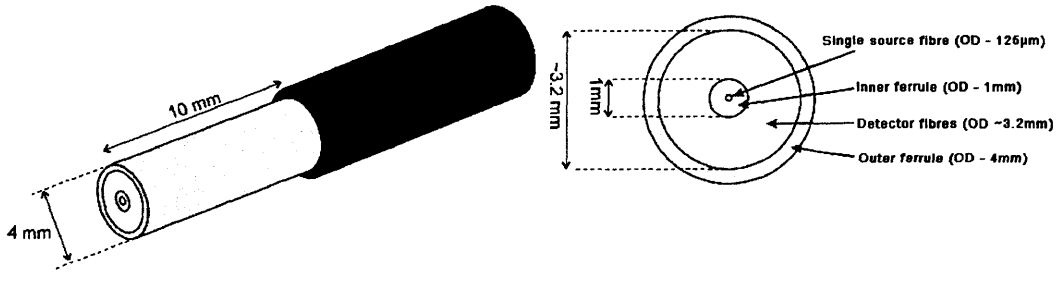

Figure 2-20 Layout of the source / detector bundle ends (Jennions 2003).

The output of the laser is sequentially coupled to one of 32 fibres by a software-controlled fast fibre switch (VX500, DiCon, USA). A short source fibre leads from the outputs of the switch to shutter unit (Piezo Systems, Germany). The mechanical shutters operate by translating the input fibre end in and out of alignment with an output fibre. This reduces cross-talk between channels to -120 dB. The source fibres (125 µm diameter, 900 µm outer jacket) are graded index to minimise temporal dispersion. These become the centres of fibre bundles that are terminated with small ferrules, as shown in Figure 2-20. The bundles are 2500 mm long, with the source fibre splitting from the detector bundle for the last 750 mm.

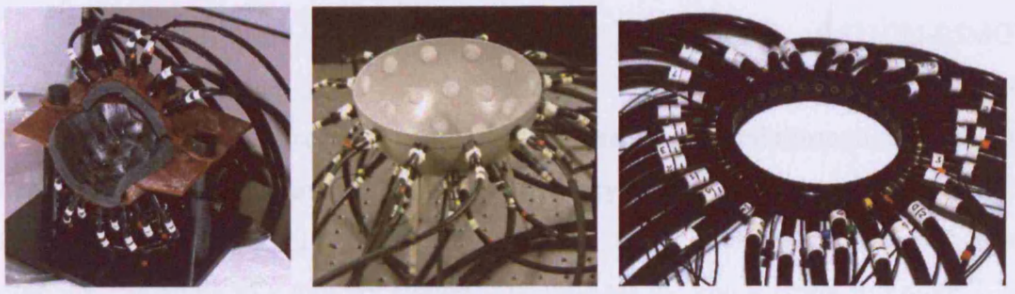

Figure 2-21 Pictures of three fibre holders, intended for: (from left to right), the neonatal head, the female breast, and a cylindrical phantom. (Jennions 2003)

The ferrules are fixed to various fibre holders, which have been moulded from rigid plastic to fit the surface of the subject (Hebden et al. 2001). Examples of fibre holders are shown in Figure 2-21

Scattered photons are picked up as they exit the subject in parallel by the other 31 bundles. The remaining area of the bundle end is made up of 2880 45 μm diameter fibres, which are individually sheathed (outer diameter 50 μm) and are of equal length (to within <6 mm) to minimise temporal dispersion. The geometry of the bundle is close-packed, which results in the highest possible fibre area, 73 % of the optode surface.

VOAs

The detector bundle's other end terminates in the back of one of four Variable Optical Attenuator (VOA) units (each holding eight VOAs) (Schmidt 1999). As discussed in §2.2.4.4, the range of the optical signal carried to the detectors can exceed the safe range of the detectors. MONSTIR-03 VOAs use a set of apertures, mounted on a disc that can be rotated between fibre ends, to attenuate the light to a safe level. A "closed" position is used if the VOAs do not have the required dynamic range to attenuate the beam to a level that is safe for the detectors. This cuts off the channel completely. VOA design is discussed further §3.5.2.

A single polymer fibre of roughly 30 cm length guides the attenuated beam from the back of the VOAs to the detectors.

Detectors

Four, eight-anode, microchannel plate PMTs (MCP-PMT - R4110U-05MOD, Hamamatsu, Japan) are used in MONSTIR. The electrons emitted from the photocathode (left in Figure 2-22) in MCP-PMTs are accelerated through microchannel tubes (~10 μm), causing amplification by secondary emission from collisions with the walls of the channels. The channels keep the photoelectrons, and the secondary emissions, travelling in a roughly straight line towards the anode (right in Figure 2-22), minimising the transit time. The electrons in standard PMTs can be emitted at any angle, temporally broadening the incoming photons' distribution. The FWHM of the broadened output pulse from a delta function input is called transit time spread (TTS), and is a measure of the error in the arrival time of the counts. MCP-PMTs have a typical TTS of 25 ps, whereas standard PMTs have a typical TTS of a few hundred ps. Detector design and timing characteristics are discussed in further detail in §2.2.4.3.

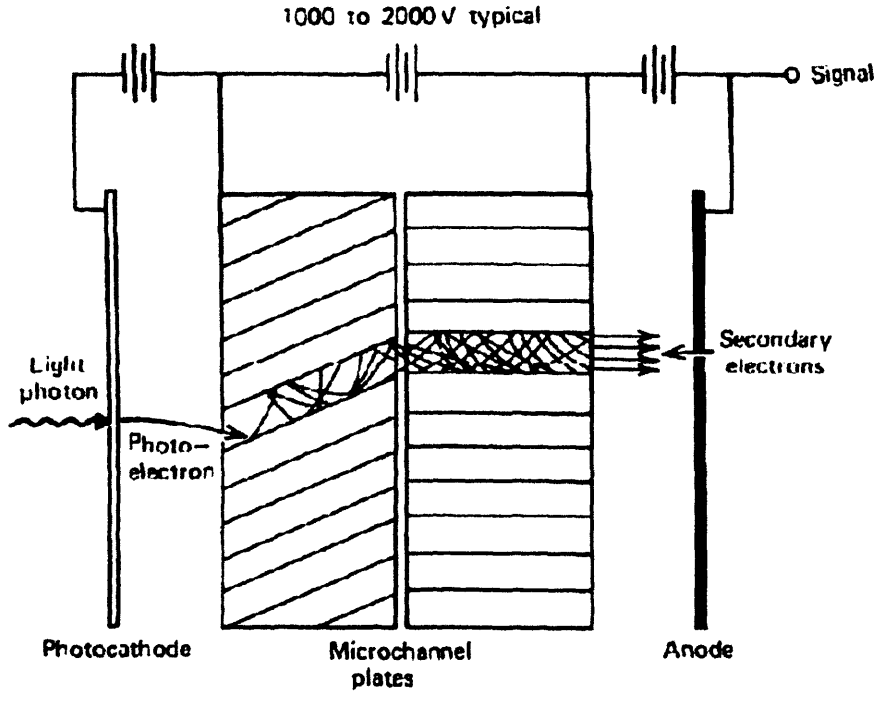

Figure 2-22 Diagram of the internal structure of the MCP-PMTs (Schmidt 1999)

Solid-state Peltier coolers are used to reduce the temperature of the MCP-PMTs to about -25°C, reducing dark counts (§2.2.4.3) to a few per second. The Peltier coolers are coupled to a water cooling system, and require a few hours to reduce the MCP-PMTs to their operating temperature.

2.2.5.2 *Electronic System*

Having converted the photons into an analogue electronic pulse, a histogram of the flight-times is built up by comparing the arrival times with the reference pulse from the laser.

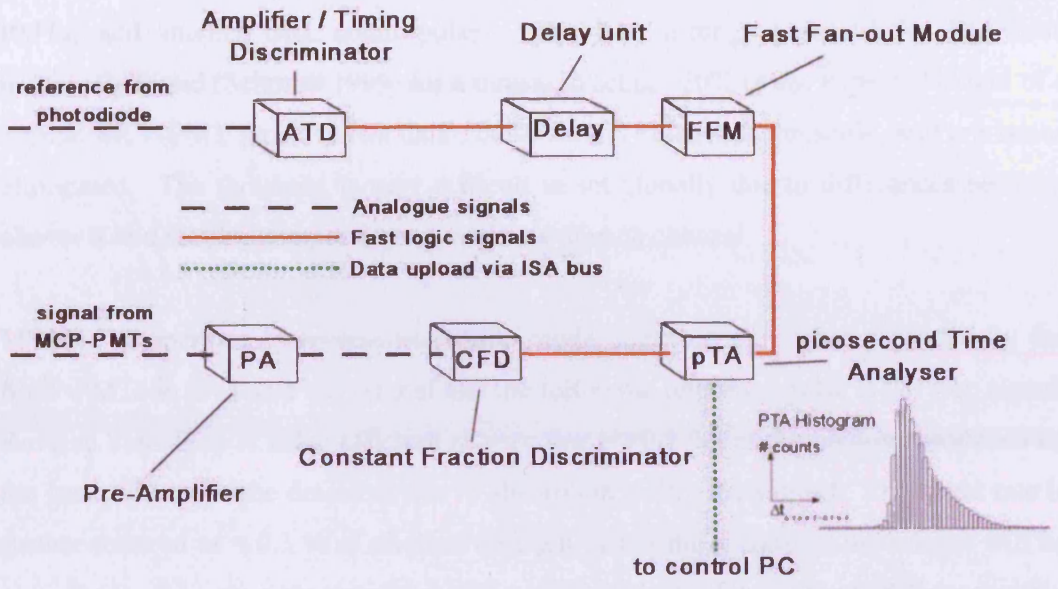

Figure 2-23 Diagram of the electronic system within MONSTIR

Reference Pulse

Part of the beam from each wavelength individually illuminates two photodiodes within the laser. Either wavelength can hence be chosen as the 40 MHz reference. The top line in Figure 2-23 shows the path of the reference pulses in MONSTIR. The reference pulses are taken to an amplifier / timing discriminator (ATD) unit, which precisely marks the arrival time of each pulse and converts the analogue pulse into a fast logic pulse (as CFDs below). The discriminator's output is then delayed to ensure the whole TPSF fits in the temporal window. The single reference is then split for the 32 channels by a fast fan-out module (FFM).

Signal Conditioning

The pulses from the MCP-PMTs are passed into a constant fraction discriminator (CFD, §2.2.4.5), via a pre-amplifier, as shown as the bottom line in Figure 2-23. The CFDs were Ortec Model 935 (EG&G, USA) in the original system. The CFDs eliminate dark counts by discriminating between pulses produced from photons incident on the MCP-PMTs, and smaller dark count pulses. The best timing characteristics had been previously found (Schmidt 1999) for a threshold set at ~20% of the expected height of a normal MCP-PMT pulse. Most dark counts do not reach this threshold, and are hence eliminated. The threshold is very difficult to set globally due to differences between channels and varying temporal characteristics of each channel.

MONSTIR operates in reverse Start-Stop mode, meaning the signal produced by the MCP-PMTs is used as a start signal and the following reference pulse is the stop signal. Reverse Start-Stop is more efficient as very few (<<0.1 %) of the photons produced by the laser will reach the detectors due to absorption within the subject. The count rate is further reduced as < 0.1 % of photons emerging from the surface of the subject will be recorded by the timing electronics due to systematic loses, for example 98 % loss within the fibre bundles and a detector QE of 4 %.

Timing electronics

The timing modules in MONSTIR-03 were the picosecond Time Analyser (pTA, Ortec Model 9208 EG&G, USA). These are TCSPC modules, that use time-to-digital conversion (TDC, §2.2.4.5) to measure photon flight times. The pTAs calculated the flight time of the photons, and stored the resulting TPSFs with a bin width of 1.6 ps. The pTAs had only one memory segment and therefore needed a delay between acquisitions, during which the data was uploaded to a PC.

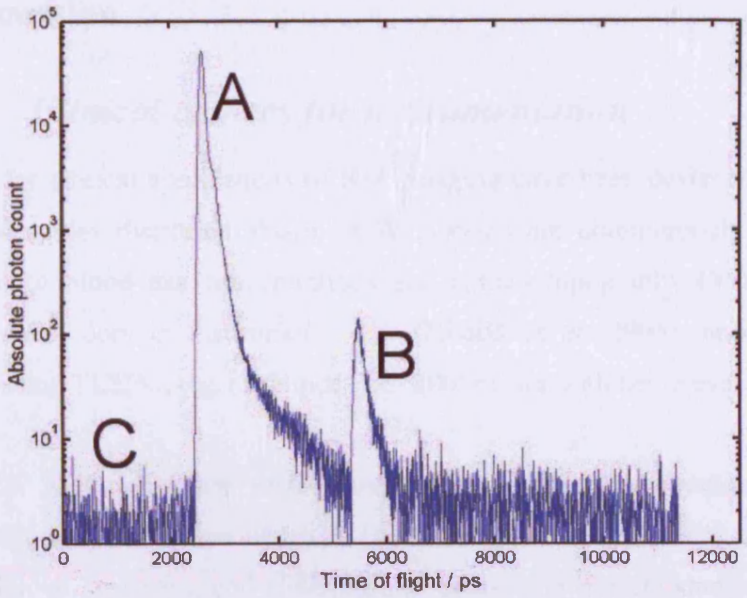

Figure 2-24 An example of a good TPSF, containing 1.3 million photons and collected over 10 seconds. (Jennions 2003)

Ideal TPSFs would contain only a single peak (A in Figure 2-24), with no other signals present. However, optical reflections and crosstalk within MONSTIR cause smaller, secondary peaks. Post-peaks (B) originate in the polymer fibre between VOAs and MCP-PMTs, whereas pre-peaks (not shown) are caused by crosstalk between source fibres or leakage around the surface of the subject. The temporally un-correlated background (region C) can be caused by external lighting, dark counts from the detectors, or crosstalk between detector channels.

Other Units

In addition to the signal processing electronics, MONSTIR requires high voltage power supplies, cooling units, and safety monitors to operate. These can operate completely independently of the control PC, allowing manual override.

The original PC interfaced to MONSTIR-03 via three ISA cards and a serial port. The serial port controlled the VOAs' stepper motors and initialisation positioning. One ISA card was a multifunction Input / Output (I/O) card, which interfaced to the temperature sensors, the coolers, and the fibre switch. Another ISA card was a digital I/O card which interacted with the system monitor, power supplies and the laser shutter. A third ISA card was for collecting data from the pTAs.

2.2.6 Discussion

2.2.6.1 Clinical choices for instrumentation

Instruments for clinical applications of NIR imaging have been designed based on all three methodologies discussed above. CW systems are commercially available for measurement of blood gas concentrations and optical topography (Yamashita et al. 1999). Frequency-domain instruments, e.g. (Nissilä et al. 2005), and time-domain instruments using TCSPC, e.g. (Schmidt et al. 2000a), are both being evaluated.

Although CW techniques are widely used, time- and frequency-domain methods provide additional information which is likely to improve the quality of the images. The separation of scattering and absorption in breast and muscle studies can only be possible with more than one measurement type (Schweiger et al 1997).

2.2.6.2 Frequency vs. Time Domain instruments

A comprehensive overview of frequency-domain DOT techniques is given in (Gibson et al. 2005a). The benefit of the frequency-domain techniques is their short acquisition times at high intensity. A problem is that crosstalk between the amplitude and the phase is difficult to avoid, making it harder to obtain absolute optical tissue properties.

TCSPC (Becker 2005b) is superior in terms of precise measurement of the arrival time of the photons and all photons contributing to the histogram. Moreover, the effective detection bandwidth is much higher than for frequency-domain systems. TCSPC obtains a better signal-to-noise ratio (SNR) from a given number of detected photons than any other technique, but is limited to a few MHz per TCSPC channel. The excellent results obtained with TCSPC-based DOT instruments under clinical conditions (Grosenick et al. 2003, Liebert A et al. 2003, Hebden et al. 2004, Grosenick et al. 2004, Taroni et al. 2004) demonstrate the applicability of TCSPC.

In collaboration with the Helsinki University of Technology (HUT) we compared their frequency-domain instrument to the MONSTIR-03 system, looking at RMS differences between a Monte Carlo simulation and data recorded at different measurement times. The MONSTIR-03 results were Fourier transformed to calculate amplitude and phase taken at 100 MHz. The data taken with MONSTIR-03 were independent of measurement time for phase, and produced a minimum at 5 s for amplitude, as shown in Figure 2-25. The HUT system provided time-independent amplitude data, and phase data that decreased in error with longer measurement times. Full results are published in (Nissilä 2006).

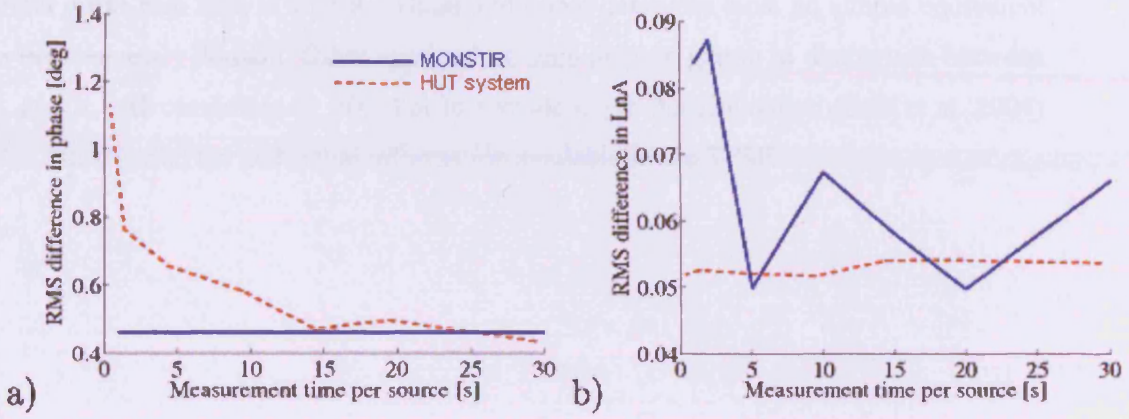

Figure 2-25 Graphs of the accuracy of datatypes for the HUT frequency domain instrument (dotted) and MONSTIR (solid). (Nissilä 2006)

MONSTIR-03 was designed to accurately record absolute time-resolved datatypes only. It was found (Schmidt 1999) that problems inherent in measuring intensity, e.g. coupling coefficients of the optodes with the subject, meant that acquiring useful absolute intensity was not feasible. It has been proven more recently that a single time-resolved datatype is insufficient to find the unique solution in reconstruction (§2.3.3.5) and it has been suggested that multiple datatypes might be used to find the unique solution, but only if the refractive index of the tissue is known.

The information content in a TPSF is inevitably greater than that in a single phase and amplitude measurement at one source frequency, but the magnitude of this benefit has yet to be thoroughly explored. The frequency content of the TPSF extends to several GHz, and while it would be possible to design a detection system which could acquire this frequency-domain information, it is not yet possible to modulate high-intensity sources at these high frequencies. The intensity and mean photon flight time calculated from the TPSF are almost equivalent to the amplitude and phase of a frequency-domain system (Arridge et al. 1992). Other datatypes calculated from the TPSF such as variance, skew and the Laplace transform can provide enhanced separation between μ_a and μ_s' (Schweiger and Arridge 1999b), but may be more sensitive to noise, and their effect on *in vivo* data is unclear. These additional datatypes have no simple equivalent in the frequency domain. Other approaches, such as time-gating to distinguish between μ_a and μ_s' (Grosenick et al. 2003) or to provide depth discrimination (Selb et al. 2004) also demonstrate the additional information available in the TPSF.

2.3 Image Reconstruction

Reconstructions of data collected by MONSTIR are performed by a software package developed at UCL called TOAST (Time-resolved Optical Absorption and Scattering Tomography). TOAST can simulate light transport and reconstruct the distribution of absorbing and scattering objects from time-resolved measurements. Reviews of modelling and image reconstruction techniques are given in (Arridge and Hebden 1997, Gibson et al. 2005a).

2.3.1 Data

TOAST does not use entire TPSFs for reconstruction, as it is too computationally expensive to do so. Instead, image reconstruction involves extracting representative characteristics, or datatypes, from the measured data. The extracted datatypes must be sufficiently free from systematic sources of noise and uncertainty to provide a good correspondence with those calculated directly by the forward model (§2.3.3.1). Calibration of the data is therefore needed to remove any systematic effects on the data, and to remove channel-specific characteristics, such as variations in fibre length which result in temporal offsets in the recorded TPSFs.

2.3.1.1 Datatypes

All datatypes are expressed as normalised integral functions, equal to a transform applied to the data divided by the total intensity (Hebden et al. 1998b). The main datatypes used are intensity, E, and mean flight time, $\langle t \rangle$. It is also useful to consider the nth temporal moments of the TPSF, specifically the second and third central moments called variance and skew. These higher moments can be used in reconstruction but are more susceptible to noise. Fourier equivalents can also be used, e.g. amplitude and phase for intensity and meantime. $\Gamma(t)$ is the distribution of counts in a TPSF.

Intensity: $$E = \int_0^\infty \Gamma(t)dt \quad \text{(xv)}$$

Meantime: $$M = \langle t \rangle = E^{-1} \int_0^\infty t\Gamma(t)dt \quad \text{(xvi)}$$

Variance and Skew: $$C_n = E^{-1} \int_0^\infty (t - \langle t \rangle)^n \Gamma(t)dt \quad \text{(xvii)}$$

Meantime and intensity together, or their Fourier equivalents phase and amplitude, have been suggested as the best datatypes to separate μ_a and μ_s` (Hebden et al. 1998b). Hence the following chapters will only refer to these two datatypes.

2.3.1.2 *Calibration Theory*

Pre-processing and calibration before reconstruction can remove unwanted characteristics present in the shape of experimentally recorded TPSFs, e.g. pre-peaks due to leakage around the surface of the object, and post-peaks due to reflections within MONSTIR. There are two methods for removing these distortions of the TPSFs.

The first method is calibration. The delta-function response of each source and detector is recorded and removed from the final data, resulting in TPSFs that have been broadened and reduced in intensity by the subject only (Hillman et al. 2000).

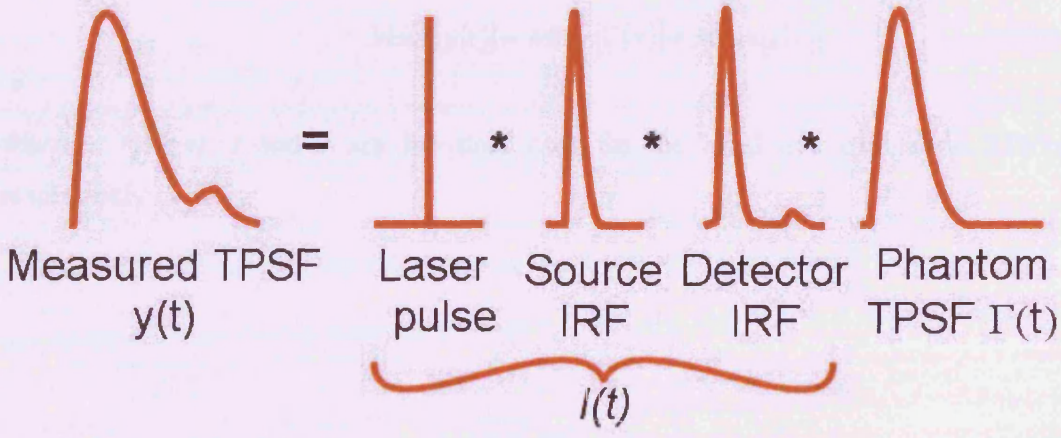

Figure 2-26 Diagram of how the recorded TPSF is built up from the response functions of the source fibres, detector system, and the original TPSF from the subject.

The recorded TPSFs, *y(t)*, are built up from the impulse response functions (IRFs) of the laser pulse, source fibre and switches, and detectors, convolved with the TPSF from the subject, *Γ(t)*. Figure 2-26 shows:

$$y(t) = I(t) * \Gamma(t) \tag{xviii}$$

I(t) is the IRF specific to one source-detector pair, * indicates convolution, and *f(t)* is noise.

Starting from an expression of the convolution integral as a summation (Hillman et al. 2000):

$$y(t) = \sum_{v} \Gamma(t-v) I(v) \tag{xix}$$

and defining the meantime as:

$$Mean[y(t)] = \frac{\sum_{t} y(t)t}{\sum_{t} y(t)} \tag{xx}$$

gives:

$$Mean[y(t)] = \sum_{x}\sum_{v} \Gamma(x) I(v)(x+v) \Big/ \sum_{x}\sum_{v} \Gamma(x) I(v) \tag{xxi}$$

$$Mean[y(t)] = \frac{\sum_{x} x\Gamma(x)}{\sum_{x} \Gamma(x)} + \frac{\sum_{v} vI(v)}{\sum_{v} I(v)} \tag{xxii}$$

resulting in:

$$Mean[y(t)] = Mean[\Gamma(x)] + Mean[I(v)] \tag{xxiii}$$

where $x = (t-v)$. t and v are the time axes for the ideal and calibration TPSFs respectively.

Therefore subtracting the meantime of the IRF, $\langle I(v) \rangle$ from the recorded TPSF, $\langle y(t) \rangle$, results in the subject TPSF's meantime, $\langle \Gamma(t) \rangle$. The same process can be applied to the second and third temporal moments, skew and variance. It can also be shown that (Hillman et al. 2000):

$$Intensity[y(t)] = Intensity[\Gamma(x)] \times Intensity[I(v)] \qquad \text{(xxiv)}$$

Thus, removing datatypes calculated for IRFs from those calculated for measured data is equivalent to calculating datatypes after the IRF has been removed from the data by deconvolution.

The second method for removing unwanted characteristics is difference imaging (Hillman et al. 2000). This method repeats all measurements on a homogenous reference phantom or after a physiological change has occurred. Any crosstalk or temporal instabilities in MONSTIR are recorded in both subject and reference acquisitions. Therefore the differences in datatypes are due only to the differences in optical properties measured by the two acquisitions. The resulting difference data is free from channel differences and day to day variability in MONSTIR's temporal characteristics.

In terms of the time-domain calibration presented above, this equates to (Hillman et al. 2000):

$$\begin{aligned} Mean[y(t)]_{diff} &= \left[Mean[\Gamma(x)]_{subject} - Mean[I(v)]\right] - \left[Mean[\Gamma(x)]_{reference} - Mean[I(v)]\right] \\ &= Mean[\Gamma(x)]_{subject} - Mean[\Gamma(x)]_{reference} \end{aligned} \qquad \text{(xxv)}$$

In all of the above, it is assumed that a perfect TPSF (and hence IRFs) can be recorded without noise. However, stochastic noise is present as a temporally uncorrelated background (see C in Figure 2-24). This can be mitigated by maintaining a high count rate, though this is not always possible, and by thresholding with the CFDs (§2.2.4).

2.3.1.3 *Calibration in Practice*

To practically achieve the calibration described above, two calibration data sets are used: source and absolute (Hebden et al. 2003). To record the source calibration for channel m, S_m, the optode is attached at a fixed radius to a transparent disc phantom with a central, isotropically scattering, target. All 32 sources fibres are connected to the phantom and a single detector fibre is attached to the target, which is then illuminated by each source in turn. The recorded TPSF is broadened only by system components, and reveals the differences between source channels. Absolute calibrations, A_n, are recorded using back-reflection, with a 7 OD filter (§2.1.1) in the laser to prevent damage to the PMTs, and represent the calibration measurements for source n and detector n coupled together. Each source is illuminated in turn, the same channel detecting the reflected photons.

The shape of the TPSF due solely to the photon transit through the subject can be extracted using a fast Fourier transform (FFT) written in C. The calibrated TPSF for source i and detector j, $I_{i,j}$, can be acquired from the measured TPSF $M_{i,j}$ as follows (Hebden et al. 2003):

$$I_{i,j} = \left(M_{i,j} * S_j\right) \otimes \left(A_j * S_i\right) \qquad \text{(xxvi)}$$

* represents a convolution operation, and $\otimes$, a deconvolution operation. After deconvolution, an iterative smoothing algorithm is used to constrain the low frequencies within the TPSF and remove unwanted high frequency noise.

As shown in §2.3.1.2 the same calibration can be performed in the time domain rather than the Fourier domain. Time domain calibration results in significantly quicker computation – 50 s vs. 30 min for a 32 channel dataset – due to the time required to perform iterative (de-)convolutions. However, the C program written for deconvolution has not been optimised.

A calibration routine written in MatLab (The Mathworks Inc, USA) allows TPSFs to be edited by hand, further removing systemic and stochastic errors. The script displays the recorded TPSFs for all channels, and allows the user to select the start and end points of the TPSFs. All bins outside these points are filled with zeros, retaining only the signal portions of the recorded TPSFs. This process is called windowing. Subtracting the average of the background (values outside the window at the end of the TPSF) from all counts within the window is also intended to remove noisy counts. Datatypes are calculated from the windowed TPSFs, and calibration is performed as described the previous section.

2.3.2 Modelling

A Radon transform, as used for reconstructing computed tomography (CT) images, cannot be used in optical imaging as biological material is a highly-scattering medium. Instead, the transport model is used based on diffusion of the photons through the tissue.

The most widely applied equation in optical imaging is the radiative transfer equation (RTE), which governs photon interactions in a material:

$$\frac{1}{c}\frac{\partial I(r,\hat{s},t)}{\partial t}+\hat{s}.\nabla I(r,\hat{s},t)+\mu_{tr}I(r,\hat{s},t)=\frac{\mu_{tr}}{4\pi}\int_{4\pi}p(\hat{s},\hat{s}')I(r,\hat{s}',t)d\hat{s}'+q(r,\hat{s},t) \qquad \text{(xxvii)}$$

where:

$I(r,\hat{s}',t)$	=	specific intensity (number of photons per unit volume) at position r, time t, travelling in direction $\hat{s}$
$p(\hat{s},\hat{s}')$	=	scatter phase function (probability for $\hat{s}\rightarrow\hat{s}'$)
$q(r,\hat{s},t)$	=	radiation source term
μ_{tr}	=	transport attenuation coefficient (§2.1.1)
c	=	speed of light, in vacu

If the intensity term is expanded in spherical harmonics, and the following assumptions are made:

- Scatter is the dominant interaction, $\mu_a << \mu_s'$
- The phase function is independent of absolute angle, $p = p(\hat{s} \cdot \hat{s}')$
- The photon flux (J) changes slowly, $\partial J / \partial t = 0$
- The source and specific intensity terms are all nearly isotropic

the result is the diffusion equation (DE):

$$-\nabla.\kappa(r)\nabla\Phi(r,t)+\mu_a\Phi(r,t)+\frac{1}{c}\frac{\partial\Phi(r,t)}{\partial t}=q_0(r,t) \qquad \text{(xxviii)}$$

with Φ being the photon density. The first term is the product of the gradients of the photon density and diffusion coefficient, κ, defined as:

$$\kappa(r)= \Big/ 3\left(\mu_a(r)+\mu_s'(r)\right) \qquad \text{(xxix)}$$

This gives the diffusion rate for photons within a volume. The second term in the DE is the overall absorption per volume. The third is the unimpeded flow of photons out of the volume with time. A source term is included on the right-hand side of the DE. Green's functions can be used as approximate solutions if the source term is replaced with an impulse response function.

The Green's function solution to the DE, for an infinite medium, is:

$$\Gamma(t)=\frac{A}{(\mu_a+\mu_s')^{\frac{3}{2}}t^{\frac{5}{2}}}\exp(-\mu_a ct)\exp\left(-\frac{3d^2(\mu_a+\mu_s')}{4ct}\right) \qquad \text{(xxx)}$$

where:

- $\Gamma(t)$ is the temporal distribution of transmitted light.
- μ_a is the absorption coefficient
- μ_s' is the transport scatter coefficient
- A is an arbitrary amplitude term
- c is the speed of light
- d is the source-detector separation

2.3.3 Reconstruction

2.3.3.1 Forward Problem

Image reconstruction has two distinct parts: the forward and inverse problems. The forward problem deals with simulating measurements from known geometries and source positions. The solution to this problem can be found by analytically solving the diffusion equation, but only if the geometry is simple, such as in the case of infinite slabs. For smaller complex geometries, the solutions must be created numerically. The finite element method (FEM), for instance, models the object as a finite set of tetrahedral volumes. The resulting mesh of polyhedrons is called the finite-element mesh. The diffusion equation can then be used to simulate photon transport through the mesh (Arridge et al. 1993).

2.3.3.2 Back-Projection

For two-dimensional topography reconstruction, back-projection can be used to reconstruct images (Franceschini et al. 2000). Franceschini's reconstruction method uses time of flight measurements to calculate the Differential Pathlength, DP. DP is the average distance the scattered photons have travelled through the material:

$$DP = c\langle t \rangle / n \qquad \text{(xxxi)}$$

$<t>$ is the mean flight-time, c is the speed of light, and n is the refractive index. The change in absorption can then be calculated by:

$$A_2 - A_1 = DP \times \Delta\mu_a \qquad \text{(xxxii)}$$

A_2 and A_1 are the optical densities calculated from intensity measurements. The left-hand side of the above equation is hence the difference in log intensity between the activated and reference acquisitions. The change in absorption, $\Delta\mu_a$, for each source-detector pair is then be used to build up contributions, in fixed multiples of 25 %, to each point on a coarse grid. The changes are then scaled and added together to calculate the change in absorption at every point in the grid.

2.3.3.3 *Linear Reconstruction*

Another, more complex, method for topography and tomography reconstructions is called linear reconstruction (Arridge 1999). Given a set of optical topography measurements, one can map the optical properties, x, to the measurements, y. Taking the difference between two measurements gives:

$$\Delta y = J\Delta x \tag{xxxiii}$$

$\boldsymbol{J}$ is the Jacobian, also called the sensitivity matrix. The sensitivity matrix can be calculated by using the forward model on a given mesh. Measurements for a single source-detector pair are simulated whilst altering the optical properties of a single point in the mesh. In this way, the dependence of the measurement on every point in the mesh can be calculated. This is done for every source-detector pair, with the results forming $\boldsymbol{J}$. TOAST (see next section) calculates $\boldsymbol{J}$ via the adjoint method, which multiplies the photon density fields from both source and detector (as if it was a source) positions (Arridge and Schweiger 1995).

For linear reconstruction, the solution is:

$$\Delta x = J^{-1}\Delta y \tag{xxxiv}$$

Inverting the sensitivity matrix is difficult as it is ill-posed, underdetermined, and huge – for a system taking 20 measurements on a cube with 20 cm sides, the sensitivity matrix could have 1.6×10^5 entries. Mathematically equivalent, but computationally simpler, is the Moore-Penrose pseudo-inversion (Moore 1920, Penrose 1955):

$$\Delta x = J^T\left(JJ^T\right)^{-1}\Delta y \tag{xxxv}$$

Hence, the inversion is attempted on a much smaller matrix (e.g. with 400 elements in the above example). $\boldsymbol{JJ^T}$ is also useful for checking by eye that $\boldsymbol{J}$ is correct for the geometry and as a measure of how ill-posed the matrix is. $\boldsymbol{JJ^T}$ is still ill-posed and needs regularisation. One method is Tikonov regularisation, which adds a diagonal to the matrix before inversion. λ is a regularisation parameter, and is typically the maximum value of $\boldsymbol{JJ^T}$ multiplied by ~0.01.

$$\Delta x = J^T\left(JJ^T + \lambda I\right)^{-1}\Delta y \tag{xxxvi}$$

2.3.3.4 *Non-linear Reconstruction*

Non-linear reconstructions, as computed by TOAST (Arridge and Schweiger 1993), use the same sensitivity matrices. However, instead of taking one reconstruction step, TOAST uses an iterative routine to approximate the correct solution. Any *a priori* knowledge (§2.3.3.6) is used to create an initial estimation of the distribution of optical coefficients within the volume, otherwise taken to be homogenous. The forward model is then used to simulate data. The difference between simulated and real data is used to improve the estimation. Once the difference has been reduced below a pre-determined convergence limit, the estimation is taken to be a reasonable match for the subject, and an image is produced showing the distribution and range of the absorption and scatter coefficients in the volume.

If used on a perfectly homogenous phantom, the approach outlined above should terminate instantly and produce a perfectly uniform image. This requires the measured data to match the modelled data. Therefore, if there are errors in either the measurements (due to photon counting errors, variations in the attenuation provided by the VOAs (§3.5.2), etc.) or the model (due to geometric inaccuracies, discretisation errors from the FEM, etc.) the iteration might not converge to the correct result. To reduce the effect of the measurement and modelling errors, the differences between datasets (§2.3.1.3) are used for reconstruction rather than single absolute values. Repeatability is hence paramount, as the difference between homogenous reference and subject can be imaged without blurring only if the entire system is identical for each data set.

2.3.3.5 *Uniqueness*

Optical imaging has a large range of unknowns (refractive index, anisotropy, μ_s' and μ_a etc.). It has been proven that there is no unique solution to the inverse problem for absorption and scatter if only intensity is measured at one wavelength (Arridge and Lionheart 1998). In addition, if refractive index is not known, even frequency- or time-domain measurements are insufficient unless a further approximation to the RTE is taken in modelling (Arridge 1999). (Schweiger et al 1997) plotted the objective function of the inverse problem against μ_s' and μ_a for a range of different datatypes and showed that the solution set found for intensity was approximately $\mu_s'\mu_a$ = constant. Hence, either multiple datatypes or multiple measurements are required. It has been argued that multiple datatypes are essential (Schweiger and Arridge 1999a). Intensity measurements are more affected by absorption, and meantime is influenced more strongly by scatter. Therefore simultaneous measurements of the two may allow separation in reconstructions.

However, it may be possible to find the unique solutions corresponding to identical datasets using *a priori* information or multiple wavelengths, as has been shown by reconstructions from intensity alone that have achieved some separation between μ_s' and μ_a (Pei et al. 2001, Schmitz et al. 2002, Jiang et al. 2002). It remains to be seen how non-uniqueness affects clinical reconstructions, where it is unacceptable for the reconstructions to converge to the incorrect solution.

2.3.3.6 *A priori information in reconstructions*

Reconstruction of images from optical data is an ill-posed, underdetermined problem, limiting the spatial resolution and quantitative accuracy that can be achieved. Structural information can be added to reconstructions, improving the accuracy of the model and allowing measurements to be used more effectively. The structural information can be obtained from anatomical imaging techniques or by considering the applicable physiology. (Ntziachristos et al. 2000) used an MR image of the internal structure of a breast to provide the location of a tumour *a priori*. Using this method, the spatial resolution of the optical image becomes roughly that of the MR image. Truly quantitative images of the haemodynamic properties of the tumour can hence be obtained.

The most straightforward way to include prior information into image reconstructions is to use an anatomically realistic forward model (§2.3.3.1). This increases the accuracy of the forward model so that it can represent the measurements more precisely, thereby improving the image reconstruction.

Prior knowledge of the anatomy can also be incorporated into the inverse problem. In the example of a breast tumour given above, the change in optical properties is assumed to come from either a region of interest defined from anatomy (Ntziachristos et al. 2002) or be heavily biased towards that region (Brooksby et al. 2003, Li et al. 2003). The degradation in image quality due to uncertainties in the anatomical prior, and the best way to minimise this degradation are as yet uncertain (Schweiger and Arridge 1999b).

Overall, the use of prior information in both the forward and inverse problems reduces the time required to reach convergence, improves the quantification of the optical properties found in reconstruction, and constrains regions of functional changes for the final image, resulting in improved specificity and spatial resolution.

2.4 Conclusion

This chapter has presented the fundamentals of optical interactions in tissue and how those interactions can be applied for use in optical imaging (§2.1). Three methodologies can be used to acquire data with near-infrared: continuous wave (§2.2.1), frequency domain (§2.2.2), and time-resolved (§2.2.3), each requiring a specific combination of instrumentation (§2.2.4).

MONSTIR-03 (§2.2.5) was constructed to record data of mean photon flight time. Reconstruction investigations have concluded that more information may be required for unique reconstructions (§2.3.3.5). In addition, some of the components are now reaching the end of their lifetimes, whilst others need to be replaced with newer technology. The instrumentation used must now be revisited to create a second generation imaging system.

3 Instrumentation development

3.1 Introduction

The intention of this work is to update MONSTIR by:

- Improving clinical acceptability:
  - Reduce the size
  - Allow faster data acquisition
  - Reduce the delay required to reach thermal stability
- Improving data quality:
  - Replace failing components
  - Remove error sources

A reduction in size and delay between transport and acquisition is needed to improve MONSTIR's clinical usability, providing easier movement and more flexibility for clinical testing. Replacing the timing electronics (§3.4) has led to a huge reduction in the size of MONSTIR. The 19" rack mount electronics have been replaced by four PCI cards in the control PC, which will allow MONSTIR to be reduced to only one rack. The new timing electronics can acquire repeated datasets at 10 Hz, radically increasing MONSTIR's potential imaging speed. In addition, the necessity of leaving MONSTIR on for 12 hours before acquisitions, required for the electronics and cabling to reach thermal stability, has been reduced to .the ~2 hours required to cool the detectors.

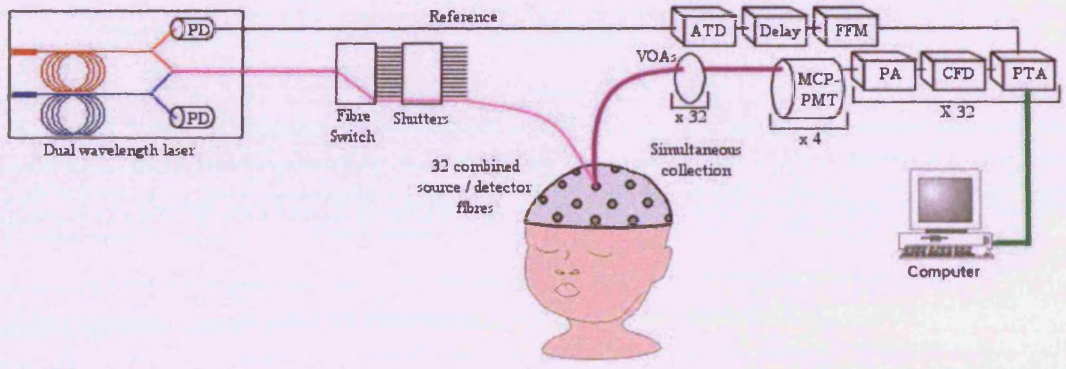

Figure 3-1 Diagram of components of MONSTIR-03. PD: Photodiode, ATD: Amplitude Timing Discriminator, FFM: Fast Fan out Module, VOA: Variable Optical Attenuators, MCP-PMT: Microchannel Plate Photomultiplier Tubes, PA: Pre-Amplifier, CFD: Constant Fraction Discriminator, PTA: picosecond Time Analyser.

Repeated measurements on a cylindrical phantom have identified large intensity and small meantime errors. This chapter describes and discusses an initial investigation into the data accuracy of the MONSTIR-03 system. I concluded from this investigation that two instrumentation improvements were necessary for MONSTIR, aiming to improve intensity accuracy: laser power calibration (§3.5.1), and a new design for the variable attenuators (§3.5.2).

3.2 Required specification

MONSTIR is intended to be a portable system for use in the diagnosis of neonatal cerebral damage and malignant breast carcinomas. From the point of view of a clinical user, a new MONSTIR should have the following qualities:

Data Accuracy

Informal investigation and simulations of haemodynamic and functional studies performed on infants suggest that the differences between resting and active states are on the order of 10 ps for meantime measurements and ~10 % for intensity. If systematic errors in datatypes are greater than this over an active and resting acquisition pair, the variations in datatypes due to haemodynamic changes cannot be distinguished from noise. The effect of calibration (§2.3.1.3) is also reduced as data and reference acquisitions will not have equal systematic additions. The precision of the system should be at least twice that of the changes in the detected signal. Therefore:

- Meantime measurements must be accurate to within 5 ps.
- Intensity measurements must be accurate to 5 %.

Clinical Impact

Clinical time and space are always under pressure, and are hence valuable. MONSTIR needs to have a minimal impact on these commodities:

- MONSTIR should be as compact as possible. It needs to be easy to move from ward to ward for widespread clinical use, and should occupy a relatively small space in order that it can be conveniently used bed- or cot-side. An example of the ideal size and mobility would be that of an ultrasound system.
- The system should be ready for data acquisition shortly after transport. MONSTIR should be able to be moved, switched on, and used almost immediately. Any delay between positioning and data acquisition uses up time and ward space.

Acquisition Time

Minimal patient contact time is desirable for any imaging system, specifically in the case of neonates, who are best imaged when asleep. Shorter acquisition times result in improved temporal resolution of haemodynamic changes, and reduce the impact of systematic instabilities on difference data.

- Calibration and setup should occur as quickly as possible. In addition to achieving thermal stability after transport, MONSTIR needs to perform calibrations and calculate variable attenuator positioning before data acquisition can start. This involves repeatedly acquiring at each source position. Any small gains in single acquisition time are therefore multiplied, resulting in significant reductions in setup time.
- Datasets need to be acquired in as short a time as possible. First, patient contact time should be minimised for efficient ward operation. Second, haemodynamic responses occur at timescales of the order of seconds, hence full datasets need to be acquired in roughly the same timeframe to produce accurate images. Third, calibration removes the system's impulse response from the recorded data. This systematic response changes slowly with time, therefore all data should be acquired as soon after calibration as possible.

3.3 Performance of the original MONSTIR

MONSTIR uses a technique called time correlated single photon counting (TCSPC – §2.2.3) for measuring the flight-times of single photon pulses across an object. The histogram of flight-times, called a temporal point spread function (TPSF), is collected by the timing electronics before upload to the control PC. Using full TPSF datasets for tomographic image reconstruction is too computationally expensive, though methods for using full time-resolved data have been investigated (Gao F et al. 2002). Datatypes (§2.3.1.1) which characterise the shape of the TPSF are therefore calculated. Datatypes should ideally have sensitivity to changes in absorption and scatter at large depths, and be resistant to the effects of intrinsic noise (Hebden et al. 1998b).

The datatypes produced by MONSTIR should be constant when acquiring data on a fixed subject. Variations in the data acquired can be caused by temporal instabilities, for example drift in the high voltage supply to the detectors, or by small repeatability errors in various components, such as exact alignment of fibres in the source switch or positioning of the VOAs discs (§3.5.2).

The calibration routine described in §2.3.1.3 is only valid if the calibration TPSFs remain constant for the duration of the data acquisition. However, continuously recording calibration data reveals systematic drift or instabilities. Measuring these instabilities requires a fixed system, with no switching or resetting components between acquisitions, in order that variations in data can only be caused by systematic changes. Similarities and differences in data recorded by separate channels can then be attributed to specific components.

MONSTIR requires a period after power-up to cool the detectors and reach stable operation, e.g. thermal equilibrium of cabling with environment. The results from the experiment described in the previous paragraph define stable operation for MONSTIR. The time taken to reach this stability can be quantified by recording calibration data from the first moment MONSTIR is switched on.

There is also a data error associated with switching sources during image acquisitions. Datatype errors for a single source-detector pair can be calculated from repeatedly acquiring full 32-channel datasets on a homogenous phantom. Repeated measurements can then again be used to identify the sources of the errors.

The rest of §3.3 describes the measurement of MONSTIR-03's performance in terms of stability over time, the time taken to reach that stability after transport, and repeatability of full 32-channel datasets.

3.3.1 Method

Stability After Transport

The time taken for the datatypes to stabilise after transport was tested using a homogenous clear phantom with $\mu_s' \approx 0$ mm^{-1} and $\mu_a \approx 0$ mm^{-1}. A source fibre was coupled into an isotropically scattering target at the centre of the phantom, as shown in Figure 3-2. All 32 detector bundles were coupled to the radius of the phantom, and illuminated with 10-100 kcps (kilo-counts per second).

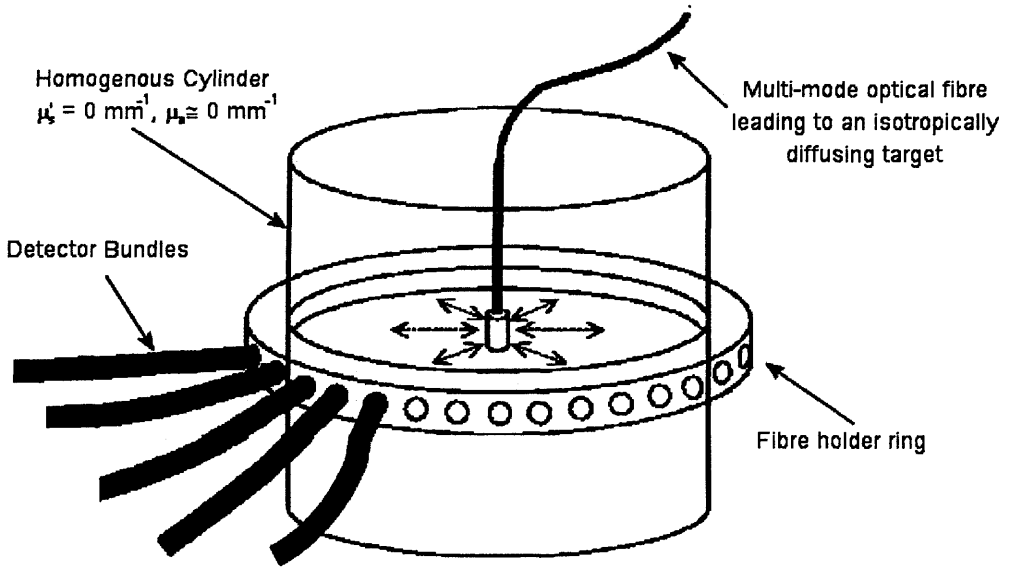

Figure 3-2 System stability investigation: An isotropically scattering target at the centre of a homogenous phantom is illuminated. Data were simultaneously recorded by detector bundles coupled at a fixed radius. (adapted from (Hillman et al. 2000))

Two separate sets of data were acquired using the clear phantom: starting with MONSTIR cold, and again after the normal delay for the system to reach thermal stability. The initial delay was examined by leaving MONSTIR off for 36 hours, then recording TPSFs for 10 seconds every minute from the moment the control software started. Datatypes were investigated by windowing the TPSFs to measure signal only. Full datasets were then normalised based on their final measurements to display variations during the initial period after MONSTIR was switched on.

Operational Stability

The phantom and setup used for quantifying the initial delay was also used to measure system stability during normal operation. Data were recorded after the recommended time of over 10 hours (Schmidt 1999). Data were acquired for 1 s in every 10 s for 3 hours.

Switching Error

The errors associated with switching between sources were investigated using a solid cylindrical phantom with optical properties similar to those of tissue. The phantom was made from a mixture of titanium dioxide particles and NIR-absorbing dye within epoxy resin (Firbank et al. 1995), with a diameter of 69.2 mm and a height of 110 mm and optical properties of $\mu_s' = 1.0\ mm^{-1}$ and $\mu_a = 0.01\ mm^{-1}$ at a nominal wavelength of 800 nm. The refractive index at 800 nm is n = 1.56 and the anisotropy factor g (§2.1.1) is approximately 0.5. Due to uncertainties involved in the process of manufacture, the nominal optical properties of the phantom are correct within 3%. The phantom was also checked for gas bubbles using x-rays, which were found not to be present. Two rings holding 16 source-detector bundles each were fixed around the central plane of the phantom. Data were acquired 10 times for 5 s per source, with 4 hours elapsing between first and last acquisition.

Systematic errors need to be distinguished from random errors that can be quantified statistically. Poisson error is a statistical approximation for the binomial distribution, as applied to low probability counting. Intensity, i.e. the number of photons counted in TCSPC (§2.2.3), N, can be modelled as low probability counting, and hence the error in counting can be described as $\sqrt{N}$. This is the statistical baseline for intensity uncertainty. The uncertainty in recorded intensity will therefore contain Poisson errors plus any additional uncertainty added by system components.

In each of the experiments described in this section, the MONSTIR-03 system was used as described in §2.2.5, and the raw data was used for error calculations before calibration or post-processing.

3.3.2 Results

Stability After Transport

Stability measurements, acquired as the system' reached thermal e, are shown in Figure 3-3. Meantime results were similar for all channels, and are hence shown in the upper graph averaged over all channels, with the average peak position of the TPSFs given for comparison. The plots in Figure 3-3 shows values normalised based on the final recorded value. However, it is the error across an individual hour, roughly the time to record a complete clinical dataset, that is of interest. The error in meantime across an hour does not drop below 10 ps within the 8 hours recorded. Intensity results from some selected channels are shown in the lower graph. These have errors less than 2 % across any individual hour after a delay of less than 4 hours.

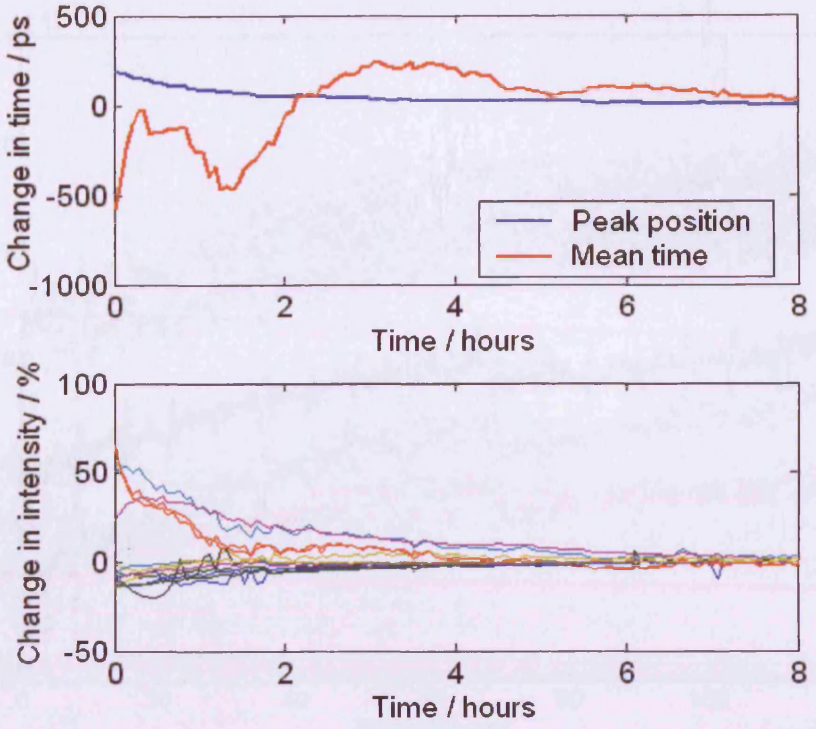

Figure 3-3 Data collected for 10 s each minute from initial start-up. The upper plot shows the meantime and peak position of the TPSFs, averaged for all channels. The lower graph shows the percentage change in intensity measurement for representative channels.

Operational Stability

Acquisition after an initial delay of 12 hours revealed similarities in the intensity variations between channels. Intensities acquired on five of the 32 channels are shown as the dotted lines in Figure 3-4. Variations common to all channels were extracted by normalising data and averaging across all channels. This average variation is shown as the solid line in Figure 3-4. Intensities with the mean removed, i.e. original data divided by the average, are shown in Figure 3-5.

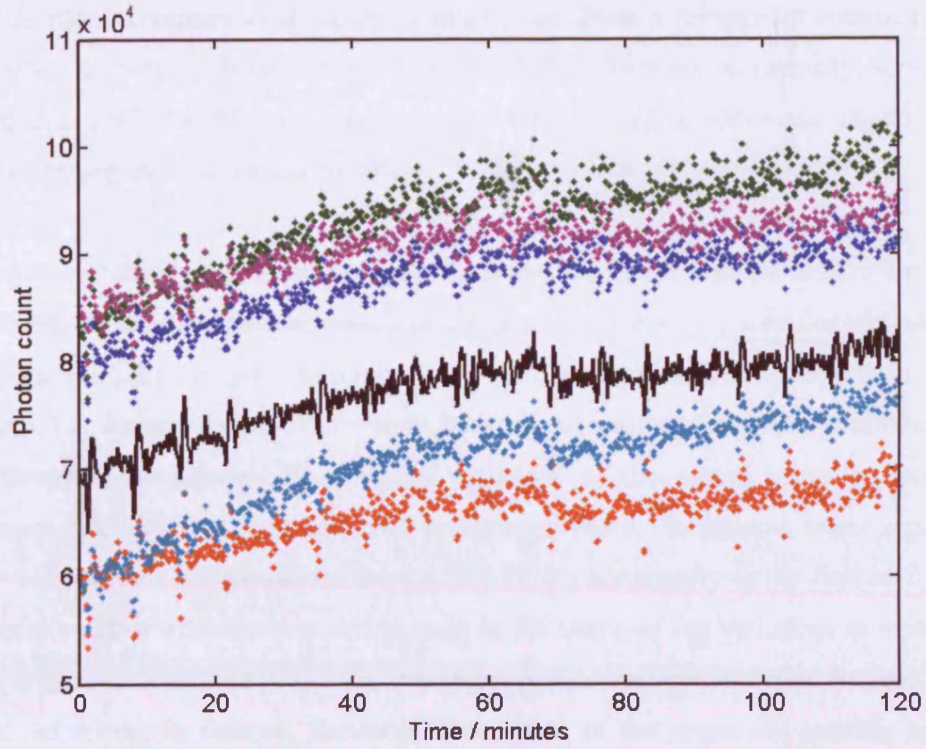

Figure 3-4 Plot of intensity variations recorded on five separate channels (dotted lines), and the common variations between channels (solid black line, arbitrarily offset), recorded after a 12 hr delay to allow the system to reach thermal stability.

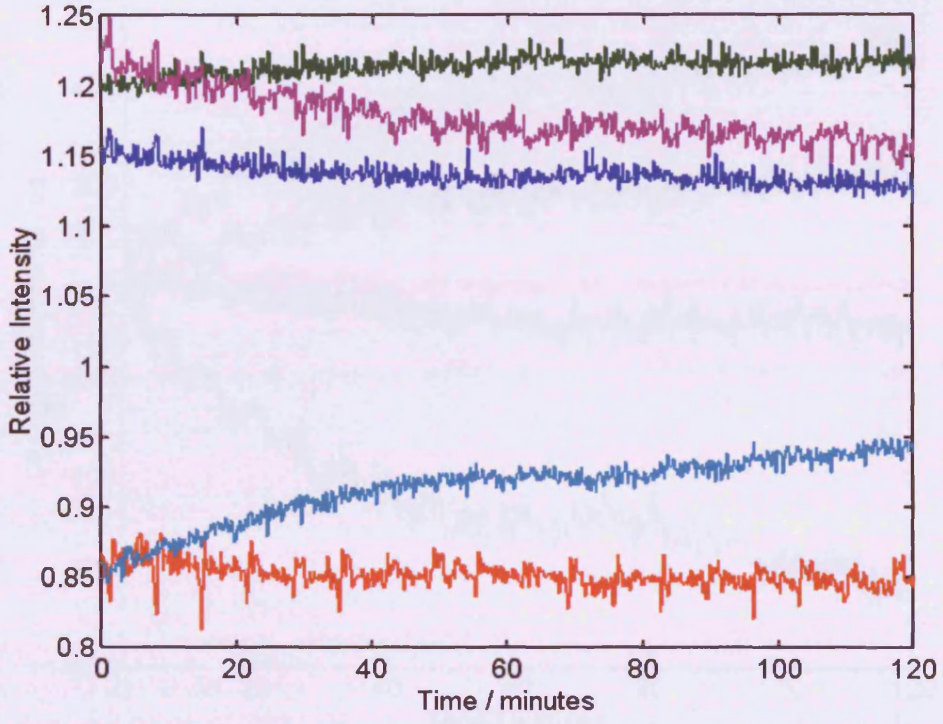

Figure 3-5 Plot of the intensity variations remaining in data recorded on five channels after dividing through by the average, as shown in Figure 3-4.

The variations common to all channels must result from a component common to all channels. However, there remained up to 10 % variations in intensity across the recorded period after the average was removed, indicating individual channels are affected by separate error mechanisms.

Meantime variations for the same channels across the same time period are shown in Figure 3-6. Background noise, optical or electrical, does not vary significantly once the detectors are fully cooled. Variations in intensity are therefore variations in signal strength, i.e. the size of the TPSF versus background counts. Meantime measurements will therefore be affected by intensity variations as the signal intensity decreases relative to the temporally uncorrelated background noise. In general, lower signal-to-noise will increase the meantime as recorded TPSFs are usually in the first half of the temporal window. Similarities can be seen in the shape of the variations in meantime when compared to Figure 3-4. However, there are no specific common features in the meantime results to remove, indicating the causes of the errors are specific to each channel.

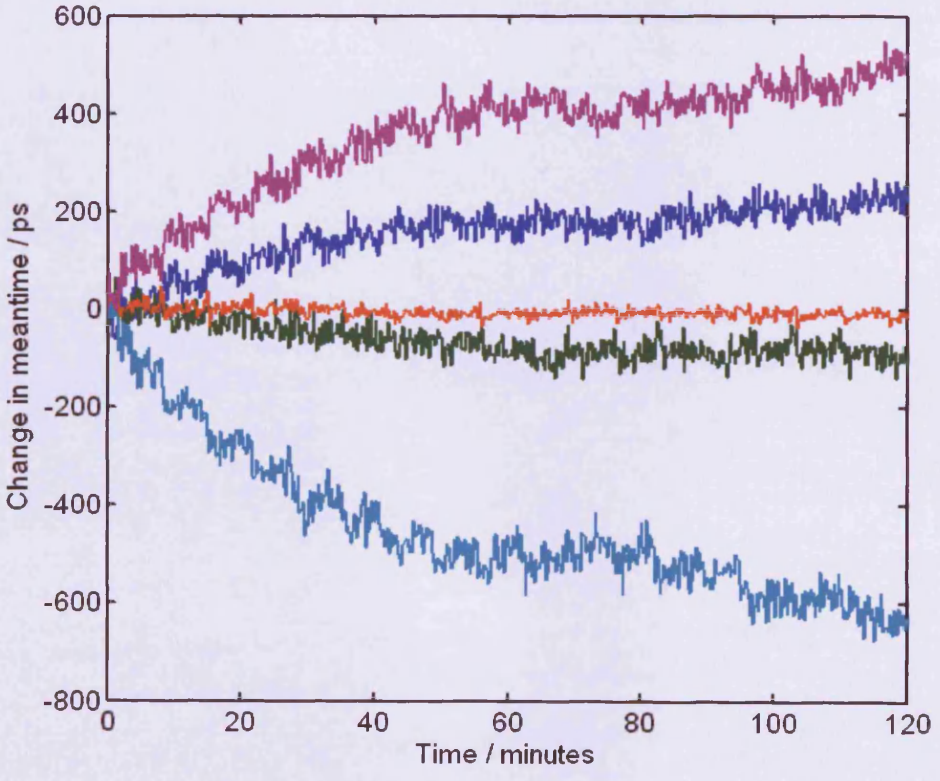

Figure 3-6 Plot of meantime variations recorded on five channels after a 12 hr delay to allow the system to reach thermal stability

Switching

Stability measurements were performed without any source switching or VOA movement. Repeated accuracy of MONSTIR, including channel switching, was tested by acquiring datasets on a homogenous phantom. Errors calculated from the raw data are shown in Figure 3-7 for intensity, and Figure 3-8 for meantime. Each point in these plots represents the mean and uncertainty for a single source-detector pair across 10 repeated acquisitions.

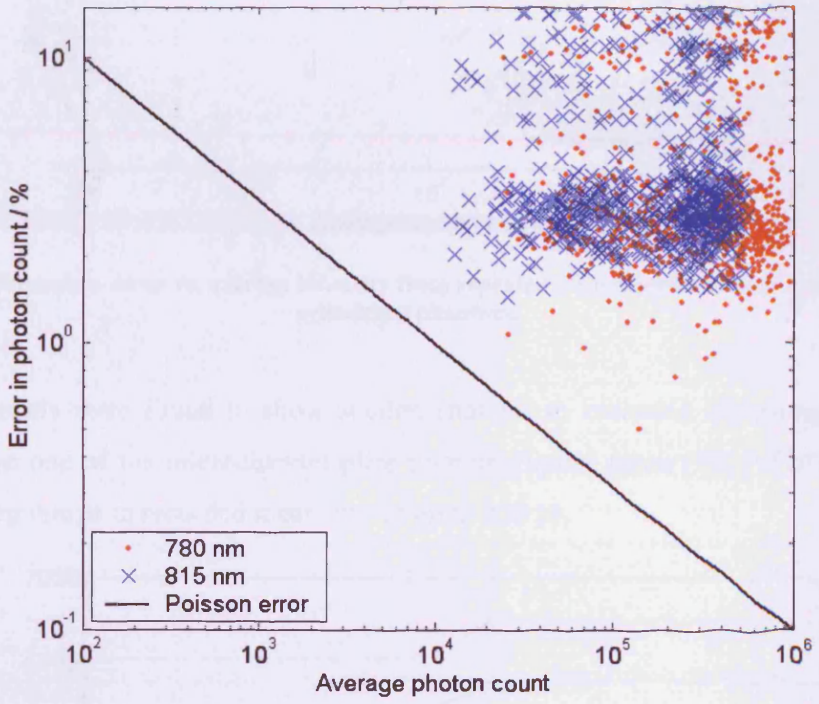

Figure 3-7 Intensity percentage errors vs. average intensity from repeated 5 s measurements on a homogenous cylindrical phantom. Poisson error is given for comparison.

Intensity varied by 6.55 % and 7.04 % for the two wavelengths. The standard deviations of meantime measurement were 18.3 ps and 20.8 ps respectively.

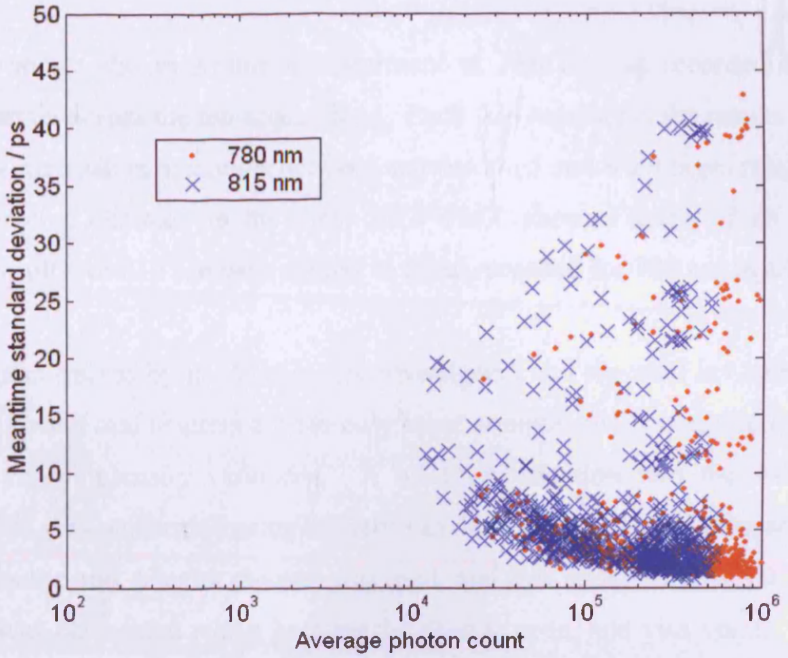

Figure 3-8 Meantime error vs. average intensity from repeated 5 s measurements on a homogenous cylindrical phantom.

Some channels were found to show sudden changes in recorded meantimes. A few channels on one of the microchannel plate photomultiplier tubes (MCP-PMTs, §2.2.5) showed step jumps in recorded meantime of up to 250 ps.

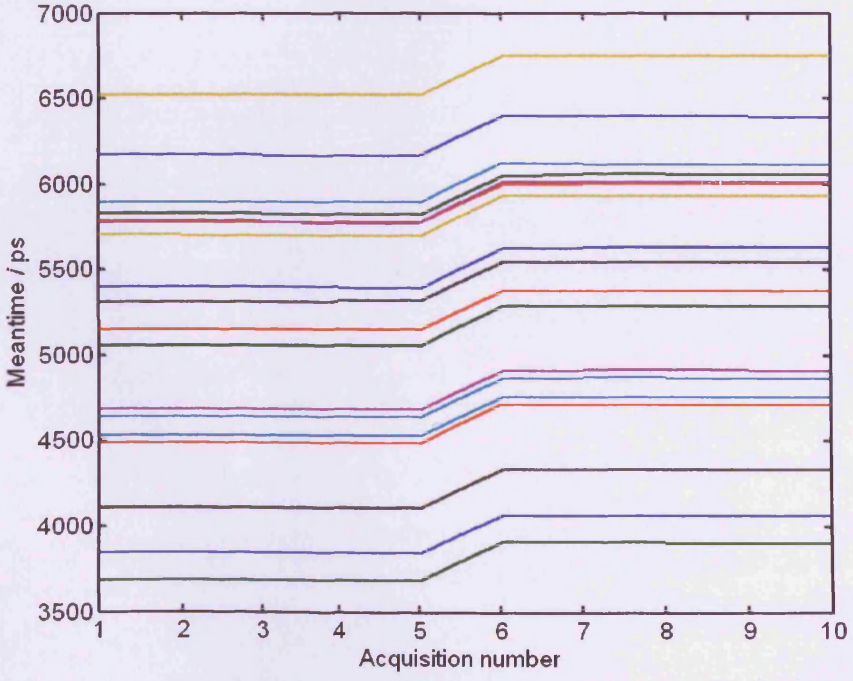

Figure 3-9 Meantime (in ps) against measurement number for one detector channel. Each line represents the acquisitions for a different source.

Figure 3-9 shows the meantime measurement at 780 nm, as recorded by a single detector channel across the ten acquisitions. Each line represents the results for a single source. The increase in meantime between acquisition 5 and 6 averages roughly 230 ps. Another detector channel on the same MCP-PMT showed steps of an average of ~120 ps. Results for 815 nm were similar to those recorded for 780 nm in all cases.

Intensity errors caused by the VOAs were investigated and reported in (Jennions 2003). The source switch and shutters are the only other components containing moving parts that could cause intensity variations. A brief investigation into the switching and shutter speeds was performed using the setup as described above for repeated accuracy. The same source and detector channel was used, and data acquired at 10 Hz. Testing of the switch was performed whilst keeping the shutter open, and visa versa. The switch was found to move into position within 0.1 s of the control signal being provided for all channels. The response time for each shutter channel are shown in Figure 3-10. The two highlighted channels showed delayed responses, with channel 5 taking more than 30 s to open fully.

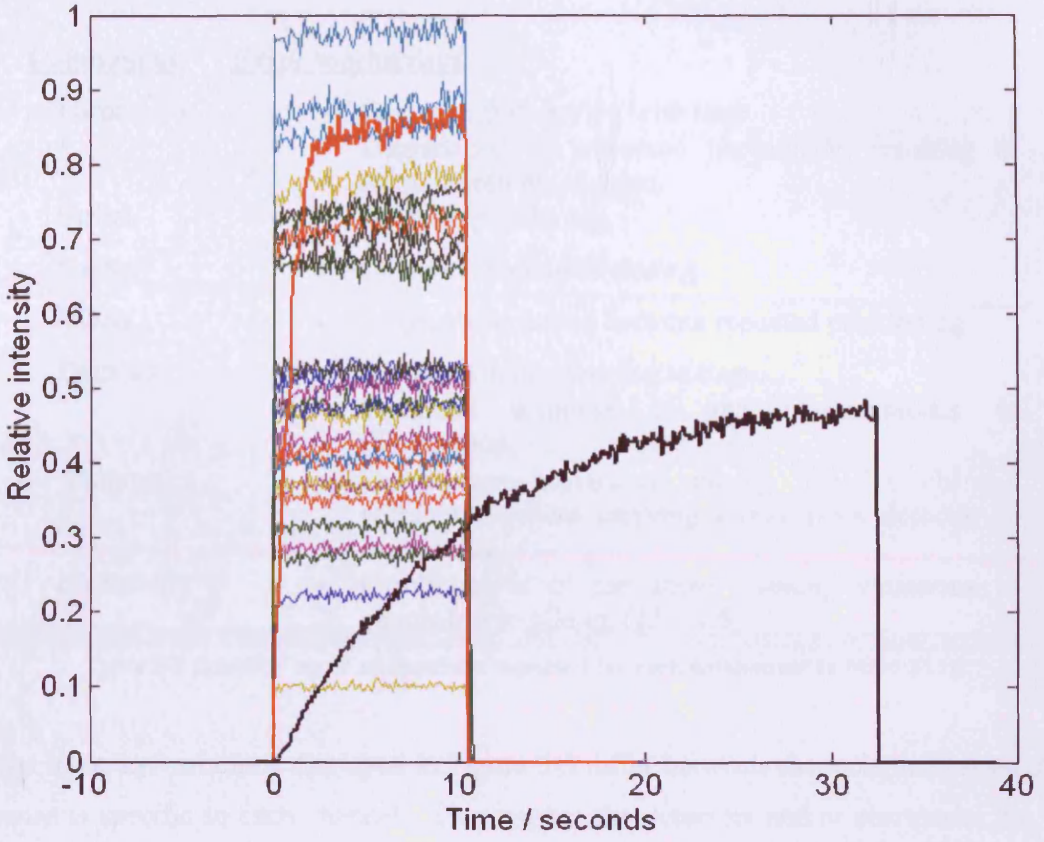

Figure 3-10 Plot of shutter response times. Each line represents a single channel, acquiring data at 10 Hz, starting one second prior to opening. The two highlighted channels are 5 (black) and 16 (red).

3.3.3 Discussion

3.3.3.1 Intensity

MONSTIR-03 was primarily designed to record time-resolved datatypes, and not accurate intensity measurements. Each component in MONSTIR could have an effect on intensity measurements if not operating ideally. The components expected to cause variations in intensity are listed in Table 3-1 below, each with suggested error mechanisms.

Component	Error mechanism
Laser	• Power output varying with time. • Degradation of reference photodiode, resulting in irregular reference pulse.
Switch	• Delay in positioning.
Shutter	• Delay in opening or closing.
VOAs	• Error in attenuation between repeated positioning.
Detector	• Variation in accelerating voltage. • Temporal response of the photocathodes to illumination.
Cabling	• Temperature variations causing resistive changes within the cables carrying signal from detector to electronics.
Electronics	• Combinations of the above causing variations in counts lost to pile-up (§2.2.4.5).

Table 3-1 Intensity error mechanisms expected for each component in MONSTIR.

The intensity variations displayed in Figure 3-3 differ between channels, indicating the cause is specific to each channel. This implies the detectors and/or electronics are at fault. The initial delay of 12 hrs, as suggested in (Schmidt 1999), is mainly to allow the electronics and surrounding cabling to reach thermal equilibrium. In addition, the efficiencies of the photomultiplier tubes (PMTs, §2.2.4.3) varying with time during constant illumination due to saturation of the photocathodes and hysteresis in the electron flow replacing charge to the dynodes and photocathode. These PMT effects are amplified as the detectors, bought in 1998, are reaching the end of their useful lifetimes.

The average temporal instabilities shown in Figure 3-4 are present in data recorded on all channels. There are only two possibilities for varying intensity that are common to all channels: variations in the power output of the laser source, and instabilities in the power supply to the photomultiplier tubes and timing electronics. The power supplies to the electronics and PMTs are regulated and provide a constant power source. Any other count losses in the electronics are due to changes in the incoming photon count, and hence depend on variations caused by other components. The power output of the laser is therefore felt to be the cause of large intensity variations.

Repeated acquisition on an homogenous phantom would contain any errors found for a static system, but the errors would be increased due to source switch, shutter, and VOA movement. Errors in the movements of the switch or shutter units would be expected to be repeatable, occurring each time the specific channel was selected, and affect the magnitude of the intensity rather than the error. In addition, the switch and 30 channels of the shutter unit are operating as per the manufacturer specifications. This means the VOAs are a source of added intensity errors.

3.3.3.2 Meantime

It has been suggested that the water-cooling for one unit has leaked and allowed water vapour into the previously hermetically sealed housing surrounding the MCP-PMT. Prior to the work described in this thesis, the temporal stability of these channels was investigated during the cooling period of the detectors. It was observed that instability increased and then decreased (over a period of several minutes) during cooling, suggesting an increased instability due to condensation forming on the face of the MCP-PMT, and that the subsequent improvement occurred when the condensation reached freezing point. As a result ice could form at the back of the MCP-PMT, creating capacitive changes and causing the step changes in meantime.

MONSTIR-03 was designed to measure mean flight time. Excluding these defective detector channels, meantime measurements show accuracies close to the 5 ps bin-size of the TPSFs – an average error of 5.3 ps for 780 nm and 6.5 ps for 815 nm.

3.3.3.3 Overall

The detectors' age is thought to be the cause of the remaining intensity variations and of the meantime steps. Photocathodes slowly degrade over their lifetime. The illumination of the MCP-PMT during previous acquisition affects the detector's quantum efficiency for the following acquisition; for example high illumination followed by low illumination produces an initially reduced measurement in the latter. The recorded intensity then increases with time as the photocathode recovers.

Other detector issues, such as cross-talk between neighbouring detector channels, have not been discussed but also impact on intensity and meantime measurements. For these reasons, and the above, the detectors are the highest priority for replacement along with the electronics, but are much higher in cost (see §3.4.2).

It should be noted that all results described above are for raw data, and do not show results as would be used for imaging. Image reconstruction takes place after post-processing, during which each TPSF and dataset is examined by eye. Data points are eliminated if the TPSF is contaminated by noise, either due to low count rate or excessive noise. In addition whole datasets from a single source or detector channel are occasionally removed due to detector or source switch malfunction.

Average errors calculated from processed data are far lower, due to the removal of poor data. The average intensity error dropped to ~4 % and the average meantime error was 3 ps for 780 nm and 3.5 ps for 815 nm, after processing using Fourier domain calibration (§2.3.1.3).

3.3.4 Conclusion

MONSTIR was designed to record time-resolved datatypes only (Schmidt 1999), and performs meantime measurements very accurately – to within 5 ps for most channels. Intensity, however, has up to 20 % changes between acquisitions.

Due to the problem of uniqueness in image reconstruction (§2.3.3.5), it is advantageous to measure more than one datatype, and intensity in particular. I have implemented the instrumentation changes described in this chapter to achieve this by resolving the issues raised previously in this chapter. The result of the changes to MONSTIR is an intensity datatype that has less than a one percent error. The detectors are to be replaced in the near future, removing the mean-time steps and the temporal variation in detection efficiency.

Haemodynamic and functional studies on infants suggest that the differences between signal and reference acquisitions are of the order of 10 ps for meantime measurements and ~10 % for intensity. If the systematic errors in the datatypes are greater than this over active and resting acquisitions, the difference in data between the two states due to haemodynamic changes cannot be separated from the systematic variations. Other benefits of difference imaging (§2.3.1.3) is also reduced as the errors in data and reference acquisitions won't cancel.

This section has reported on the initial investigations into datatype stability with the original MONSTIR-03 system. The following sections describe the instrumentation advances to be used with MONSTIR to resolve the concerns raised in this section, amongst others.

3.4 New electronics

3.4.1 Introduction

A range of possible detector and timing electronics were investigated to replace the ten-year-old components in MONSTIR-03. The detectors are coming to the end of their useful lifetime and their performance is slowly degrading with time. In addition, individual detectors are needed to replace the multi-channel microchannel plate (MCP) detectors currently used, due to problems with cross-talk (§2.2.4.3) between neighbouring channels.

The timing electronics in MONSTIR-03 are bulky and require a few hundred ms per channel to upload the temporal point spread function (TPSF) to the control PC. Replacements for the picosecond Time Analysers (pTAs, §2.2.5) would greatly reduce the overall size and remove the delay due to the upload time. However, a high count rate is also a priority. Count rates and losses due to dead times in timing electronics are discussed in (§2.2.4.5).

PCI cards made by Becker and Hickl GmbH, Germany, were selected to replace the timing electronics used in MONSTIR-03 (§2.2.5). The new TCSPC units (§2.2.4.5), called the SPC-134, provide:

- a significant reduction in the size of MONSTIR
- faster acquisitions of full datasets
- greater efficiency for shorter acquisition times per source

The SPC cards are limited to a lower maximum count rate, as compared to the original electronics. However, acquisitions at large source-detectors seperations are of greatest import to MONSTIR as they carry information from the deepest areas of the subject, and these larger seperations correspond to the lowest count rates. The SPC cards have been found to provide datatypes (§2.3.1.1) as stable as the original electronics over a large intensity range.

3.4.2 Review of alternative detection technologies

3.4.2.1 Photomultipliers

The following attributes are desirable for MONSTIR's detectors:

- High sensitivity for photon counting resolution
- Low temporal dispersion (TTS)
- Highest possible quantum efficiency
- Linear count rate response over a large dynamic range
- Good spectral response across 700 - 900 nm

A full discussion on photomultiplier tube design is given in §2.2.4.3

Microchannel plate photomultiplier tubes (MCP-PMTs), such as the MCP-PMTs used in MONSTIR (§2.2.5), have excellent time resolution in comparison with standard PMTs. The MCPs consist of a two-dimensional array of a great number of glass capillaries (channels) bundled in parallel and formed into the shape of a thin disk. Each microchannel has an internal diameter on the order of 10 s of microns with the inner wall processed to have the selected electrical resistance and emissive properties. These channels restrict the photoelectrons' and secondary emissions' motion and minimise the temporal dispersion of the output pulse.

Hamamatsu Photonics, Japan, supplies a wide range of photon-counting PMTs. Two possible MCP-PMTs are the R3809-51 and -59. These have a transit time spread (TTS, §2.2.4.3) of 25 ps, but the -51 has quantum efficiency (QE) $\approx$ 4%, whereas the -59 has QE $\approx$ 0.3% but a much flatter wavelength response. Standard PMTs have also been considered, e.g. the H7422P-50 and H8224P-50. These have QE $\approx$ 12% and few dark counts, but have a greatly increased TTS $\approx$ 300 ps. The comparison between these options, and the current MCP-PMTs (Hamamatsu R411OU-05MOD), is given in Table 3-2.

Parameter	R3809-51	R3809-59	H7422P-50	H8224P-50	R4110U-05
Wavelength Range / nm	160-910	400-1200	680-890	380-890	300-950
Peak Wavelength / nm	600	800	800	815[1]	650
Peak QE / %	4	0.3	12	12[1]	4
Dark Counts (average) / s-1	~10	~200	~50	~1000[1]	~10
TTS / ps (FWHM)	25	25	300	280	45
Cost for 32 channels	£350k	£390k	£100k	£59k	£80k

Table 3-2 Comparison of four new PMTs against the current MCP-PMTs (right).

[1]The specifications for the H8224P-50 are estimated from similar Hamamatsu products.

The MCP-PMTs in MONSTIR are to be replaced with 32 H8224P-50 (select model) outside the scope of this work. The main advantage of these PMTs is the fact that they not multi-channel, hence cross-talk between detector channels will be reduced significantly. Each PMT also has a built-in thermoelectric cooler, which should simplify cooling. The increase in TTS is felt to be mitigated by improvements in other characteristics.

3.4.2.2 Electronics

Two commercially available sets of timing electronics were investigated: Becker & Hickl GmbH SPC-134, and the Ortec EG&G 9308 system. A system proposed by the designer of the Ortec 9308, now operating as Impeccable Instruments, LLC, was also presented for comparison. An overview of the operation of timing electronics is given in §2.2.4.5.

MONSTIR-03 uses the EG&G 9308 TCSPC units, which are still available from Ortec. The EG&G units use a separate set of discriminators and timing electronics for each channel. The CFDs, which convert the MCP-PMT outputs to logic pulses, have four channels per module. Each channel has an individual module for the pTA, which calculates the flight-time and stores the TPSF. The CFD modules are standard NIM single-width (34 x 221 x 347 mm) with BNC inputs, and the pTA modules are double-width (69 mm). The CFDs (Ortec 9307) and pTAs (Ortec 9308) are both designed for use with ultra-fast detectors, specifically MCP-PMTs. The EG&G system uses time-to-digital conversion (TDC, §2.2.4.5), which allows constant readout of pulse timing, resulting in a dead time of 50 ns. The bin-width of the TPSFs recorded with the 9308 units is 1.2 ps, but this is down-sampled by the MONSTIR-03 software to 5 ps to reduce dataset size.

Becker and Hickl supply a system which is comprised of four PCI cards (225 x 125 x 85 mm in total), called the SPC-134. Each card is a complete timing engine, including discriminators for both signal and reference, and can operate totally independently. All of the operations of the SPC cards can be controlled from the software included with the SPC hardware, and full libraries are provided for writing in-house software (Becker 2005b). The SPC cards use time-to-amplitude converters (TAC, §2.2.4.5) with a dead time of 125 ns and a bin-width of 6.1 ps.

The SPC cards are designed to record eight separate TPSFs in one memory segment. A router (HRT-81, Becker & Hickl GmbH, Germany) can be used to provide a single SPC card with timing pulses and channels markers from up to eight input channels (Becker 2005a). The router does not cycle through the input channels, but passes pulses from all channels directly through to the SPC cards. This allows constant collection and has no temporal implications. The router improves dead-time loss by ignoring both photons that arrive simultaneously at the router, but all eight channels use the same timing engine (per single SPC card), which limits the maximum count rate for each channel.

The system proposed by Impeccable Instruments mounted full discriminators and histogram recording components into a system that would interface to a PC via USB, and be roughly the size of a standard PC. The Impeccable design used TDC, generating quadrature sine waves as with used in the 9308. In addition, one of the internal sinewave oscillators would be phase locked to the laser's reference pulse. This would allow all 'Stop' measurements to be simplified, as they would all be made on the phase of the sinewave.

It was proposed the Impeccable system would be have separate electronics for each of the 32 channels, and that two TDC units could be used per channel. Each unit would have a deadtime of 50-100 ns, but the units could be switched in fewer than 10 ns. If the detection probability is kept beneath the standard TCSPC limit of 1 % (§2.2.4.5), the result would be an apparent dead time of < 10 ns as the chances of a third pulse arriving in the dead time is negligible. A bin width of 2.5 ps was suggested, but realistically this would be more like 4 ps due to dataset size and minimal improvement in data quality from further reduction.

The main difference between the three systems is their maximum count rate, as summarised in Table 3-3. For this comparison the maximum useful count rate is taken as the rate at which pile-up theoretically becomes significant: five percent of the inverse of the dead time (Becker, W 2005). The EG&G 9308 system has a dead time of 50 ns, hence provides a maximum 10^6 counts per second (cps) per channel due to the TDC timing method and individual engine per channel. The SPC cards have a longer dead-time of 125 ns, providing 4.0×10^5 cps per card. This is not affected by the quad-card setup as each card runs independently (Becker, W 2005). However, the SPC cards require four 8-1 routers to create 32 channels, resulting in maximum count rates of only 5.0×10^4 cps per channel. The proposed Impeccable system would theoretically have a dead time of less than 10 ns, resulting in a maximum count rate of 5.0×10^6 cps per channel.

Parameter	SPC-134	Impeccable	EG&G 9308
Dead Time / ns	125	10	50
Average maximum count rate per channel / (cps)	5.0×10^4	5.0×10^6	1.0×10^6
Cost for 32 channels	£30 k (with routers)	£100 k	£250k

Table 3-3 A comparison between the three main options to replace the original timing electronics. The count rates for the SPC system assumes four 8-1 routers. Cps – counts per second.

Ideal electronics would have negligible dead time, effectively removing any pile-up distortion at high count rates. However, accurate datatypes can be calculated from TPSFs recorded at ~10^4 cps. Above this rate, little information or accuracy is added. In addition, our focus is on accuracy with large source-detector separations, meaning very low count rates but providing the most information as the photons have travelled through larger volumes of the subject. Accurately recording these low counts requires good dark-count suppression (e.g. CFD thresholding, §2.2.5).

The main disadvantage of the electronics used by MONSTIR-03, Ortec's EG&G 9308, is the clinical usability. The EG&G modules require a few hundred ms per module to upload data to the control computer before resetting for the next acquisition. This roughly doubles the typical acquisition time for 32 channels and introduces difficulties for trying to capture fast functional changes. A drawback of the original setup, using the 9308 units, is that the system needs roughly 12 hrs to reach thermal equilibrium before timing accuracy stabilised (Schmidt 1999). This was due to the large amount of BNC cabling situated above the 9308 units. The delay along the cable changed by 1 ps/°C per meter, and the NIM units consumed 2 kW, in effect acting like a radiator. It hence had to be left on overnight before use, consuming valuable clinical space. In addition, the EG&G system takes up roughly half of a 6' tall 19" rack, increasing the size of MONSTIR, and reducing the ease with which the system can be moved between clinical and lab space.

The photo shown in Figure 3-11 demonstrates the size of the original MONSTIR system, shown in use during neonatal imaging. Figure 3-12 shows the relative sizes of the two original MONSTIR racks, one for the electronics and PC (measuring 105 x 60 x 152 cm) the other for the laser and power supplies (55 x 60 x 117 cm). Also shown is the expected size of the new rack based around the SPC cards (90 x 49 x 150 cm).

Figure 3-11 MONSTIR in use for neonatal brain imaging. The laser rack is on the left, with the main rack central.

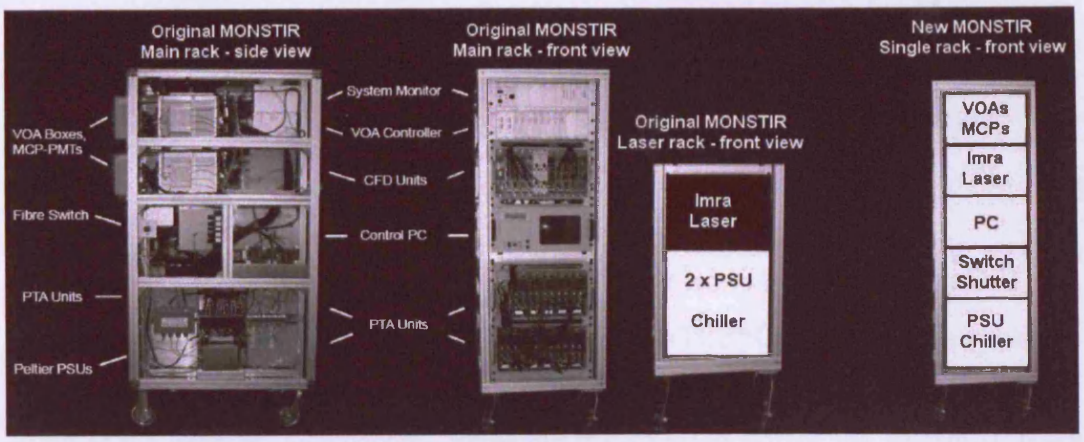

Figure 3-12 Diagram showing the relative size of the two original MONSTIR racks. Shown right is a possible layout for the new MONSTIR, shown as the correct relative size.

Both the SPC cards and the proposed Impeccable system solve all the above problems. They both use double-buffered memory, removing any upload delay by allowing simultaneous acquisition and transferring data via separate memory buffers. They are also both sufficiently compact, with cabling situated remote from any heat source, as to remove any delay due to thermal effects and dramatically reduce the overall size of MONSTIR.

We decided to purchase the Becker and Hickl SPC-134 electronics, as they solved most of the problems experienced with the EG&G system and we felt the drawbacks would not significantly effect the measurements made with MONSTIR. The Impeccable system would have been the ideal combination of improved size and increased acquisition capability, but it was a proposed system that exceeded the funds and time available for MONSTIR upgrade.

The SPC system does have two drawbacks: increased histogram bin-width and significantly reduced maximum count rate Meantime differences between resting and active states are felt to be in the region of 10 ps (§3.2). Meantime measurements are produced with a precision at least one order of magnitude finer than the histogram resolution, therefore it was felt that the increase in bin-width, 6.1 ps per bin as opposed to the current 5 ps, would not significantly affect the temporal resolution of MONSTIR.

In addition, the reduced maximum count rate was felt to be of lesser importance, as high count rates result from the smallest source-detector separations, which inherently carry the least information. The maximum count rate for each channel is also limited by the detectors' estimated maximum, currently ~1.5 x 10^5 cps per channel (§2.2.4.5).

3.4.2.3 Conclusion

In conclusion, the SPC-134 (Becker & Hickl GmbH) TCSPC electronics were chosen due to their low cost and fit with the clinical intentions of the new instrumentation, listed at the head of this chapter. Reducing the time needed for the system to reach thermal stability, the size, and acquisition time of the MONSTIR-03, ensures that the new system will have a smaller impact on the resources available in clinical situations, improving both the space requirement and the flexibility of use.

The SPC system has a reduced maximum count rate in comparison with the EG&G electronics, but can record measurements constantly without upload delay. The SPC cards were hence tested in isolation, described in the following section, and compared to the original EG&G electronics before being implemented in the full imaging system.

3.4.3 Preliminary testing of new electronics

The SPC cards require four PCI slots and significant power from the PCI bus. A new rack-mount industrial computer (Intel 2.8 GHz, 512 DDR RAM, 40 GB hard disk, Broadberry Data Systems Ltd, UK) was chosen to hold the SPC cards. This computer was chosen as the design included mounting the motherboard vertically into passive back plane, providing ten available PCI slots and an improved power supply to all busses.

The cards were slotted into the industrial PC, which could then be connected to the MCP-PMTs and reference signals without affecting any other MONSTIR components. Four aspects of the SPC cards were tested: meantime variation at low count rates, cross-talk effects at low count rates (§2.2.4.5), the count rate at which pile-up starts to distort measurements, and the time taken to reach stability from initial power-up.

The SPC cards were tested by repeatedly acquiring data on a homogenous cylindrical phantom. Eight detector bundles were distributed around one side of the phantom, diameter 70 mm and height 110 mm, and optical properties $\mu_s' = 1.0$ mm^{-1} and $\mu_a = 0.01$ mm^{-1}. A single source fibre was placed opposite the detectors such that all the detector bundles were illuminated roughly evenly, as shown in Figure 3-13. A single, eight-channel MCP-PMT was connected to a router (via the pre-amplifiers), which passed signals to a single SPC card.

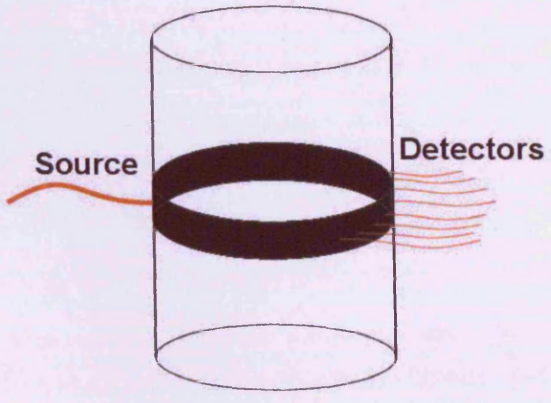

Figure 3-13 Image of experimental setup for testing the new SPC hardware.

A single detector channel was chosen to investigate meantime stability as intensity decreased. Neutral density filters were added to the laser in 0.1 OD steps, acquiring for ten seconds. The meantime and intensity values were calculated for both raw and calibrated datasets.

To examine datatype stability at low count rates, the four detector channels opposite the source were chosen. Three were left unchanged recording roughly 100 kilo-counts per second (kcps) throughout. The detected count rate on the fourth channel was increased from a few photons per second to just above 100 kcps by adjusting the VOAs. The count rates on the four channels summed to 400 kcps for the final measurement.

Another experiment used neutral density filters, inserted into the laser, to investigate the effects of pile-up at high count rates. The attenuation was increased in 0.1 OD steps. All eight detectors were used to record for five seconds starting at a total count rate of 1.6 Mcps.

3.4.4 Results

The SPC cards recorded roughly half the number of counts of the original electronics. Repeated acquisitions show a decrease in intensity errors of a few percent due to the improved dark-count removal by the SPC's software-controlled CFDs. The average meantime measurement acquired with each set of electronics was within the uncertainty of the other.

Repeated measurements with eight channels on a SPC card showed the same ~5 ps standard deviation for uncalibrated data as found with MONSTIR's original electronics (§3.3.3.2).

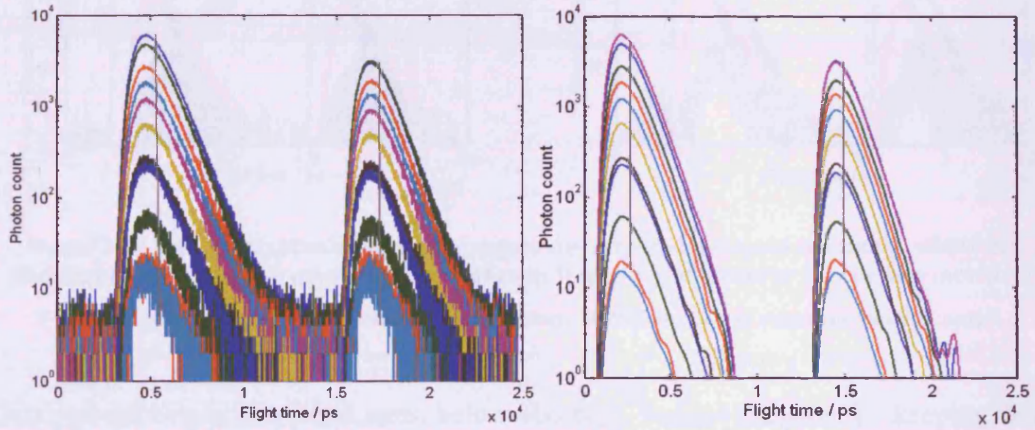

Figure 3-14 Plots showing the TPSFs (raw, left, and calibrated, right) recorded from a single channel with a new SPC card. The vertical line shows the variation in meantime as the intensity changes.

Figure 3-14 shows the TPSFs recorded on a single channel whilst reducing the intensity. The histogram bin size for the SPC cards is 6.1 ps. The standard deviation of meantimes for TPSFs with between 10^3 and 4×10^5 cps is 15 ps for each wavelength. Meantime uncertainty reduces with increasing count rate as the signal-to-noise is increased and the effect of the background noise is reduced.

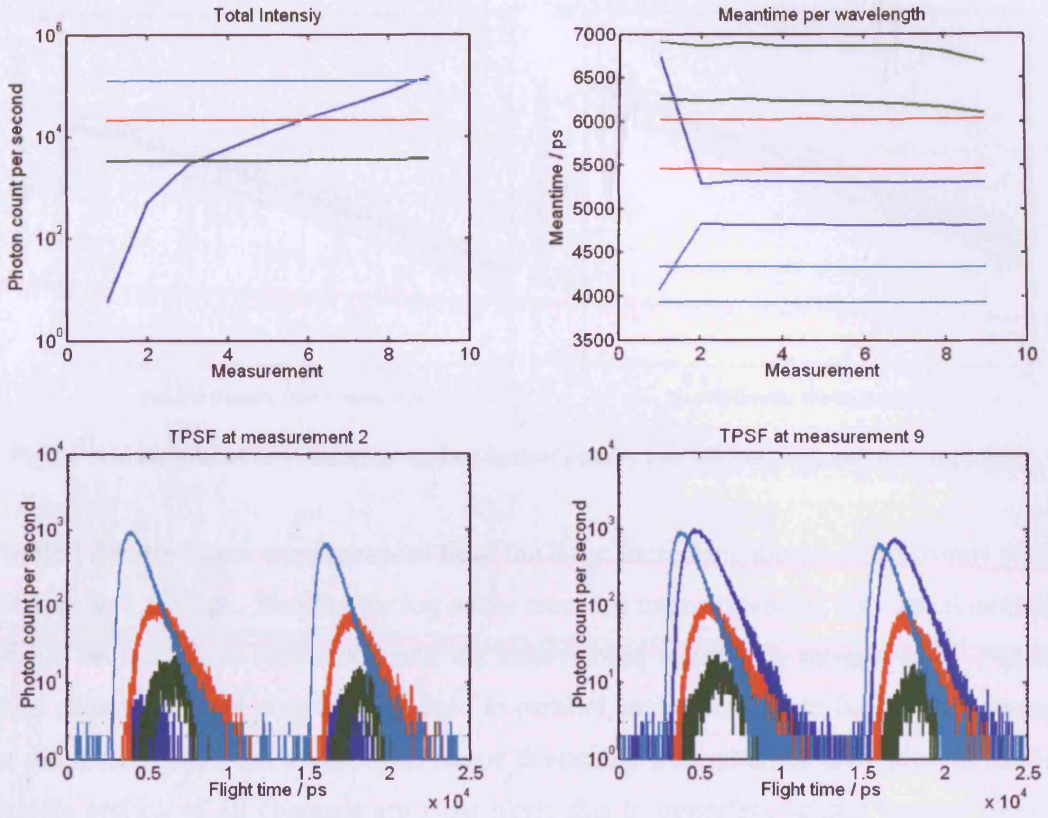

Figure 3-15 Data from three channels are repeatedly acquired (a-axis in top plots), whilst the illumination on one is increased so that count rates from a few photons to 10^5 cps are recorded.

Top: Intensity (left) and meantime(right); Bottom: TPSF shapes at measurements 2 and 9.

Datatype stability at low count rates, below 400 kcps, was investigated by keeping three channels fixed, shown in cyan red and green in Figure 3-15, and slowly increasing the count rate of the fourth, shown in blue. The intensity and meantime measurements on the three fixed channels appear constant as the count rate on the fourth channel increases. This implies that beneath this count rate no distortion occurs due to pile-up. The channel with the lowest constant count rate and largest meantime, shown in green in all of Figure 3-15, displays an irregular meantime values due to low signal to noise.

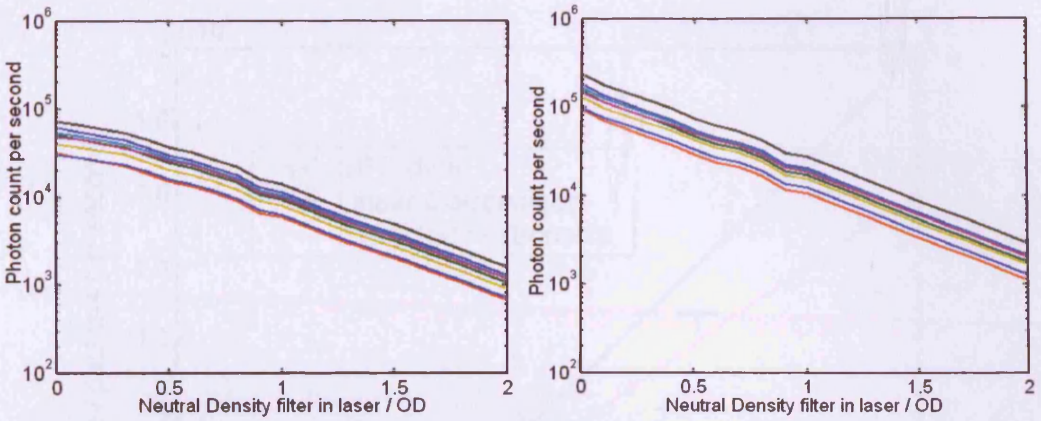

Figure 3-16 Graphs of total intensity against optical density for 780 nm (left) and 815 nm (right).

Neutral density filters were removed from the laser, increasing the recorded counts from 23 kcps to 1.6 Mcps. Plotting the log of the recorded intensity versus the optical density of the neutral filters introduced into the laser should result in a straight line. Figure 3-16 shows the eight channels recorded in parallel, and agrees up to 0.4 OD remaining in the laser (~800 kcps total). The minor deviations from straight lines present in the middle section of all channels are most likely due to imperfect neutral density filters. Above 800 kcps, the intensity of the second TPSF in the detection period, 815 nm in this case, is reduced by comparison to the first – the two highest intensity data points have both been reduced by roughly 10 % in comparison to a linear relationship, as shown in Figure 3-17. This loss in recorded intensity is thought to be due to classic pile-up (§2.2.4.5).

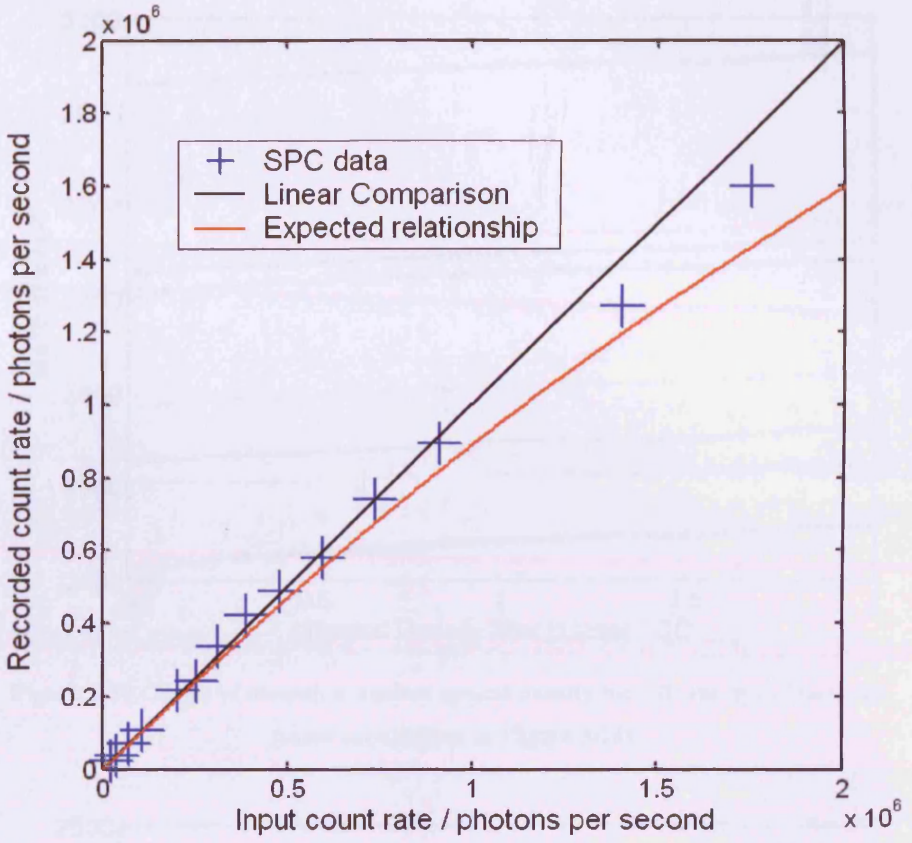

Figure 3-17 Plot of input and recorded output count rates from the SPC cards. (Compare with Figure 2-17)

The corresponding meantime measurements, shown in Figure 3-18 and Figure 3-19, show that meantimes tend to increase as intensity decreases. The meantime of the signal is typically less than half the width of the temporal window, hence the measured meantime increases with decreasing intensity due to the greater effect of temporally uncorrelated background noise. The deviation from linearity of the meantime plots between 0 - 0.4 OD in Figure 3-19, combined with the non-linear intensity, both due to the loss of photons from the end of the second TPSF, indicate that classic pile-up is distorting TPSFs above roughly 10^6 cps.

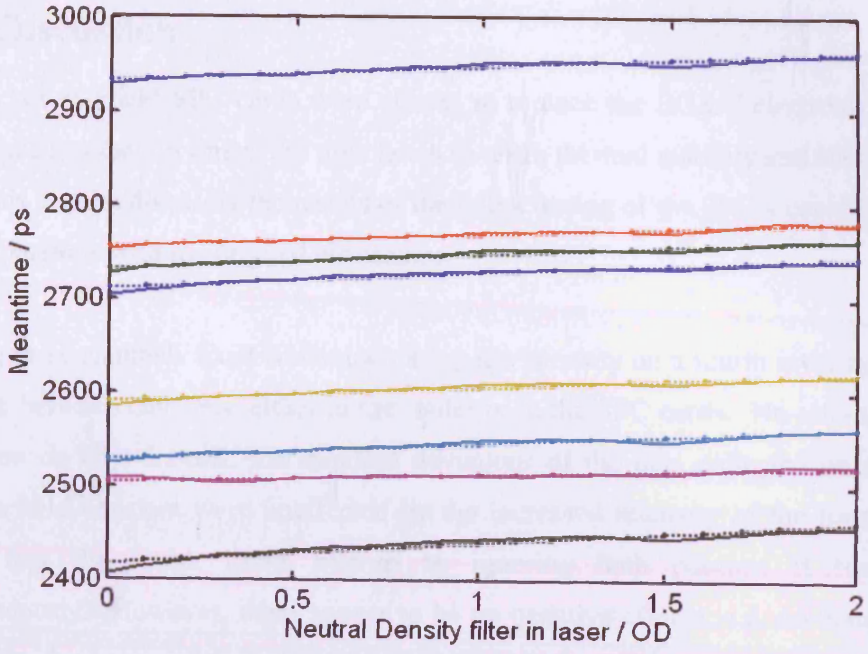

Figure 3-18 Graph of meantime against optical density for 780 nm, with linear fits.

(same acquisitions as Figure 3-16)

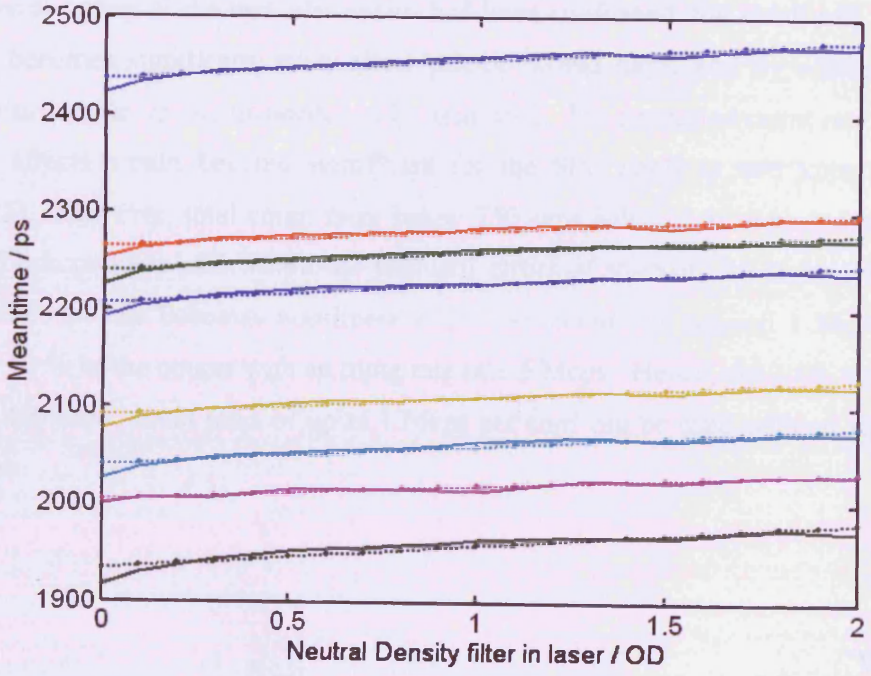

Figure 3-19 Graph of meantime against optical density for 815 nm, with linear fits.

(same acquisitions as Figure 3-16)

3.4.5 Discussion

The Becker & Hickl SPC cards were chosen to replace the EG&G electronics. They will reduce acquisition times, the time taken to reach thermal stability and MONSTIR's size. This section discusses the results of the initial testing of the SPC's capabilities and the comparisons with the original electronics.

Keeping three channels fixed whilst increasing the intensity on a fourth investigated any crosstalk between channels, either in the router or in the SPC cards. No pile-up effects were seen on any channel; the standard deviations of the data collected on the three channels held constant were unaffected by the increased intensity of the fourth. It is known that the router limits pile-up by ignoring both photons if two arrive simultaneously. However, there appear to be no negative effects, e.g. no distortion of the TPSFs, due to use of the router and multi-channel operation of the SPC cards at low count rates.

Once the accuracy of the new electronics had been confirmed, the count rate at which pile-up becomes significant, what effect pile-up would have, and by which specific mechanism(s) pile-up occurs needed to be identified. The suggested count rate at which pile-up effects would become significant for the SPC cards is 400 kcps per card (§2.2.4.5). However, total count rates below 750 kcps behaved as expected, and rates up to 900 kcps were still within the standard errors of intensity measurements. The recorded count rate becomes non-linear with input count rate beyond 1 Mcps, losing roughly 10 % of the counts with an input rate of 1.5 Mcps. Hence, although the suggest limit is 400 kcps, count rates of up to 1 Mcps per card can be used without significant distortion.

The meantime measurements from the same experiment increase linearly by 15-20 ps per OD reduction in intensity. This is due to the increasing effect of the temporally uncorrelated background noise on the meantime as signal intensity decreased. However, the meantime of the second TPSF in the acquisition window is further reduced by 10-15 ps for the final measurement. The drop in meantime means the end of the TPSFs have been distorted, caused by pile-up loses at the end of the timing window as described in §2.2.4.5. Again, if the total count per card is kept below 1 Mcps, pile-up effects are not seen.

The effects of classic pile-up, the loss of photons from the end of the acquisition window, can be seen in both intensity and meantime measurements from the second TPSF, 815 nm in these experiments. However, these effects are only seen above 1 Mcps which is more than twice the theoretical limit for the SPC cards. This mitigates the main disadvantage of the SPC cards as discussed in §3.4.2.2.

A major advantage of the new SPC cards is the reduction in the delay required after transport for the system to reach thermal stability. The original EG&G electronics and associated cabling required more than 12 hours to reach stable operation. This was attributable to the heat radiated from the electronics, which consume ~2 kW. The electronics and nearby BNC cables needed to reach thermal equilibrium before stable temporal measurements could be produced. The new SPC cards run off a PCI bus, generate minimal heat, and have cabling which is not in such close proximity. The result is a negligible delay due to the electronics before meantimes measurements become stable. The cooling of the MCP-PMTs (§2.2.5) is now the limiting factor for the time taken to reach thermal stability.

3.4.6 Conclusion

In conclusion, the Becker & Hickl SPC-134 units were chosen to replace the original EG&G timing electronics. The SPC cards reduce MONSTIR's size by roughly 50 %, and remove the delay uploading data to the PC, which roughly halves the length of the full acquisition. The new MONSTIR will therefore be more portable and easier to use, in terms of space and time requirements, in a clinical environment.

The measurements taken with the new cards place an upper limit on the count rate per card of 1 Mcps. Above this limit, both meantime and intensity measurements are distorted by losing photons due to pile-up. Below 1 Mcps the datatypes produced throughout all the experiments are roughly equal to and as stable as those described in §3.3 for the original electronics.

The SPC cards continuous recording and fast acquisition rates (<1 s) will lead to MONSTIR's use for fast functional imaging, specifically applicable to neonatal cerebral imaging.

3.5 Improvements in Intensity

MONSTIR was primarily designed to accurately record time-resolved datatypes, specifically meantime. Intensity measurements were not initially a priority, but are now felt to be beneficial for the separation of scatter and absorption in reconstructions. The laser and variable optical attenuators (VOAs) are the largest sources of intensity errors in repeated acquisitions. New instrumentation has been developed to remove these sources, and allow MONSTIR to record intensity with an error of < 1 %.

3.5.1 Laser calibration method

Repeated acquisitions using MONSTIR have shown large temporal variations in intensity. In the most extreme case, the recorded intensity dropped by 40 % over one hour. One cause of these variations is the laser, a custom-made, dual-wavelength system known as the IMRA A-70. A calibration method, using a part of the source beam to illuminate two photodiodes, has been created to remove this effect from the final measurements. In the case mentioned above, the resulting difference in intensity across one hour after correction was one percent.

3.5.1.1 Single Wavelength

Methods

Five out of the 32 available MONSTIR optodes were positioned around a homogenous cylindrical phantom (70 mm diameter, $\mu_s' = 1.0\ mm^{-1}$ and $\mu_a = 0.01 mm^{-1}$). Four optodes, connected to a single eight-anode MCP-PMT, were distributed on the one side of the cylinder, with the final optode, used as a source only, positioned on the opposite side, as shown in Figure 3-20. The new timing electronics, SPC-134 cards (Becker & Hickl GmbH, Germany, §3.4.2), were connected to the detector's pre-amplified outputs.

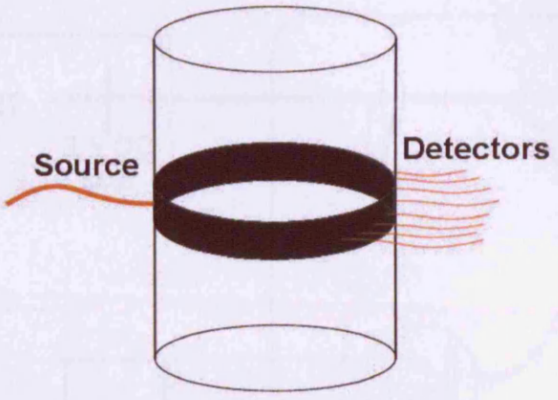

Figure 3-20 Diagram of experimental setup for testing the new laser calibration.

The SPC-134 cards use double-buffered memory to acquire new data whilst transferring the previous dataset to the computer's hard disk. Using this "continuous flow" mode of the SPC cards (Becker 2005b), TPSFs can be acquired over any acquisition length indefinitely. Each channel's data were windowed, removing surrounding noise (e.g. PMT dark counts), then summed. This produced a continuous sequence of intensity measurements, as would be recorded by MONSTIR during standard acquisitions.

A simultaneous and independent measurement of the laser's power output was built, a schematic of which is shown in Figure 3-21. A fibre splitter (125 μm core diameter, multimode, 90/10 pigtail, Oz optics, Canada), connected to the laser via a short optical fibre (0.5 m, 125 μm core diameter), was used to illuminate an amplified photodiode (OPT301, Burr-Brown, USA, with ±5 V supply) with ten percent of the laser's output. The other 90 % was fed into MONSTIR, using the normal source fibre. The voltage from the photodiode was recorded on a PC via a National Instruments data acquisition card (DAC). A 47 μF capacitor was connected to reduce noise, as shown in Figure 3-21. 2.5 OD of neutral density filters were placed in the laser to prevent saturation of the detector.

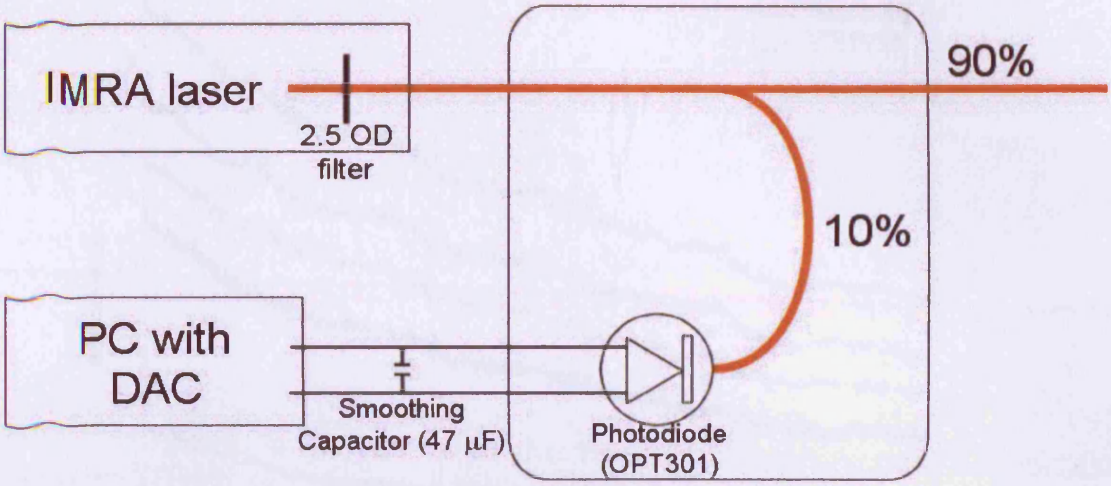

Figure 3-21 Diagram of the components used to record each wavelength individually

Initially, a shutter was placed in the laser to completely block the 815 nm beam. Two DAC measurements, taken at 2 Hz, were summed for better comparison with the SPC data, which were acquired over one second. The shutter was then moved to block the 780 nm beam and measurements were made for another hour. During acquisition, the single source was kept constantly open, and the VOAs were not moved. This removed any effect the mechanical components of MONSTIR might have on the intensity. The recorded count rate was kept above 2×10^4 counts per second, further reducing noise effects.

Results

The dataset from the SPC cards showed that the laser's power output decreased by roughly 40 % over the hour recorded, and that a beam split from MONSTIR's source fibre could be used to accurately record these variations, as shown in Figure 3-22.

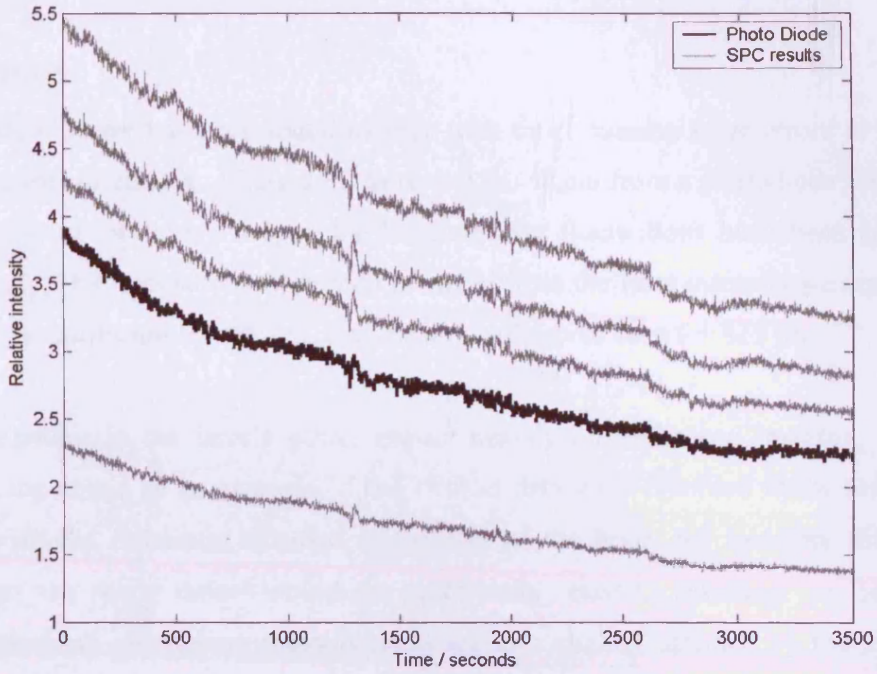

Figure 3-22 Graph of intensity at 780 nm using four SPC channels and a photodiode.

The SPC intensity measurements were divided by the normalised photodiode's output. The resulting calibrated intensities are shown in Figure 3-23. The difference in intensity across the hour was reduced to one percent.

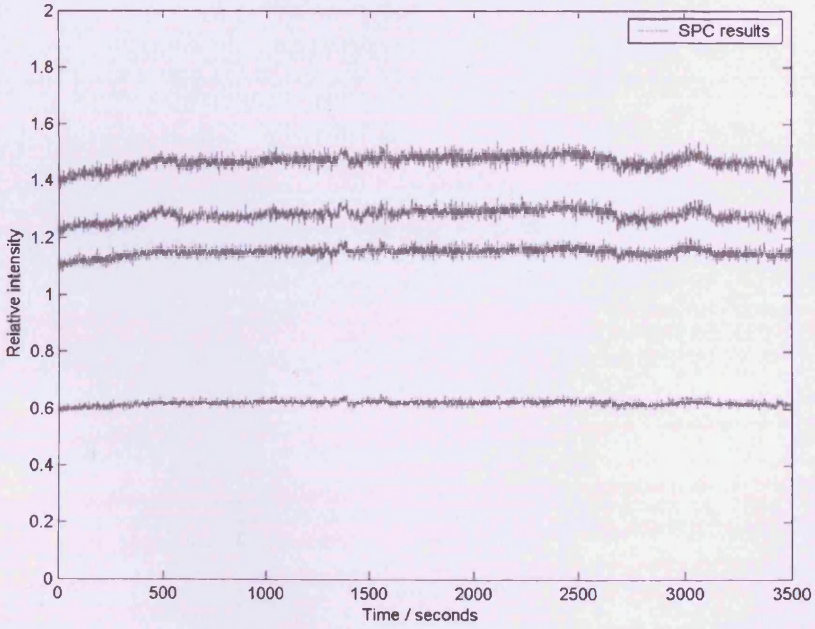

Figure 3-23 Graph of four channels' intensities at 780 nm after the laser box's normalised measurements were removed from the SPC data.

Discussion

The laser's power has been found to vary with time, causing large errors in repeated intensity measurements. Using a PC to record the signal from a photodiode illuminated with 10 % of the laser's output, the laser's power fluctuations have been accurately measured. The fluctuations were then removed from the final intensity measurements. The above results are for 780 nm, but similar results were seen for 815 nm.

The variations in the laser's power impact heavily on difference imaging, §2.3.1.3. Taking the above as an example, if the clinical data were recorded at the start of the hour, with the reference recorded at the end of the hour, the intensity differences between the two states would be artificially raised, resulting in inaccurate reconstructions. Meantime measurements are also slightly affected by the change in intensity, due the loss of signal compared to background noise, but the change is within expected error margins (§3.4.5).

Overall, the results described above prove that the new instrumentation can record the laser's power variations accurately, and the resulting data can be used to remove the variations from the final intensity measurements. However, to be useful for acquisitions with MONSTIR, both wavelengths must be recorded simultaneously.

3.5.1.2 Dual wavelength

Design of instrument for dual-wavelength measurement

To record both wavelengths simultaneously, ten percent of the source beam was extracted by the beam splitter, illuminating two photodiodes (see Figure 3-24). A fibre with an inline variable attenuator (1.0 m long, 125 μm core diameter, Oz optics) was coupled to the end of the splitter to remove the need for neutral density filters. At the end of the attenuator fibre, a cubic beam splitter (15 mm Tech Spec, Edmund Optics, UK) and right angle prism (15 mm Tech Spec, Edmund Optics) were fixed next to each other to produce two equal-intensity parallel beams. A 780 nm interference filter, (FWHM 10±2 nm, > 50 % transmission at peak, < 0.1 % outside bandwidth) was positioned in front of one of the photodiodes. One photodiode was hence illuminated by both wavelengths and the other by 780 nm and only a small fraction of 815 nm. The voltages from the photodiodes were recorded using a USB DAC unit (USB-6008, National Instruments Corporation, USA) and processing software written in LabWindows (National Instruments Corporation, USA).

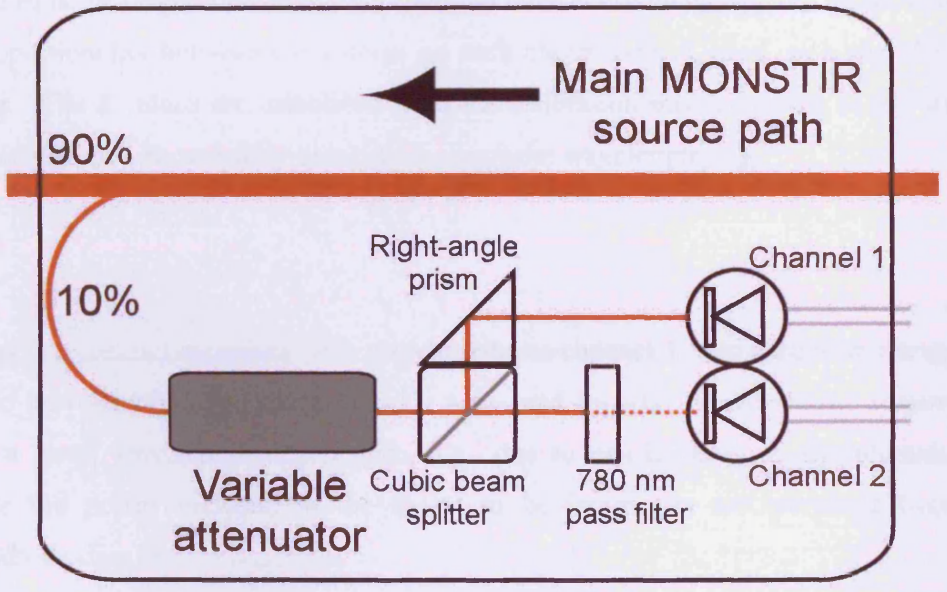

Figure 3-24 Schematic of the dual-wavelength setup.

A cylindrical phantom and five optodes were set up as for the single wavelength experiment, shown in Figure 3-20. The PC was set to record from both photodiodes simultaneously. Neutral density filters were introduced into the laser after the photodiodes and SPC cards had acquired a baseline for 6 min. Two neutral density filters were inserted sequentially into the 780 nm beam only, then the 815 nm beam only. The drops in intensity were recorded with both systems, and compared to the baseline measurement to calculate the optical density. The attenuations of the neutral density filters were recorded by taking average measurements from a power meter before the experiment.

Separation of the Wavelengths

The output of the photodiodes were recorded for each wavelength individually and both together before starting data acquisition. Simultaneously, the beam emitted from the end of the source optode was measured with a power meter. The voltage produced by each photodiode can be expressed as:

$$\begin{aligned} V_1 &= k_{11}P_{780} + k_{12}P_{815} \\ V_2 &= k_{21}P_{780} + k_{22}P_{815} \end{aligned} \qquad \text{(i)}$$

where P_λ is the original power output from the laser at wavelength λ. k_{nm} is the constant of proportionality between the voltage on each photodiode, V_n, and each wavelength's power. The k values are calculated from the calibration measurements at the start of each acquisition, recorded by blocking the opposite wavelength, e.g.:

$$k_{11} = {V_1}/{P_{780}} \qquad \text{(ii)}$$

Taking the channel recording both wavelengths as channel 1, and assuming the system has no wavelength dependence, then $k_{11} \approx k_{12}$, and $k_{22} \approx 0$. However, the system will have a small wavelength dependence, e.g., due to non-linearity in the photodiodes. Hence the power incident on the object to be imaged is reconstructed from the photodiode data by:

$$\begin{pmatrix} P_{780} \\ P_{815} \end{pmatrix} = \begin{pmatrix} k_{11} & k_{12} \\ k_{21} & k_{22} \end{pmatrix}^{-1} \begin{pmatrix} V_1 \\ V_2 \end{pmatrix} \qquad \text{(iii)}$$

Results

The powers of the two wavelengths were individually measured at the start of the acquisition at 21.3 and 8.6 mW for 780 and 815 nm respectively. The neutral density filters produced an average of 0.14 and 0.28 OD. Data were recorded continuously over a 20 minute period. The upper graph in Figure 3-25 shows the raw voltages recorded from the two photodiodes.

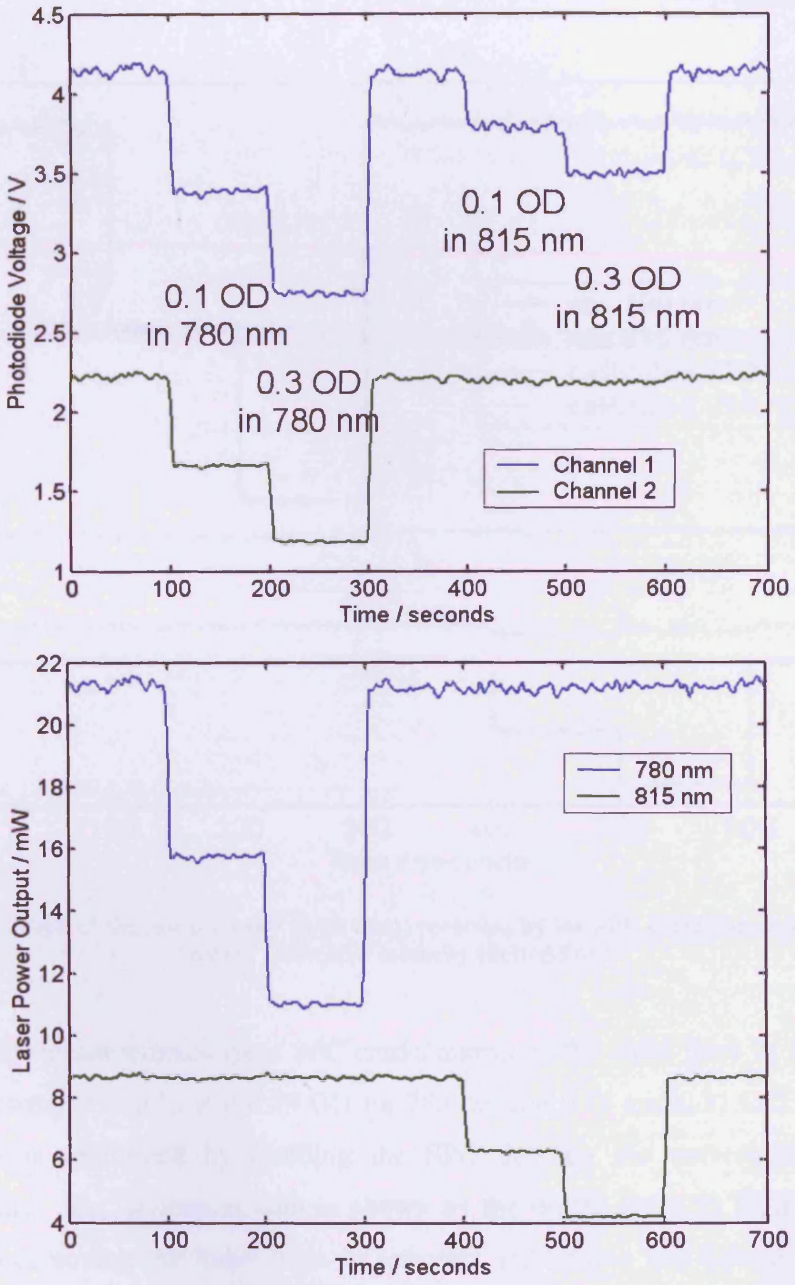

Figure 3-25 Graphs of laser power, using neutral density filters to attenuate one wavelength at a time. The upper plots are the raw photodiode data with the separated wavelengths shown below. Channel 1, recording both wavelengths, and channel 2, filtered to record 780 nm only, are as shown in Figure 3-24.

The lower plot of Figure 3-25 shows the changes in power of the separated wavelengths. Although there are noticeable variations in measured power throughout, placing filters into one of the wavelengths causes steps of less than 1 % in the power of the other wavelength. The separation of each wavelength's power is hence achieved without significant crosstalk.

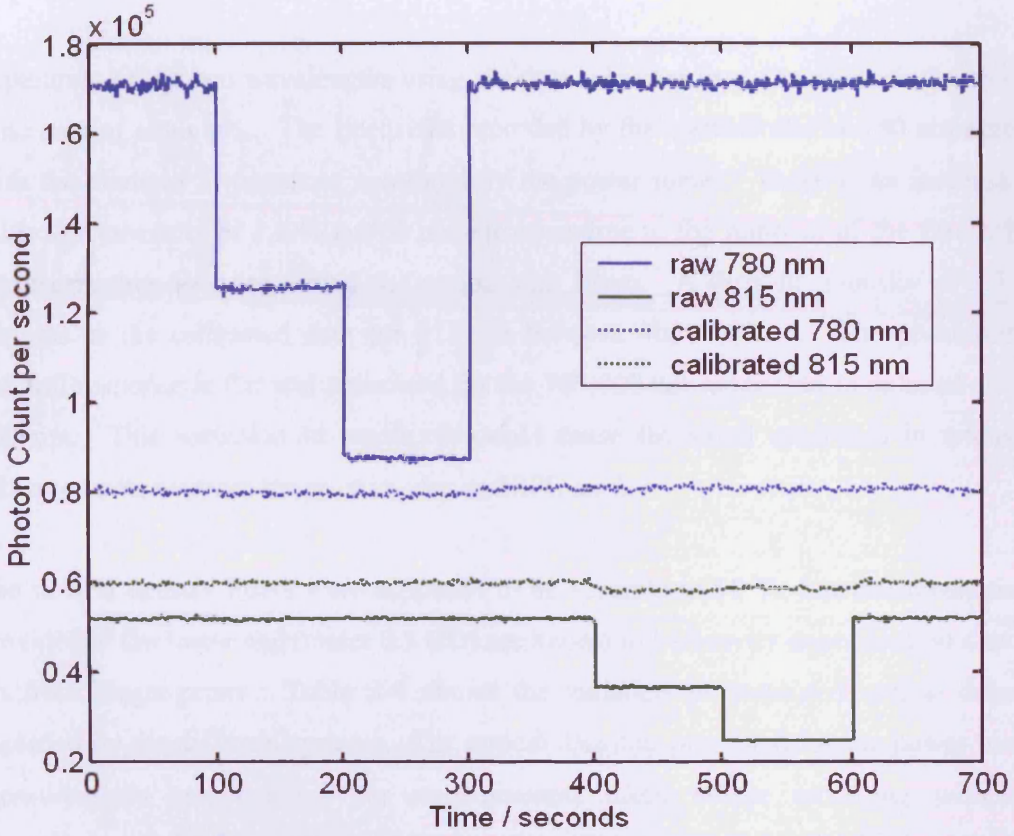

Figure 3-26 Graph of the raw intensity (solid lines) recorded by the SPC cards for each wavelength, and the calibrated intensity (dotted lines).

The intensity measurements from SPC cards, shown as the solid lines in Figure 3-26, measured changes of 0.13 and 0.29 OD for 780 nm and 0.14 and 0.31 OD for 815 nm. Calibration is performed by dividing the SPC data by the corresponding power measurement. The calibrated data is shown as the dotted lines in Figure 3-26. In addition to removing the large steps in intensity, calibration has halved the error in intensity measurements outside the stepped region, e.g. 400 – 700 s for 780 nm.

Discussion

For single wavelength measurements, the photodiodes measured the large-scale variations of the laser power, but intensity variations common to all channels remain. The suggested causes for this are: the temporal alignment of the photodiode and SPC data is not perfect, the optical alignment to the photodiodes is susceptible to noise, e.g. due to vibration, and finally there are other common influences on intensity (e.g. power supply to the MCP-PMTs).

Separation of the two wavelengths using the data collected from the photodiodes shows little sign of cross-talk. The intensities recorded by the photodiodes at 780 nm agreed with the changes in power as measured by the power meter. There is an increase in calibrated intensity of 1.2 % at 780 nm corresponding to the removal of the filters, but no discernable decrease during the period with filters. A drop in intensity of 2.5 % remains in the calibrated data for 815 nm between 400 – 600 s. The photodiodes spectral response is flat and optimised for the 700-800 nm range, but is reduced above 800 nm. This reduction in sensitivity could cause the small mismatch in intensity measurements between the photodiodes and SPC cards.

The neutral density filters were supposed to be accurate to 10 %, but the attenuations provided at the lower end (under 0.5 OD) are known to be heavily dependent on dust or oil from finger-prints. Table 3-4 shows the variation in measured optical density recorded by the different systems. The optical densities presented for the power meter measurements are averages for measurements taken before recording with the photodiodes and SPC cards. The exact attenuation recorded by the SPC cards and photodiodes will hence deviate from that average depending on the exact positioning of the filters. However, the SPC and photodiode measurements were recorded simultaneously, and should hence return the same values.

	0.1 OD	0.3 OD
780 nm:		
SPC cards	0.13	0.29
Photodiodes	0.14	0.28
Power meter	0.14	0.28
815 nm:		
SPC cards	0.15	0.32
Photodiodes	0.14	0.31
Power meter	0.14	0.28

Table 3-4 showing the recorded optical densities for each wavelength and three measurement methods: A pair of photodiodes, the new SPC cards, and a power meter used at the end of the source fibre.

There are still discrepancies between the measurements made with the new instrumentation and the SPC cards. The optical path from the laser to the detectors contains the laser box, 1x32 switch, a shutter unit, the subject and a total of 6 m of optical fibre. If any of these components have a wavelength-dependent transmission, it will create errors in the calibration method, as calibration assumes the SPC cards record the same intensity variations as the photodiodes.

The measurements made by the new instrumentation accurately record the output of the laser, but there are other factors involved in the power detected by the MCP-PMTs, e.g. high voltage power supply variation to the PMTs, that must also be removed for absolute intensity measurements. In addition, there are currently coupling problems within the laser, such that introducing ND filters into the laser alters the precise beam path, changing the coupling and hence power output into the external fibre.

3.5.1.3 Conclusion

In conclusion, the power of MONSTIR's source, a custom-built dual-wavelength laser (§2.2.5), is not stable. Continuous measurements of intensity have revealed changes of up to 40 % over an hour. MONSTIR is used for difference imaging (§2.3.1.3), which assumes the differences between datasets are only due to physiological effects. A 40 % change in laser intensity, causing equivalent changes in measured intensity, would therefore badly distort any signal recorded in the data.

A new instrument has been designed to measure the power output of the two wavelengths produced by MONSTIR's laser. Ten percent of the source beam is split to illuminate two photodiodes. One of the photodiodes is set behind a 780 nm filter, such that it detects very little of the 815 nm beam, and the other records both wavelengths. The data recorded from the photodiodes can then be used to distinguish the powers of the original two wavelengths. The measurements are normalised using values recorded at the start of the acquisition, and stored in the final bins at the end of the TPSF to two decimal places. Post-processing software can read the variations from the TPSFs and remove them from the final intensity measurements.

3.5.2 Variable Attenuation

The Variable Optical Attenuators (VOAs) were designed to reduce the dynamic range of the detected light, and protect the MCP-PMTs from over-illumination (Schmidt et al. 2000a). Small apertures were used to attenuate the light between the detector bundles and the polymer fibre leading to the PMTs. Repeated measurements have shown an error in attenuation provided resulting in a roughly 4 % error in intensity measurements. A new design for the VOAs using partially-exposed x-ray film has been investigated and produced. A background to optical range compression is given in §2.2.4.4.

3.5.2.1 Background

The intensity variation between channels needs to be reduced, to prevent the PMTs being saturated or damaged, to limit the detrimental effects of detector dead-times, and to reduce the effects of cross-talk between channels (Schmidt 1999).

Detector channels nearer the source collect approximately ten times the photon count versus those distant from the source for each additional centimetre of tissue. Hence a form of variable attenuation is required. A "closed" position is used if the VOAs do not have the required dynamic range to attenuate the beam to a safe level. This cuts off the channel completely.

The original VOA design used apertures to attenuate the light before it illuminated the PMTs. This design converted the stepper-motor's positioning error into an error in intensity due to the aperture's variable alignment with the detector bundles (Jennions 2003). The new design uses x-ray film for variable attenuation, removing the attenuation's dependence on precise alignment with the bundle.

In order to create the new discs, x-ray film must be exposed in discrete sections and to well-defined levels. X-rays are attenuated according to (§2.1.1)

$$N = N_0 e^{-\mu_a x} \qquad \text{(iv)}$$

Hence, for a thickness, x, of a material with absorption coefficient μ_a, the incident number of photons on the film, N, can be calculated from a previously known initial intensity, N_0. Mass attenuation coefficients, absorption divided by density, for different x-ray sources and materials are given at www.nist.gov.

Intensity measurements with MONSTIR are sums of photon counts, recorded using TCSPC (§2.2.3). Given the count rate is kept low enough to avoid pile-up (§2.2.4.5), the probability of photon arrival is small enough that Poisson statistics are a good approximation for the errors. Repeated measurements of a TPSF containing N photons have a statistical standard deviation of $\sqrt{N}$. This provides a lower threshold for intensity errors in TPSFs recorded with MONSTIR. Errors described in the following sections are therefore taken with reference to the increased error above the expected Poisson error.

3.5.2.2 Theory

Original Design

Apertures of various sizes (0.2 mm to 3.5 mm diameter) are located at a constant distance from the centre of a thin disc of stainless steel. The disc is mounted on a stepper motor, which holds the disc between the ends of the detector bundle and the short polymer fibre leading to the PMTs. The stepper motor is computer controlled, and each position is mapped to one of the 800 steps via a user-defined text file. The disc is initialised using an offset LED and photodiode to detect the position of a reference aperture (position A in Figure 3-27), which defines a initialisation position. Rotating one of the apertures to a position between the two fibres blocks part of the beam illuminating the polymer fibre. The attenuation (in OD) provided is given by the log of the ratio of the aperture's area to that of the bundle end.

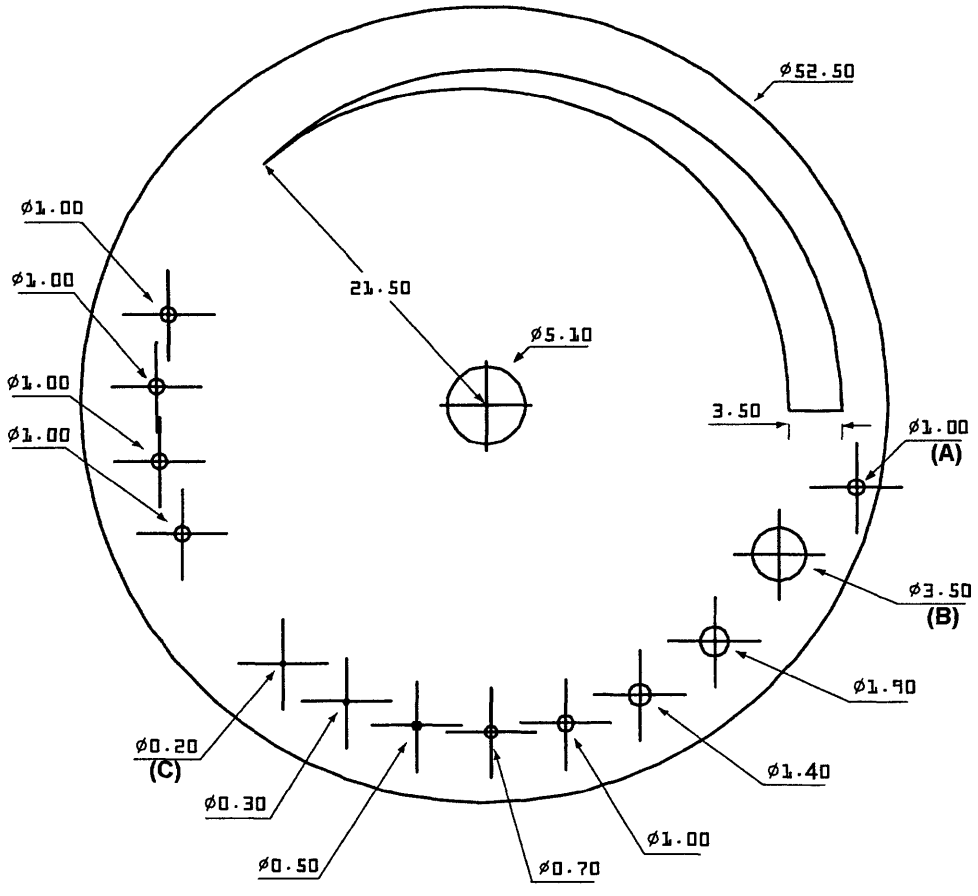

Figure 3-27 Schematic of the original VOA discs (all measurements in mm). (Schmidt 1999)

$$OD = \log_{10}\left(I_T / I_0\right) = \log_{10}\left(\frac{Area_{Aperture}}{Area_{Fibre}}\right) \qquad \text{(v)}$$

Eight holes with diameters between 3.5 mm and 0.2 mm (B and C in Figure 3-27) allow discrete attenuations between zero and 2.2 OD. Reflections are minimised as the steel discs have been chemically blackened.

The key advantages of this design are that it is small, simple, quick, and cheap to manufacture. At the time of design, it was also felt that the attenuation was reproducible, produced minimal optical reflections, could have a larger dynamic range than other options available at the time, and was wavelength insensitive.

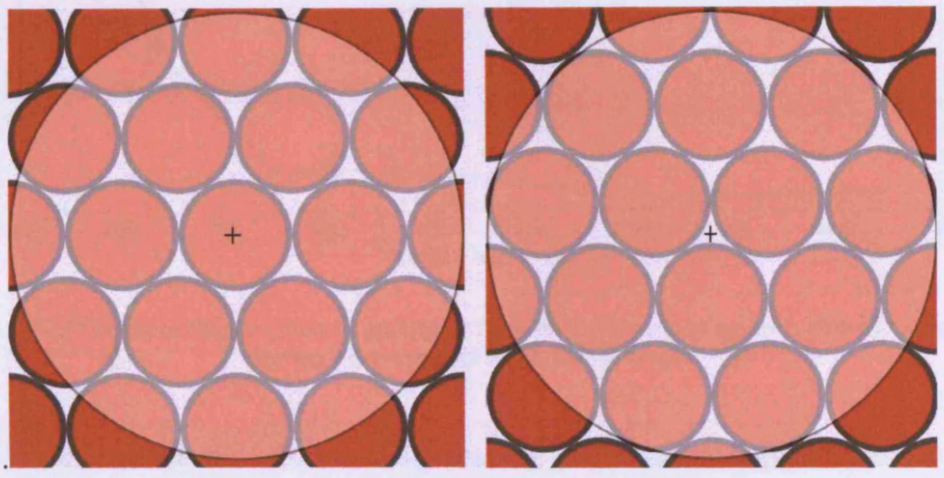

Figure 3-28 Diagrams of the detector bundle end. The smallest aperture is shown aligned to the centre of a fibre (left) and aligned with the space between fibres (right). (Jennions 2003)

The disadvantage is that the attenuation is dependent on the precise alignment of the aperture and the detector bundle. The alignment has two sources of error. First, the bundles are close-packed, resulting in a 73 % packing-fraction. For the smallest aperture, the fibre area unblocked is at a maximum when the centre of the aperture is aligned to a single fibre, shown in Figure 3-28 (left), and at a minimum when aligned with the space between fibre ends (right). Figure 3-29 shows the calculated increase in the maximum versus minimum fibre area under each aperture as the radius is decreased. The stepper motor's error in holding position is much larger than the size of a single fibre. Hence, each measurement with the same size aperture will have a variation in attenuation if the disc has been moved away and moved back.

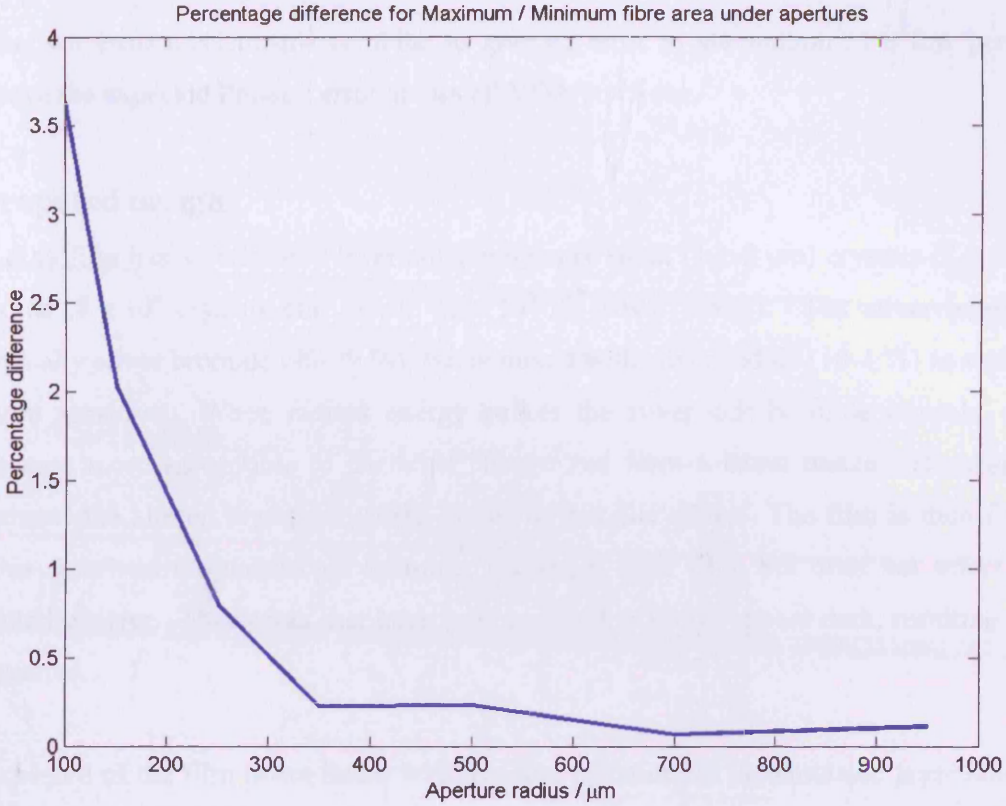

Figure 3-29 Graph of the variation of maximum / minimum fibre area under a circular aperture versus aperture radius. (Jennions 2003)

The second error mechanism is mis-alignment of the bundle and aperture, as shown in Figure 3-30. The stepper-motor occasionally misses steps causing the apertures to be aligned with the edge of the bundle. This mechanism only effects larger apertures, as mis-steps are not large enough to move smaller apertures wholly off the bundle, and results in an error of ~1 %, similar to that of the first mechanism.

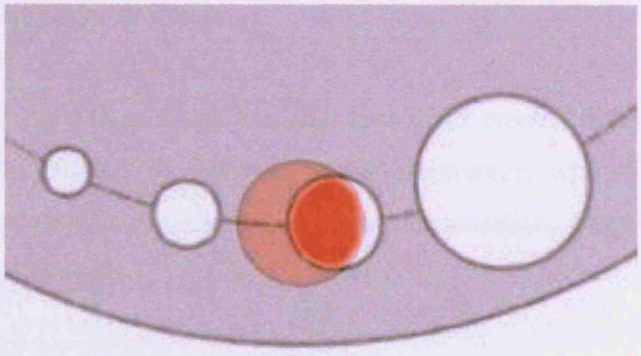

Figure 3-30 Illustrations of the result of a mis-step by the stepper motor. (Jennions 2003)

The two error mechanisms combine to give an error in attenuation of a few percent above the expected Poisson error across all VOA positions.

Proposed design

X-Ray film has an emulsion layer containing very small (1-1.5 μm) crystals of a silver halide (8×10^6 crystals cm^{-2}, each with 10^6-10^7 silver atoms). The silver halide is typically silver bromide (90-99 %), but is mixed with silver iodide (10-1 %) to make it more sensitive. When radiant energy strikes the silver-iodo-bromide crystals, they become more susceptible to chemical change and form a latent image. Developing reduces the altered crystals to small grains of metallic silver. The film is then fixed. This dissolves the unaffected bromide, leaving a clear film, but does not affect the metallic silver. Thus areas that have been exposed to x-rays appear dark, resulting in a negative.

Exposure of the film is not linear with incident radiation, as the emulsion layer holds a finite number of silver halide crystals. Hence, various films have different, non-linear, exposure speeds. The optical density of a film depends on the exposure, but also on the development. Most x-ray films have two emulsion layers to improve contrast. (Munro et al. 2001)

Using film removes the requirement for precise alignment between the aperture and fibre bundle. Sections of film would be made wide enough to accommodate the error in holding position of the stepper motor, as the film provides a constant attenuation for a given exposure. X-ray film has been specifically chosen as it offers the best maximum optical density of any film available.

The conclusion of my MRes thesis was that new discs created from x-ray film would remove the errors caused by aperture-based attenuation with fibre bundles. A manufacturing process was suggested, but the implementation, described further in this section, is new to this thesis.

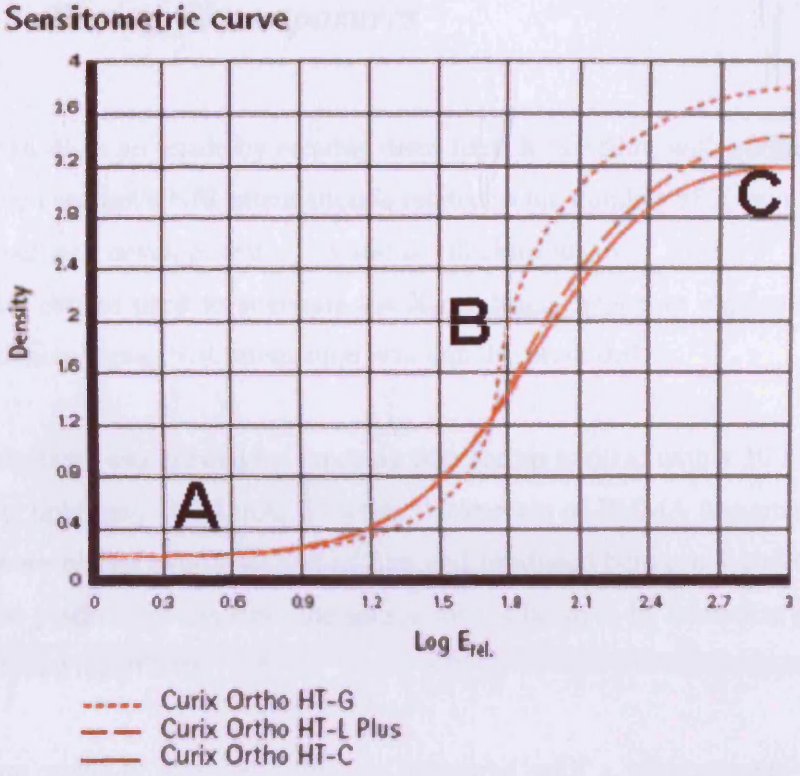

Figure 3-31 Gamma (or exposure) curves showing the relationship between relative exposure and optical density at visible wavelengths for Agfa Curix X-Ray Films. (AGFA 2003)

All x-ray films have associated gamma curves – the relationship between the exposure (E_{rel}, also known as dose) and the resulting optical density after development. The important characteristics of the gamma curves are:

- the "fog", the minimal optical density present throughout and caused by the remaining emulsion layer, and reflections (A in Figure 3-31)
- a central region, in which the relationship between optical density and exposure is roughly linear (B above)
- a maximum optical density which occurs when all crystals in the emulsion layer have been altered (C above)

The central linear region (B) is of greatest interest, as small changes in exposure lead to the largest optical density changes, resulting in better contrast. The three curves in Figure 3-31 show the response curves for different films intended for different clinical uses, for example mammography as opposed to chest cavity imaging.

3.5.2.3 Testing film exposures

Methods

The new VOA discs are made by creating discs from X-ray film, with variably-exposed sections. Each section's NIR attenuation is related to the number of X-rays incident on the film before development. Various thicknesses of PMMA (Polymethyl methacrylate) can be used to attenuate the X-ray beam, hence an exposure curve for PMMA thickness versus NIR attenuation was initially produced.

An exposure curve was created by exposing film for up to 60 s, with a 30 kVp Mo-Mo x-ray source, operating at 0.4 mA. Discrete thicknesses of PMMA (ranging from 3.0 - 17.8 mm) were placed over a section of film and irradiated between 1 and 60 seconds. The film was placed 76.5 cm from the source for the beam to be treated as parallel and to reduce shadowing effects.

The resulting partially exposed film was measured with a spectrometer to find the optical density corresponding to the thickness of PMMA. A scanning monochromator and CCD (SPEX 270M) were used to record the changes in intensity at 780 and 815 nm using MONSTIR's IMRA laser (§2.2.5) as the source. Optical densities were calculated by comparing the film's spectrum against the spectrum recorded without film.

Results

The IMRA laser's spectrum is shown in Figure 3-32. The initial testing of the laser in 2001 gave the peak wavelengths as 777.3 nm and 817.8 nm. The spectrograph results show the peaks at 777.5 nm (mean at 778.0 nm) and 817.4 nm (mean at 818.5 nm)

The distribution of wavelengths around 777 nm has broadened since the laser was first delivered, with a noticeable increase of a secondary peak at 775 nm. Spectroscopic measurements and the initial absorption and scatter coefficients used in future reconstructions will need to take the broadening at both wavelengths into account.

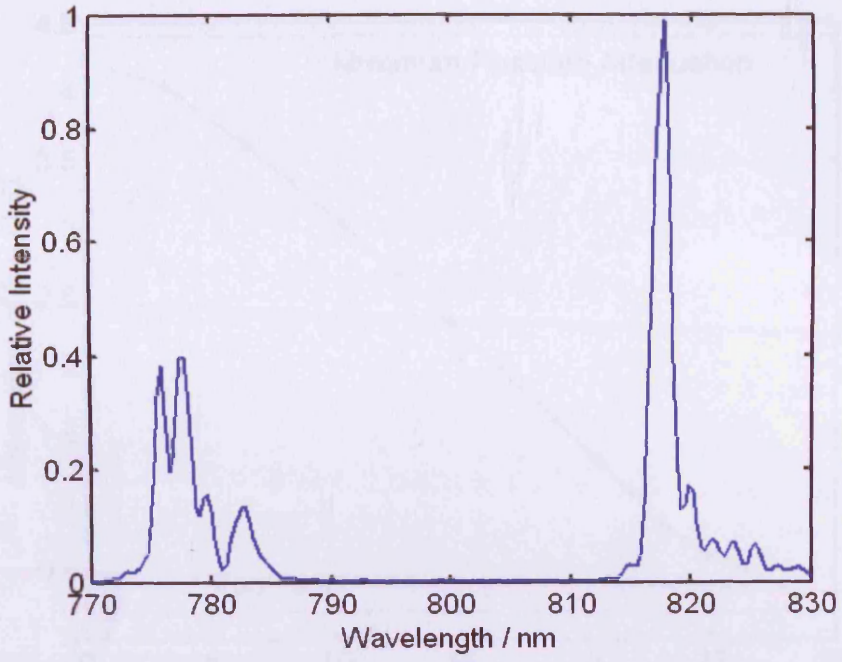

Figure 3-32 Graph of the intensity distribution with wavelength for MONSTIR's IMRA laser.

Optical densities were recorded from film at nine exposure times (1, 2, 3, 5, 8, 12, 17, 23, and 30 s) using six thicknesses of PMMA (3.0, 6.1, 9.0, 11.9, 14.8, and 17.8 mm). The resulting optical densities were used to calculate an exposure curve, shown in Figure 3-33 for 30 s exposures. This curve is a mirror of Figure 3-31 due to the inverse relationship between thickness of PMMA and the resulting exposure of the film.

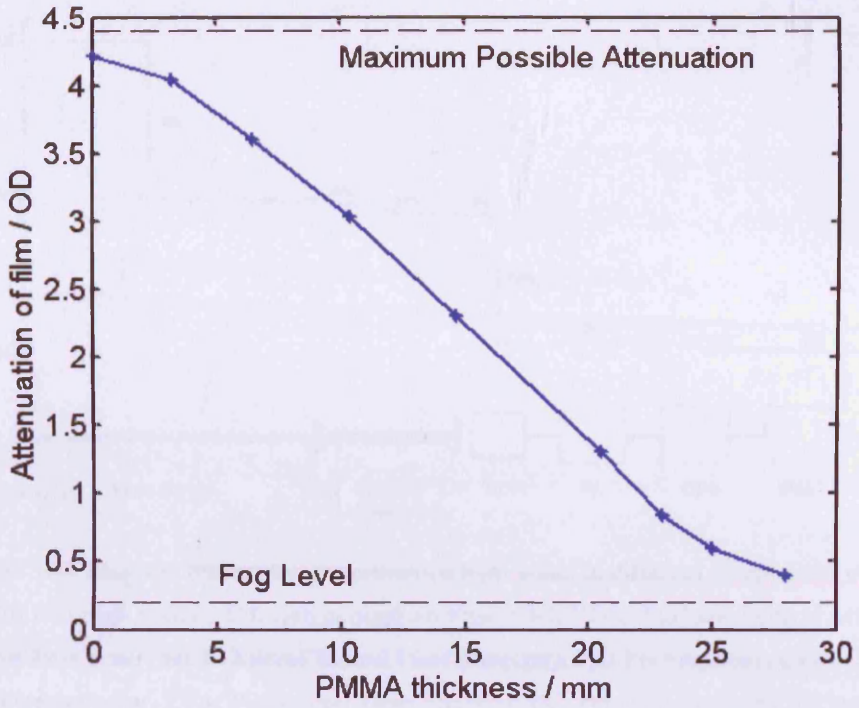

Figure 3-33 Graph of the optical density of partially exposed x-ray film against the PMMA thickness attenuating the x-ray beam calculated for 30 s exposure.

Discussion

The purpose of variable attenuators is to compress the dynamic range of the incoming light to safe levels for the detectors. The required range of the VOAs can be found by calculating the ratio of the number of photons that could reach a detector, against the detector's dynamic range. The power output of MONSTIR's laser has been measured at the end of the source path (see §3.5.1.2), and is 21.3 mW at 780 nm. The power output at 815 nm should be roughly equivalent, but is currently reduced due to poor coupling within the laser housing.

Assuming both wavelengths are produced equally, the total power output is 42.6 mW. The energy per photon, E, can be calculated from:

$$E = hc/\lambda \qquad \text{(vi)}$$

where λ is the wavelength, c is the speed of light, and h is Planck's constant. Hence, roughly 1.7×10^{17} counts per second (cps) are emitted from the end of the source fibre.

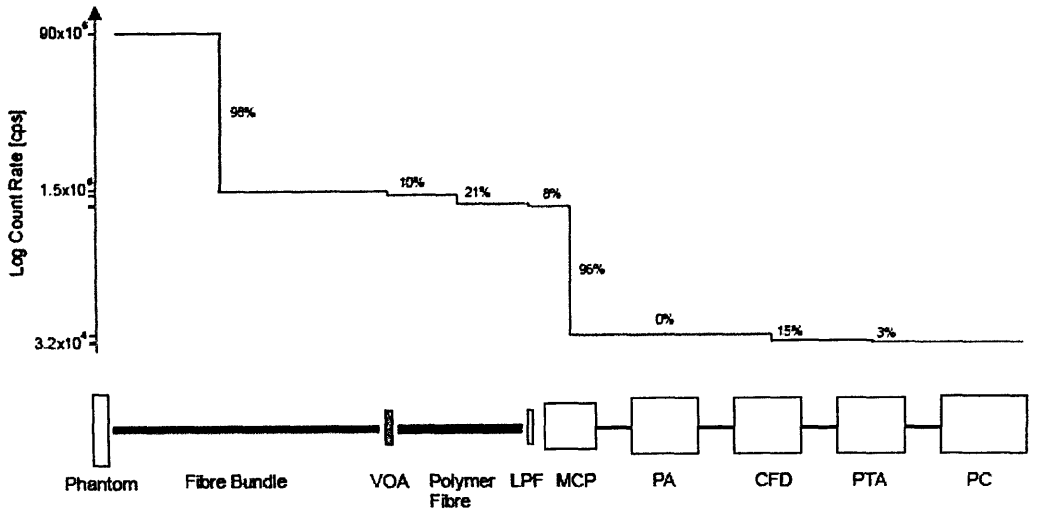

Figure 3-34 Diagram illustrating the estimated light losses in different components of the MONSTIR detection system. C.f. system diagram Figure 3-1. VOA: Variable Optical Attenuator, LPF: Low Pass Filter, MCP: MicroChannel Plate (detector), PA: PreAmplifier, CFD: Constant Fraction Discriminator, PTA: Picosecond Time Analyser, PC: Personal Computer (Schmidt 1999)

The efficiency of the detection path is defined as the ratio of the number photons emerging from the surface of the tissue through an aperture the size of the fibre bundles, to the number of counts recorded by the electronics. The detection efficiency of MONSTIR has been measured to be roughly 0.03 % (Schmidt 1999) Figure 3-34 shows estimations for the loses per component. From the estimations, the photon loss between subject and MCP is roughly 98.7 % Therefore, if all photons emitted from the source fibre were collected by the detection bundle end, 2.2 x 10^{15} cps would reach the detectors.

The number of photons transmitted into the detector bundle from the source fibre is reduced by coupling efficiency and the attenuation within the interrogated volume. The efficiency of photo transport between source and detector fibres can be estimated from detector calibrations (§2.3.1.3). During this calibration routine, reflected photons are collected from the source fibre to the detector bundles of the same channel. Neutral density filters totalling 7 OD are placed into the laser to prevent damage to the detector, and a signal of ~10^5 cps is typically recorded. The coupling efficiency for a source and detector pair can therefore be estimated at roughly 0.1 %..

The maximum safe illumination for the detectors currently used in MONSTIR is roughly 10^5 cps (§2.2.4.3). If count rates cannot be attenuated beneath this level, then a 'closed' position is used, blocking all light from the detector and losing all information for that source-detector (s-d) pair. The attenuators would ideally have a range that would fully attenuate the signals from any s-d separation. Including in fibres and coupling loses, ~10^{12} cps could reach the detectors, assuming the power of the laser. A full range of 12 OD would therefore cover all current possibilities. This would also allow calibration without additional filters, and have an additional error margin.

The original design of the VOAs provided a maximum of 2.2 OD. Without the presence of any additional attenuation between source and detector fibre ends due to the interrogated tissue, the detectors would be illuminated with up to ~10^{10}. Tissue normally causes an attenuation of 1 OD per centimetre. The minimum s-d separation with the original VOA discs is therefore ~ 5 cm. Any s-d pair closer together therefore has to be fully shut to protect the detectors, and hence records no data. For a simple cylindrical geometry with diameter of 7.0 cm, this means only 15 out of 32 s-d pairs can be acquired.

A PMMA cylinder with sections of different heights can now be produced to create any disc size and attenuations, up to 4.3 OD. The curve presented in Figure 3-33 is calculated for 30 s exposures. Shorter exposure times result large attenuation differences being produced by minimal changes in PMMA thickness. PMMA section heights can therefore have larger differences when used with longer exposure times, decreasing the accuracy required in producing the PMMA cylinder.

The diameter of the polymer fibre is 3.0 mm, and is centred 21.5 mm from the axis of rotation of the disc. In theory each disc could therefore have 45 sections, but in practice fewer sections must be used due to stepper motor positioning and mis-stepping errors. In addition, attenuator positions are found for each new subject using an iterative guess and check method. Increasing the number of sections would increase the time required to perform this function, see Appendix B for further discussion.

The number of sections used also needs to be balanced with the difference between the attenuations of each section. Ideally the attenuations would be continuous between zero and the maximum, and hence the maximum signal could be recorded for each channel. For MONSTIR, count rates in the range 10^4 to 10^5 are desired for good signal to noise and minimal pile-up effects (§3.4.5). Discrete attenuations of 1 OD increments could therefore be used, but would reduce rates just over the maximum to close to the minimum. Increments of roughly 0.4 OD, which would halve the count rate between each section, are felt to be the best compromise.

3.5.2.4 New VOA discs

Production method

Initial experiments, exposing thicknesses of PMMA to an X-ray beam, have resulted in the creation of PMMA "staircase" with varying height, as shown in Figure 3-35 (a). In order for any stepper motor error to be removed, sections were designed to be at least three times the diameter of the fibre end. In addition, the manufacturing method for the PMMA staircase limited the sections size. The final design has twelve sections: an 'open' section with minimal attenuation, eight sections with discrete attenuations, and three with maximum attenuation.

A fully-attenuating 'closed' position was created by covering a portion of the maximum attenuation section of the disc with NIR-absorbent paint. Preliminary measurements which involved illuminating the painted section directly from the laser, found that there was light leaking around the edges of painted section. Coating two neighbouring sections and using the central point as the 'closed' position reduced the detected photon count to background noise.

Lead sheets were arranged such that an entire film could be placed behind the lead, with a small exposure window in which the PMMA staircase was suspended. The cassette holding the X-ray film was moved into three orientations relative to the lead shield, in order for three identical discs to be produced per film. The orientation of the staircase was set such that the largest step was in line with the centre of the X-ray beam. This was done to limit shadowing effects, such as blurring of section boundaries. A small lead insert was placed next to the PMMA staircase to produce a section with minimal attenuation.

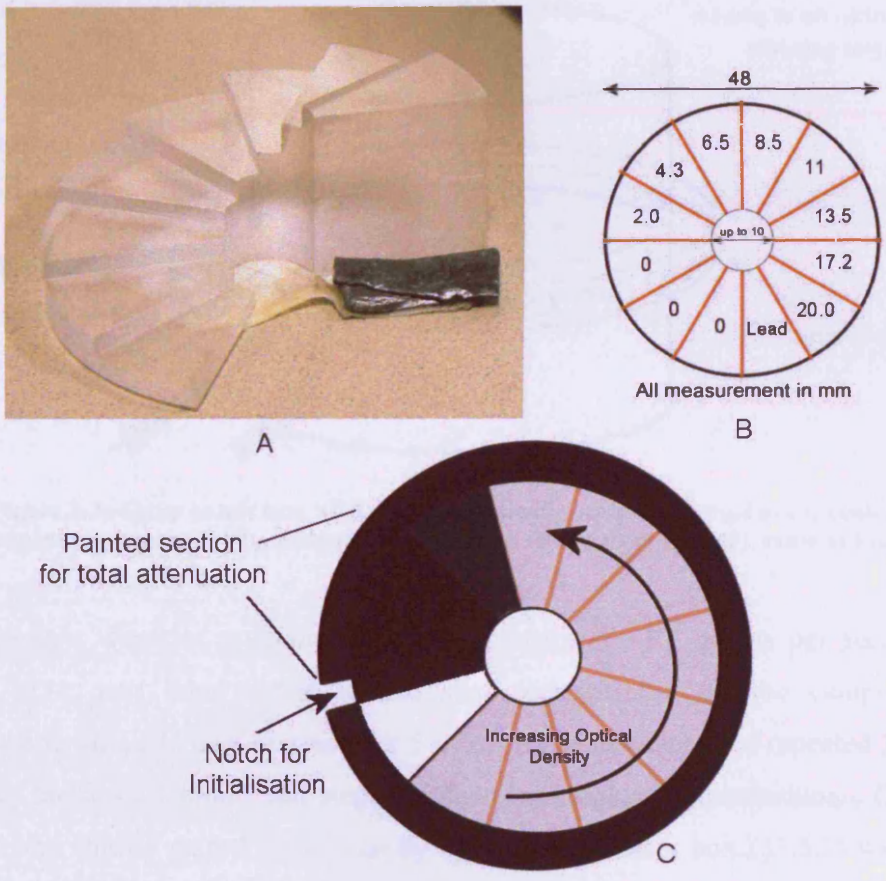

Figure 3-35 VOA disc construction - a) photo of final PMMA staircase with lead insert (b) technical drawing with step heights, and (c) final disc design

The film was developed and discs cut from the film. A section with roughly 10 OD was created by covering two disc sections with black paint. In addition, an initialisation position was created by cutting a notch into the side of the disc. The final disc design is shown in Figure 3-35 (c).

Testing Method

To test the reproducibility and attenuations provided, eight optodes were coupled to the circumference of a homogenous clear phantom with $\mu_s' = 0$ mm^{-1} and $\mu_a \approx 0$ mm^{-1}. Four VOAs were fitted with the new discs and the original discs were left on the other four channels. A source fibre was coupled into an isotropically scattering target at the centre of the phantom, as shown in Figure 3-36.

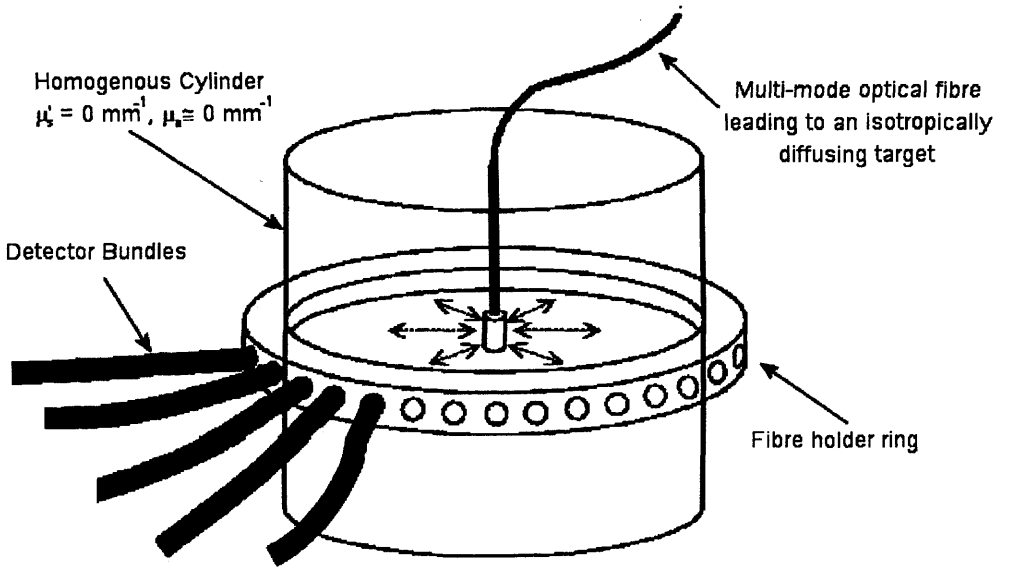

Figure 3-36 Setup to test new VOAs - an isotropically scattering target at the centre of a homogenous phantom is illuminated. (adapted from (Hillman et al. 2000), same as Figure 3-2)

All channels were set to record an initial intensity of ~10^5 counts per second (cps). Each VOA was then moved to the step corresponding to the centre of each section/aperture, and data acquired for 5 s. All measurements were repeated 100 times, rotating the discs forward 100 steps and then back between acquisitions. The source switch and shutter were kept constantly open, and the laser box (§3.5.1) was used to remove any laser power variations. The experiment was repeated 8 times, using the same original discs but replacing the new discs each time such that all 32 were tested.

Results

The discs provide attenuation between 0 and 3.7 OD. Figure 3-37 shows a comparison of repeated measurements made with the original and new VOA discs.

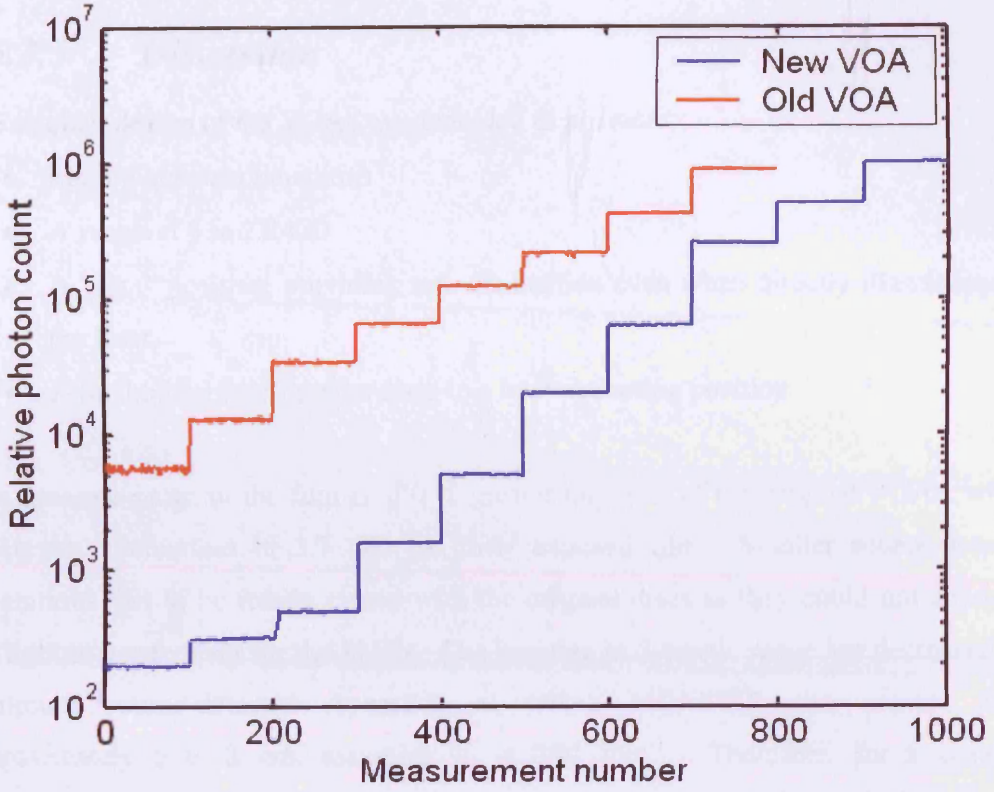

Figure 3-37 Graph of repeated 5 s measurements made with the new and original VOA discs. Each line represents results averaged over four channels.

The average photon counts recorded for each PMMA step are given in Table 3-5. The percentage standard deviation for each repeated measurement is presented with the associated Poisson error. Variations in X-Ray beam intensity and energy result in small differences in the exposure of each disc. The attenuation shown for each position is therefore calculated from an average across all discs. The standard deviations of the attenuations across each section of the discs are also shown.

PMMA thickness / mm	0	2.0	4.3	6.5	8.5	11	13.5	17.2	20.0	Lead
Photon count / kcps	0.2	0.3	0.5	1.6	5.0	20	63	251	501	1000
Standard deviation / %	7.8	6.2	5.0	2.7	1.7	0.8	0.5	0.4	0.2	0.1
Poisson error / %	7.1	5.6	4.5	2.5	1.4	0.7	0.4	0.2	0.1	0.1
Attenuation / OD	3.7	3.5	3.3	2.8	2.3	1.7	1.2	0.6	0.3	0.05
Standard deviation across 32 discs / OD	0.06	0.08	0.07	0.07	0.09	0.09	0.06	0.04	0.03	0.04

Table 3-5 Results from 100 repeated 5 s measurements at each VOA position, averaged over all channels. Cps = Counts per second.

In the range most important to MONSTIR, 10^4-10^5 cps, intensity errors are kept below 1 %, and are roughly Poisson at lower count rates.

3.5.2.5 *Discussion*

The original design of the VOAs was intended to provide:

- Eight discrete attenuations
- A range of 0 to 2.2 OD
- A "shut" position, providing safe attenuation even when directly illuminated by the laser.
- A method for resetting the discs to a known starting position

The dynamic range of the film is ~70 % greater than that of the original VOAs, with a maximum attenuation of 3.7 OD for fully exposed film. Smaller source-detector separations had to be totally closed with the original discs as they could not attenuate the light to a safe level for the PMTs. The increase in dynamic range has decreased the minimum source-detector separation at which MONSTIR can acquire from approximately 5 to 3 cm, assuming $\mu_a \approx 0.01$ mm^{-1}. Therefore, for a standard cylindrical phantom (e.g. as described in §3.5.1.1) surrounded by 32 optodes, MONSTIR can now acquire data from four more detectors per source pairs than previously, allowing an extra 128 measurements per 32-channel dataset. The disc sections are three times the size of the bundle end, removing both of the error mechanisms of the original design.

In addition to the attenuating positions, the two other features of the original VOAs were a position for complete attenuation and an initialisation aperture. The layers of paint, applied to the final disc to perform the closed function can provide at least 10 OD. This means each channel can be protected even if it becomes directly illuminate by the laser. The initialisation position operates as before, the photodiode illuminating a photo-detector only at the position of the notch.

The Poisson error is $\sqrt{N}$ for N counts. The aim of improving the VOAs was to reduce the intensity error introduced by the attenuations to less than 1 % where possible and achieve as close to Poisson error outside that limit, below 10^4 cps. Figure 3-38 shows the comparison between the Poisson error and the error in the data for the new and original discs, averaged over all channels.

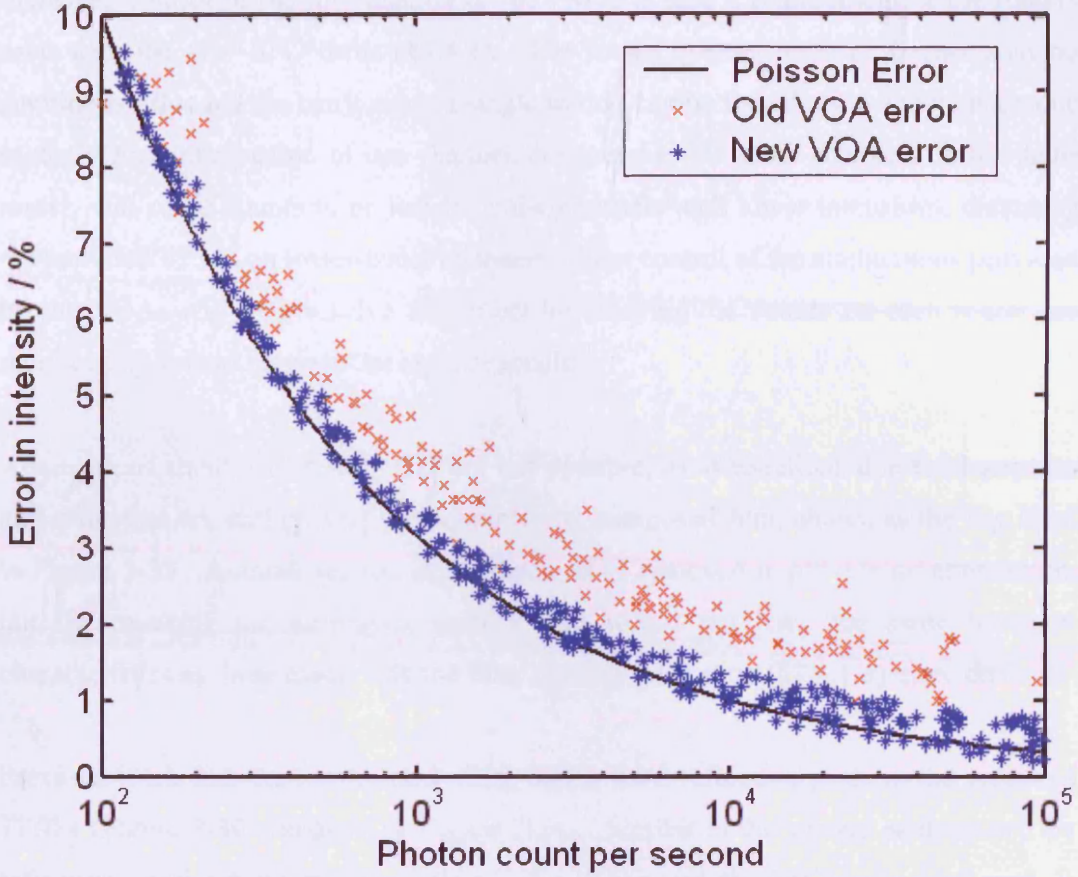

Figure 3-38 Plot of intensity error vs. count rate for original and new VOAs. The Poisson error is also shown in the same range for comparison.

The lower line in Figure 3-38 plots the statistical minimum for the intensity error as calculated from Poisson statistics. The other two datasets are for the original and new designs of the VOA discs. The original VOAs, shown as the upper points, produced intensity errors typically 1 % greater than Poisson error, whereas the new VOAs, lower points, have almost no additional error.

Comparing the disc to the size of the fibre, many discrete attenuations could be provided on one disc, resulting in a large improvement on the original VOAs. Further work could be undertaken to optimise the number of sections and attenuations provided. A larger number of sections, evenly spread over the full dynamic range would help reduce the effect of cross-talk by illuminating neighbouring MCP-PMT channels more evenly.

Increased control of the illumination of the PMTs is also a requirement of the routers used with the new SPC cards (§3.4.2). The router ignores pairs of counts arriving simultaneously, and the cards share a single timing engine for all eight channels on one router. Over-illumination of one channel, compared to the other channels on the same router, will cause counts to be lost from the channels with lower intensities, distorting the recorded TPSFs on lower-count channels. Finer control of the attenuations provided by the VOAs will help resolve this effect by ensuring the counts on each router are more evenly spread between the eight channels.

Attenuations smaller than 0.05 OD are not possible, as attenuations due to absorption and reflection are still present with completely unexposed film, shown as the fog level in Figure 3-33. A small section of the disc can be removed to provide no attenuation, but the resulting measurements without film would not have the same temporal characteristics as those made with the film, making calibration (§2.3.1.3) more difficult.

Previous work has shown the new discs add a third reflection peak to the recorded TPSFs (Figure 3-39 compared to Figure 2-24). Similar to the second peak caused by reflections in the polymer fibre between the VOAs and the PMTs, the third peak is caused by reflections between the VOAs and the subject. The effects of both added peaks are removed by calibration.

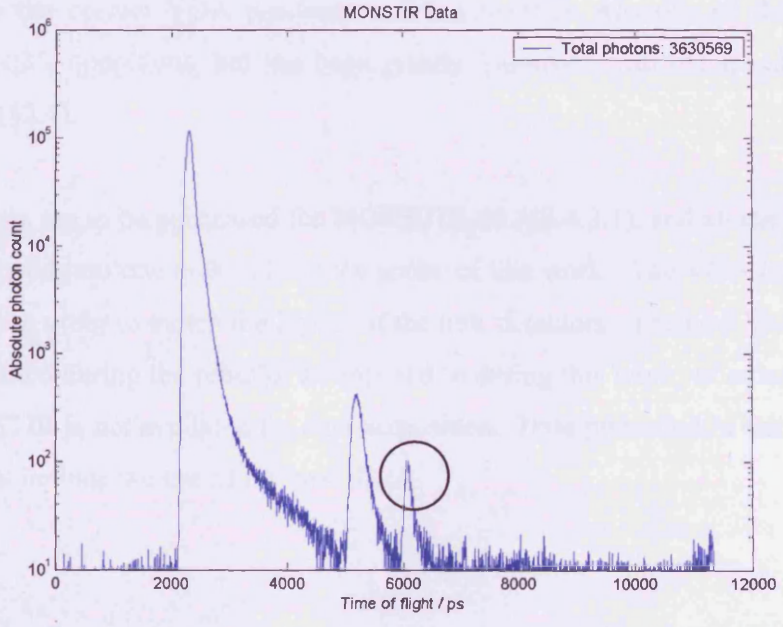

Figure 3-39 A TPSF recorded using the new VOA discs, showing the presence of a third peak (encircled), due to the added reflections.(Jennions 2003)

An additional error occurs due to the aperture selection of individual fibre ends in the detector bundles, due to their spatial incoherence between opposite ends of the bundle. Both meantime and intensity are affected, but the magnitudes of the errors are much smaller than the errors discussed previously in this section.

The attenuation provided by the apertures would be equivalent to selecting a reduced area on the surface of the subject, if the bundles' ends were coherent (e.g. an imaging bundle). The incoherence of the bundles scrambles the temporal distribution of the transmitted photons across the bundle end. The error in positioning of the original VOA discs hence causes a variation in the recorded temporal distribution, and therefore an error in meantime measurement. The new VOA discs remove this error on the same basis as the intensity errors.

The in-house control software, called MIDAS (MONSTIR Image-Data Acquisition Software, (Schmidt 1999)) can use an acquisition definition file (ADF) to perform a full acquisition. The ADFs contain the order in which to activate sources, the acquisition time per source, and all 32 VOA positions corresponding to each source. ADFs can be generated by MIDAS, finding the correct VOA positions by an iterative guess and check method. This involves acquiring for a set time and using the recorded count rate to calculate the correct VOA position. ADF generation was one of the slowest of MONSTIR-03's operations, but has been greatly improved with the speed of the new electronics (§3.4).

New detectors are to be purchased for MONSTIR-03 (§3.4.2.1), and all the components are to be moved into one rack outside the scope of this work. The VOA housings have to be rebuilt in order to match the layout of the new detectors. The new VOA discs will be implemented during the rebuild, as opposed to during this work, in order to limit the time MONSTIR is not available for data acquisition. Data presented in chapter §5 does therefore not include the use of the new discs.

3.5.2.6 Conclusion

In conclusion, the aperture-based design of the original VOA discs has been found to be causing additional intensity errors. The intensity errors are due to the holding error of the stepper motor, varying the alignment of the apertures and detector bundles between repeated measurements.

A new design of the VOA discs has been investigated, creating discs from x-ray film that has been variably exposed, resulting in sections with discrete attenuations. The new design removes the errors caused by the misalignment of the apertures and bundle end, and additionally increases the number and range of attenuations available.

32 new VOA discs have been created for MONSTIR. The main effect of the new VOA design has been to reduce the intensity errors to under 1 % where possible, in conjunction with the laser calibration described in §3.5.1. The increase in maximum attenuation of the new design reduces the minimum source-detector distance, which can be used for optical tomography measurements, allowing more channels to be used in a full dataset.

3.6 New MIDAS software

Control software, nicknamed MIDAS (MONSTIR Image Data Acquisition Software), was written in LabWindows (National Instruments Corporation, USA) for use with Windows XP Pro. MIDAS controls all hardware functions of MONSTIR:

- Digital TTL signals from two USB data acquisition (DAQ) units (USB-6008 and USB-6501, National Instruments Corporation, USA) control the laser, source switch and shutter, detector high-voltage, and Peltiers.
- Analogue acquisition from the cooling flow meters, temperature gauges and laser calibration instrument is performed by the USB-6008.
- The VOA discs are mounted on stepper motors, which are connected to a series of control cards (LC4E, SmartDrive Ltd, UK). These communicate via the serial port.
- Data acquisition is performed by the SPC-134 cards (§3.4, Becker & Hickl, Germany) via functions and data structures provided by B&H.

A full user manual for MIDAS, including MONSTIR hardware connections, is given in Appendix A.

3.6.1 User Interface

The user interface of MIDAS gives the operator control over the system's hardware functions, allows the monitoring of various system parameters, enables the acquisition and display of timing histograms (e.g. TPSFs), and facilitates fully automatic execution of complete imaging scans.

The initial panel displayed upon program start-up is shown in Figure 3-40. Individual component control, operation readiness and single TPSF acquisition are all presented to the user from the front panel. The left-hand section of the front panel contains feedback information for the user as operations are performed.

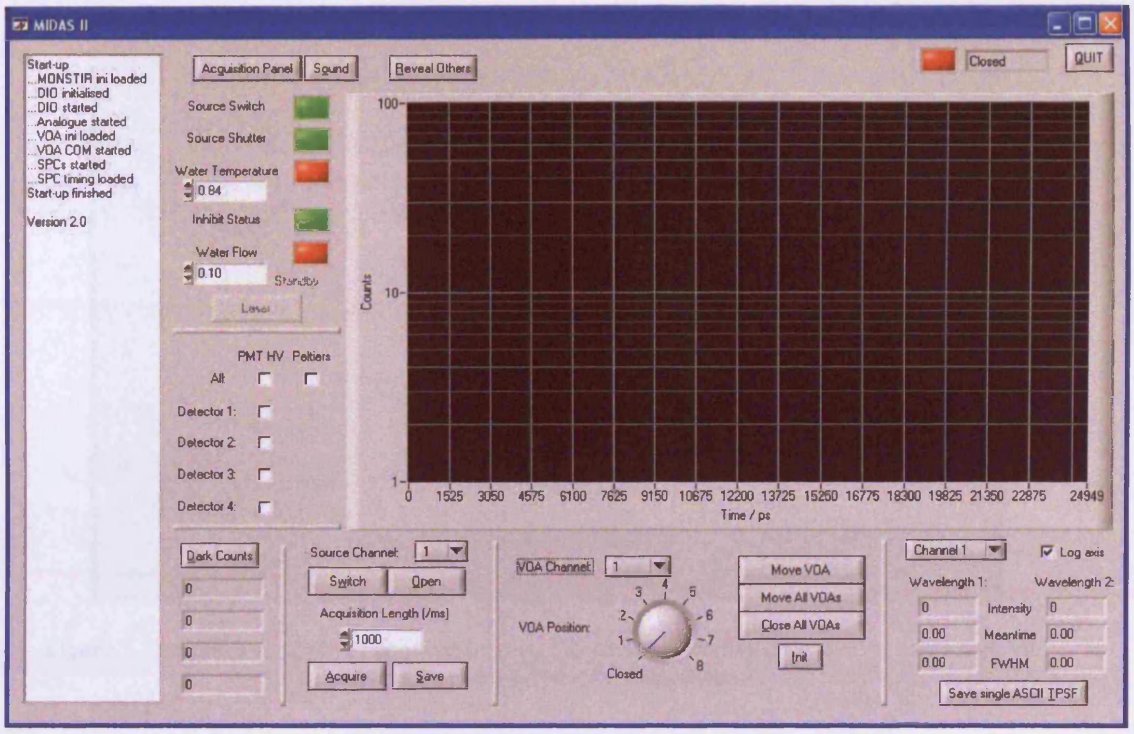

Figure 3-40 Screen shot of the panel shown when MIDAS is started.

Controls for performing full acquisitions are displayed on a second panel, shown in Figure 3-41. Before dataset acquisition can begin, acquisition definition files (ADFs) need to be generated for each new subject to find the correct positions for the VOAs. ADF generation theory is given in Appendix B. The ADFs are stored once generated, and can be re-loaded if the subject is to be scanned at a later date. Once an ADF is loaded, the number of steps, source channel, and acquisition length are displayed, and MONSTIR is ready for acquisition. Each step can be executed individually, or as a complete set. Absolute and source calibrations (§2.3.1.3) can also be performed from this panel.

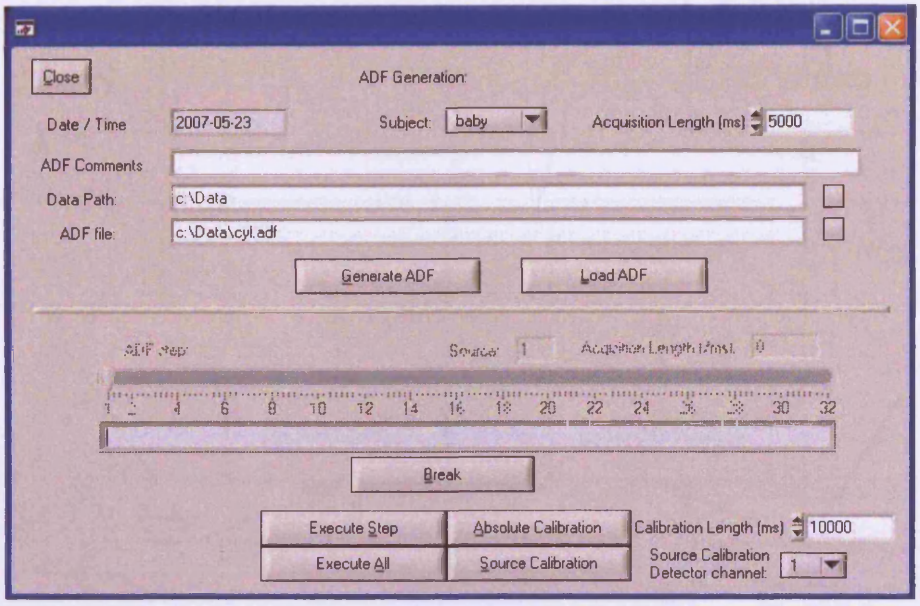

Figure 3-41 Screen shot of the acquisition panel, containing controls for ADF generation, and calibration and full dataset acquisition

3.6.2 Code Structure

The LabWindows environment provides general user interface (GUI) construction, whilst having the functional possibilities of programming in C and built-in functions for instrumentation control and communication. The coding structure was designed to be modular with cascading functions, see Figure 3-42, to ease development and any implementation of future changes to MONSTIR. Four files were written for basic functionality of the hardware: three written in-house (DIO.c, VOA.c, and Analogue.c) and one provided by Becker& Hickl for communication with the SPC cards (spcm32.dll). Higher-level functions were then constructed for specific uses. The GUI has a dedicated file (Callbacks.c) to handle all user interaction, and this then executes specific functions from any of the lower-levels files.

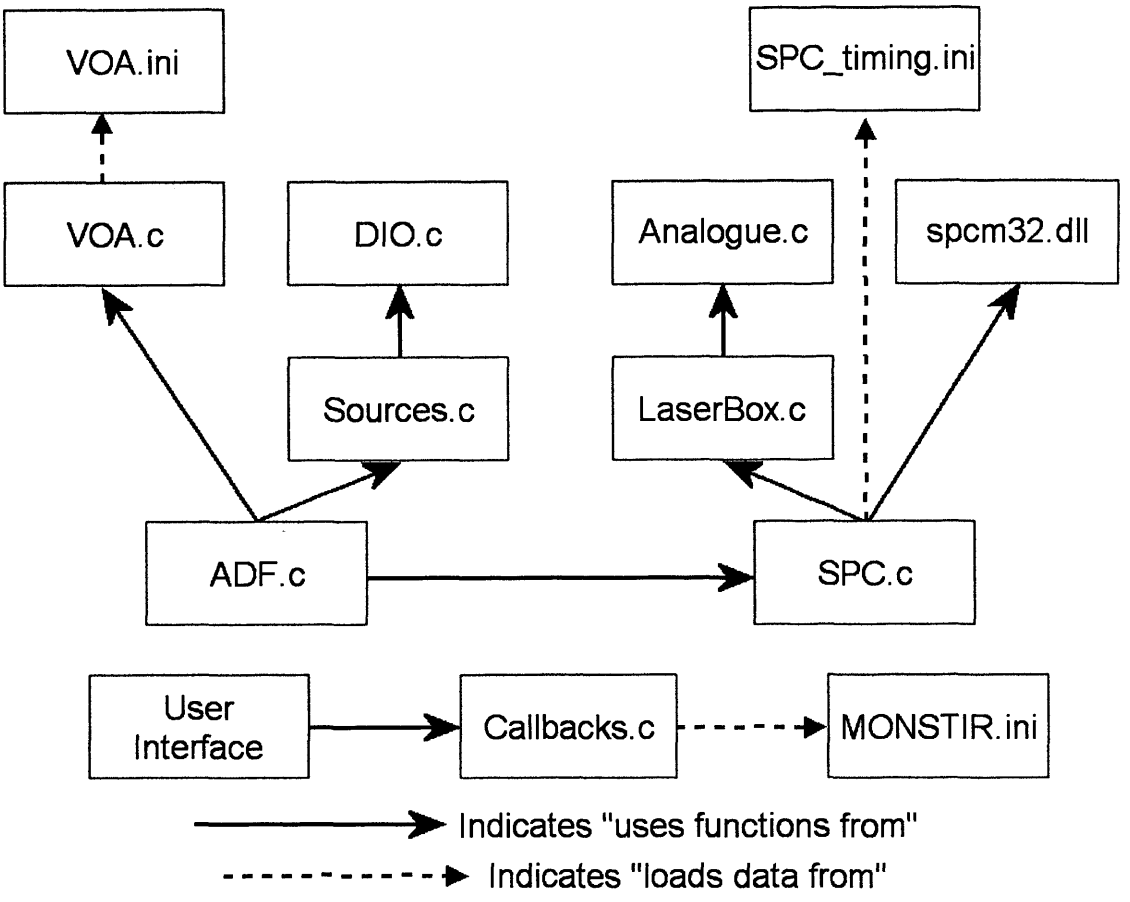

Figure 3-42 Diagram of MIDAS code structure

Initialisation files (.ini) are editable text files used to set variables and hardware mapping that an operator may wish to change prior to starting MIDAS. MONSTIR.ini contains the active channels and the VOA and shutter addresses corresponding to each channel. VOA.ini maps a nominal position number to each attenuation and stepper motor position. SPC_timing.ini stores the initial values of the discriminator thresholds, temporal offsets and zero crossings (see §2.2.4.5) for each SPC card.

3.6.3 Overview of new system

This chapter has described and discussed the results from improvements made to intensity measurements and the clinical usability on MONSTIR:

- new timing electronics, which decrease the time required for acquisitions and MONSTIR's size (§3.4).
- a method for recording the variations in the laser's power output, in order to remove them from intensity measurements (§3.5.1),
- a new design for the VOA discs, improving the reproducibility of the attenuations provided (§3.5.2),

The calibration recorded from the laser and the new VOA discs are both intended to create absolute intensity measurements, containing only stochastic noise errors. The intensity errors have been reduced from 40 % to 1 % by implementing the new instrumentation into MONSTIR. There are other sources of intensity errors, such as the instability in detector gain, but those are of smaller magnitude and will need to be resolved after further investigations have been made.

The SPC cards have a longer dead-time than the original electronics. The maximum recordable rate is further reduced by connecting eight channels via a router to each timing engine. Pile-up theory suggests a detection probability limit of 1 % per reference pulse. Therefore, if the TPSFs are not to be distorted, a maximum count rate of 400 kilo-counts per second (kcps) should not be exceeded. The new electronics were thought to have a limit of 50 kcps per channel, but have been found to be linear up to 100 kcps per channel, as compared to 300 kcps per channel for the original electronics. Recording at a reduced maximum count rate is not problematic, as accurately measuring large source-detector separations with very low count rates is of higher importance for image reconstruction. A secondary problem with a router is uneven illumination of neighbouring channels. For instance, if channel A is detecting double the count rate of channel B, the probability of losing B's counts due to pile-up is greater than that of losing A's.

The new VOA discs aid in resolving the problem of the reduced maximum count rate of the SPC cards. The new discs have a larger dynamic range and a greater number of discrete attenuations. The greater range keeps all count rates under that at which pile-up could occur, and the larger number of discrete attenuations ensures that smaller count rates are not lost. The increased range of attenuations also reduces differences in illumination on neighbouring MCP-PMT channels, reducing the effects of cross-talk.

The SPC's meantime measurements are reasonably stable, but have slightly lower temporal resolution than the original electronics. The original electronics have a native bin size of 1.2 ps, but the MIDAS control software re-samples the data using 5 ps bins across the 25 ns window, resulting in 5000 bins. The new SPC cards use 4096 bins for a slightly larger window, resulting in a bin-width of 6.1 ps. In spite of this the absolute values and standard deviations of the measurements are comparable for the two systems, suggesting the increase in bin-width does not affect meantime accuracy. This is probably due to the MCP-PMT's transit time spread (TTS, §2.2.4.3) of 30 ps.

New software has been written for MONSTIR to include controls for the SPC cards and the laser beam measurement. All operations, e.g. VOAs, source switching, and laser control, have been incorporated into MIDAS II to create a completely new imaging system.

The time taken for the new electronics to reach thermal stability was examined by leaving MONSTIR off for 36 hours, then recording TPSFs from the moment MIDAS started. TPSFs were recorded through a transparent phantom. As for calibration acquisitions (§2.3.1.3), this means data were measuring changes in MONSTIR impulse response function (IRF). Datatypes were investigated by windowing the TPSFs to measure signal only, and the full dataset were then normalised based on the final measurements to display variations during the initial period after switching the system on.

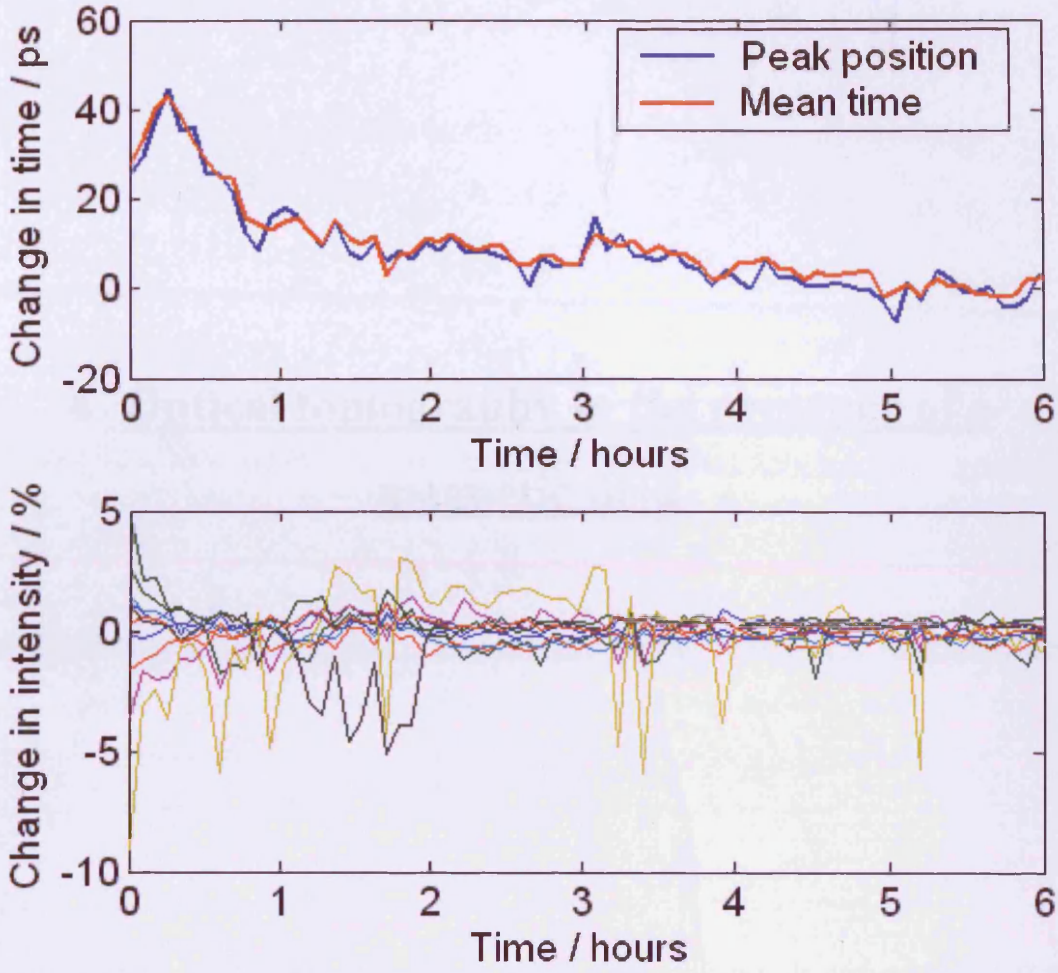

Figure 3-43 SPC data collected for 10 s every minute for 6 hours from power-up. The upper plot shows the meantime and peak position of the TPSFs, averaged for all channels. The lower graph shows the percentage change in intensity for each channel.

Errors in repeated measurements across an hour of less than 2 % intensity and 5 ps meantime means the system is ready for imaging, see §3.3. Figure 3-43 shows that the new MONSTIR electronics reach temporal stability within 2 hours of being switched on, and intensity measurements are stable within roughly the same period.

4 Optical tomography in the presence of a magnetic field

4.1 Introduction

Near-infrared (NIR) tomography generally suffers from comparatively low spatial resolution. In contrast, magnetic resonance imaging (MRI) can achieve a high resolution, but suffers from a lack of functional data. By incorporating the fine structural detail available from MRI into reconstructions of optical data, it is possible to improve the resolution of optical images (Chang J. et al. 1997, Pogue and Paulsen 1998, Dunn et al. 1998, Schweiger and Arridge 1999b, Ntziachristos et al. 2000).

MRI and NIR signals are independent of each other and can hence be acquired simultaneously. Acquisition with both systems concurrently is preferable to imaging separately for a number of reasons. Fiducial markers can be added to the ends of the optical fibres, allowing automatic registration of the images in reconstruction without loss of accuracy from warping or misalignment. Furthermore, the amplitudes of functional evoked response data from fMRI can only be directly compared to NIR data if acquisition is simultaneous (Strangman et al. 2002).

However, simultaneous acquisition presents a number of instrumentation issues. The magnetic field produced by MRI systems can damage mechanical equipment and can turn metallic objects into dangerous projectiles. The same metallic objects can also cause the MR field within the scanning region to be distorted, causing problems for imaging. MRI systems are hence installed in rooms with fixed magnetic shielding and have well defined fields outside the immediate area of the system. Standard clinical equipment, e.g. computers and other scanning systems, are certified up to a known magnetic immunity, the field strength above which damage / distortion will occur. Site diagrams of the magnetic field strengths are produced upon installation so that equipment can be used at safe distances from the scanner.

Previous combined MRI/NIR studies have therefore kept all equipment outside the external field of the MRI using long optical fibres. This leads to high temporal dispersion in the fibres and reduces temporal accuracy (Ntziachristos et al. 2000). Most of the components our optical imaging system, MONSTIR, should not be placed inside the imaging suite of an MRI due to health and safety and the effect they would have on the MR imaging. However, optical fibres, e.g. the source fibre, are not affected by magnetic fields and signals in electric cabling laid parallel to the field will not be significantly affected. Photomultiplier tubes (PMTs) can therefore be placed in the MR suite, minimising the losses and dispersion caused by additional fibre lengths. PMTs are quoted as withstanding a maximum magnetic field for correct operation, but there is no data for the effect on time-resolved data above this field strength. This chapter hence examines the temporal shifts introduced into time-resolved data from a PMT placed in a large magnetic field.

4.2 Background

4.2.1 Multimodality Imaging

Optical tomography suffers from the disadvantage that light transport in tissue is dominated by scatter. This limits the spatial resolution and results in reduced quantitative accuracy. Anatomical data from other imaging modalities can be used as an initial estimate in optical reconstructions, improving accuracy and resolution in the final images. The use of images from other imaging modalities in reconstructions as prior information is discussed in §2.3.3.6.

Dehghani et al. studied the resolution, contrast, and localisation of small objects within 3-D reconstructions and found that the properties may vary depending on the location of said objects (Dehghani H et al. 2003). Quantitative images of absorption, scattering, and haemoglobin parameters have been obtained at moderate resolutions in phantom studies (Jiang et al. 1998a, Jiang et al. 1998b, Pogue et al. 2000, Hebden et al. 2001) and for several tissues in vivo (Chance B et al. 1988, Hillman et al. 2001, Pogue et al. 2001b).

Combining medical images obtained from different modalities is currently one of the most active areas of research in medical physics. Typically, PET images are acquired at the same time as CT or MRI images and then registered so the functional information from the PET image can be superimposed on the anatomical information from CT or MRI (Hill et al. 2001).

Ultrasound or X-Ray data could also be used to improve optical images. Cranial ultrasound could provide some limited useful information such as the size and depth of a haemorrhage, and mammography or breast ultrasound could give the size and approximate location of a breast lesion. X-ray mammograms can provide information about breast lesions but it is difficult to use information from mammograms of the compressed breast with optical images of an uncompressed breast (Yam et al. 2001).

(Schweiger and Arridge 1999b) demonstrated that incorporation of a correct first estimate of optical properties can significantly enhance quantitative reconstruction of localised perturbations in the absorption and scattering coefficients for a complex, multilayered neonatal brain model.

The advantage of using *a priori* anatomical knowledge provided by MRI has been demonstrated in phantoms (Torregrossa M et al. 2003), the rat cranium (Pogue and Paulsen 1998, Pogue et al. 1999), female breast (Barbour et al. 1995, Brooksby et al. 2003). The structural information improved the reconstructions via three mechanisms: it allowed finer meshing around the areas of interest, assignment of the relevant optical properties for individual segments, and additional constraints to be added between reconstruction iterations. Overall, the quality of the reconstructed images were notably improved, both in terms of resolution and quantitative accuracy, when information about the internal geometry was added.

(Pogue et al. 2001a) used a realistic breast model for optical tomography modelling and reconstruction, and (Ntziachristos et al. 2000) performed simultaneous MRI and optical mammography using an optical contrast agent. Gibson has used *a priori* information from a CT image of a test phantom to improve the quality of reconstructed optical images (Gibson et al. 2003).

(Strangman et al. 2002) have shown in simulation that reliable quantitative accuracy of optical tomography of the brain can be obtained, and that during in vivo simultaneous fMRI and optical topography measurements, the optical and fMRI changes are closely correlated.

4.2.2 NMR and MRI principles

Nuclear magnetic resonance (NMR) is a physical phenomenon based upon the magnetic property of an atom's nucleus. In its simplest form, NMR allows identification of individual atoms in a molecule, analogous to infrared spectroscopy identifying functional groups. Analysis of a one-dimensional NMR spectrum indicates which atom environments, and in some cases how many atoms of each type, exist within a sample. NMR is based on quantum mechanical properties of nuclei, and as such is very reliable, predictable and reproducible. Since its advent, it has become the most important analytical tool available for organic chemists (Farrar T.C. 1987).

Magnetic resonance imaging (MRI) is used primarily in medical settings to produce high quality images of the inside of the human body from NMR signals. MRI is based on the natural magnetisation that is induced in the human body when it is placed into an MR scanner. Initially, the magnetisation is aligned with the main, static field of the scanner (usually referred to at the z-axis or longitudinal direction). The strength of the magnetisation depends on the proton density (PD) of the tissue, which in turn depends on the number of hydrogen atoms in the tissue. There are three main tissue types: fluids, such as cerebrospinal (CSF) and blood, which have over 95 % PD, water-based, e.g. muscle, brain and cartilage, and fat-based tissues, e.g. fat and bone marrow, which typically have 60 % to 85 % PD due to water and lipid content. These tissues can be easily differentiated by their NMR signal (McRobbie D.W. et al 2003).

At equilibrium, the net magnetisation lies along the direction of the applied magnetic field B_0 and is called the equilibrium magnetisation M_0. In this configuration, the z-component of magnetisation M_z equals M_0. M_z is referred to as the longitudinal magnetisation. There is no transverse (M_x or M_y) magnetisation.

It is possible to change the net magnetisation by exposing the system to a radio-frequency (RF) pulse of the correct frequency. The correct energy input can saturate the transverse magnetisations, resulting in $M_z = 0$.

Volume imaging requires localisation of the measured MR signal. Each position must therefore have slightly different field strengths before the RF pulses are introduced and data recorded. Addition fields are applied along all axes, inducing gradients in the main magnetic field. Full volume data are then acquired with spatial information encoded in the magnetic frequencies.

The time constant which describes how M_z returns to its equilibrium value is called the spin-lattice relaxation time (T_1). The equation governing this behaviour as a function of the time, t, after displacement is (Hornak J.P 2004):

$$M_z = M_0\left(1 - e^{-t/T_1}\right) \qquad \text{(i)}$$

The net magnetisation can be knocked into the XY plane. It will then rotate about the z-axis. This precession has the same frequency as a photon which would cause the transition between quantum energy levels. This frequency is called the Larmor frequency.

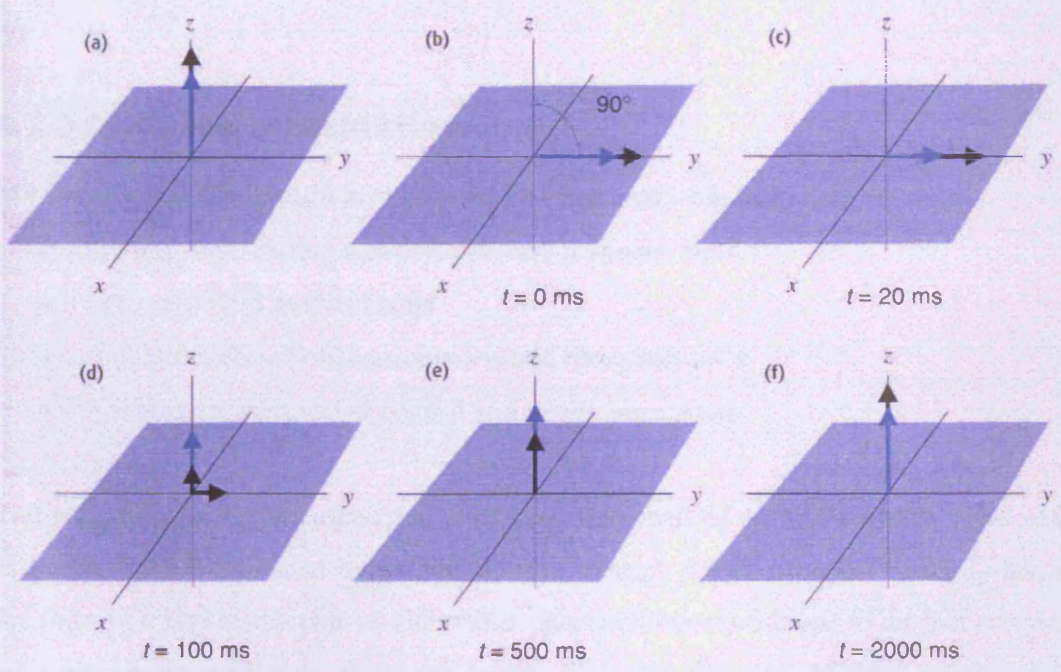

Figure 4-1 An example of the two tissues' magnetisations, represented by blue and black arrows, during an MR sequence. (a) Initially aligned with the z-axis. (b) A 90° pulse knocks the magnetisation into the XY plane. (c-f) Relaxation occurs, with T_2 reducing magnetisation in the XY plane, and T_1 controlling recovery along the original z-axis. In this example, the blue tissue has much shorter T_1 and T_2. (McRobbie D.W. et al 2003)

In addition to the rotation, the net magnetisation will start to dephase and rotate at its own Larmor frequency. The time constant which describes the decay of the transverse magnetisation, M_{xy}, is called the spin-spin relaxation time, T_2:

$$M_{xy} = M_{xy0}\left(e^{-t/T_2}\right) \qquad \text{(ii)}$$

The spin-spin relaxation time, T_2, is the time to reduce the transverse magnetisation by a factor of $1/e$, whilst the spin-lattice relaxation, T_1, is the time to for the magnetisation to return to the z-axis. Both processes occur simultaneously with the only restriction being that T_2 is less than or equal to T_1. Table 4-1 shows the relaxation time for both T_1 and T_2 for three tissue-types

Tissue type	T_1 / ms	T_2 / ms
Fluids	1500-2000	700-1200
Water-based	400-1200	40-200
Fat-based	100-150	20-100

Table 4-1 MRI relaxation times for different tissue types. (McRobbie D.W. et al 2003)

4.2.3 MRI Instrumentation

MR imaging (MRI) systems are comprised of four main sub-systems:

- A magnet producing a strong, constant magnetic field
- Magnetic field gradient coils
- Radiofrequency (RF) transmission and reception coils
- A computer for scanner control and image processing

The main magnet is the largest and most expensive part of an MR scanner. The main magnetic field is produced by passing current through a pair of coils, typically taking the form of a Helmholtz pair. A Helmholtz pair is two coaxial loops of current carrying wire placed symmetrically about the origin, such that the ratio of their separation to their radii gives optimal field homogeneity at the origin. In MRI more than two coils are used in creating the main magnetic field, with extra coils added at specific positions to increase homogeneity. A Helmholtz pair is shown as the outer pair of coils in Figure 4-2.

Early systems were based around permanent or water-cooled resistive magnets, but the majority of modern scanners use superconducting magnets. Whole body resistive and permanent magnets are limited to around 0.3 T before their weight becomes prohibitively large. Superconducting magnets are able to generate much larger fields, and there are a number of 4.0 T whole body scanners now available (McRobbie D.W. et al 2003). These magnets are constructed from materials such as NbTi alloy, which need to be kept below the superconducting limit of about 9 K using liquid helium. Once started, current will flow through the material indefinitely, provided the temperature is kept below the critical temperature. The fields from such magnets are very stable with time, which is essential for MRI systems.

One of the most important requirements for MRI is that the field is as homogeneous as possible, with tolerances as low as 1 p.p.m. required over the volume of interest (Hornak J.P 2004). The field is therefore evened out as much as possible during installation using ferromagnetic blocks placed inside the bore. In addition, a set of resistive coils known as shim coils are placed within the bore of the magnet. These generate fields that can be used in combination to improve not only the intrinsic homogeneity of the magnet, but also reduce field effects due to susceptibility differences in the objects scanned.

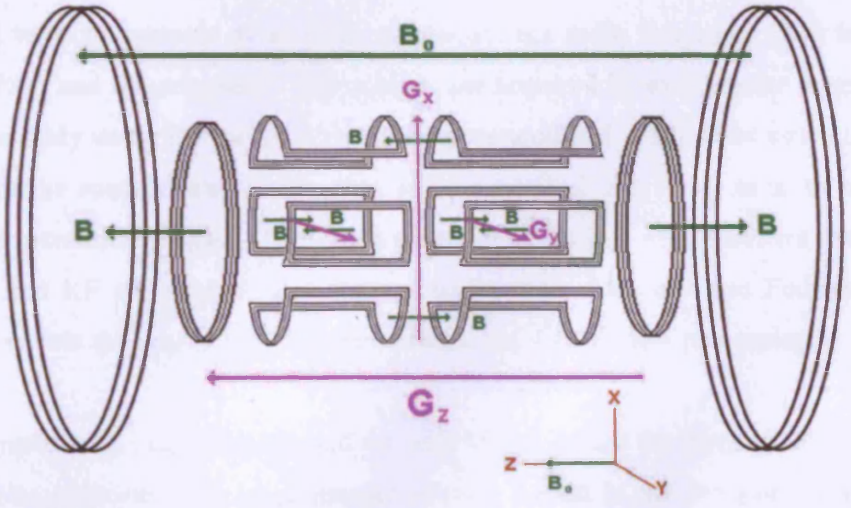

Figure 4-2 Exploded diagram of MRI coils, used to produce the magnetic fields (B) and gradients (G). The main field (B0) is created by a Helmholtz pair (additional magnet / blocks used for field homogeneity not shown). The gradient along the z-axis (G_z) is created using a Maxwell pair, and x- and y-gradients (G_x and G_y respectively) and created by Golay coils.

Localisation of the MR signal in the body is achieved by generating short-term spatial variations in the magnetic field strength across the area of interest. Gradient coils are therefore required to produce linear variations in magnetic field along each axis. These must have a high efficiency, low inductance and low resistance to minimise the current requirements and heat deposition. Variation along the direction of the main field, traditionally labelled the z-axis and running along the centre of the MR bore, is usually produced by a Maxwell coil (Hornak J.P 2004). This consists of a pair of coils with current flowing in opposite senses, and produces a very linear gradient. The inner loops shown in Figure 4-2 represent the Maxwell pair.

Production of the linear gradient in the other two axes requires wires running along the bore of the magnet. This is typically done using a saddle-coil, such as a Golay coil, consisting of four saddles running along the bore of the magnet. Saddle coils creating x- and y-axis gradients are shown central in Figure 4-2. A linear variation in magnetic field is produced along the x- or y-axis, depending on the axial orientation. This configuration produces a very linear field on the central plane, but this linearity is lost rapidly with distance. A number of coil-sets can be used with different axial separations to improve the linearity. However, the gradient coils are designed to have only minimal effect on the magnetic field outside the MR bore.

The final two components of an MRI system are the radio frequency (RF) transmitter and receiver, and the computer. MR signals are acquired by exciting the magnetisation within the body using RF pulses. These are generated and received by coils that can be shaped for the specific area of the body to be examined, e.g. head, neck, or torso. All scanning operations are controlled from a central computer. This specifies the shape of gradient and RF waveforms, and timings to be used. The raw and Fourier data are stored to enable the application of corrections to the data in post processing.

The magnetic field extending beyond the MRI unit is called the fringe field. The fringe field can be reduced using large masses of iron, bolted to the sides of the scanner or walls of the room, but typically an additional set of shielding coils are added to the MRI unit for this purpose (see Figure 4-9).

4.3 Magnetic Sensitivity of MONSTIR

4.3.1 Magnetic effects on instrumentation

The individual components most at risk from a magnetic field in MONSTIR are:

- Electronics, Computer Case, PSUs – Projectile risk
- Computer – Processor and hard disk drive
- Switch – Stepper motor controlling switch head
- VOAs – Stepper motor
- Detectors – Electron path
- Shutter – Piezoelectric shutters
- Laser – Pump laser diodes.

There are three main concerns when using any equipment in a magnetic field: objects being drawn towards the magnet, moving parts being slowed or damaged, and distortion of electron motion. MONSTIR is comprised of components that will be affected by the above. This section discusses the relevant components and the respective effect of a strong, >1 T, magnetic field.

First, any ferromagnetic object introduced into a magnetic field will be acted upon by a force proportional to the object's volume, V, and magnetic susceptibility, χ, and the magnetic field, B, and field gradient ($\partial B/\partial r$) at that distance, r, from the magnet (Shellock 2001):

$$F \propto \chi V B \cdot \partial B/\partial r \qquad \text{(iii)}$$

Such objects can become dangerous projectiles if introduced into the vicinity of an MR scanner, as the magnetic field extends beyond the physical confines of the scanner itself. Although the external field decreases rapidly with distance from the scanner, the large gradient of the field near the scanner also increases the danger from any objects brought into the magnetic field (American Society for Testing and Materials (ASTM) International 2005)

The components in MONSTIR that would be affected by this are any power supply units (PSUs) and the computer case. However, to become projectiles these components would have to be placed much closer to the scanner, i.e. in higher magnetic fields, than other components in MONSTIR could withstand.

Second, electrical potentials are induced in any conductor moving through a magnetic field. In the case of a conducting disc spinning in a magnetic field, circulating flows of electrons, called eddy currents, are induced. Typically they oppose the motion of the disc and cause frictional heating. The computer's hard disk, CD drive, the source switch, and VOAs in MONSTIR all contain motors susceptible to damage by eddy currents. In addition the VOAs use magnetic potentials to hold stepper motor positions, and hard disk data is stored magnetically onto metallic platters.

The final effect a magnetic field would have on MONSTIR takes the form of distortions of electron paths. Charged particles moving through a magnetic field experience a force, F, proportional to the field strength, B, the particle's velocity, v, and charge, q, and the angle between the field and the velocity vectors, θ:

$$F = B \times vq \sin\theta \qquad \text{(iv)}$$

Motion parallel to the field results in no additional force exerted on the charge. However, if the charged particle's motion is perpendicular to the field, the force applied to the charge is perpendicular to both the particle's motion and the field. For a charge travelling at an arbitrary angle θ to the field, the velocity of the particle parallel to the field is unchanged, but the particle will spiral around the field due to the perpendicular force, as shown in Figure 4-3. This effect is negligible for currents in wires. However, photomultiplier tubes (PMTs) contain electrons moving in a vacuum, which can be deviated from their normal path through the PMT body. This is discussed in the next section.

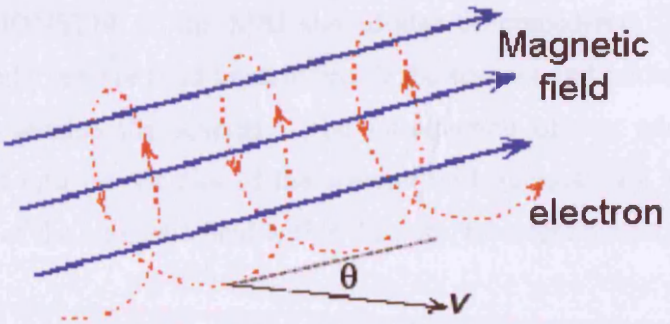

Figure 4-3 Illustration of a charged particle's motion when travelling at an angle to a magnetic field.

It is difficult to estimate an overall magnetic immunity on MONSTIR as most component manufacturers do not quote or test their component for magnetic immunity. Table 4-2 lists objects that are common with most hospital environments, and the magnetic field at which they would cease operating. The manufacturers of the laser diode used as a pump in the MONSTIR laser (IMRA America, USA) and piezoelectric shutters (Piezo Systems, Germany) were unable to provide magnetic immunities for their components, but suggested a value of 1 mT in personal communications. From the values listed in Table 4-2 the computer has a magnetic immunity of roughly 1 mT, and the components containing small motors, the source switch and VOAs, have immunities of up to 3 mT.

Item	Acceptable magnetic field strength / mT	Minimum Distance /m	
		Axial direction (along z-axis)	Radial direction (x/y axes)
Small motors, watches, cameras, magnetic data carriers	3	2.8	2.0
Processors, magnetic disk drives, oscilloscopes	1	3.5	2.3
Pacemakers, B/W monitors, X-Ray tubes, insulin pumps	0.5	4.0	2.5
Colour monitors, CT systems	0.1	6.0	3.5

Table 4-2 A comparison of the magnetic immunities of various objects, and the corresponding distances at which the fringe field has that strength for a typical 1.5T MR scanner. Summarised from (McRobbie D.W. et al 2003) and (Siemens AG (Medical) 2004)

The effect of MONSTIR on the MRI should also be considered. MR scanners are carefully shielded to ensure field linearity inside the scanner and minimise the effects of the fringe field outside the scanner. The introduction of any additional magnetic material or field into the vicinity of the scanner will interact with the MR field and cause distortion of the magnetic field within the bore, therefore distorting images.

Two types of interference are defined for MR systems: static interference from ferromagnetic objects, and dynamic interference from ferromagnetic objects in motion or low frequency magnetic fields (GE Medical Systems 2005). Static interference is usual considered in terms of iron beam reinforcement in floors and walls, and is typically quoted as a limiting amount of 100 kgm^{-2} at a distance of 1.5 m from the centre of the scanner. Dynamic interference can be caused by as little as a wheelchair passing within 5 m of the scanner, or a car passing within 10 m.

The static ferromagnetic mass of MONSTIR is insufficient to cause interference, but two sources of dynamic interference are present. Power cables and transformers both produce magnetic fields and hence AC interference. Cables carrying up to 50 A at 50 Hz must be kept at least 3 m distant from the scanner centre, and it is suggested that transformers up to 100 kVA be kept 10 m away (Siemens AG (Medical) 2004). All components in MONSTIR are powered through an isolation transformer and require 10 A. The power cabling must be kept roughly 3 m distant from the scanner, and the transformer roughly 5 m distant, both from the scanner centre. The power supply and isolation is therefore the limit on the minimum separation between MONSTIR and an MR system currently.

Most components in MONSTIR will operate as designed in magnetic fields of less than 1 mT. Photo detectors are available with known magnetic immunities, and can be designed to have minimal effects on the magnetic field. The detectors could hence be placed closer to the subject than the rest of MONSTIR. The possible effects of a magnetic field on time-resolved data are discussed in the next sections.

4.3.2 Magnetic effect on photomultiplier tubes

For combined MRI-Optical imaging, it is advantageous to position the photomultiplier tubes (PMTs) as near to the magnet as possible, and hence limit fibre length and resulting optical dispersions and losses. PMTs have been designed for various purposes, and each design performs differently in a magnet field. A discussion on general PMT design is given in §2.2.4.3.

The internal structure of a typical PMT is shown in Figure 2-8. The photocathode, labelled (a), and dynode construction, labelled (b), determines this electron path and gives each PMT design its timing characteristics. A magnet field's effect on a PMT will be manifested mainly in deviations in the electrons' paths through these sections of the PMT body.

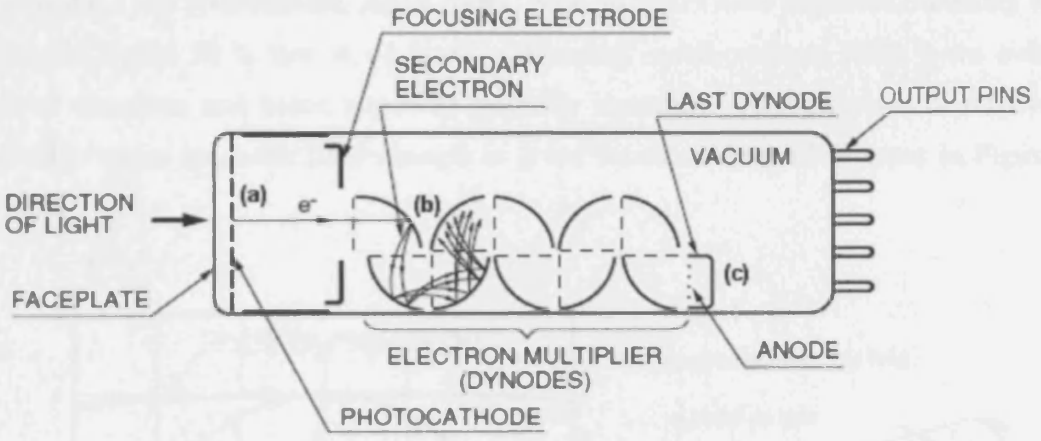

Figure 4-4 Basic PMT design, showing the electron path into dynode section (Hamamatsu, Japan 2006)

Magnetic immunity is defined as the maximum field, along the most susceptible PMT axis, at which the output does not deviate from given tolerances. PMTs have low-energy electrons travelling relatively long paths (mm-cm) in a vacuum. Electron paths are susceptible to deviations by magnetic fields (§4.3). The output of the PMTs can hence be distorted by a magnetic field. The main reason for distortion is the influence of the magnetic field on the electron trajectories onto the first dynode, as the distance from the photocathode to the first dynode is the largest free path within the PMT body. PMTs with longer distances to the first dynode will hence be more susceptible to the effects of a magnetic field.

In general, the shorter distance from the photocathode to the first dynode in side-on, as compared to head-on, PMTs restricts the path of the photoelectrons, and provides less distance for deviation from the designed path. A head-on PMT's sensitivity can be reduced by up to 50 % due to magnetic fields parallel to the photocathode surface of less than 0.1 mT (Hamamatsu, Japan 2006). Side-on PMTs have improved immunity to magnetic fields, 50 % loss at ~3.5 mT. However, metal-package PMTs have even shorter distances, and hence improved magnetic immunity. A comparison of relative intensity versus magnetic field strength is given for these three PMT types in Figure 4-5.

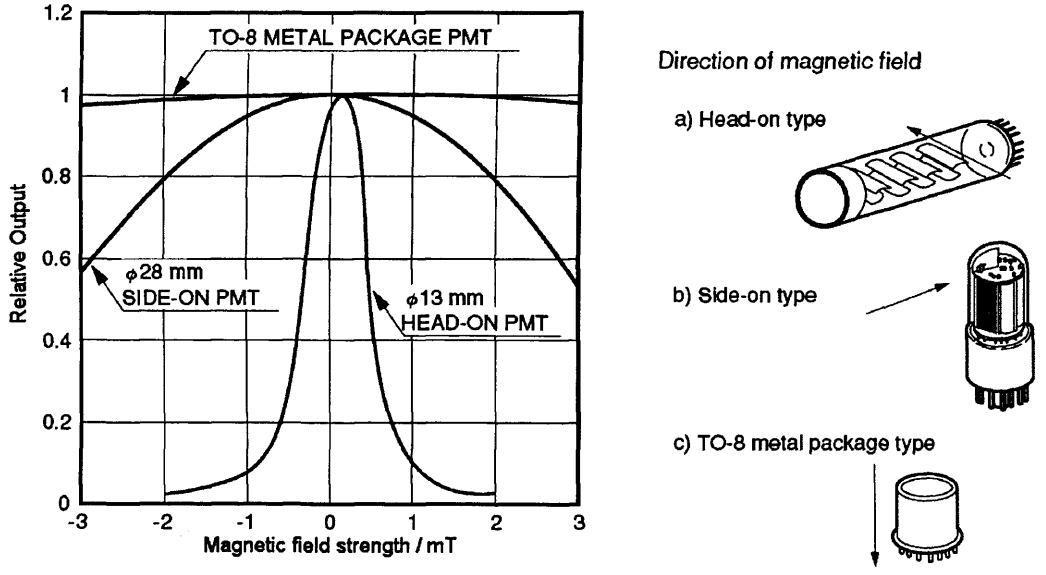

Figure 4-5 Magnetic characteristics of typical PMT types (Hamamatsu, Japan 2006)

A second reason for distortion of the output signal from a PMT due to a magnetic field is the deviations in electron transit through the dynodes. The more constrained the path, e.g. in mesh or microchannel plate versus box and grid dynodes, the smaller the effect of the magnetic field on the mean electron path through the PMT body. However, a magnetic field's interaction with the electron motion could have a focussing effect on the electrons. This would reduce the effective area of the dynodes, and lead to saturation. The end result would be a reduction in secondary emission for each dynode plate. This would account for reductions in earliest transit time (ETT), transit time spread (TTS), and output pulse height (§2.2.4.3).

PMT dynodes and housings can retain some magnetisation after being introduced into high fields. The gain of the PMT will be affected, but the residual magnetisation should dissipate quickly once used outside the field. PMTs can be made from nonmagnetic materials (Hamamatsu, Japan 2006), but wiring connections and cooling system still typically contain magnetic materials.

The MCP-PMTs used in MONSTIR (§2.2.5) constrain the electron trajectory through the PMT body more than any other dynode design, giving them the best timing characteristics (see Table 2-1). The dynode design also proves to be the most magnetically resistant. Figure 4-6 shows the expected relationship between recorded intensity and magnetic field strength for a field parallel (top) and perpendicular (bottom) to an MCP-PMT.

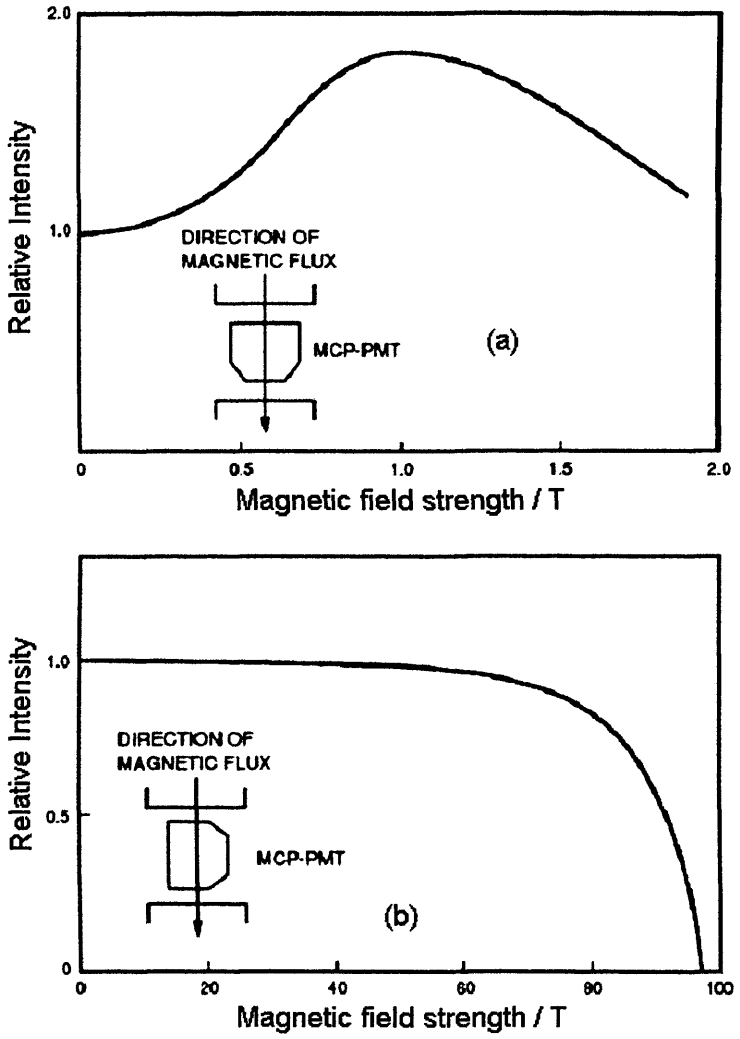

Figure 4-6 Typical MCP-PMT response to a magnetic field. (a) Field parallel to the tube axis (b) Field perpendicular to tube axis (Hamamatsu, Japan 2006)

An H5783 metal-package PMT was chosen to determine the effect of a magnetic field on time-resolved data. The H5783 has requires no external cooling, and is smaller than the MCP-PMTs, making it preferable for this experiment.

The H5783 has a lower magnetic immunity than the MCP-PMTs currently used in MONSTIR, 5 mT as opposed to 1500 mT, but higher than most other PMT types, see Table 2-1. Results from the H5783 would therefore be a lower limit on the safe magnetic field the MCP-PMTs would operate normally in, and as an upper limit for other PMT types.

In addition, the H5783 is similar in design to the H8224P-50 which were chosen to replaced to the MCP-PMTs in MONSTIR (§3.4.2.1). Both H5783 and H8224P are metal-package PMTs with metal channel dynodes (§2.2.4.3). Results for the H5783 can therefore be used to guide future experiments using MONSTIR for combined MRI / optical imaging.

4.3.3 Magnetic effects on data

MONSTIR records histograms of photon flight times, called temporal point spread functions (TPSFs - §2.2.3). The TPSFs recorded by MONSTIR are Fourier convolutions of the impulse response function (IRFs) of the system's components and the interrogated volume between source and detector fibre ends (§2.2.3). Calibration (§2.3.1.2) can remove the system's IRF from the final TPSF by deconvolution, but only if the IRF of the system is well defined. The IRF broadening and delay due to the PMTs is caused by the electron transit through the body of the PMT (§2.2.4.3).

Variations in electron paths through the PMT could affect electron transit time (ETT), transit time spread (TTS), and output pulse height (§4.3.2). Changes in ETT would shift the whole TPSF earlier or later. Changes to TTS would alter the uncertainty in the arrival time of each photon, but would have little effect on TPSFs overall, assuming sufficient counts for good statistics. The conversion of the PMTs' analogue output to logical pulse in the CFDs (§2.2.4.5) would mostly remove any changes in PMT output, as the resulting logic pulse used for timing is not dependent on pulse shape, but some broadening or narrowing of the recorded TPSFs would still result. Variations in pulse height, e.g. due to losses of secondary emissions, could cause more counts to be disregarded by the CFDs as dark counts.

Assuming no change in magnet field strength between calibration, data and reference acquisitions, the distortions introduced should mostly cancel in post-processing, as the same IRF would still apply to all datasets.

4.4 Performance of photomultipliers in a magnetic field

4.4.1 Introduction

Previous investigations into combined MRI/optical imaging have typically kept optical instrumentation outside the room containing the MR scanner. Source and detector fibre lengths need to be extended to accommodate this separation. Optical fibres have associated intensity losses, e.g. absorption within the fibre, and temporal dispersions per unit length. Extending the source and detector fibres hence reduces the detected signal strength and adds flight time uncertainty. Positioning the PMT as close to the patient as possible minimises these effects. However, PMT output is highly susceptible to magnetic fields. A PMT was therefore tested in increasing magnetic fields to investigate the effect on the data. The result of this investigation establishes the nearest point the PMTs could be taken to an MR scanner. In conjunction with the magnetic immunity of other components, this would give a minimum safe distance for MONSTIR from all similar scanners.

Most components in MONSTIR are not expected to be affected by small magnetic fields (§4.3). MONSTIR could be hence placed in a corner of the MR room, and the effect on the MR system also investigated. However, for this investigation it was felt safer to keep the bulk of MONSTIR outside the MR room. The danger of PSUs / other steel component in MONSTIR being pulled into the scanner by the magnetic field is not high, but health and safety always errs on the side of caution.

The MCP-PMTs used in MONSTIR are unsuitable for removal and use in isolation in a magnetic field. The H5783 is a head-on metal-package PMT with a metal channel dynodes (§2.2.4.3), and is similar to the PMTs chosen to replace the MCP-PMTs in MONSTIR. The dynode design is smaller than the MCP-PMTs and requires no cooling hence can be tested more readily. The metal channel dynodes have the second best timing characteristics next to the MCP-PMTs, and can hence record similar data when used with the SPC cards (§3.4). The metal channel construction constrains the electron trajectory through the dynodes, giving this PMT the second highest magnetic immunity, the highest being the MCP-PMTs.

4.4.2 Method

The H5783 PMT was placed into the static field of a typical clinical 1.5 T MR scanner (Signa Excite 1.5 S3, General Electrics, USA), and data were recorded as the PMT was moved closer to the bore entrance. The PMT, power supply, and cables were attached to a wooden back-plane, as shown in Figure 4-7, which was in turn attached to the MRI's patient table, see Photo 4-8. This ensured the PMT could not be moved by the magnetic field.

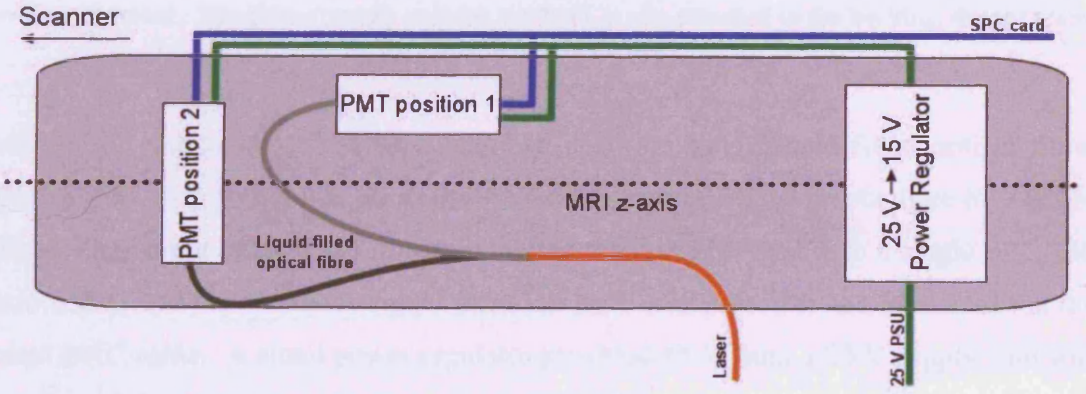

Figure 4-7 The setup used for MRI measurements, showing the PMT in two positions with associated equipment mounted on a wooden backplane.

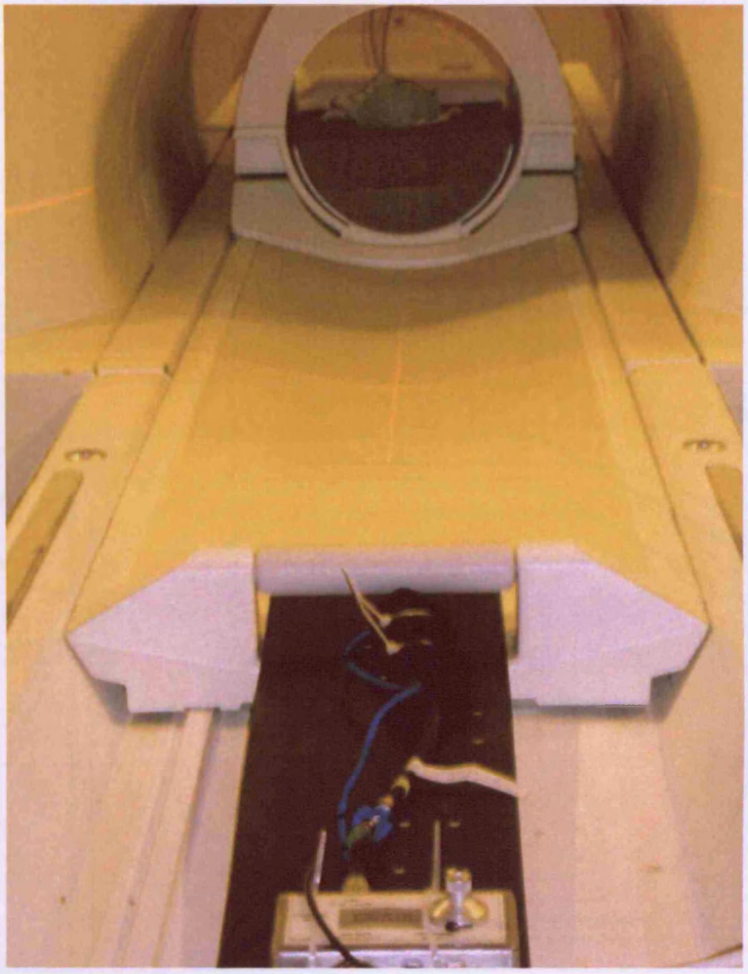

Photo 4-8 Experimental setup: The PMT is wrapped in NIR-absorbent cloth and cable-tied to a wooden backing. The power supply unit for the PMT is also attached to the backing, distant from the scanner entrance.

MONSTIR's laser (§2.2.5) was coupled to a 20 cm long, liquid-filled optical fibre. MONSTIR was kept outside the magnetic field by extending the source fibre by a 6.2 m fibre. The output of the PMT was transmitted via 7 m SMA cable to a single SPC-130 card (§3.4) and the reference signal from the laser was passed to the SPC card via the usual BNC cable. A small power regulator provided 15 V from a 25 V supply, and was attached to the scanning table 25 cm behind the PMT.

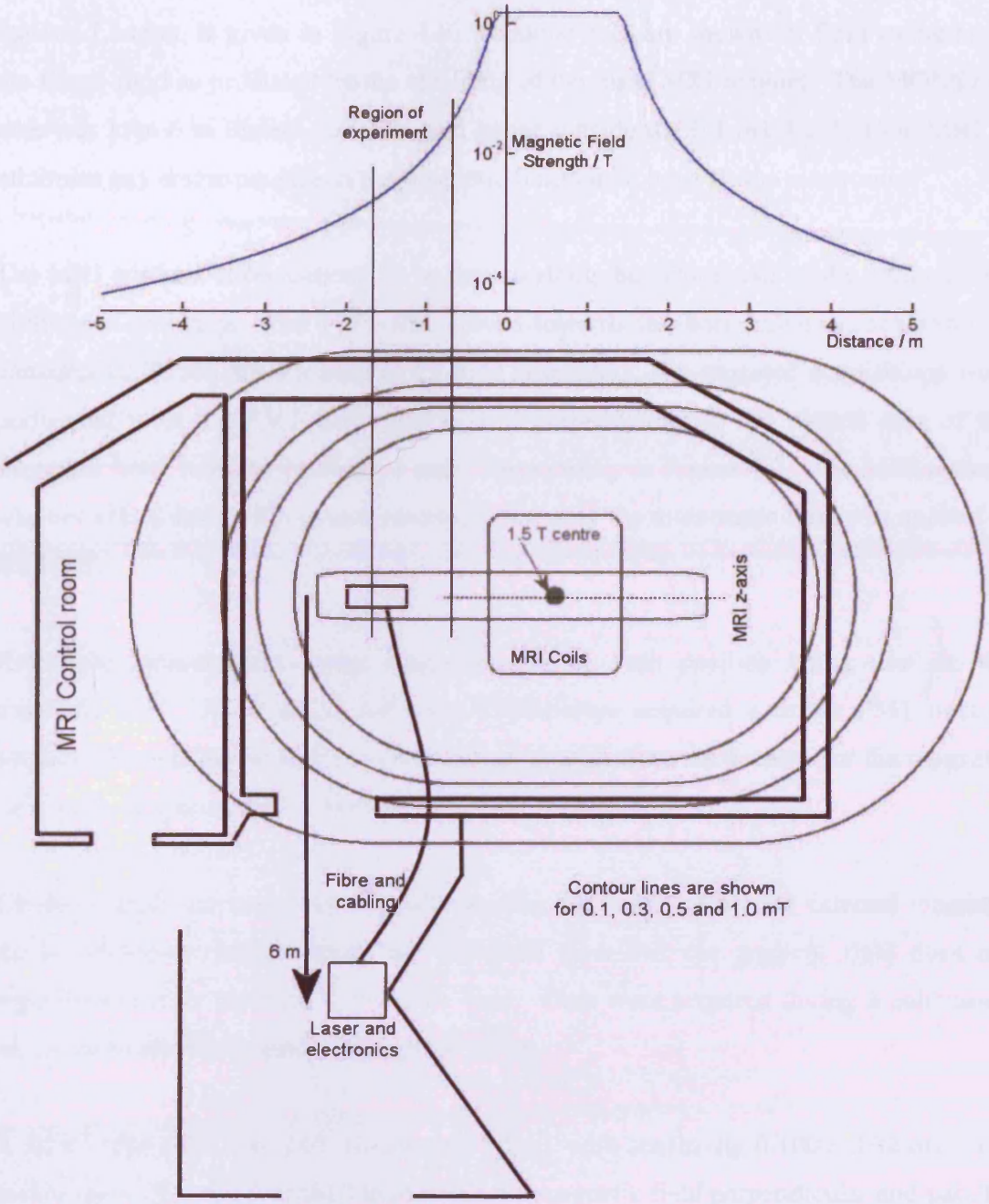

Figure 4-9 Layout of MRI suite at the Department of Neurology, Queen's Square (taken from GE installation documentation). Field contours and positioning of the electronics rack are given for reference. The upper plot of magnetic field strength with distance is from data collected along the z-axis of the scanner with a Hall probe.

A diagram of the layout of the MRI suite at the Department of Neurology, Queen's Square, London, is given in Figure 4-9. Contour lines are shown for field strengths of the fringe field as produced by the shielding of the main MRI magnet. The MONSTIR rack was kept 6 m distant, off axis, and hence outside the 0.1 mT field of the MRI to minimise any distortive effects the magnetic field might have on the electronics.

The MRI controls allow patients to be moved along the central axis of the scanner with millimetre accuracy. The PMT was moved towards the bore entrance, acquiring 32 consecutive TPSFs for 5 s each at 11 field strengths. The repeated acquisitions were performed with the PMT both parallel and perpendicular to the central axis of the magnetic field, labelled Positions 1 and 2 respectively in Figure 4-7. The MRI scanner was not active during the measurements, hence only the main static field was applied to the PMT.

Reference measurements were acquired prior to each position being used in the magnetic field. A set of 32 reference TPSFs were acquired with the PMT next to MONSTIR, outside the MR suite and distant enough from the scanner for the magnetic field to be at approximately background level.

Gradient fields are necessary for MR imaging and might affect the external magnetic field. However, MRI systems are designed such that the gradient field does not significantly alter the field outside the bore. Data were acquired during a calibration sequence to check the gradient magnets' effect.

A Hall probe (RS 244-3140, Honeywell, USA), with sensitivity $0.100 \pm .002$ mT / mV and range $\pm$ 250 mT, was used to measure the magnetic field perpendicular and parallel to the z-axis of the scanner. These measurements were used to create the plot of magnetic field strength along the z-axis of the scanner shown in Figure 4-9.

4.4.3 Results

The distances to the MRI field centre and corresponding magnetic field strengths are given in Table 4-3. For comparison, the Earth's magnetic field is 0.05 mT.

Distance / mm	846	896	946	996	1046	1096	1146	1246	1346	1546	1646
Position 1 field / mT	30.22	26.32	22.96	20.04	17.59	15.26	13.30	10.07	7.55	3.99	2.73
Position 2 field / mT	32.40	28.20	24.58	21.45	18.42	16.33	14.25	10.81	8.13	4.35	3.02

Table 4-3 Distances to the centre of the MRI field and respective magnetic field strengths. Position 1 and 2 are shown in Figure 4-7 and are the body of the PMT parallel and perpendicular to the MR z-axis respectively.

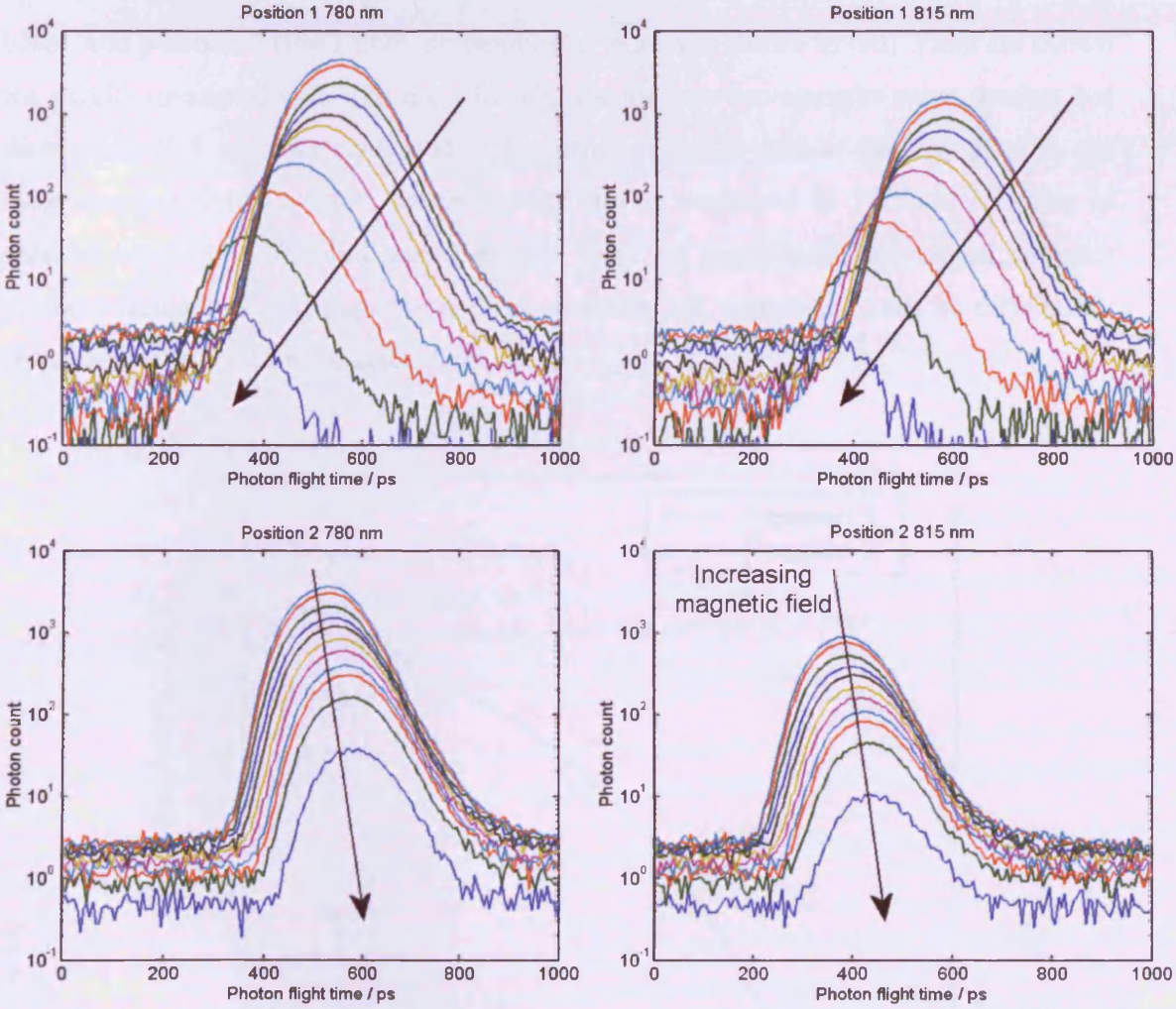

Figure 4-10 Averaged TPSFs at various distances from the MR scanner. All x-axes are time in picoseconds, with an arbitrary offset due to windowing, and y-axes are photon count. The arrows indicate the effect of increasing magnetic field. The weakest signals correspond to the largest fields given in Table 4-3.

The TPSFs were averaged and datatypes (§2.3.1.1) extracted. Figure 4-10 shows the averaged TPSFs at each position. The TPSFs shown have been windowed to best show the effects of the magnetic field. The photon count of the TPSFs decreases with increasing magnetic field, but the shape is not obviously distorted. The TPSFs recorded with the PMT in position 1 (Figure 4-10, top) were shifted earlier in the temporal window as the magnetic field increased, whereas the TPSFs recorded in position 2 (Figure 4-10, bottom) were delayed slightly. There was no significant difference between results recorded for 780 or 815 nm.

Figure 4-11 and Figure 4-12 present graphs of average intensity and mean flight time against magnetic field strength for position 1 (PMT body parallel to z-axis, shown in blue), and position 2 (PMT body perpendicular to z-axis, shown in red). Plots are shown for results measured with 780 nm. Results for the two wavelengths were similar, but those from 815 nm data contained higher errors. At the time of this experiment, the laser was producing a lower power for 815 nm as compared to 780 nm, resulting in reduced signal to noise and higher errors. Data for acquisitions performed with the gradient fields switched on, as would occur during MR imaging, shows no differences from those acquired for the static field.

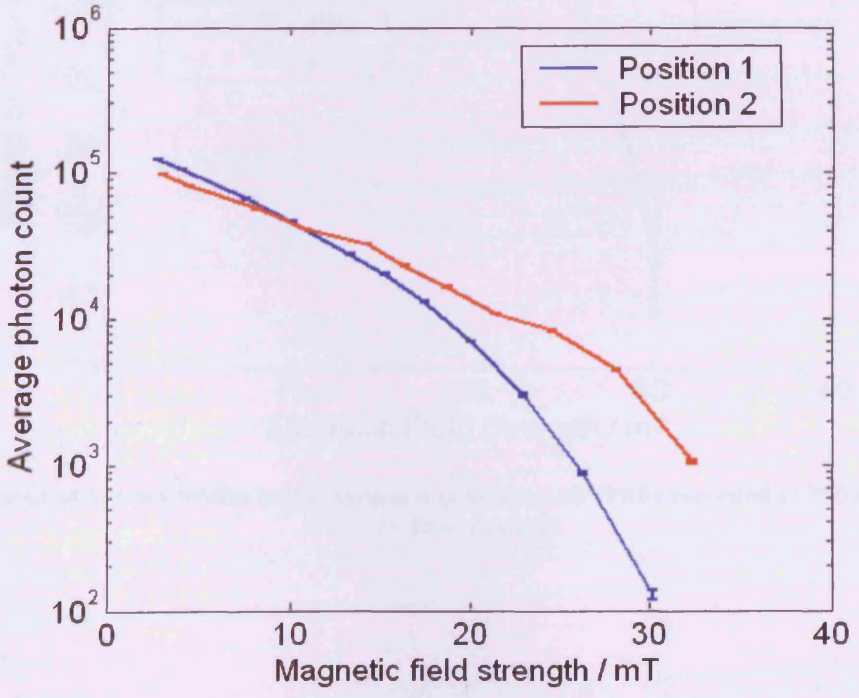

Figure 4-11 Intensity at 780 nm for a PMT in an increasing magnetic field.

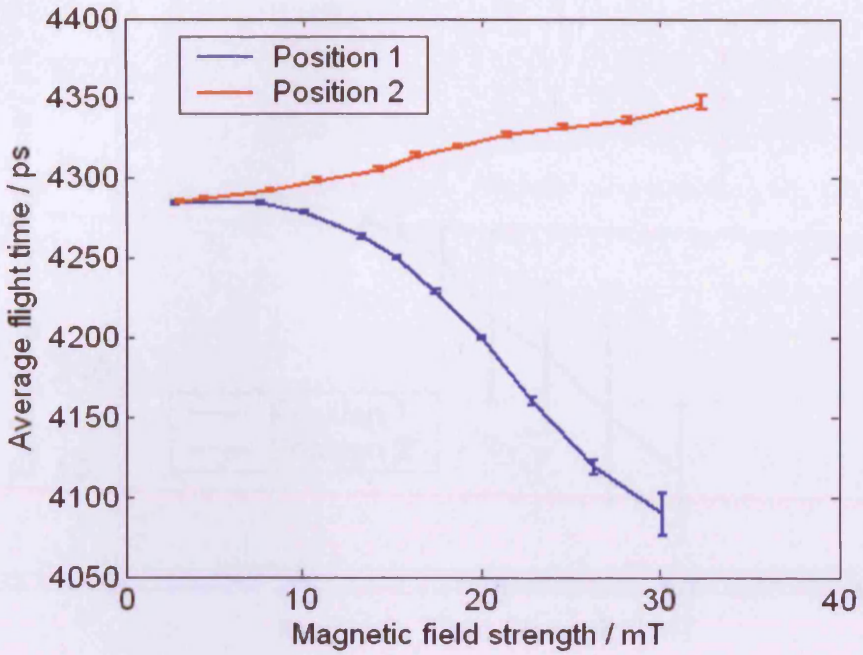

Figure 4-12 Mean flight time measurements at 780 nm for a PMT in an increasing magnetic field.

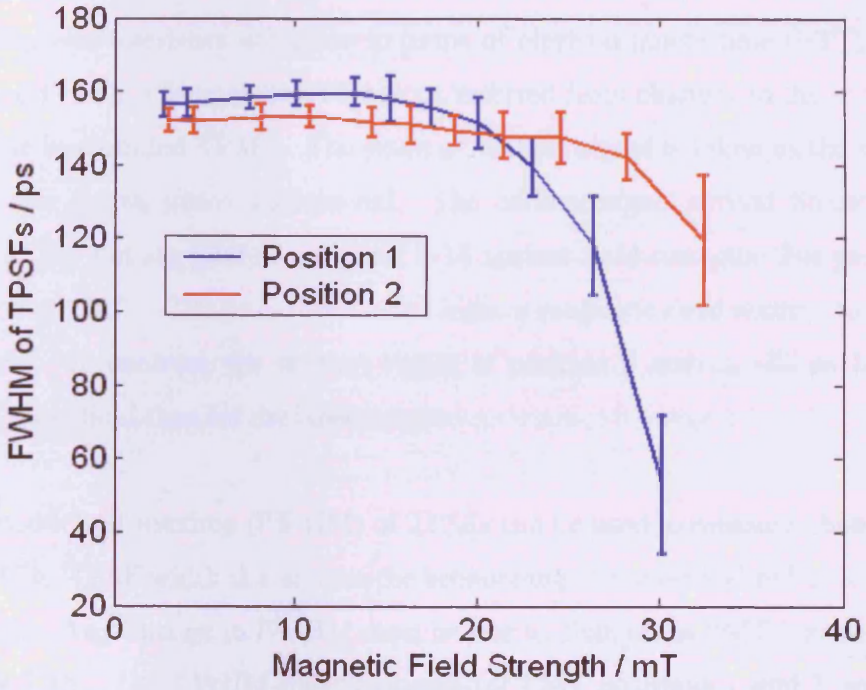

Figure 4-13 Graph of full-width half-maximums (FWHMs) of TPSFs recorded at 780 nm against magnetic field strength.

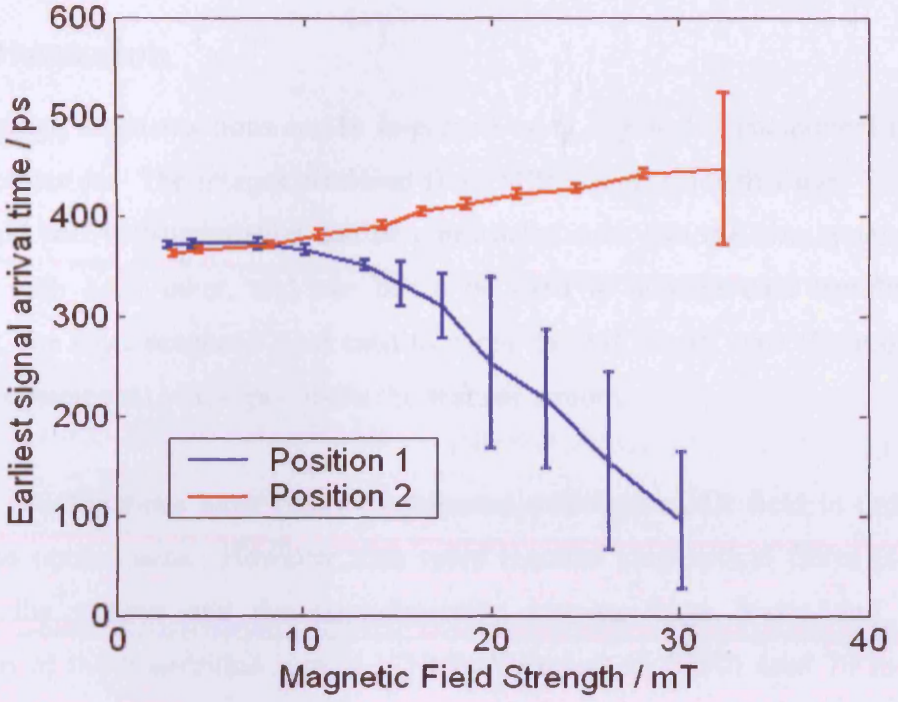

Figure 4-14 Graph of the time of earliest photon arrival time against magnetic field strength in TPSFs recorded for 780 nm.

PMT timing characteristics are given in terms of electron transit time (ETT) and transit time spread (TTS). Changes in ETT can be inferred from changes in the earliest signal arrival time in recorded TPSFs. The point of earliest signal is taken as the time for the signal to rise to ten times background. The earliest signal arrival times for TPSFs recorded at 780 nm are plotted in Figure 4-14 against field strength. For position 1 the earliest arrival shifts ~290 ps earlier for the highest magnetic field relative to that for the lowest field. In contrast, the earliest signal in position 2 arrives ~80 ps later for the second highest field than for the lowest case.

The full-width half-maxima (FWHM) of TPSFs can be used to measure changes in TTS of the PMTs. TPSF width is a sum of the broadening of the optical pulse due to system components. Any change in FWHM must be due to changes in PMT impulse response, and hence TTS. The FWHM measurements for PMT positions 1 and 2 are shown in Figure 4-13 Magnetic fields up to 20 mT do not cause significant changes in FWHM, but TPSFs at 30 mT are half the width of those outside the field for position 1.

4.4.4 Discussion

Optical image reconstructions can be improved using segmented anatomical images as prior information. The images produced from MRI are ideal for this use. In addition, optical and MR instrumentation can be constructed such that the two systems do not interfere with each other, and can hence be used to acquire data simultaneously. However, the large magnetic field used to excite the MR signal typically requires any powered equipment to be kept outside the scanner's room.

Previous investigations have kept all equipment outside the MR field in order not to distort the optical data. However, this setup requires long optical fibres to be used between the subject and the photodetectors, causing large losses and temporal dispersion of the transmitted signals. (Ntziachristos et al. 2000) used 10 m stepped-index fibre-bundles to place the NIR imager outside the field of the MR. The original laser pulses had a FWHM of 50 ps, with the electronics adding 40 ps, and the TTS of their MCPs was 100 ps. The fibres added another 200 ps. This was reduced to 100 ps using focussing optics.

The dispersion caused by extending the fibres is undesirable, as it introduces an added uncertainty to meantime measurements. On the other hand, performing combined MR/optical imaging whilst keeping the fibre length short requires placing the system in the magnetic field of the MRI scanner. Most MONSTIR components have magnetic immunities of ~1 mT, and hence MONSTIR could be situated inside the MRI room, though much care would have to be taken to ensure no damage occurred to either system. The PMTs could be placed closer to the patient to further minimise distortion, but they are susceptible to magnetic interference as the electron trajectories could be deviated by the magnetic field whilst passing between photocathode and anode.

The H5783 was chosen to be a good representative for the MCP-PMTs due to its metal channel dynode construction, which gives it a sufficient temporal resolution for time-resolved imaging and has some magnetic immunity (~5 mT). It was also small enough to place into the MRI field without safety concerns.

In position 1 the magnetic field was parallel to the main direction of travel of the electrons through the dynodes, see Figure 4-15. Electron travel parallel to this field is unaffected, but travel perpendicular would be severely affected. As the field increased from 0 to 30 mT, intensity dropped to ~0.1 % of its original value, meantime was reduced by ~200 ps, and ETT dropped by ~300 ps. TTS changed insignificantly up to 20 mT. This indicates that electrons were being focussed through the dynodes, reducing the length of the path but also reducing the effective area, and hence efficiency, of the secondary dynodes. This would lead to faster transit times, hence the lower ETT and meantime, but causing saturation of the dynode plates, reducing secondary emission and therefore the output pulse height. This would cause fewer pulses to reach the CFD cut-off limit, and resulting in the drop in intensity.

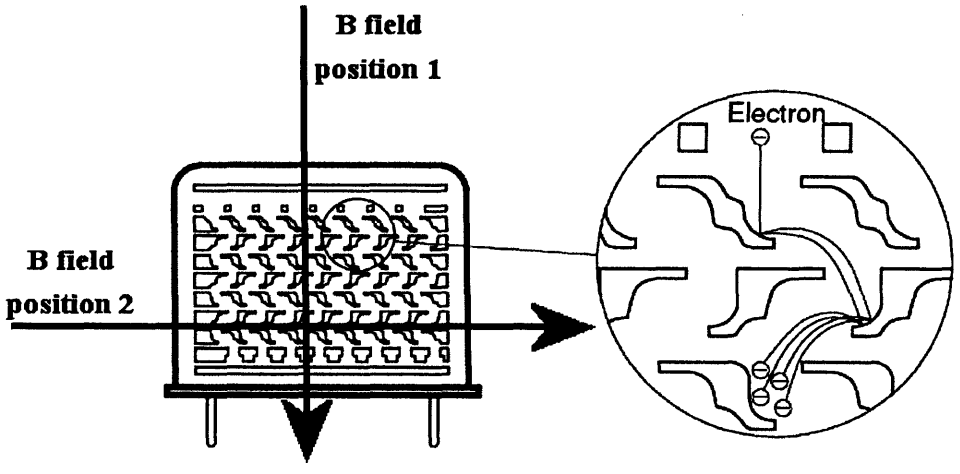

Figure 4-15 Diagram of the field directions relative to the dynode construction for positions 1 and 2.

For position 2, the field is perpendicular to all electron trajectories through the dynodes. In this case, the intensity dropped to ~1 % of its original value, meantime increased by ~50 ps, and ETT increase by ~100 ps. TTS changed insignificantly up to almost 30 mT. From the TPSFs shown in Figure 4-10 (lower plots) the changes in meantime, TTS, and ETT can all be explained by the drop in intensity. A field perpendicular to the main axis of electron travel would cause more electrons to be deviated from their paths. In the case of the metal-channel PMT, this would simply reduce the output pulse height, due to the reduction in number of electrons reaching the PMT anode.

Measurements were performed during MR acquisition to check any effects of the gradient fields on the TPSFs. Similar errors to the static field were produced, indicating the gradient fields inside the scanner do not affect the field outside. The results reported above would therefore be valid for simultaneous MRI / NIR acquisition. Optical fibre holders (§2.2.5) could be redesigned to fit the MRI bore and display high MR contrast, allowing them to be automatically identified for image registration.

The MCP-PMTs currently used in MONSTIR (§2.2.5) have higher magnetic immunities than the metal-package PMT used in this experiment, due to the higher constraints placed on the electron trajectories. The expected response of the MCP-PMTs to an external magnetic field is provided by Hamamatsu, and is shown in Figure 4-6 for both orientations of the tube axis to the magnetic field. By comparison to Figure 4-11 it is clear the MCP-PMTs have far greater magnetic immunity than the metal-channel PMT used in this investigation.

MONSTIR could be positioned 2.5 m to the side of the MRI scanner, experiencing less than 0.5 mT, and causing the electronics no adverse effects. The tubes themselves could be placed much closer to reduce fibre length, reducing additional dispersions.

4.4.5 Conclusion

Anatomical images from structural imaging modalities, e.g. MRI, can be segmented and included as *a priori* (§2.3.3.6) information in optical reconstructions. Simultaneous MR/optical acquisition presents a number of instrumentation issues, mostly due to the large magnetic field. A metal-package PMT with a metal channel dynode construction was chosen to test the effect of magnetic fields on time-resolved data. The effect of the field on the data is dependent on the relative orientation of the PMT body to the magnetic field, but both cases tested found data to be distorted above roughly 5 mT. This confirms the manufacturers quoted magnetic immunity for a metal channel dynode design.

The main rack of MONSTIR could be placed inside the MR suite against a wall with significant effect on MONSTIR's components or MR imaging. The detectors that have been purchased to replace the aging MCP-PMTs, (§3.4.2.1) have metal channel dynodes, the same as used in this investigation, and will hence have similar responses to a magnetic field. An overall magnetic immunity for the system of 1 mT should be observed for all future tests.

This investigation has resulted in a few design criteria for the optical instrumentation used in combined optical-MR imaging:

- All power supplies, transformers, and computers should be positioned outside the MR suite, in order that no distortion of the magnetic field takes place.
- Fibre lengths should be kept to a minimum by constructing a small rack containing the laser and source switches, to be positioned in the MR suite outside the 1 mT field.
- Detectors should be positioned as close to the subject as the detector will tolerate. This further reduces fibre lengths by extending electronic signal cabling, which is unaffected by a magnetic field.
- Either microchannel plate or metal channel detectors should be used.:
    - If a combined optical/MR system was to be constructed from scratch, microchannel plate detectors would ideally be used. MCP-PMTs have a quoted magnet immunity of 1.5 T. Figure 4-6 would indicate that distortion of time-resolved data would occur earlier at 0.5 T, but this reduced immunity would still allow the MCPs to be placed within a meter of the centre of the MR field.
    - For an optical instrument that could be used with MRI when needed, metal-package PMTs would be preferable. The magnetic immunity is sufficient for the PMTs to be placed close to the MR system, and the timing characteristics are suitable for time-resolved data. In addition, metal-package metal channel PMTs, such as the H5783 used here or the new H8224P chosen for MONSTIR, are small and contain individual cooling units, making them far more flexible than MCP-PMTs.

5 Improvements to imaging

5.1 Introduction

The main aim of this work has been to acquire datasets with the highest accuracy and within the shortest possible time, in order to image haemodynamic responses in the neonatal brain during evoked responses. In order for this to be achieved, the capabilities and setup for optimum performance must be quantified. Accuracy and changes in accuracy with imaging time are the most important of these. This chapter describes experiments performed on plastic phantoms to quantify the performance of the new MONSTIR system, including new electronics and instrument for measuring laser power as described in §3.

5.1.1 Background

Investigations into data accuracy of the original MONSTIR-03 system (§2.2.5) were initially reported by (Schmidt 1999), but have more recently been compared to the HUT frequency-domain system as published in (Nissilä 2006) (§2.2.6.2). The most recent results are given in §3.3 as preliminary work for the new instrumentation.

This chapter quantifies MONSTIR's performance in three areas: accuracy, acquisition speed and imaging speed. Accuracy is defined in this context as the error in repeated acquisitions on a fixed, homogenous subject. Intensity errors are presented as the standard deviation percentage of the mean, and meantime error refers to the standard deviation of measurements. It could be expected that as the acquisition time per source increases, signal to noise increases, and accuracy improves. However, due to temporal instabilities in various components of MONSTIR, e.g. detector gain drift, there is an ideal acquisition time at which repeated measurements are most accurate. Imaging speed includes channel switching and data upload delays, but more importantly identifies the minimum acquisition time at which differences between active and resting states can be accurately measured. In this chapter, acquisition time will refer to the time during which tissue is illuminated for a single source, whereas imaging time is the total time for a full 32-channel dataset.

MONSTIR has 32 detector channels which run in parallel so that only the sources need to be multiplexed. The imaging time equals the acquisition time per source plus the time required switching between sources, multiplied by the total number of source positions. The operations required during the switching period are:

- moving the variable optical attenuators (VOAs, §3.5.2) to the positions dictated by a pre-determined setup file (see appendix B),
- advancing the fibre switch,
- reading out the data from the timing electronics (§3.4), as well as resetting them in preparation for the next acquisition,
- some basic processing of the raw data.

The data, temporal point spread functions (TPSFs, §2.2.3), are saved to disk as binary files while the next acquisition is being performed with both new and original systems.

MONSTIR-03 took roughly 12 s to switch between sources and upload and process the data for a single acquisition. Each VOA was moved individually, waiting for each to reach the correct position before sending the command to move the next. This took roughly 100 ms per VOA. Source switching took 50 ms, but an additional delay of 500 ms was needed to ensure the shutters were correctly positioned. Uploading data from each channel took 250 ms, but processing was completed simultaneously. A timing diagram for the original system is given in the lower plot of Figure 5-1

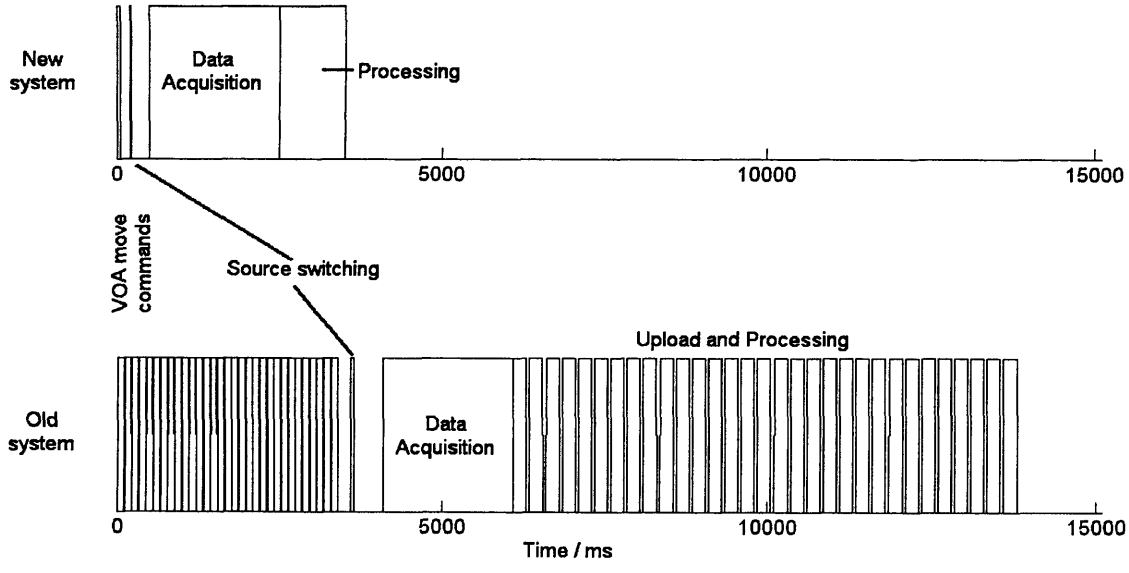

Figure 5-1 Timing diagrams for the process used to acquire data on each channels with new and original MONSTIR systems. A two-second acquisition is shown as an example.

The new system executes all VOA move command simultaneously, followed by a source switch. A delay of 300 ms allows any movement to finish before acquisition starts. Processing at the end of the acquisition takes roughly 1 s after acquisition has finished. Therefore the total time added to the acquisition for each channel is roughly 1.5 s.

Collection efficiency can be defined as the percentage of the sum of acquisition times for all 32 channels divided by the total imaging time. The initial experiments (Schmidt 1999) with the original electronics (EG&G 9308, Ortec, USA, §3.4.2.2) suggested that reasonable photon statistics were obtainable from acquisitions of ~15 s per source. Combined with a source switching speed of 12 s this corresponded to a total acquisition time for a complete 32-channel scan of approximately 14 minutes. Using these numbers, the original system has a collection efficiency of ~55 %. The new electronics (SPC 134, Becker & Hickl, Germany) has eliminated most of the delay between sources. The new switching time of 1.5 s means the same efficiency can be obtained using an acquisition time of 1.8 s. The resulting imaging time would be less than two minutes.

5.2 System Performance

5.2.1 Method

System accuracy and speed were quantified using a pair of tissue-equivalent phantoms. Both phantoms were made from a mixture of titanium dioxide particles and NIR absorbing dye within epoxy resin (Firbank et al. 1995), and each has optical properties of $\mu_s' = 1.0\ mm^{-1}$ and $\mu_a = 0.01\ mm^{-1}$ at a nominal wavelength of 800 nm. The refractive index at 800 nm is n = 1.56 and the anisotropy factor is approximately g = 0.5 (§2.1.1). Due to uncertainties involved in the process of manufacture, the nominal optical properties of the phantoms are correct within 3 %. The phantoms were also checked for gas bubbles using x-rays, which were found not to be present.

The first phantom is homogenous, with a diameter of 69.2 mm and a height of 110 mm. This phantom was used in the first two experiments for testing repeated accuracy and acquisition speed. The second phantom, used for testing imaging speed, took the form of a hollow cylindrical phantom, with diameter 70.0 mm, height 140 mm, and wall-thickness 5.0 mm. The phantom was filled with a liquid resin, also with optical properties of $\mu_s' = 1.0\ mm^{-1}$ and $\mu_a = 0.01\ mm^{-1}$, to produce a homogenous cylinder. Two inclusions could then be introduced and removed in order to collect difference data and produce images. The inclusions had three times the absorption coefficient of the background but an equal scatter coefficient, and measured 10.0 mm and 17.0 mm respectively in both diameter and height. A diagram of the setup for the second phantom is given in Figure 5-2.

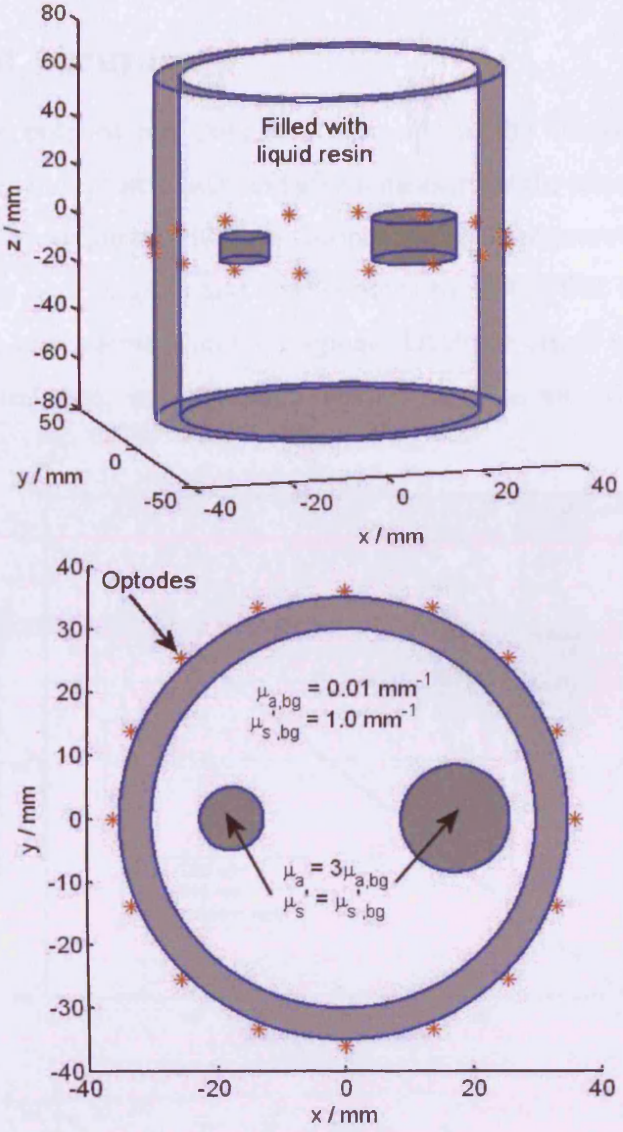

Figure 5-2 Diagrams of the setup for imaging speed experiments. Datasets using 16 channels were acquired for both reference and with two inclusions inserted as shown. The optodes were positioned around the circumference of the central plane as shown.

5.2.2 Repeated Accuracy

One ring of sixteen optodes was coupled to the side of the homogenous phantom to investigate the errors in repeated data, and give a measure of the accuracy of the system. Ten full datasets were acquired with five seconds of data per source. This experiment was performed with both original and new systems to ensure that the accuracy of the new system was an improvement on the original. Datatype errors were produced from the raw, uncalibrated data, as calibration simply removes an offset value from all measurements (§2.3.1.2).

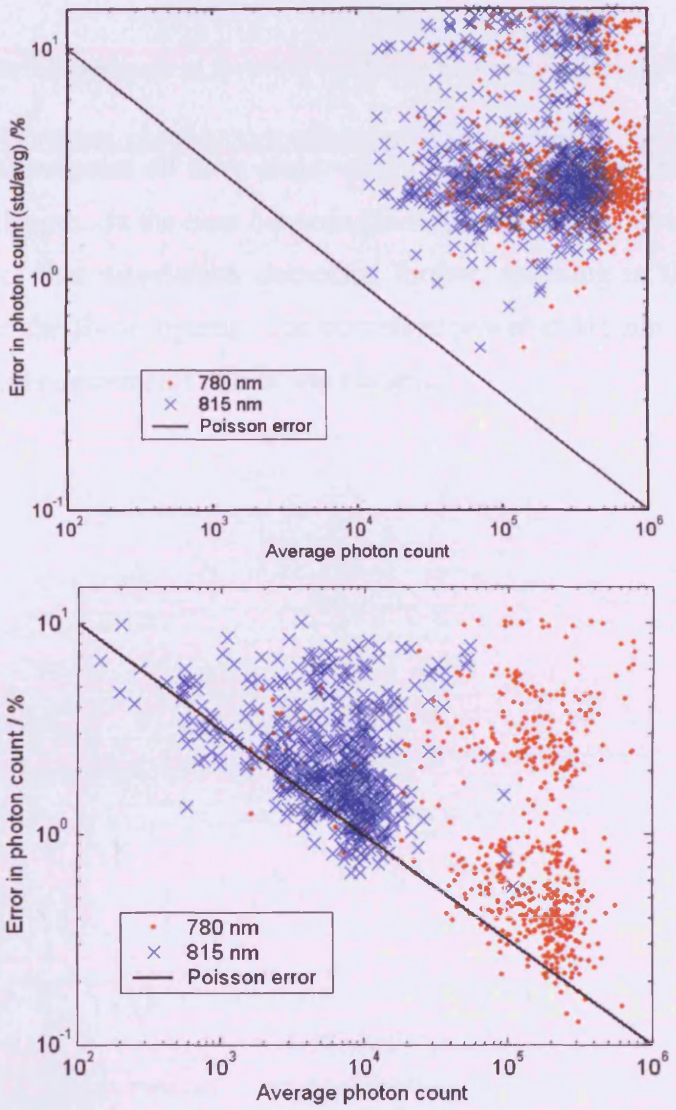

Figure 5-3 Intensity error, expressed as a normalised standard deviation, vs. mean intensity from repeated 5 s measurements on a cylindrical homogenous phantom. Results from the original system are shown in the upper graph, the new system results in the lower. Poisson error (§3.3.3.1) is given for comparison.

Figure 5-3 shows the average photon count versus standard deviation in intensity, expressed as a percentage of the mean, and Figure 5-4 shows average meantime against standard deviation, with results for the original system shown in the upper graphs and the new system in the lower ones. Each point in the plots represents the average and error for a single source-detector pair. Laser power variations were removed from the new dataset before processing (§3.5.1). The results are summarised in Table 5-1

Datatype error	**Original system**		**New system**	
	780 nm	**815 nm**	**780 nm**	**815 nm**
Intensity / %	6.55	7.04	1.86	2.54
Meantime / ps	18.3	20.8	5.2	22.6

Table 5-1 Summary of accuracy results for new and original systems.

The 815 nm measurements all have larger errors due to the lower power of the fibre laser at that wavelength. In the time between the original and new systems being tested, the laser power of that wavelength decreased further, resulting in the differences in count rates seen in the above figures. The decreased power at 815 nm also increases the error in meantime measurements at that wavelength.

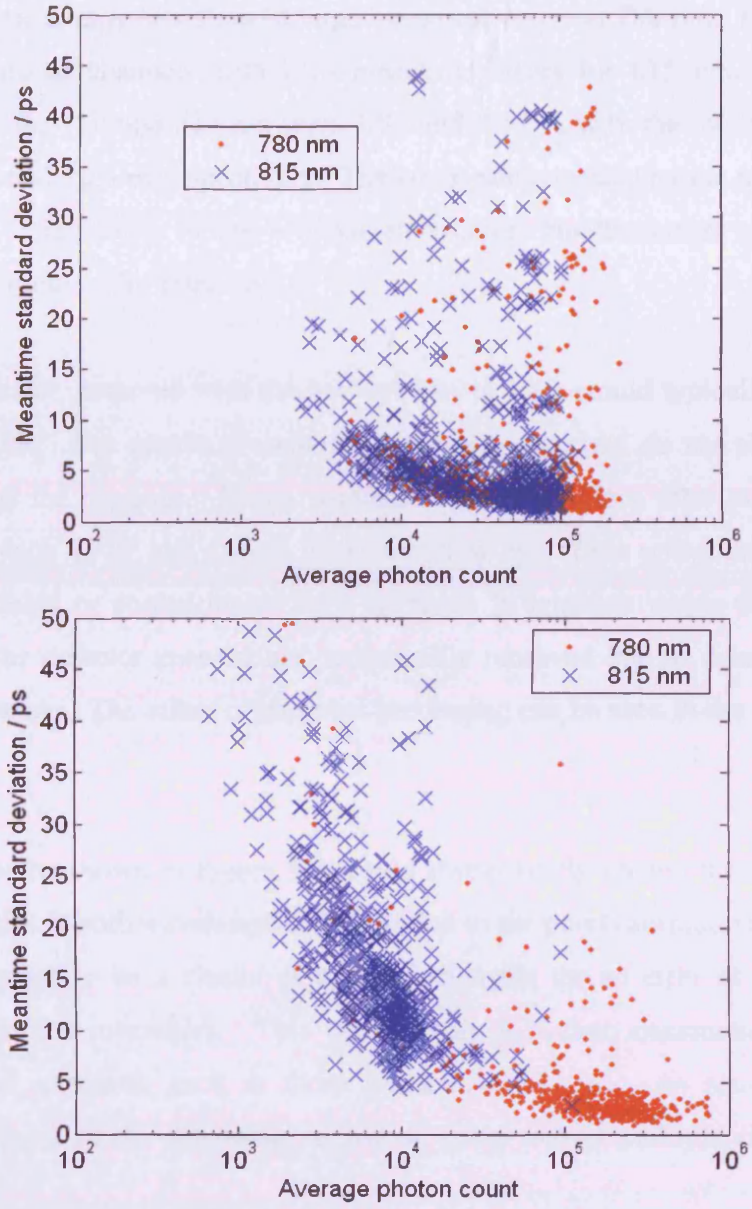

Figure 5-4 Meantime errors vs. mean intensity from repeated 5 s measurements on a cylindrical homogenous phantom. Results from the original system are shown in the upper graph, the new system results in the lower.

The original system recorded roughly 100 data points that do not fit within the displayed limits in Figure 5-3 and Figure 5-4 due to excessive errors, 50 source-detector pairs at each wavelength. However, only half of the channels with excessive intensity errors correlate with those with large meantime errors. Averaged over all data, the intensity errors were 6.55 and 7.04 % with the meantime standard deviations of 18.3 and 20.8 ps for 780 and 815 nm respectively.

Only 10 data points recorded with the new system were outside the displayed intensity error, and the same channels showed large meantime errors at 780 nm. However, there were 20 additional channels with high meantime errors for 815 nm. The average intensity error for 780 and 815 nm were 1.86 and 2.54 % with the meantime standard deviations 5.2 and 22.6 ps respectively. The count rate recorded by the new electronics is reduced in comparison to the original electronics, but the errors are similar for meantime and reduced for intensity.

The 780 nm result, acquired with the new system, is what would typically be expected from MONSTIR. The results presented are for raw data, and do not show results as would be used for imaging. Image reconstruction takes place after post-processing, during which each TPSF and dataset is examined by eye. Data points are eliminated if the TPSF is noisy or contaminated with artefacts. In addition whole datasets from a single source or detector channel are occasionally removed due to detector or source switch malfunction. The effect of this post-processing can be seen in the data presented in §3.3.

Ideally, the results shown in Figure 5-3 would scatter solely around the line shown for Poisson statistics at both wavelengths. In addition to the points surrounding the Poisson line, there appears to be a cluster at both wavelengths for an error of a few percent across all recorded intensities. This could imply a further systematic error source common to all channels, such as those listed in Table 3-1. As also suggested in §3.4.2.1, the most likely remaining source of errors across multiple channels is the detectors.

5.2.3 Acquisition Speed

The TPSFs recorded by MONSTIR are histograms of the flight times of photons arriving over the course of the acquisition time (§2.2.3). Efficient operation and clinical requirements, e.g. space and time costs, dictate that the shortest acquisition time consistent with acceptable signal to noise ratio (SNR) should be used. In addition, the shorter the acquisition time, the more suitable for imaging functional changes. Ideally, meantimes and count rate would be independent of acquisition time, but in practice shorter acquisitions will be affected more by statistical and background noise.

The experimental setup for the repeated accuracy (above) was used to test the accuracy at decreasing acquisition times. Ten full datasets were acquired on the homogenous phantom with the new system, using acquisition time of 30, 10, 3, 1, 0.3, and 0.1 seconds. Datatypes were calculated from the raw TPSFs to show the change in errors. In order to better approximate typical post-processing, as mentioned at the end of the previous section, data were viewed for 30 s acquisitions and source-detector pairs that recorded poor quality TPSFs were removed. Poor quality TPSFs are those with pre-peaks or low signal strength, demonstrating suboptimal coupling, or those recorded by detector channels that are known to be faulty. The remaining pairs were then used for all datasets.

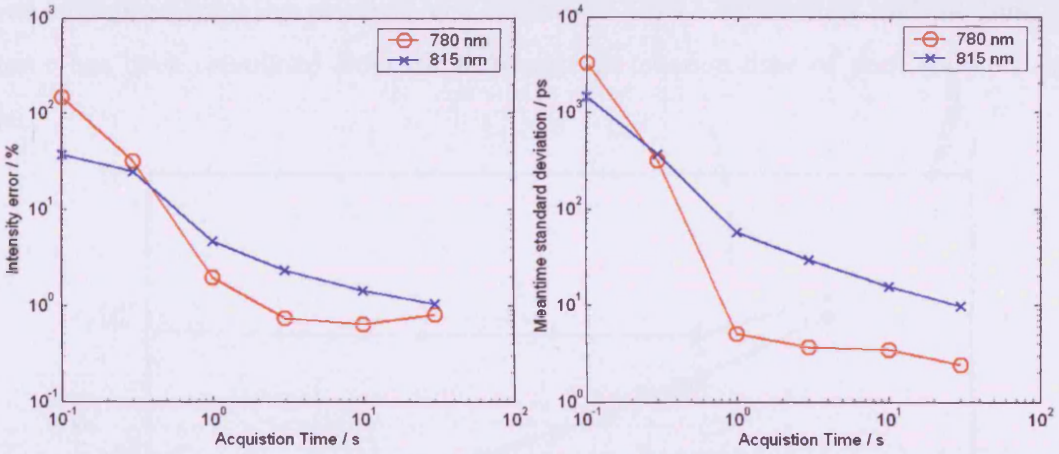

Figure 5-5 Graphs of intensity error (right) and meantime standard deviation (right) versus acquisition time per source, averaged over all channels of data. The intensity error is expressed as the standard deviation percentage of the mean.

The changes in intensity and meantime accuracy with acquisition time are shown in Figure 5-5, and given in detail in Table 5-2. Each point is the average accuracy for the whole system, as it would be during an imaging experiment. The errors for 780 nm for both intensity and meantime are roughly flat in the 3-30 s range, but increase sharply for acquisition times below one second, whilst the errors in data acquired at 815 nm are again elevated due to the lower power of the laser. Equivalent acquisition speed results for the original MONSTIR are in (Nissilä 2006) and (§2.2.6.2).

Acquisition time / s		0.1	0.3	1	3	10	30
Intensity error / %							
	780 nm	147.5	32.0	2.0	0.7	0.6	0.8
	815 nm	36.9	25.1	4.7	2.3	1.4	1.0
Meantime error / ps							
	780 nm	3259.9	319.2	5.0	3.7	3.4	2.4
	815 nm	1458	370.5	56.6	29.7	15.6	9.8

Table 5-2 Data corresponding to Figure 5-5, giving percentage errors in intensity and standard deviations in meantime measurements at various acquisitions times per source

The collection efficiency of the system decreases dramatically as time per source decreases. The changes in imaging time with decreasing acquisition time for each set of electronics is shown in Figure 5-6. In addition, data time for each set of electronics has been calculated from the photon count relative to a 30 s acquisition, and the time per source has been calculated from the difference in creation time of each source's data file.

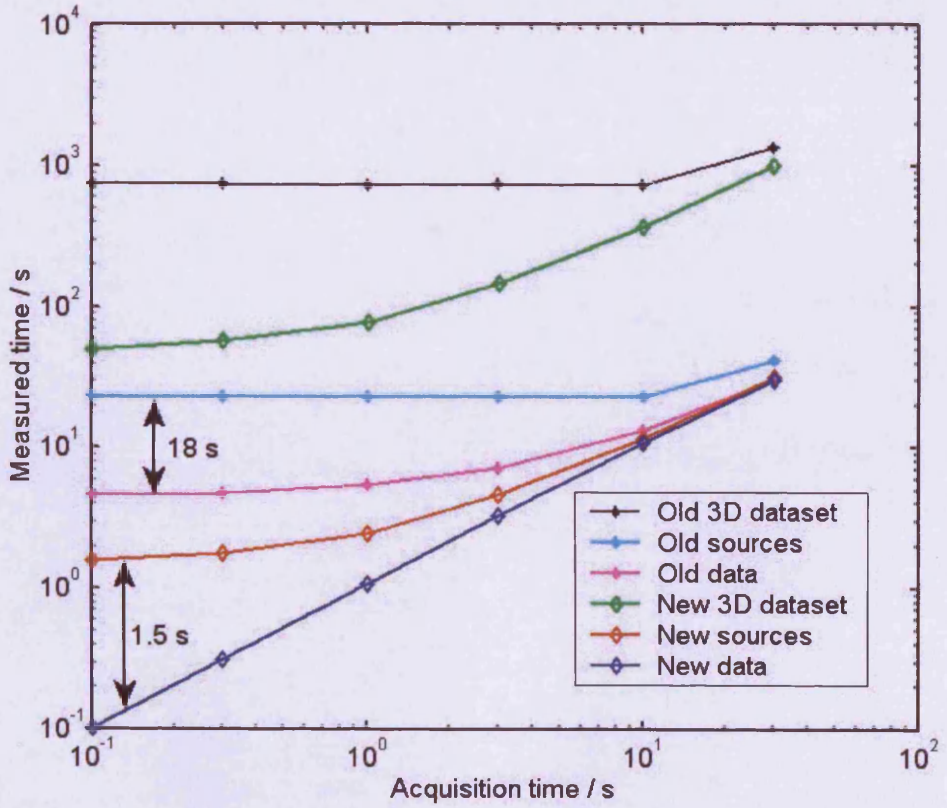

Figure 5-6 Plot of relative acquisition times between the old EG&G and new SPC electronics. The x-axis is the acquisition time as dictated by the operator, the y-axis is the time as measured in three different ways: 1) Data time – time as calculated from the intensity measurement, 2) Source time – time between sources, and 3) Dataset time – the time taken for a full 32 channel 3D dataset. The time added by each system to switch sources is indicated on the graph. 1.5 s for the new system and ~18 s for the original.

The original system appears to have a minimum acquisition time of about 3 s per source, as calculated from the recorded intensities, shown as the cyan line in Figure 5-6. This is independent of the acquisition time input by the user, and is felt to be due to the slow response speed of the original electronic units. In addition, the time between sources seems to extend as the acquisition time reduces, resulting in each data file being written roughly every 20 s, irrespective of acquisition time.

Acquisitions of less than a few seconds are also dominated by source-switching and data storage for the new SPC (§3.4) electronics. However, the number of photons correlates with the acquisition time entered by the user. The source switch and shutter units responds to digital inputs within a few ~10 ms. However, the VOAs require roughly half a second per acquisition step to ensure the correct attenuation is provided, and processing takes roughly a second at the end of acquisition. Acquisitions shorter than one second are therefore inefficient.

5.2.4 Imaging speed

The imaging capability of the new MONSTIR was tested against decreasing acquisition time using the hollow phantom and two small inclusions. The scatter coefficients of the inclusions were kept constant, and the absorption coefficients increased to simulate functional images, as variations in blood oxygenation or concentration mainly affect absorption.

Ten repeated datasets were acquired for a homogenous liquid-filled reference and again after two small inclusions were introduced into the resin. This procedure was repeated for 30, 10, 3, 1, 0.3, and 0.1 second acquisition times per source. 16 optodes were coupled around the phantom in the central plane of the phantom as the inclusions, as illustrated in Figure 5-2.

Images were created using a linear reconstruction algorithm (§2.3.3.3) written in MatLab (Mathworks, USA) by Dr. Adam Gibson. This reconstruction method has been used in order that the mesh, Jacobian, and associated image regularisation can all kept constant for all acquisition times, reducing variations introduced in reconstruction.

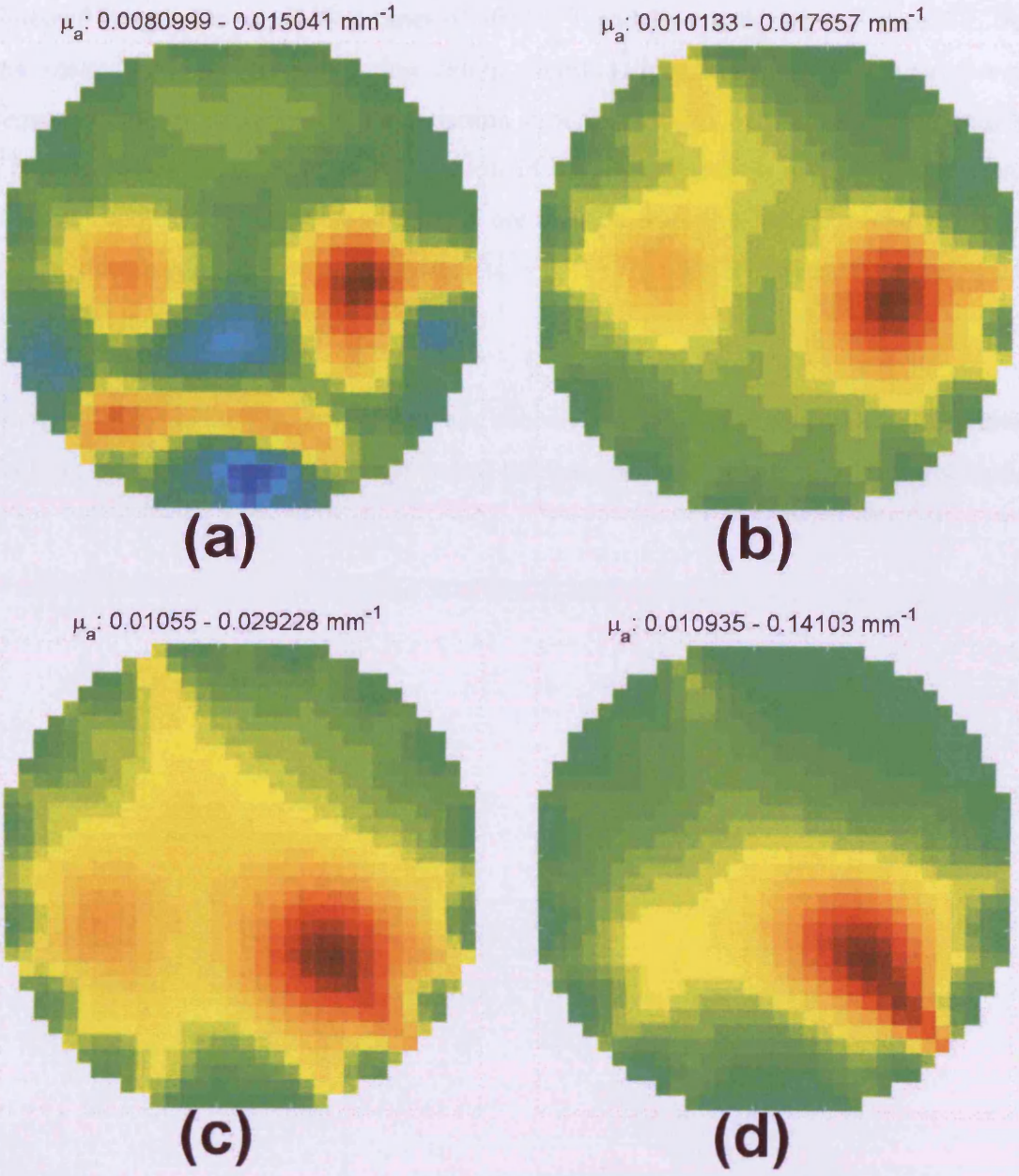

Figure 5-7 Selected images produced from calibrated reference and datasets for (a) 30 s, (b) 10 s, (c) 3 s, (d) 1 s, with associated absorption coefficient ranges. All images were reconstructed from 780 nm data only. No images could be reconstructed from data with acquisition times less than 1 second.

Selected images for acquisition times of 30, 10, 3, and 1 s are shown in Figure 5-7. All ten images for each acquisition time can be found in Appendix C. The inclusions were removed and replaced for each acquisition time in order to record reference datasets. There is therefore an associated variation in the exact location of the inclusions for different acquisition times. The images are created from the inclusion and reference data with a fixed time between the datasets, e.g. the first dataset is taken with reference to the first homogenous dataset etc.

Images for acquisition times less than one second could not be produced from calibrated data, as the signal to noise ratio was below the limit needed for accurate deconvolution.

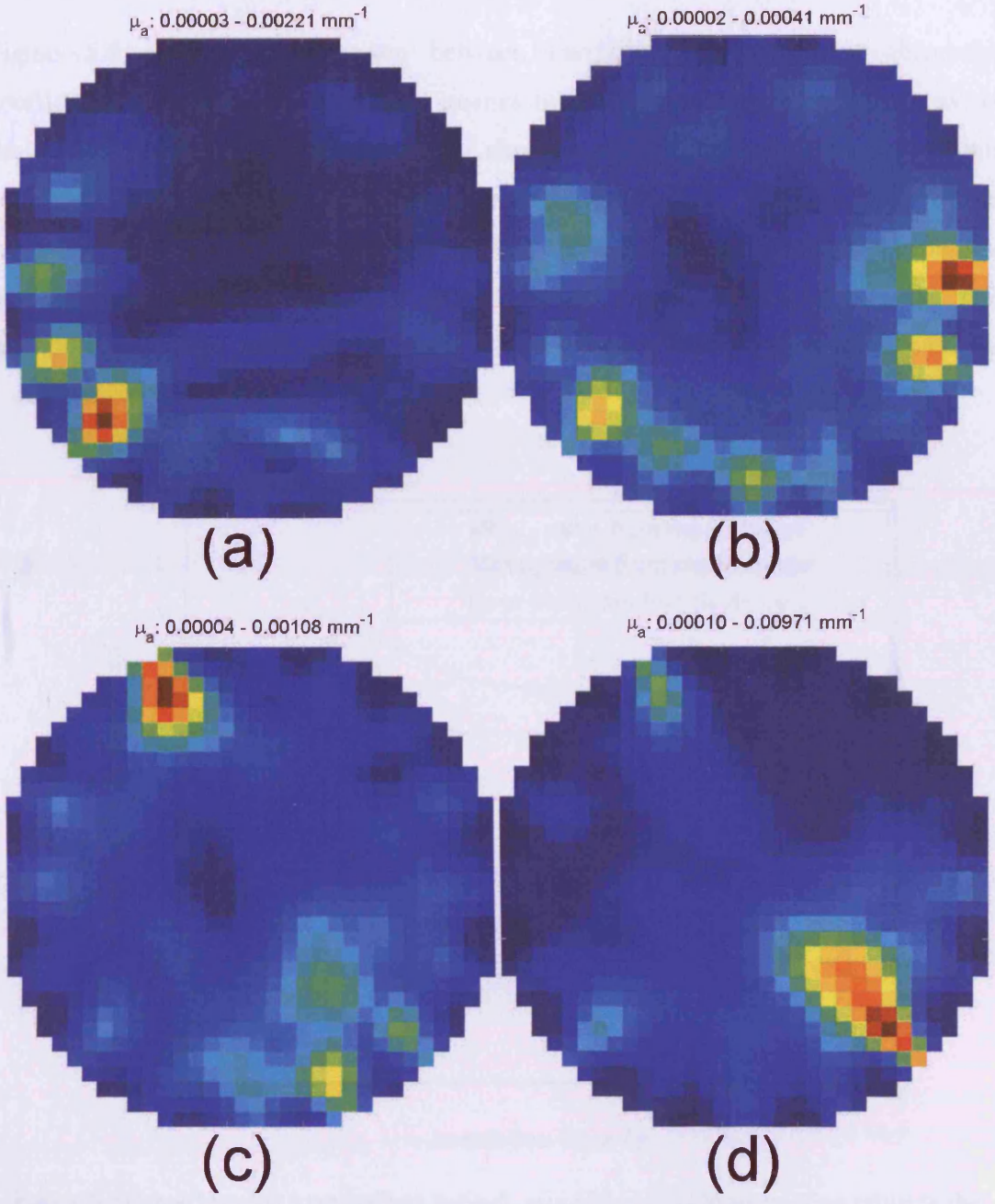

Figure 5-8 Standard deviation ranges and images produced from ten images reconstructed from data acquired for (a) 30 s, (b) 10 s, (c) 3 s, (d) 1 s. The images have been rescaled for display purposes. The data for the images can be found in Table 5-3.

Data from the repeated images can be combined to produce image statistics. The standard deviations of the absorption coefficient of each pixel displayed in the images can be calculated, giving a measure of the error in the images produced. Images of the standard deviation data for 30-1 s are given in Figure 5-8. Bright areas near the edges of the image could indicate temporal instabilities in specific detector channels over the time period between the data and reference acquisitions.

Figure 5-9 shows a comparison between maximum and minimum absorption coefficients as produced in the mean images for each acquisition time, shown as the dashed and dotted lines respectively. The correct range for the images is a lower limit, equal to the background, of 0.01 mm^{-1} and an upper limit, the absorption of the inclusions, of 0.03 mm^{-1}. An average was also taken over all the pixels in the standard deviation image to measure the error between images for a single acquisition time. This data is plotted as the solid line in Figure 5-9. Average images for all acquisition times are also given in Appendix C.

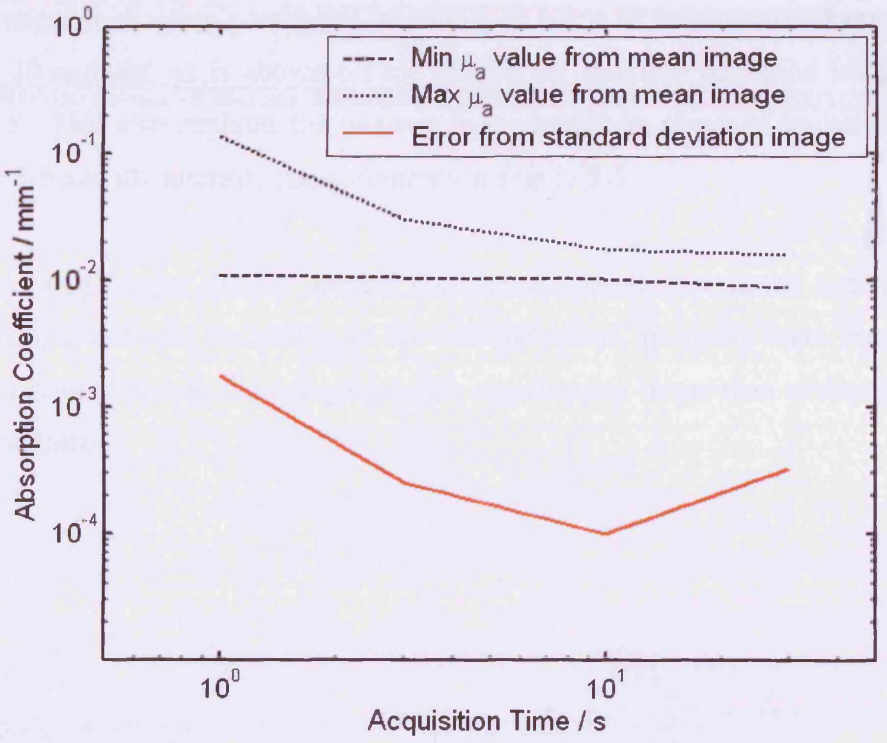

Figure 5-9 Graph showing a comparison between acquisition times in terms of μa values in the resulting images. Shown on a log scale to include all values.

Acquisition time / s	1	3	10	30
Maximum μ_a / mm^{-1}	0.141	0.029	0.018	0.015
Minimum μ_a / mm^{-1}	0.011	0.011	0.010	0.008
Average μ_a / mm^{-1}	0.036	0.016	0.012	0.011
Standard deviation μ_a / mm^{-1}	0.0017	0.0002	0.0001	0.0003

Table 5-3 Data from repeated images reconstructed from various acquisition times. The ideal values for maximum and minimum are $\mu_{a,max} \approx 0.03$ mm^{-1} and $\mu_{a,min} \approx 0.01$ mm^{-1}. The average value is the average absorption coefficient across all images, and the standard deviation value is taken from the standard deviation image.

The images produced with ten- and three-second acquisition times all show good quantification of the two inclusions. Both also show minor reconstruction artefacts, e.g. the increase in absorption coefficient in the vicinity of each optode, which are slightly more prevalent in the case of the shorter acquisition time. The absorption coefficient range and distribution in the three-second images is closer to the correct values. However, this is possibly due to the closer proximity of the inclusions to the side of the cylinder in the three-second images, which could also explain the large peak μ_a value in the one second acquisitions.

The images reconstructed from data collected for 30 s shows a systematic change across the ten images, indicating a temporal instability in a few of the detector channels of the order of 10 minutes, as is shown on the left of the standard deviation image, (a) in Figure 5-8. This also explains the increase in measurement standard deviation, as seen in Figure 5-9 and the intensity measurements in Figure 5-5.

The one-second images display roughly the correct overall appearance, but are unable to differentiate between the effects of the two inclusions, grouping them into a single area. The errors between the images are also significantly larger than at slightly longer acquisition times.

5.3 Clinical Results

Breast cancer is responsible for nearly a third of cancer cases and one fifth of cancer deaths in women in the UK, which represents about 40,000 cases and ~12,000 deaths each year (Ferlay et al. 2001). Early detection decreases mortality (Tabar et al. 2003), so many countries in the developed world routinely screen for breast cancer. The most commonly used breast imaging tool is x-ray mammography (Blamey et al. 2003). However, x-ray mammography has a number of disadvantages: specificity is poor for some types of tumour, which can lead to unnecessary biopsies; it uses potentially hazardous ionizing radiation; and some women report that the required compression of the breast is painful. Mammography is also less suitable for younger women due to the increased density of the breast tissue. In cases involving younger women ultrasound or magnetic resonance imaging (MRI) is used (Schnall 2000, Pavic DD et al. 2003), although neither of these techniques is suitable for screening asymptomatic women. Therefore a safe and effective imaging technique that can provide a distinction between benign and malignant lesions would be of very considerable benefit.

The use of near infrared (NIR) light to examine the breast has been actively researched since the 1980s, when developments in source, detector, and computing technology made diffuse optical imaging feasible. So-called optical mammography provides discrimination between tissues due to their optical properties, (Peters et al. 1990, Colak et al. 1999, Cerussi et al. 2001). Valuable physiological information can be derived from the optical properties with the identification of healthy and diseased tissue based on images of blood volume and blood oxygen saturation. Many research groups have started clinical evaluation of optical systems, using various measurements techniques and wavelengths (Pogue et al. 1997, Young et al. 1997, Culver et al. 2003, Grosenick et al. 2004, Pogue et al. 2004, Taroni et al. 2004, Yates et al. 2005, Schmitz et al. 2005)

The resolution achieved by optical mammography is limited, as compared to other imaging modalities. However, optical imaging could be of great benefit when used as a secondary screening tool to add functional information to the structural images already used for diagnosis. The effect would be to reduce the occurrence of false positives and reduce the number of unnecessary invasive surgery.

The new MONSTIR system has been used over the course of the last year by Dr. Louise Enfield, who has been investigating the optical characterisation of breast disease. The setup used for breast imaging with MONSTIR is shown in Figure 5-10. The patient lies with a single breast pendant in a hemispherical cup. Optical fibre positions are distributed over the surface of the cup. A scattering fluid fills the cup to provide optical coupling to the breast.

The improvements to MONSTIR have had little effect on the imaging capability of the system, but the patient contact time has gone down from half an hour to roughly ten minutes. In addition, the setup and calibration time has been halved.

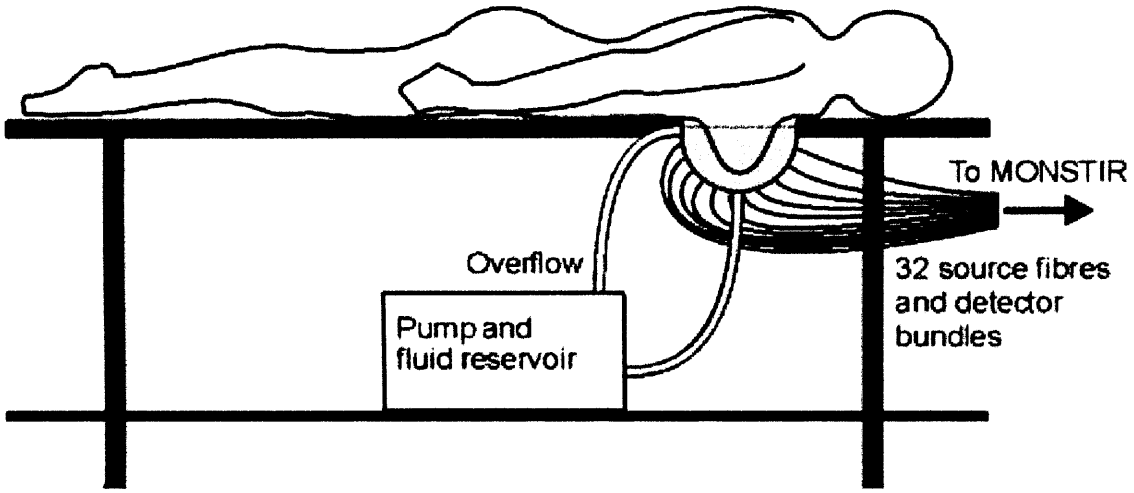

Figure 5-10 The fluid-coupled patient interface for the 3D optical breast imaging. The patient lies with her breast pedant in a hemispherical cup filled with scattering fluid.

Nearly forty patients have been scanned, with a variety of abnormalities, most importantly benign and malignant tumours. Malignant tumours need fuel to grow, so are typically associated with large capillary density. This hypervascularisation provides very high contrast against background breast tissue due to the increased absorption of haemoglobin.

Nineteen women with some form of malignancy in one or both breasts were scanned, with ages in the range 26 to 56 years old. The first three patients were scanned using only one wavelength, due to technical difficulties. Therefore only absorption and scatter images at 780 nm were obtained and it was not possible to derive the blood volume and blood oxygen saturation images. These first optical images are presented in Figure 5-11. The images shown are coronal slices of the 3D image of the breast, through the region with maximum contrast.

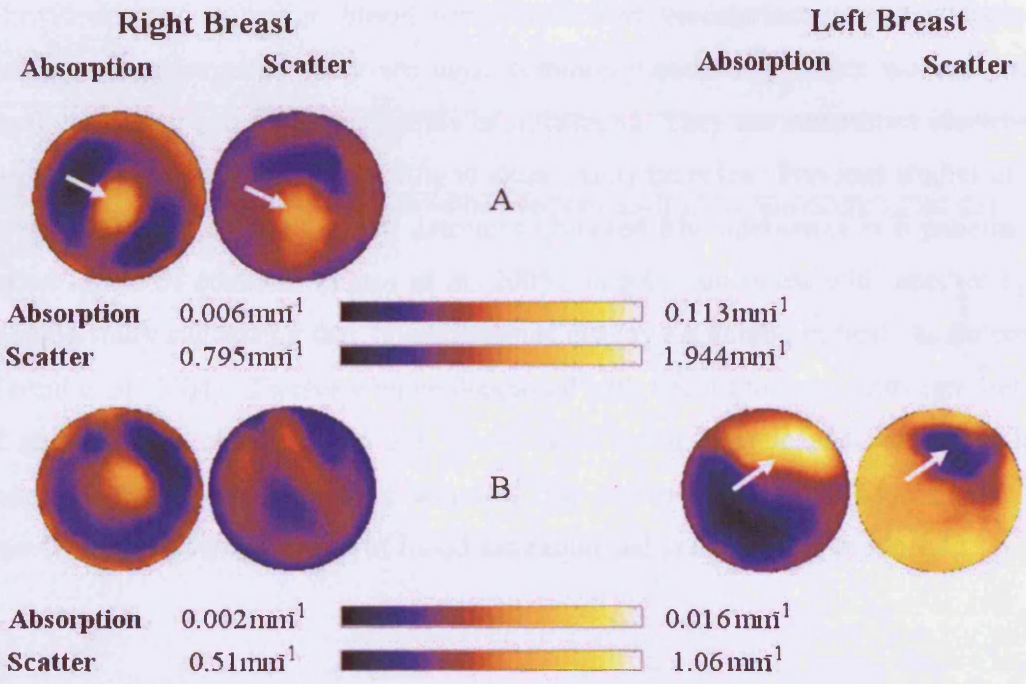

Figure 5-11 Images reconstructed of malignant tumours from data acquired with the new system

(a) Absorption and scatter images from a 53-year-old woman with a large cancer in her right breast behind the nipple

(b) Absorption and scatter images of a 52-year-old woman with breast cancer. MRI showed a distortion in the right breast and increased stroma in the right upper and lower outer quadrants of the breast. In the left breast there is a malignant mass in the left upper outer quadrant.

Figure 5-11 (a) is of 53-year-old women with a large carcinoma behind the nipple of her right breast. The left breast only was scanned due to discomfort of the patient as a result of a bad back. An MRI scan revealed a 4.3 x 5.1 cm high density mass. The absorption image shows a region of increased absorption in the centre of the image consistent with the known position of the mass. The scatter image shows a corresponding region of increased scatter. This increase in scatter may be due to physiological changes in the cancerous cells, or due to parameter crosstalk, i.e. insufficient separation between the absorption and scatter parameters.

The optical images from a 52-year-old woman with bilateral breast cancer are shown in Figure 5-11 (b). MRI images revealed a distortion in the right breast with increased tissue density in the right upper and lower outer quadrants of the breast and a malignant mass in the left upper outer quadrant of the left breast. An increased region of absorption and decreased scatter can be seen in the images of the left breast in the upper outer quadrant. No obvious malignant regions are seen in the right breast.

Fibroadenomas are benign breast lumps with low vascularisation and a distinctive histological appearance. They are most commonly seen in younger women and are usually assessed using mammography or ultrasound. They are sometimes identified as suspicious on mammograms, leading to unnecessary biopsies. Previous studies at UCL using fixed rings of sources and detectors observed fibroadenomas in 6 patients with varied levels of contrast, (Yates et al. 2005), largely consistent with another optical imaging study suggesting that fibroadenomas display no unique optical characteristics, (Taroni et al. 2004). Twelve women diagnosed with fibroadenomas, with ages between 22 and 48 years old (mean 26 ± 6 years), have so far been scanned using the liquid coupled interface. Data were acquired for patients with fibroadenoma at both wavelengths, allowing images of blood saturation and volume to be produced.

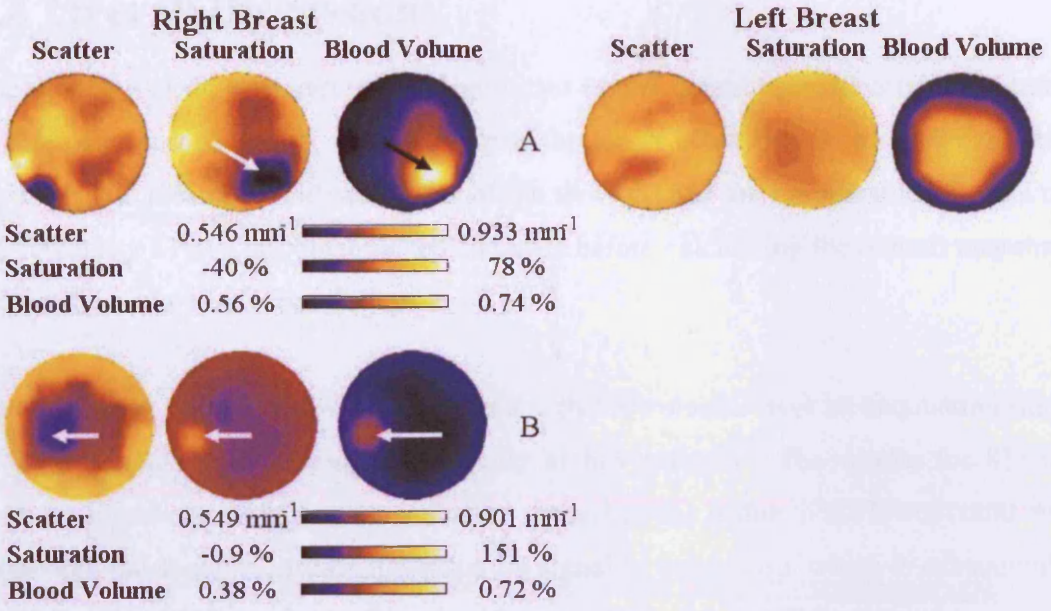

Figure 5-12 Images reconstructed of fibroadenomas from data acquired with the new system:

(a) Images of a 29-year-old, with a fibroadenoma in the lower inner quadrant of her right breast. The ultrasound revealed a lump of 8 x 11 x 5 mm.

(b) Images of a 48-year-old woman with a 11 x 5 x 7 mm fibroadenoma in the upper outer quadrant of her right breast.

Figure 5-12 (a) shows optical images from a 29-year-old, with a fibroadenoma in the lower inner quadrant of her right breast. The ultrasound revealed a 8 x 11 x 5 mm discrete mass. A region of increased blood volume, and decreased oxygen saturation is seen in the images of the right breast.

The optical images in Figure 5-12 (b) are from a 48-year-old woman with a fibroadenoma reported to be in the upper outer quadrant of her right breast. The fibroadenoma measured 11 x 5 x 7 mm size on ultrasound and was positioned 3 cm from the nipple. The optical images show a region of decreased scatter at the expected location, shown with a slightly increased blood oxygen saturation and blood volume.

5.4 Overall Discussion

The accuracy of the new system is a significant improvement over the original in terms of intensity reproducibility. This is despite the lower count rate recorded by the new system. The meantime measurements of the two systems are comparable. Removing the few noisy TPSFs or contaminated channels before calculating the overall meantime error reduces the result from ~20 ps to ~5 ps

The results for 780 nm show accuracy results that are similar over an acquisition range of 1-30 seconds, but increase dramatically at lower times. The results for 815 nm continue improving with longer acquisition times, but this is due to the lower count rate. Extending the acquisition time increases the signal to noise ratio, which is substantially less than that at 780 nm due to the reduced power of the laser at 815 nm.

Clinical images of functional changes needed to be acquired as fast as possible, both to capture the haemodynamic changes, and to ensure system stability between measurements. The time required to acquire a full 3D dataset is dominated by ~12 s switching time for the original system. An acquisition time of 15 s was suggested in (Schmidt 1999), but adequate statistics have been produced from datasets with 10 s acquisitions.

The new system can acquire data accurately at 1 s per source. However, two phantom inclusions could not be reliably identified in images produced from data acquired at that speed. The images produced from 3 s data are blurry, but the inclusions can be differentiated, and the total acquisition time remains relatively low. 10 s images are the best produced in this investigation, but the extra time per source would extend the overall patient contact time, and movement artefacts could become an additional concern. In addition, a delay of roughly 1.5 s is needed to switch between sources, suggesting the acquisition time should be at least this long for efficient operation. An acquisition time of 5 s per source appears to be a fair compromise between accuracy, imaging ability, and patient contact time.

An image can be produced from two datasets: during activity and reference. The decrease in acceptable acquisition time from 10 s to 5 s, and the reduction in source-switching time from 12 s to 1.5 s, has resulted in a reduction in total image time from ~24 to ~7 minutes. The new system can record data required to create an image in less than a third of the time of the original system.

5.5 Conclusion

The new system can acquire data more accurately and faster than the original system. Intensity errors have been reduced without any reduction in temporal accuracy, resulting in the production of accurate datatypes from data acquired at 5 s per source. In combination with the new electronics, this has resulted in an optical imaging system that can record a full 3D dataset in less than 3.5 minutes, a third of the time of MONSTIR-03 for comparable signal to noise.

6 Conclusion

6.1 Conclusion

The aim of this PhD was to build a second-generation optical imaging system to provide the highest data accuracy possible in order that the images produced from data collected in clinical trials will lead to improved diagnosis of infant brain trauma and female breast cancers, and image fast haemodynamic activation in the neonatal brain.

The specification for the second-generation system from the point of view of a clinical user was as follows (§3.2):

Data Accuracy

- Meantime measurements must be accurate to within 5 ps.
- Intensity measurements must be accurate to 5 %.

Clinical Impact

- MONSTIR should be as compact as possible.
- The system should be ready for data acquisition shortly after transport.

Acquisition Time

- Calibration and setup should occur as quickly as possible.
- Datasets need to be acquired in as short a time as possible.

The new MONSTIR system produces measurements for intensity and meantime accurate to 2 % and 5 ps respectively for acquisition times per source greater than 1 s. The overall size of MONSTIR has been halved. The time taken for the system to reach thermal stability after transport has been reduced from >12 hrs to roughly 3 hrs. Source switching time has been reduced from 12 s to 1.5 s, result in faster calibrations. Accurate data can now be produced from 5 s of data per source, and when combined with the reduction in switching time, this results in the collection of full 32-channel datasets within 3.5 minutes, a third of that of the original system. The improvements of the new MONSTIR system in comparison to the original are summarised in Table 6-1.

	Original System	New System
Maximum useful count rate per channel / counts per second	~300,000	~100,000
TPSF Bin-width / ps	5.0	6.1
Time taken to reach thermal stability / hours	>12	< 3
Intensity error due to laser power fluctuations / %	Up to 40	< 2
Number of VOA steps	8	10
VOA maximum attenuation / OD	2.2	3.7
Intensity uncertainty / %	6.55	1.86
Meantime uncertainty / ps	18.3	5.2
Suggested acquisition time per source / s	10	5
Upload delay between sources / s	12	1.5
Total acquisition time for a full 32 channel dataset / min	12	3.5
Physical size (L x W x H) / m	105 x 60 x 152 and 55 x 60 x 117	90 x 49 x 150

Table 6-1 A comparison of the performance of the new MONSTIR system to that of the original. Intensity and meantime errors are given for 780 nm, due to current low power output of 815 nm.

6.2 Future Work

I would identify one specific area where further research in instrumentation would result in significant gains for an optical tomography system like MONSTIR: optical range compression. The maximum count rate of the detectors is ~10^5 and signals with a dynamic range of up to 10^{12} are possible depending on geometry, hence a solution which can provide range compression of at least ~7 OD needs to be found. Such a solution would not only allow absolute calibrations to be recorded during data acquisition, but data could be recorded on all detector channels for every source. Photons detected from channels nearest the source are those with the highest count rates but contain information about the smallest volumes. Topographic reconstructions could be produced from these superficial measurements and added to tomographic reconstructions as *a priori* information, probably constraining the regions in which haemodynamic changes occur. Preferably a solution could be found that is not mechanical, significantly reducing both the setup and switching time currently needed. A number of possible solutions are discussed in (Jennions 2003), but an ideal solution has yet to be found.

More generally, if a further system were to be constructed, I would focus on a system redesign based on matching source, detectors and timing electronics. There have been further thoughts on source selection since the IMRA laser was purchased (§2.2.4.1). It has been suggested that wavelengths other than 780 and 815 nm would improve differentiation between oxy-/deoxy-haemoglobin. In addition, a greater number of wavelengths could be simultaneously acquired. This would allow the resulting images to be registered against one another in order to improve spatial resolution and accuracy, and images of further chromophores could be produced (§2.2.4.1).

Simultaneously acquiring a greater number of wavelengths would have to be balanced against a reduction in the repetition rate of the laser, and hence result in a likely reduction in the maximum data acquisition rate due to pile-up (§2.2.4.5).

Laser diodes can currently produce a few mW in the near-infrared. This is insufficient for use in optical tomography, which requires tens of mW, but difference is being rapidly reduced. Laser diodes of sufficient power output could be mounted directly on the surface of the subject, in pairs if two wavelengths are desired. This will simplify both source wavelengths and control, but also remove the need for switching and source cross-talk. For combined MR/optical imaging, laser diodes are possibly the most suitable source available, as they tend to have very high magnetic immunities.

However, as mentioned previously data recorded with large source-detector separations are of greater import to optical reconstructions. These have reduced count rates due to the attenuation of tissue. Detectors with higher quantum efficiencies (QE) would reduce the large number of counts lost in the conversion from optical to electronic signal by the detectors, increasing the sensitivity of the system to the measurements at larger distances.

Timing electronics could then be selected to ensure the dead time corresponds well with the maximum count rates of the detectors. Any change in source repetition rate would also have to be considered.

Most other problems currently experienced with MONSTIR are due to components not performing to their specification, for example shutters, laser, and detectors. Replacing or servicing these components will solve the associated problems and result in a fully operational system. The majority of these small issues are to be fixed in the near future.

6.3 The Future of Optical Tomography

In the years leading up to the mid-nineties, biomedical optics as a field of applied research flourished. One of the principal goals of biomedical optics, and arguably its most ambitious, was the development of a diagnostic imaging modality based on near-infrared (NIR) radiation. Potentially the most important was the development of a means of screening for breast cancer, particularly if a specificity and sensitivity exceeding that of x-ray mammography could be achieved. Another significant goal was to extend the success of NIR spectroscopy (Jobsis 1977, Cope and Delpy 1988) to develop a cerebral imaging modality for mapping structure and function in newborn infants, with the possibility of imaging adults also. There was also considerable interest in the development of methods to obtain submillimetre resolution images of tissue a few millimetres in thickness (Yadlowsky et al 1995, Bouma et al 1995) or transparent tissues such as the eye (Huang et al 1991).

Since then, the technology used in optical instrumentation has been rapidly catching up with the methods. In the last ten years, imaging systems have become faster, more robust, with reduced susceptibility to error. Moreover, they are now able to acquire data with more source-detector combinations and at more wavelengths. Images are now routinely reconstructed in 3D, which can include prior information and compensate for unavoidable course of measurement error.

Optical imaging is now used routinely in many research establishments to investigate a wide variety of functional studies in neonates and adults. Cerebral mapping of all ages from neonates to adults, with respect to functional studies or oxygen consumption, and investigations into cerebral injury in neonates are all areas for expansion for appropriate types of optical imaging.

For neonatal cerebral imaging, it has been proven that images can be reconstructed from clinical data in agreement with known anatomy and physiology. However, the spatial resolution is relatively poor and reconstruction artefacts still occur. The limiting factor was believed to be the lack of accurate knowledge of the shape of the head and the positions of the optodes upon it. A robust adjustable helmet has been created to hold the connectors in fixed positions, which can be measured more accurately than previously. In addition, a photogrammetric technique is being developed which allows the shape of the head and respective optode positioning to be calculated accurately from multiple photographs. Ultimately, simultaneous optical/MRI imaging will allow the internal and external anatomy to be identified from MRI. Special optode holders can be used to provide contrast in the MR image, and can then be used to align the optical and MR images. This technique allows the optical data to be used for accurate reconstruction of blood volume and oxygenation within a region of interest.

The use of optical tomography as a diagnostic tool has demonstrated significant potential specifically in the field of mammography. A number of companies have been set up for the commercialisation of optical imaging systems based on various methods: continuous wave measurements for a compressed geometry (DOBI Medical International, Inc USA) or for a circular scanning geometry (Imaging Diagnostic Systems, Inc, USA), and time-resolved measurements similar to those acquired by MONSTIR (Advanced Research Technologies, Canada). The main problem still encountered with optical mammography is lack of specificity - the absolute accuracy of the optical properties and the relationship of those to the identification of the respective tissues. This problem will hopefully be resolved in time with larger datasets.

7 References

References

1. AGFA (2003), "Technical Data Sheet, F-AF-E6" *Http://Www Agfa.Com/Photo/Products/Pdf/F-AF-E6_En. Pdf* (6th)

2. American Society for Testing and Materials (ASTM) International (2005), "Designation: F2503-05 - Standard Practice for Marking Medical Devices and Other Items for Safety in the Magnetic Resonance Environment"

3. Arridge S R (1999), "Optical tomography in medical imaging" *Inverse Problems* **15** R41-R93.

4. Arridge S R, M Cope, and D T Delpy (1992), "The theoretical basis for the determination of optical pathlengths in tissue: temporal and frequency analysis" *Phys. Med. Biol.* **37** 1531-1559.

5. Arridge S R and J C Hebden (1997), "Optical imaging in medicine: II. Modelling and reconstruction" *Phys. Med. Biol.* **42**(5) 841-853.

6. Arridge S R and W R B Lionheart (1998), "Nonuniqueness in diffusion-based optical tomography" *Opt. Lett.* **23** 882-884.

7. Arridge S R and M Schweiger (1993), "The use of multiple data types in time-resolved optical absorption and scattering tomography (TOAST)" *Proc. SPIE.* **2035** 218-229.

8. Arridge S R and M Schweiger (1995), "Photon measurement density functions. Part II: Finite element method calculations" *Applied Optics* **34** 8026-8037.

9. Arridge S R, M Schweiger, M Hiraoka, and D T Delpy (1993), "Finite element approach for modelling photon transport in tissue" *Med. Phys.* **20**(2) 299-309.

10. Barbour R L, H L Graber, J Chang, S S Barbour, Koo P.C., and R Aronson (1995), "MRI-guided optical tomography: prospects and computation for a new imaging method" *IEEE Computing in Science and Engineering* **2** 63-

11. Barbour R L, H Graber, Y Pei, S Zhong, and C H Schmitz (2001), "Optical tomographic imaging of dynamic features of dense-scattering media" *J. Opt Soc. Am. A* **18**(12) 3018-3036.

12. Becker W, *Advanced Time-Correlated Single Photon Counting Techniques*, (Springer-Verlag Berlin Heidelberg, 2005).

13. Becker W (2005a), "Routing Modules for Time-Correlated Single Photon Counting" *Http://Www.Becker-Hickl. De/Pdf/Hrt. Pdf*

14. Becker W (2005b), "Time-Correlated Single Photon Counting Modules" *Http://Www.Becker-Hickl. De/Pdf/Spc800ps01. Pdf*

15. Becker W, A Bergmann, A Gibson, N Everdell, D Jennions, M Schweiger, S R Arridge, and J C Hebden (2005), "Multi-dimensional time-correlated single photon counting applied to diffuse optical tomography" *Proc. SPIE.* **5693**

16. Blamey R, A R M Wilson, and J Patnick (2003), "Screening for breast cancer" *British Medical Journal* **689** 693-

17. Brooksby B, H Dehghani, B W Pogue, and K D Paulsen (2003), "Near infrared (NIR) tomography breast image reconstruction with a priori structural information from MRI: algorithm development for reconstructing heterogeneities" *IEEE Quantum Electronics* **9**(2) 199-209.

18. Cerussi A E, A J Berger, F Bevilacqua, N Shah, D Jakubowski, J Butler, R F Holcombe, and B J Tromberg (2001), "Sources of absorption and scattering contrast for near infrared optical mammography" *Acad. Radiol.* **8** 211-218.

19. Chance B, J S Leigh, H Miyake, Smith D S, Nioka S, Greenfield R, Finander M, Kaufmann K, Levy W, Young M, Cohen P, Yoshioka H, and Boretsky R (1988), "Comparison of time-resolved and -unresolved measurements of deoxyhaemoglobin in brain" *Proc. Natl. Acad. Sci. USA* **85** 4971-4975.

20. Chance B, M Cope, E Gratton, N Ramirez, and B J Tromberg (1998), "Phase measurement of light absorption and scatter in human tissue" *Rev. Sci. Instrum.* **69** 3457-3481.

21. Chang J., H L Graber, Koo P.C., R Aronson, S-L S Barbour, and R L Barbour (1997), "Optical imaging of anatomical maps derived from magnetic resonance images using time independent optical sources" *IEEE Trans. Med. Imag.* **16** 68-77.

22. Colak S B, M B van der Mark, G W Hooft, J H Hoogenraad, E S van der Linden, and F A Kuijpers (1999), "Clinical optical tomography and NIR spectroscopy for breast cancer detection" *IEEE Quantum Electronics* **5**(4) 1143-1158.

23. Cope M (1991), "The application of near infrared spectroscopy to non invasive monitoring of cerebral oxygenation in the newborn infant" *University of London* PhD thesis.

24. Culver J P, R Choe, M J Holboke, L Zubkov, T Durduran, A Slemp, V Ntziachristos, B Chance, and A G Yodh (2003), "Three-dimensional diffuse optical tomography in the parallel plane transmission geometry: Evaluation of a hybrid frequency domain/continuous wave clinical system for breast imaging" *Med. Phys.* **30**(2) 235-247.

25. Danen R M, Y Wang, X D Li, W S Thayer, and A G Yodh (1998), "Regional imager for low resolution functional imaging of the brain with diffusing near-infrared light" *Photochem. Photobiol.* **67** 33-40.

26. Dehghani H, B W Pogue, Shudong J, B Brooksby, and K D Paulsen (2003), "Three dimensional optical tomography: Resolution-contrast tradeoff in small object imaging" *Appl. Opt* **42** 3117-3128.

27. Dittmer DA, *Blood and Other Body Fluids*, (Federation of American Societies for Experimental Biology, Washington DC, 1961).

28. Dunn J F, Y Zaim-Wadghiri, B W Pogue, and Kida I (1998), "BOLD vs NIR spectroscopy: Will the best technique come forward?" *Adv. Exp. Med. Biol.* **454** 103-113.

29. Eda H, I Oda, Y Ito, Y Wada, Y Oikawa, Y Tsunazawa, M Takada, Y Tsuchiya, Y Yamashita, M Oda, A Sassaroli, Y Yamada, and M Tamura (1999), "Multichannel time-resolved optical tomographic imaging system" *Rev. Sci. Instrum.* **70**(9) 3595-3602.

30. C. E. Elwell, *A practical users guide to near infrared spectroscopy*, (UCL Reprographics, London, UK, 1995).

31. Everdell N, A P Gibson, I D C Tullis, T Vaithianathan, J Hebden, and D T Delpy (2004), "A frequency multiplexed near infra-red topography system for imaging functional activation in the brain" *OSA Biomedical Topical Meetings, Miami* WF33.

32. Fantini S, S A Walker, M A Franceschini, M Kaschke, P M Schlag, and K T Moesta (1998), "Assessment of the size, position and optical properties of breast tumors in vivo by noninvasive optical methods" *Appl. Opt.* **37**(10) 1982-1989.

33. Farrar T.C., *An introduction to Pulse NMR Spectroscopy*, (Farragut Press, Chicago, 1987).

34. Ferlay J, F Bray, P Pisani, and D M Parkin (2001), "GLOBOCAN 2000: Cancer incidence, mortality and prevalence worldwide, Version 1.0" *IARC CancerBase No 5*

35. Firbank M, M Oda, and D T Delpy (1995), "An improved design for a stable and reproducible phantom material for use in near-infrared spectroscopy and imaging" *Phys. Med. Biol.* **40**(5) 955-961.

36. Franceschini M A and D A Boas (2004), "Noninvasive measurement of neuronal activity with near-infrared optical imaging" *Neuroimage* **21** 372-386.

37. Franceschini M A, S Fantini, J H Thompson, J P Culver, and D A Boas (2003), "Hemodynamic evoked response of the sensorimotor cortex measured noninvasively with near-infrared optical imaging" *Psychophysiology* **40** 548-560.

38. Franceschini M A, K T Moesta, S Fantini, G Gaida, E Gratton, H Jess, W W Mantulin, M Seeber, P M Schlag, and M Kaschke (1997), "Frequency-domain techniques enhance optical mammography: initial clinical results" *Proc. Natl. Acad. Sci. USA* **94** 6468-6473.

39. Franceschini M A, V Toronov, M E Filiaci, E Gratton, and S Fantini (2000), "On-line optical imaging of the human brain with 160 ms temporal resolution" *Optics Express* **6**(3) 49-57.

40. Gao F, Zhao H, and Y Yamada (2002), "Improvement of Image Quality in Diffuse Optical Tomography using Full Time-Resolved Data" *Appl. Opt* **41**(4) 778-791.

41. GE Medical Systems (2005), "GE Signa Excite Pre-Installation guide" *General Electric Company Inc. Documentation*

42. Gerstman I, Thompson CR, S L Jacques, and M Rogers (1995), "Laser-induced bubble formation in the retina" *Proc. SPIE.* **2391** 60-71.

43. Gibson A P, J C Hebden, and S R Arridge (2005a), "Recent advances in diffuse optical imaging" *Phys. Med. Biol.* **50** R1-R43.

44. Gibson A P, J C Hebden, J Riley, N L Everdell, M Schweiger, S R Arridge, and D T Delpy (2005b), "Linear and non-linear reconstruction for optical tomography of phantoms with non-scattering regions" *Applied Optics* (in press)

45. Gibson A P, R M Yusof, H Dehghani, J Riley, N Everdell, R Richards, J C Hebden, M Schweiger, S R Arridge, and D T Delpy (2003), "Optical tomography of a realistic neonatal head phantom" *Appl. Opt.* **42**(16) 3109-3116.

46. Götz L, S H Heywang-Köbrunner, O Schütz, and H Siebold (1998), "Optische mammographie an praoperativen patientinnen" *Akt. Radiol.* **8**(1) 31-33.

47. Grosenick D, K T Moesta, H Wabnitz, J Mucke, C Stroszczynski, Macdonald R, P M Schlag, and H Rinneberg (2003), "Time-domain optical mammography: initial clinical results on detection and characterization of breast tumors" *Applied Optics* **42**(16) 3170-3186.

48. Grosenick D, H Wabnitz, K T Moesta, J Mucke, M Möller, C Stroszczynski, J Stössel, B Wassermann, P M Schlag, and H Rinneberg (2004), "Concentration and oxygen saturation of haemoglobin of 50 breast tumours determined by time-domain optical mammography" *Phys. Med. Biol.* **49** 1165-1181.

49. Grosenick D, H Wabnitz, H H Rinneberg, K T Moesta, and P M Schlag (1999), "Development of a time-domain optical mammography and first in vivo applications" *Appl. Opt.* **38** 2927-2943.

50. J. Hamamatsu, *Photomultiplier Tubes, Basics and Applications*, 2006).

51. Hebden J C, A P Gibson, T Austin, R M Yusof, N Everdell, D T Delpy, S R Arridge, J H Meek, and J S Wyatt (2004), "Imaging changes in blood volume and oxygenation in the newborn infant brain using three-dimensional optical tomography" *Phys. Med. Biol.* **49**(7) 1117-1130.

52. Hebden J C, F E Schmidt, M E Fry, M Schweiger, E M Hillman, and D T Delpy (1998a), "Simultaneous reconstruction of absorption and scatter images by multichannel measurement of purely temporal data" *Optics Letters* **24**(8) 534-536.

53. Hebden J C, T D Yates, A P Gibson, N Everdell, S R Arridge, W Chicken, M Douek, and M R S Keshtgar (2005), "Monitoring recovery following laser surgery of the breast using optical tomography: a case study" *Appl. Opt.* **44**(10) 1898-1904.

54. Hebden J C, S R Arridge, and D T Delpy (1997), "Optical imaging in medicine: I. Experimental techniques" *Phys. Med. Biol.* **42**(5) 825-840.

55. Hebden J C, S R Arridge, and M Schweiger (1998b), "Investigation of alternative data types for time resolved optical tomography" *OSA Technical Digest, Biomedical Topical Meetings (OSA, Washington DC)* **21** 162-167.

56. Hebden J C, A P Gibson, R M Yusof, N Everdell, E M Hillman, D T Delpy, T Austin, J Meek, and J S Wyatt (2002), "Three-dimensional optical tomography of the premature infant brain" *Phys. Med. Biol.* **47** 4155-4166.

57. Hebden J C, F M Gonzalez, A P Gibson, E M Hillman, R M Yusof, N Everdell, D T Delpy, G Zaccanti, and F Martelli (2003), "Assessment of an in situ temporal calibration method for time-resolved optical tomography" *J. Biomed. Opt* **8**(1) 87-92.

58. Hebden J C, H Veenstra, H Dehghani, E M Hillman, M Schweiger, S R Arridge, and D T Delpy (2001), "Three-dimensional time-resolved optical tomography of a conical breast phantom" *Appl. Opt.* **40**(19) 3278-3287.

59. Hill D L, P G Batchelor, M Holden, and D J Hawkes (2001), "Medical image registration" *Phys. Med. Biol.* **46**(3) R1-45.

60. Hillman E M C, J C Hebden, F E W Schmidt, S R Arridge, M Schweiger, H Dehghani, and D T Delpy (2000), "Calibration techniques and datatype extraction for time-resolved optical tomography" *Rev. Sci. Instrum.* **71**(9) 3415-3427.

61. Hillman E M C, J C Hebden, M Schweiger, H Dehghani, F E Schmidt, D T Delpy, and S R Arridge (2001), "Time resolved optical tomography of the human forearm" *Phys. Med. Biol.* **46**(4) 1117-1130.

62. Hintz S R, D A Benaron, J P v Houten, J L Duckworth, F W H Liu, S D Spilman, D K Stevenson, and W-F Cheong (1998), "Stationary headband for clinical time-of-flight optical imaging at the bedside" *Photochem. Photobiol.* **68** 361-369.

63. Hintz S R, D A Benaron, A M Siegel, A Zourabian, D K Stevenson, and D A Boas (2001), "Bedside functional imaging of the premature infant brain during passive motor activation" *J. Perinat. Med.* **29**(4) 335-343.

64. Hornak J.P (2004), "The Basics of MRI" *Center for Imaging Science, Rochester Institute of Technology, Rochester, NY 14623-5604*

65. Hoshi Y, Oda Y, Y Wada, Y Ito, Y Yamashita, M Oda, K Ohta, Y Yamada, and M Tamura (2000), "Visuospatial imagery is a fruitful strategy for the digit span backwards task: a study with near-infrared optical tomography" *Cog Brain Res.* **9** 339-342.

66. Jennions D. K. (2003), Thesis: "Variable Attenuation for Near-Infrared Time-Resolved Tomography", *University College London, Department of Medical Physics and Bioengineering, UK*

67. Jennions D K, A Gibson, N L Everdell, J C Hebden, and W Becker (2006), "Fast Time-Resolved Optical Tomography for 3D Neonatal Functional Imaging (Poster)" *OSA Biomedical Topical Meetings, Miami*

68. Jiang H, N V Iftimia, Y Xu, J A Eggert, L L Fajardo, and K L Klove (2002), "Near-infrared optical imaging of the breast with model-based reconstruction" *Acad. Radiol.* **9** 186-194.

69. Jiang H, K D Paulsen, U L Osterberg, and M S Patterson (1998b), "Improved continuous light diffusion imaging in single- and multi-target tissue-like phantoms" *Phys. Med. Biol.* **43**(3) 675-693s.

70. Jiang H, K D Paulsen, U L Osterberg, and M S Patterson (1998a), "Frequency-domain near infrared photo diffusion imaging: Initial evaluation in multitarget tissuelike phantoms" *Med. Phys.* **25**(2) 183-193.

71. Kaschke M, H Jess, G Gaida, J-M Kaltenbach, and W Wrobel (1994), "Transillumination imaging of tissue by phase modulation techniques" *Proc. OSA Advances in Optical Imaging and Photon Migration* **21** 88-92.

72. G. F. Knoll, *Radiation Detection and Measurement*, (John Wiley & Sons, Inc., 2000).

73. Koizumi H, T Yamamoto, A Maki, Y Yamashita, H Sato, H Kawaguchi, and N Ichikawa (2003), "Optical topography: practical problems and new applications" *Appl. Opt.* **42**(16) 3054-3062.

74. Koizumi H, Y Yamashita, A Maki, T Yamamoto, Y Ito, Y Ito, H Itagaki, and Kennan R (1999), "Higher-order Brain Function Analysis by Trans-cranial Dynamic NIRS imaging" *J Biomed Opt* **4** 403-413.

75. Lampton M and Raffanti R (1994), "A high-speed wide dynamic range time-to-digital converter" *Rev. Sci. Instrum.* **65** 3577-3584.

76. Laser Institute of America (2005), "An Introduction to Laser Safety" *Http://Www.Laserinstitute.Org/Publications/Safety_Bulletin/Laser_Safety_Info/*

77. Li A, E L Miller, M Kilmer, T J Brukilacchio, T Chaves, Stott J J, Zhang Q, T Wu, M Chorlton, R H Moore, D B Kopans, and Boas D A (2003), "Tomographic optical breast imaging guided by three-dimensional mammography" *Appl. Opt.* **42**(25) 5181-5190.

78. Liebert A, H Wabnitz, J Steinbrink, H Obrig, Moller M, Macdonald R, and H Rinneberg (2003), "Intra- and extracerebral changes of hemoglobin concentrations by analysis of moments of distributions of time of flight of photons" *Proc. SPIE.* **5138** 126-130.

79. Maki A, Y Yamashita, Y Ito, E Watanabe, Y Mayanagi, and H Koizumi (1995), "Spatial and temporal analysis of human motor activity using noninvasive NIR topography" *Medical Physics* **22** 1997-2005.

80. McRobbie D.W., Moore E.A., Graves M.J., and Prince M.R., *MRI: From Proton to Picture*, (Cambridge University Press, 2003).

81. Mendelson Y, Cheug PW, Neuman MR, Fleming DG, and Cahn SD (1983), "Spectrophotometric investigation of pulsatile blood flow for transcutaneous reflectance oximetry." *Adv. Exp. Med. Biol.* (159) 93-102.

82. Merrick EB and Hayes TJ (1976), "Continuous non-invasive measurements of arterial oxygen levels" *Hewlett-Packard J.* **28** 2-9.

83. Moesta K T, H Kaisers, S Fantini, M Tönnies, M Kaschke, and P M Schlag (1996), "Lasermammografie der Brustdrüse - Sensitivitätssteigerung durch Hochfrequenzmodulation" *Langenbecks Arch Chir Suppl 1* 543-548.

84. Moore E H (1920), "On the reciprocal of the general algebraic matrix" *Bulletin of the American Mathematical Society* **26** 394-395.

85. G. A. P. R. a. K. U. Müller D., (2004) "Ultrashort pulse thin-disk lasers and amplifiers", *Femtosecond technology for technical and medical applications,* (Springer Series "Topics in Applied Physics", Vol. 96, Springer,

86. Munro P, K Jordan, C Lewis, and T Heerema (2001), "Technique charts for EC film: direct optical measurements to account for the effects of X-ray scatter" *International Journal of Radiation Oncology* **50**(3) 829-836.

87. Nissilä I, K Kotilahti, Fallstrom K, and T Katila (2002), "Instrumentation for the accurate measurement of phase and amplitude in optical tomography" *Rev. Sci. Instrum.* **73**(9) 3306-3312.

88. Nissilä I, T Noponen, K Kotilahti, T Katila, L Lipiainen, T Tarvainen, M Schweiger, and Arridge S R (2005), "Instrumentation and calibration methods for the multichannel measurement of phase and amplitude in optical tomography" *Rev. Sci. Instrum.* **76** 044302-1-044302-10.

89. Nissilä, I, Hebden, JC, Jennions, D, Heino, J, Schweiger, M, Kotilahti, K, Noponen, T, Gibson, A, Järvenpää, S ,Lipiäinen, L, and Katila, T (2006), "A comparison between a time-domain and a frequency-domain system for optical tomography" *J Biomed Opt* **11**(6) 064015(1)-

90. Ntziachristos V, X Ma, and B Chance (1998), "Time-correlated single photon counting imager for simultaneous magnetic resonance and near-infrared mammography" *Rev. Sci. Instrum.* **69**(12) 4221-4233.

91. Ntziachristos V, X Ma, A G Yodh, and Chance B (1999), "Multichannel photon counting instrument for spatially resolved near infrared spectroscopy" *Rev. Sci. Instrum.* **70** 193-201.

92. Ntziachristos V, A G Yodh, M Schnall, and Chance B (2000), "Concurrent MRI and diffuse optical tomography of breast after indocyanine green enhancement" *Proc. Nat. Acad. Sci.* **97**(6) 2767-2772.

93. Ntziachristos V, A G Yodh, M Schnall, and B Chance (2002), "MRI-guided diffuse optical spectroscopy of malignant and benign breast lesions" *Neoplasia* **4**(4) 347-354.

94. Obata A, K Morimoto, H Sato, A Maki, and H Koizumi (2003), "Acute effects of alcohol on hemodynamic changes during visual stimulation assessed using 24-channel near-infrared spectroscopy" *Psychiatry Research: Neuroimaging* **123** 145-152.

95. Obrig H and A Villringer (2003), "Beyond the visible - imaging the human brain with light" *J. Cereb. Blood Flow & Metab.* **23** 1-18.

96. Okada E, M Firbank, M Schweiger, S R Arridge, M Cope, and D T Delpy (1997), "Theoretical and Experimental investigation of near-infrared light propogation in a model of the adult head" *Appl. Opt* **36**(1) 21-31.

97. Paschotta R.and Keller U., (2003) "Ultrafast solid-state lasers", *Ultrafast Lasers: Technology and Applications,* (Marcel Dekker, Inc., New York,

98. Pavic DD, Koomen MD, Kuzmiak CD, and Pisano ED (2003), "Ultrasound in the management of breast disease" *Current Women's Health Rep* **3** 156-164.

99. Pei Y, H L Graber, and R L Barbour (2001), "Normalized-constraint algorithm for minimizing inter-parameter crosstalk in DC optical tomography" *Opt. Express* **11** 97-109.

100. Penrose R (1955), "A generalized inverse for matrices" *Proceedings of the Cambridge Philosophical Society* **51** 406-413.

101. Peters V G, D R Wyman, M S Patterson, and G L Frank (1990), "Optical properties of normal and diseased human breast tissue in the visible and near infrared" *Phys. Med. Biol.* **35** 1317-1334.

102. Pifferi A, P Taroni, A Torricelli, F Messina, and R Cubeddu (2003), "Four-wavelength time-resolved optical mammography in the 680-980 nm range" *Optics Letters* **28**(13) 1138-1140.

103. Pogue B W, S Giemer, T McBride, S Jiang, U L Osterberg, and K D Paulsen (2001a), "Three-dimensional simulation of near-infrared diffusion in tissue: boundary condition and geometry analysis for finite-element image reconstruction" *Appl. Opt.* **40**(4) 588-600.

104. Pogue B W, S Jiang, H Dehghani, C Kogel, S Soho, S Srinivasan, X Song, T D Tosteson, S P Poplack, and K D Paulsen (2004), "Characterization of hemoglobin, water and NIR scattering in breast tissue: analysis of intersubject variability and menstrual cycle changes" *J. Biomed. Opt.* **9**(3) 541-552.

105. Pogue B W, T McBride, C Nwaigwe, U L Osterberg, J F Dunn, and K D Paulsen (1999), "Near-infrared diffuse tomography with a priori MRI structural information: Testing a hybrid image reconstruction methodology with functional imaging of the rat cranium." *Proc. SPIE.* **3597** 484-

106. Pogue B W and K D Paulsen (1998), "High-resolution near-infrared tomographic imaging simulations of the rat cranium by use of a priori magnetic resonance imaging structural information" *Opt. Lett.* **23**(21) 1716-1718.

107. Pogue B W, K D Paulsen, C Abelem, and Kaufman H (2000), "Calibration of near infrared frequency-domain tissue spectroscopy for absolute absorption coefficient quantitation in neonatal head-simulating phantoms" *J Biomed Opt* **5**(2) 182-193.

108. Pogue B W, S P Poplack, T McBride, W A Wells, K S Osterman, U L Osterberg, and K D Paulsen (2001b), "Quantitative haemoglobin tomography with diffuse near-infrared spectroscopy: Pilot results in the breast" *Radiology* **218** 261-266.

109. Pogue B W, Testorf M, T McBride, U L Osterberg, and K D Paulsen (1997), "Instrumentation and design of a frequency domain diffuse optical tomography imager for breast cancer detection" *Opt. Express* **1**(13) 391-403.

110. Schmidt F. E. W. (1999), Thesis: "Development of a time-resolved optical tomography system for neonatal brain imaging", *University College London, Department of Medical Physics and Bioengineering, UK*

111. Schmidt F E W, M E Fry, E M C Hillman, J C Hebden, and D T Delpy (2000a), "A 32-channel time-resolved instrument for medical optical tomography" *Rev. Sci. Instrum.* **71**(1) 256-265.

112. Schmidt F E W, J C Hebden, E M C Hillman, M E Fry, M Schweiger, H Dehghani, D T Delpy, and S R Arridge (2000b), "Multiple-slice imaging of a tissue-equivalent phantom by use of time-resolved optical tomography" *Appl. Opt.* **39**(19) 3380-3387.

113. Schmitz C H, D P Klemer, R Hardin, M S Katz, Y Pei, H L Graber, M B Levin, R D Levina, N A Franco, W B Solomon, and R L Barbour (2005), "Design and implementation of dynamic near-infrared optical tomographic imaging instrumentation for simultaneous dual-breast measurements" *Appl. Opt.* **44**(11) 2140-2152.

114. Schmitz C H, M Locker, J M Lasker, Hielscher A H, and R L Barbour (2002), "Instrumentation for fast functional optical tomography" *Rev. Sci. Instrum.* **73**(2) 429-439.

115. Schnall M (2000), "Application of magnetic resonance imaging to early detection of breast cancer" *Breast Cancer Research* **3** 17-21.

116. Schweiger M and S R Arridge (1999a), "Application of temporal filters to time-resolved data in optical tomography" *Phys. Med. Biol.* **44** 1699-1717.

117. M. Schweiger and S. R. Arridge, (1997) "Optimal data types in optical tomography", *Lecture Notes in Computer Science 1230: Information Processing in Medical Imaging,* J. a. G. G. Duncan, ed., (Springer-Verlag: Berlin,71-84.

118. Schweiger M and S R Arridge (1999b), "Optical tomographic reconstruction in a complex head model using a priori region boundary information" *Phys. Med. Biol.* **44**(11) 2703-2721.

119. Schweiger M, A P Gibson, and S R Arridge (2003), "Computational aspects of diffuse optical tomography" *IEEE Computing in Science and Engineering* **Nov/Dec 2003** 33-41.

120. Selb J, Stott J J, M A Franceschini, A G Sorensen, and Boas D A (2005), "Improved sensitivity to cerebral hemodynamics during brain activation with a time-gated optical system: analytical model and experimental validation" *J Biomed Opt* **10**(1) 011013-1-011013-12.

121. Selb J, J J Stott, M A Franceschini, and D A Boas (2004), "Improvement of depth sensitivity to cerebral hemodynamics with a time domain system" *OSA Biomedical Topical Meetings, Miami* FC3.

122. Shellock F G (2001), "Magnetic Resonance Procedures: Health Effects and Safety"

123. Siegel A M, J P Culver, J B Mandeville, and D A Boas (2003), "Temporal comparison of functional brain imaging with diffuse optical tomography and fMRI during rat forepaw stimulation" *Phys. Med. Biol.* **48** 1391-1403.

124. Siegel A M, J J Marota, and D A Boas (1999), "Design and evaluation of a continuous-wave diffuse optical tomography system" *Opt. Express* **4**(8) 287-298.

125. Siemens AG (Medical) (2004), "Siemens site planning guide" *Siemens AG Medical Solutions Documentation*

126. Steinbrink J, H Wabnitz, H Obrig, A Villringer, and H Rinneberg (2001), "Determining changes in NIR absorption using a layered model of the human head" *Phys. Med. Biol.* **46** 879-896.

127. Strangman G, J P Culver, J H Thompson, and D A Boas (2002), "A quantitative comparison of simultaneous BOLD fMRI and NIRS recordings during functional brain activation" *Neuroimage* **17**(2) 719-731.

128. Strangman G, M A Franceschini, and D A Boas (2003), "Factors affecting the accuracy of near-infrared spectroscopy calculations for focal changes in oxygenation parameters" *Neuroimage* **18** 865-879.

129. Swets JA, Getty D , Pickett R, D'Orsi C, Seltzer S, McNeil BJ (1991), "Enhancing and evaluating diagnostic accuracy." *Med Decis Making* **11**(1) 9-18.

130. Tabar L, M-F Yen, B Vitak, H-H T Chen, R A Smith, and S W Duffy (2003), "Mammography service screening and mortality in breast cancer patients: 20-year follow-up before and after introduction of screening" *Lancet* **361** 1405-1410.

131. Takahashi K, S Ogata, Y Atsumi, R Yamamoto, S Shiotsuka, A Maki, Y Yamashita, T Yamamoto, H Koizumi, H Hirasawa, and T Imai (2000), "Activation of the visual cortex imaged by 24-channel near-infrared spectroscopy" *J. Biomed. Opt.* **5**(1) 93-96.

132. Taroni P, G Danesini, A Torricelli, A Pifferi, L Spinelli, and R Cubeddu (2004), "Clinical trial of time-resolved scanning optical mammography at 4 wavelengths between 683 and 975 nm" *J. Biomed. Opt.* **9**(3) 464-473.

133. Torregrossa M, Zint C.V., and Poulet P (2003), "Effects of prior MRI information on image reconstruction in diffuse optical tomography" *Proc. SPIE.* **5143** 29-40.

134. Uludag K, J Steinbrink, A Villringer, and H Obrig (2004), "Separability and cross-talk: optimizing dual wavelength combinations for near-infrared spectroscopy of the adult head" *Neuroimage* **22** 583-589.

135. Villringer A and R J Dolan (1995), "Coupling of brain activity and cerebral blood flow: basis of functional neuroimaging" *Cerebrovasc. Brain Metab. Rev.*

136. Volpe J J (1997), "Brain injury in the premature infant" *Clin. in Perinatol* **24** 567-587.

137. Watanabe E, A Maki, F Kawaguchi, K Takashiro, Y Yamashita, H Koizumi, and Y Mayanagi (1998), "Non-invasive assessment of language dominance with near-infrared spectroscopic mapping" *Neurosci. Lett.* **256** 49-52.

138. Watanabe E, A Maki, F Kawaguchi, Y Yamashita, H Koizumi, and Y Mayanagi (2000), "Noninvasive cerebral blood volume measurement during seizures using multichannel near infrared spectroscopic topography" *J. Biomed. Opt.* **5**(3) 287-290.

139. Watanabe E, Y Nagahori, and Y Mayanagi (2002), "Focus diagnosis of epilepsy using near-infrared spectroscopy" *Epilepsia* **43**(Suppl. 9) 50-55.

140. Webster G J, (1998) "Non-Invasive Blood-Gas Monitoring", *Medical Instrumentation: Application and Design,* (John Wiley & Sons, Inc,468-474.

141. Wells K, J Hebden, F E W Schmidt, and D T Delpy (1997), "The UCL multichannel time-resolved system for optical tomography" *Proc. SPIE.* **2979** 599-607.

142. Wyatt J S (1993), "Near Infrared spectroscopy in asphyxial brain injury" *Clin. in Perinatol* **20** 369-378.

143. Yam M, Brady M, Highnam R., Behrenbruch C, English R, and Kita Y (2001), "Three-dimensional reconstruction of microcalcification clusters from two mammographic views" *IEEE Trans. Med. Imag.* **20**(6) 479-489.

144. Yamashita Y, A Maki, and H Koizumi (2001), "Wavelength dependence of the precision of noninvasive optical measurement of oxy-, deoxy-, and total-haemoglobin concentration" *Med. Phys.* **28**(6) 1108-1114.

145. Yamashita Y, A Maki, and H Koizumi (1999), "Measurement system for noninvasive dynamic optical topography" *J. Biomed. Opt.* **4**(4) 414-417.

146. Yates T D, J C Hebden, A P Gibson, N L Everdell, S R Arridge, and M Douek (2005), "Optical tomography of the breast using a multi-channel time-resolved imager" *Phys. Med. Biol. (in Press)*

147. Yoshiya I, Y Shimada, and Tanaka K (1980), "Spectrophotometric monitoring of arterial oxygen saturation in the fingertip." *Med Biog Eng Comput.*

148. Young Y, M Shnall, S Zhao, S Orel, C Xie, Nioka S, B Chance, and A Solin (1997), "Optical Imaging of Breast Tumour by means of Continuous Waves" *Adv. Exp. Med. Biol.* **441** 227-232.

149. Zworykin V.K. R J A (1939), "*Proc IRE* **27** 558-

Appendices

Appendix A - Operation Manual for MIDAS II

Setup

If the system has already been switched on, with MIDAS II running, the screen should look something like this:

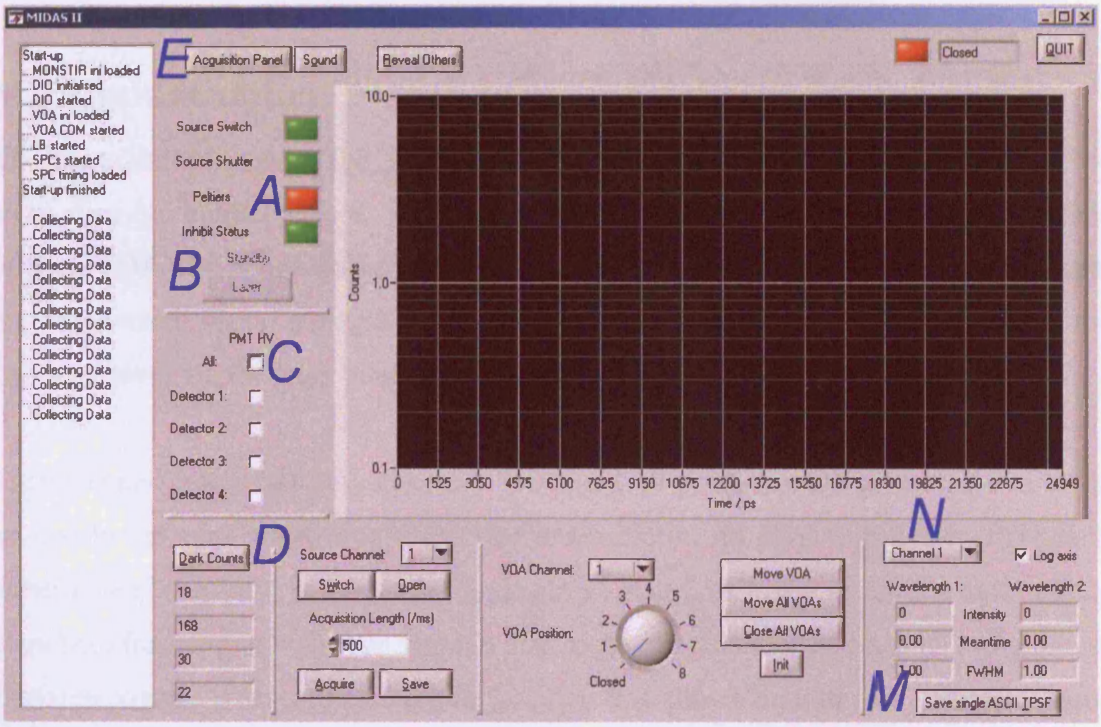

Three hours (less will result in noisy data) before starting an experiment, two hardware switches need to be enabled: the chiller, laser key, and external Peltier power supply. The chiller and Peltiers will start immediately and operate without further action. Indicator *A* should turn green once the Peltier power supply is on.

After a roughly 30 s delay for the laser to warm up, button *B* ("Standby") will become active (not greyed). Clicking it will change the text to "Wait", and after another 3 s, the button will turn red, meaning the laser is lasing.

The PMT HV should be switched on with tick-box *C*. Once the HV and laser are on, clicking button *D* ("Dark Counts") a few times should give you an idea of the dark counts per second for each router, via the four boxes beneath the button. The dark counts can start at anything up to a few 10k before cooling, but for good data the counts should be no higher than 50 (typically below 20, although router 2 seems a little noisy - a few hundred counts). The dark counts should drop noticeably within 10 min if the Peltiers and cooler are operating correctly (or rise if they aren't).

VOA initialisation

The communication with the VOA controller is not perfect and the alignment of the VOA disc can contain errors. Also, if MONSTIR has been powered off, the positions of each VOA disc is not stored and must be found afresh. The USB DAC cards cannot provide enough signal strength for all 32 VOA LEDs, so the user must switch on the LEDs by hand via the front panel on the main rack.

Each stepper motor has 800 steps per 360°, and all positions are given relative to an arbitrarily set zero position in a clockwise direction. An LED and detector are held either side of the VOA disc in order to detect a small hole in the disc. The zero hole is anywhere from one up to seven steps in size, depending on disc and detector alignment. The step counter is reset to zero on the last step that allows light to pass between source and detector. All VOA positions are defined in the VOA.ini file, "closed" being 792.

Due to the imperfect communication, MIDAS II makes a series of three attempts to initialise the discs. The first assumes that the discs are already in the closed position (MIDAS II automatically does this on shut-down), resets the current position to zero and moves the discs to position eight. If a positive response is not received from the photodetector, the disc is returned to zero position and the next channel is checked. MIDAS II checks all 32 channels in this way, and then returns to the channels not initialised. The second attempt checks every position from zero to twenty in single steps, the most obvious cause of failure from the first attempt being a misalignment of one or two steps in either direction. If no positive response is recorded within these first twenty steps, every even step from 20 to 800 is checked. This is very slow due to the response time of the VOA controller, and can take up to 15 min per channel.

The manual panel (see section below) can be used to initialise the VOAs by hand, and if total misalignment of a number of discs is suspected, this is often much faster than letting MIDAS II initialise the discs automatically. The front panel of MONSTIR's main rack shows the VOA LED's and the detector's status. By moving the discs across a large range, the user can check where the VOA position is by eye (flashing on of detector LED), and use a guess and check method to find the correct position.

As long as MONSTIR is not powered down, the VOA controller will remember the absolute position of the stepper motors, and hence, even if MIDAS crashes, the VOA need not be re-initialised. However, the stepper motors do mis-step occasionally, therefore the alignment of the discs should be confirmed by moving all the discs to step zero and checking all detector LEDs are on.

Addendum: The initialisation button on the front panel now appears to be working.

Single Acquisitions

For acquisitions where ADF files are not necessary, single TPSFs can be recorded and saved using the buttons on the front panel. Next to (D – Dark counts) are source and VOA controls. "Switch" changes the active source channel, but keeps the shutter closed, whereas "Open" opens the shutter on the channel currently active (NB – this is NOT the channel selected in the drop-down – the active source channel is shown upper right on the front panel). "Acquire" opens the shutter for the required time, but the data is not stored until "Save" is clicked. This will save all 32 channels of data as an .sdt file. If only a single TPSF is required, the "ASCII save" button (lower right) might be preferable (e.g. for project work).

Full Acquisitions

The front panel should look like this:

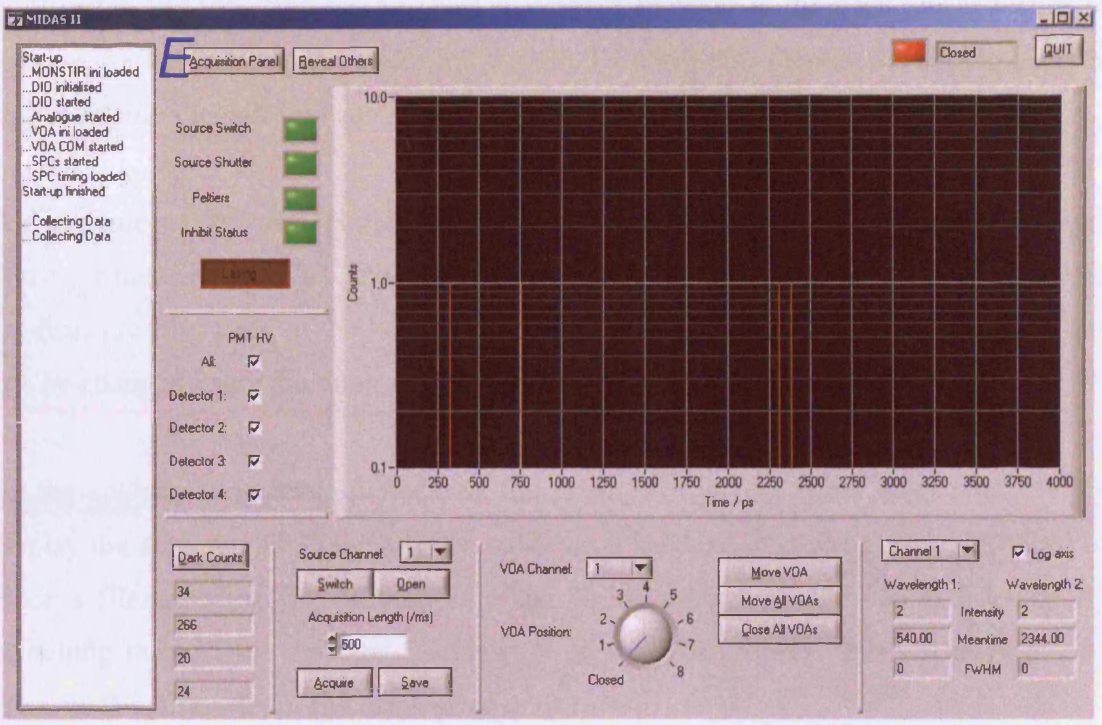

Clicking on button *E* at the top will open the acquisitions panel:

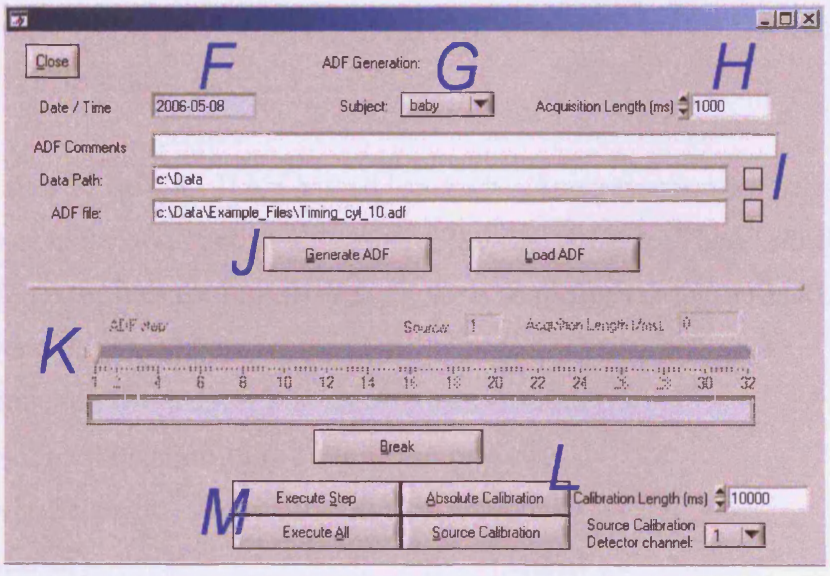

The ADF file name is created automatically from the date (*F*) and subject (*G*), so check these are correct. The acquisition length for the ADF (*H*) needs to be set and the "Data Path" field is the directory where all data files will be written (pop-up selection via *I*).

Turn all lights off / minimise stray light, then click "Generate ADF" (*J*). For a full 32 channels, this should take about ~7 minutes. The newly generated ADF is displayed in "ADF file" and the steps can be checked using the arrows at the right and left ends of slider *K* (or by dragging the slider left/right). This will also display the source channel and acquisition length for each step.

An absolute calibration should be performed before data acquisition. Insert neutral density filters up to 7 OD into the laser, then click button *L* - a popup asking you to confirm the filters are in the laser will appear. A standard calibration is 10 s, but this can be changed using the timer input right of the calibration buttons.

As the calibration is being performed, the graph on the first panel will automatically display the acquired TPSFs. Once the calibration has been completed, you will need to enter a filename for the calibration. The entire calibration file can be viewed by switching through the detector channels (*N* on the front panel). **NB - Remember to remove the filters from the laser after calibration.**

The "Execute Step" and "Execute All" buttons (*M*) do just that – acquiring just the single step currently displayed on *K*, or acquiring all steps from the first (automatically resets *K* to start from step 1).

The output files of MIDAS II are named "src#.sdt" (# representing the source channel) – they are not split "_w1" and "_w2" as with the old MIDAS. These .sdt files need to be converted to .tps files for Monstix etc. to work, so please ask for the MatLab script to do the conversion. The scripts are found at:

//Emmeline/Users/davej/Matlab/recurseConvert.m

and requires the following files in order to run properly:

convertBHset.m

Splitstr.m

If converting a single .sdt file use:

BH2tps.m

If you wish to repeat an ADF acquisition, make sure you change the "Data Path" directory, either by typing in the new path or clicking on *I*. If the directory isn't changed, the previous dataset will not be over-written, but all of the files from the second acquisition will include "_2" in the filename.

Noise / Language studies

An additional panel has been added to MIDAS II to perform language / noise studies with neonates. This code operates totally separate from the acquisition code, and can hence be rewritten to perform any set of acquisitions required.

MONSTIR Connections

The two MONSTIR racks must be separated to transport the system, e.g. to the neonatal unit. The connections between the two racks must be exactly reproduced once the system is in place, in order for the system to perform properly. The connections fall into four groups – power, laser, detectors, and digital control.

The laser rack has four power leads, shown below left: three IEC for the cooling system (F), laser (B), and control PC (C), and one 13A mains for isolation of the main electronics rack (E). A speakon connector from the back of the electronics rack should be plugged into the back of the main power unit (G).

Three connections between the main rack and IMRA laser can be fully removed and carried separately. Control of the laser is via a serial lead running from the "remote" port on the back of the laser (A, left) to the middle right-hand side of the main rack (A, right). From the front of the laser an optical source fibre connects to port zero on the left-hand side of the switch unit (middle centre of the rear of the main rack – not shown). A specific BNC cable should be connected from the "815 nm NIM out" port on the front of the laser to the right-hand delay unit on the main rack (slightly lower on the right-hand side of the rear of the main rack – B, right). If MONSTIR is being used in its old setup, then another BNC cable should be connected between the "780 nm NIM out" and the left-hand delay unit. This cable should be coiled and attached to the delay unit for storage.

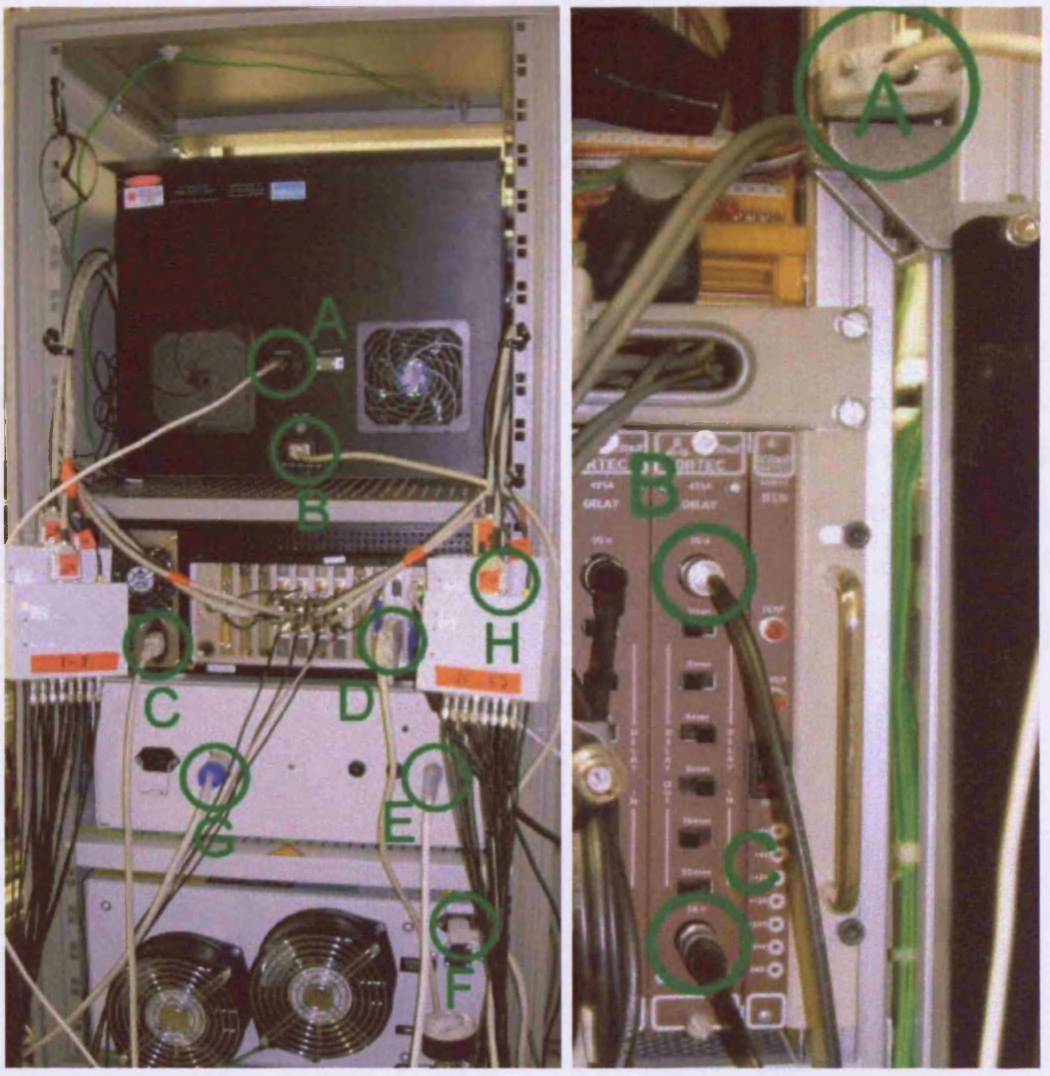

Thirty-two 1 m long SMA cables are connected to the rear of the detectors. When using the old setup, these should be screwed into the cabling built into the main rack, which lead to the counting units on the front of the main rack. The new electronics use four 8-1 routers, connected to the short SMA cables via 4 m long SMA extensions. Each router is for one eight-channel detector and should not be confused. A router can be disconnected from the industrial PC by removing the serial connector and unscrewing the single SMA, both of which at attached to the rear of the router and should be coiled and left connected to the industrial PC. The routers can be stored in the space between the VOA boxes and the detectors for transport and whilst in the clinic, but during lab time they should be kept on top of the laser rack for cable temperature purposes.

If the routers are disconnected totally from the detectors and industrial PC they are labelled with the channels they should be connected to; these run left to right in ascending order and should be connected to the back of the industrial PC in the same order – i.e. when looking at the back of the industrial PC channel 1 should be the furthest left, channel 32 the furthest right.

The final connections are for digital control (e.g. source switch / shutter units) and analogue acquisition (e.g. laser calibration box), and are switched between new and old setups via four boxes. The new industrial PC controls MONSTIR via two USB DAC units. The DAC channels have been wired into two connectors which should be attached to the relevant switch boxes. Position A on each switch is the old setup, which should be permanently connected, position B for the new system - if the switches have positions C and D, these shouldn't be connected to anything.

Manual Panel

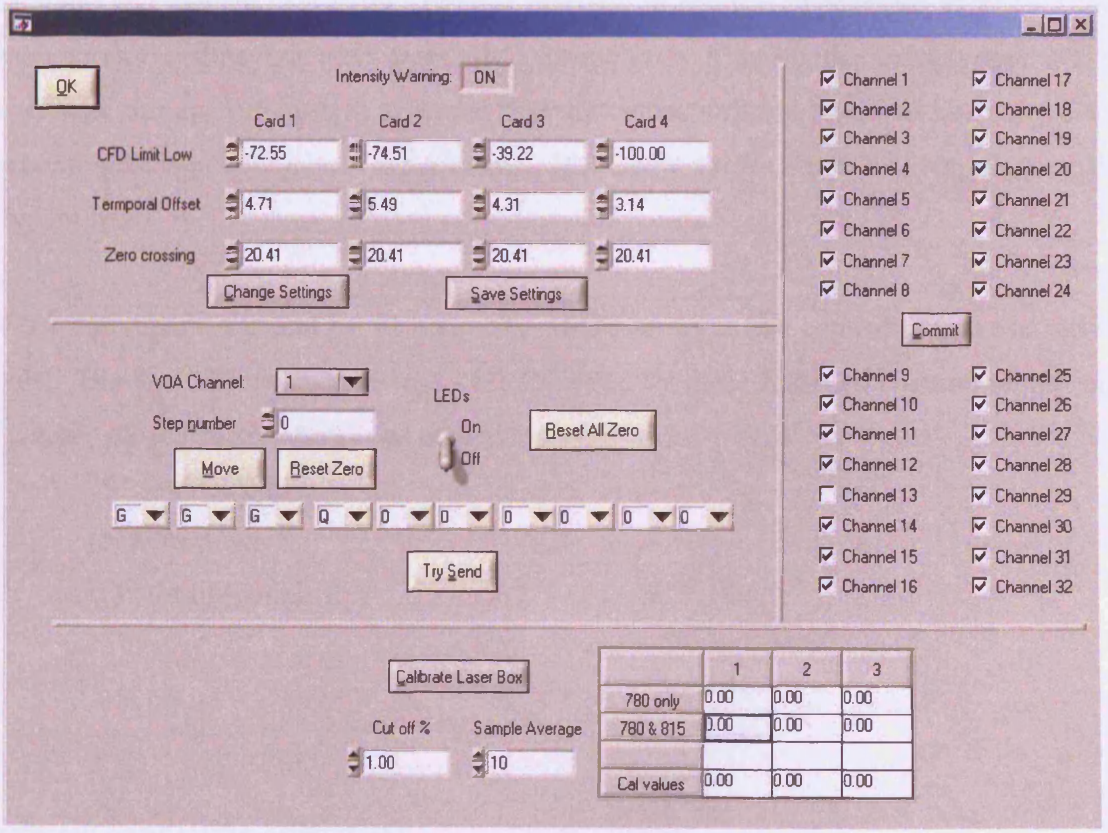

The manual panel is not normally used, so it is hidden by the "Reveal others" button on the front panel. Clicking this reveals two other panel options, one of which is the manual options.

The manual panel contains three sections to control each of the timing engines, VOAs, and active channels. The first set of controls are for fine-tuning the three properties of each of the SPC cards: TAC offset and CFD zero-crossing and threshold. The TAC offset is the initial delay at the front of the temporal window, similar to the delay units for the laser's SYNC signal. If any of the TPSFs recorded overlap with the start of the temporal window, the TAC offset value should be increased.

Warning - each of these values is for one timing engine (i.e. SPC card), and will hence affect eight channels. Also, these parameters are discrete values - once the new values have been chosen, clicking the "commit" button will send the parameters to the engines, then read the actual value back and display it in the given fields. Please check that changing the display causes the engine's property to change. The initial values set for each timing engine are read from SPC_timing.ini. Altering the values does NOT overwrite the .ini file, as it is assumed that the values will only need to be changed to accommodate specific days / experiments. If the new values are to be kept, please edit the .ini file.

VOA commands are sent by 11 character ASCII string to the controller unit via serial port. The first character is always "$", followed by three digits of channel identified ("GGG" means all channels) and an operator:

"S" for status change

"M" for move

"Q" for query status

The six numbers following these headers are then data sent / received depending on exact instruction. The 10 single-character drop-down boxes ("$" not included) allow each of these commands to be sent individually, but the "move to step" and "reset channel" controls should be used more frequently. If checking the initialisation position of all VOAs, sending "GGGM000000" should move all VOAs to the zero position, and hence all LEDs on the front panel should turn on. Again, all stepper motor positions are relative to this zero, so clicking "Close all VOAs" will still return the VOAs to the closed position, irrespective of what position the discs are in – with the exception of the zero counter having been altered.

To initialise the VOAs by hand, the following steps can be followed. On the manual panel, click "Reset all Zero". MIDAS automatically resets all the VOAs to their closed position when exiting, hence resetting the VOAs means the zero position is at step 8. Change the series of drop-downs to "GGG M 000008" and click "Try send". Switching on one set of LEDs using the hardware switch will reveal which VOAs are in the correct zero position. Any incorrect channels need to be tweaked by hand. Choose the relevant "VOA channel", select a new step, and click "Move", keeping an eye on the front of the MONSTIR rack to confirm finding the correct position. Once all channels have been correctly found, click "Reset All Zero" again to finish initialisation. For further confirmation, send "GGG M 000100", then "GGG M 000000" and switch the LEDs on, repeating the above if any channels have mis-stepped. Remember to return to the front panel and click "Close All VOAs" once finished.

The list of active channels on the right-hand side is read in from SPC_something.ini. If during an experiment, channels are found to be faulty, either by mechanical error or poor optical contact, un-checking the relevant box and clicking "Commit" will remove that channel from all displays in MIDAS II and zero all data in the output files.

Known bugs

There are several outstanding issues with MIDAS II that should be addressed given the time.

The MIDAS II GUI has a few issues in activating / disabling controls in response to inputs from the DAC. In addition, some focus on the usability of the GUI would net substantial gains from the point of view of clinicians.

Outside MIDAS II, the outputs are currently being converted to the old-style .tps format. This is due to the SPC software containing its own save function, and Monstix / MatLab scripts (e.g. viewtpsfs / viewdata) have yet to be re-written.

Appendix B - ADF creation theory

Introduction

Automatic Definition Files (ADFs) record the positions of the Variable Optical Attenuators (VOAs) for each source. These files are required to perform full acquisitions with MONSTIR. Each channel's VOA position is set to keep the detected count rate within a set range – too high and the detectors will saturate or become damaged; too low and the signal to noise ratio suffers.

Background

The old method for finding the VOA positions for each source is to loop the following:

- Acquire data
- Check all count rates against the boundary conditions
    - If correct, record the position and shut the VOA, otherwise:
        - The count rates at all other VOA positions are calculated
        - Each VOA is moved to the position corresponding to the correct rate
- If all VOA positions are known, the source is recorded with the correct positions

The old iterative methods typically takes 4 steps per source to find the correct positions for all channels, 128 steps in total for 32 sources. The count rate range search for with the old electronics is 75 - 150 kHz

The new electronics present a different problem for creating the ADFs. A router is used to multiplex eight channels of data into one timing engine. Excessive counts on one channel will increase the number lost from other channels due to pile-up. Hence all channels' count rates must be below a threshold before the VOA positions can be calculated. This is not a problem with the old electronics as all channels are independent. The average maximum count rate per channel, and therefore the threshold, is 125 kHz, and the range of count rates searched for is 10 - 100 kHz.

The ideal way to find the VOA positions with the new electronics is to acquire data on one channel per router, find the respective VOA positions, then acquire on the subsequent channel on each router. This method is inherently slower than any other, as it only calculates the VOA positions for four channels simultaneously, each requiring four steps to find the correct position - a total of 1024 steps for 32 channels split over 4 routers.

The method used for the old electronics can be adapted to cope with count rates that are inter-dependent by forcing the rates on all channels to be beneath the threshold before starting the loop to search for VOA positions, as described above. An extra two steps per source are added by including this criterion, giving a total of 172 steps.

The old ADF generation acquires data for 2 s at each step. The upload delay of the old electronics, roughly 4 s, results in a total ADF generation time of ~13 minutes. The delay between sources has been reduced to 0.5 s with the new electronics, but the vastly increased number of steps required for ideal ADF generation loses the advantage of faster acquisition and would take a total of ~40 minutes, assuming the same acquisition length per step.

The method adapted from the old algorithm, using the new electronics and same acquisition length, would take ~7 min. The drawback to the adapted method is that crosstalk between channels could not be fully removed. However, given that data acquisition will suffer from the same crosstalk, ADF generation including this effect would not be inherently detrimental to the acquired dataset.

Method

Both algorithms for generating ADF files were written into the new MIDAS software. A ring of 16 fibres were coupled to the middle of homogenous cylindrical phantom ($\mu_s` = 1.0$ mm^{-1} and $\mu_a = 0.01$ mm^{-1}), and five ADFs were created using each generation method. An ideal ADF was also generated by hand, using the manual VOA controls in MIDAS. The ADFs were compared for repeatability of the generation method and against each other and the ideal ADF to measure accuracy. Multiple VOA positions can produce count rates within the correct range. All positions generated by the two methods outside the range found by hand were noted as false.

The two algorithms were then set to create ADFs for acquisition times ranging from 0.5 - 5 s to investigate whether longer acquisitions would reduce the number of steps needed to find each VOA position for each method. Longer acquisition times produce more accurate data, but expose the detectors to damaging illumination for longer.

Results

Five ADFs were generated using a 1 s acquisition time. The average times for the ideal and adapted generations were 731 and 137 s respectively. The ideal generation method produced an average of 5 false results out per ADF. The adapted method generated roughly twice the number of false positions. However, over 80% of the false positions found by the adaptive method were presented for all ADFs generated with that method. The adapted method had a greater variance between repeats, but the results were still within the ranges found by hand.

ADFs were generated using 0.5, 1, 2, and 5s acquisitions per step. The total number of steps taken and the total generation time are tabulated against acquisition time in Table 2 and Table 3 for each method.

Acquisition time per step / s	0.5	1	2	5
Generation time / s	538	731	1020	1934
Total steps	336	338	341	335
False VOA positions	5	5	5	5

Table 2: Comparison of ADFs for varying acquisition times using an ideal algorithm. False positions are those generated outside the range found by hand.

Acquisition time per step / s	0.5	1	2	5
Generation time / s	97	137	199	307
Total steps	57	59	58	49
False VOA positions	15	12	9	6

Table 3: Comparison of ADFs for varying acquisition times using an adapted algorithm.

Conclusion

In conclusion, ADFs can be generated with the new electronics in a quarter of the time needed to generate ADFs with the old electronics, assuming the same acquisition time is used. The gain in speed is mainly due to the lack of delay for data transmission. However, the generation process has become more complex, as the count rates recorded on one channel effect all others on the same router; hence a few more VOA positions are not perfect. This will not significantly effect the data collected by MONSTIR.

It should be noted that the experimental setup for testing the ADF generation used only 16 channels. The time taken to calculate only one channel on each router would not increase with the addition of 16 more channels, whereas the method calculating all channels simultaneously would increase significantly, due to the effect of further channels' data on all other channels.

Appendix C - Reconstructed Images

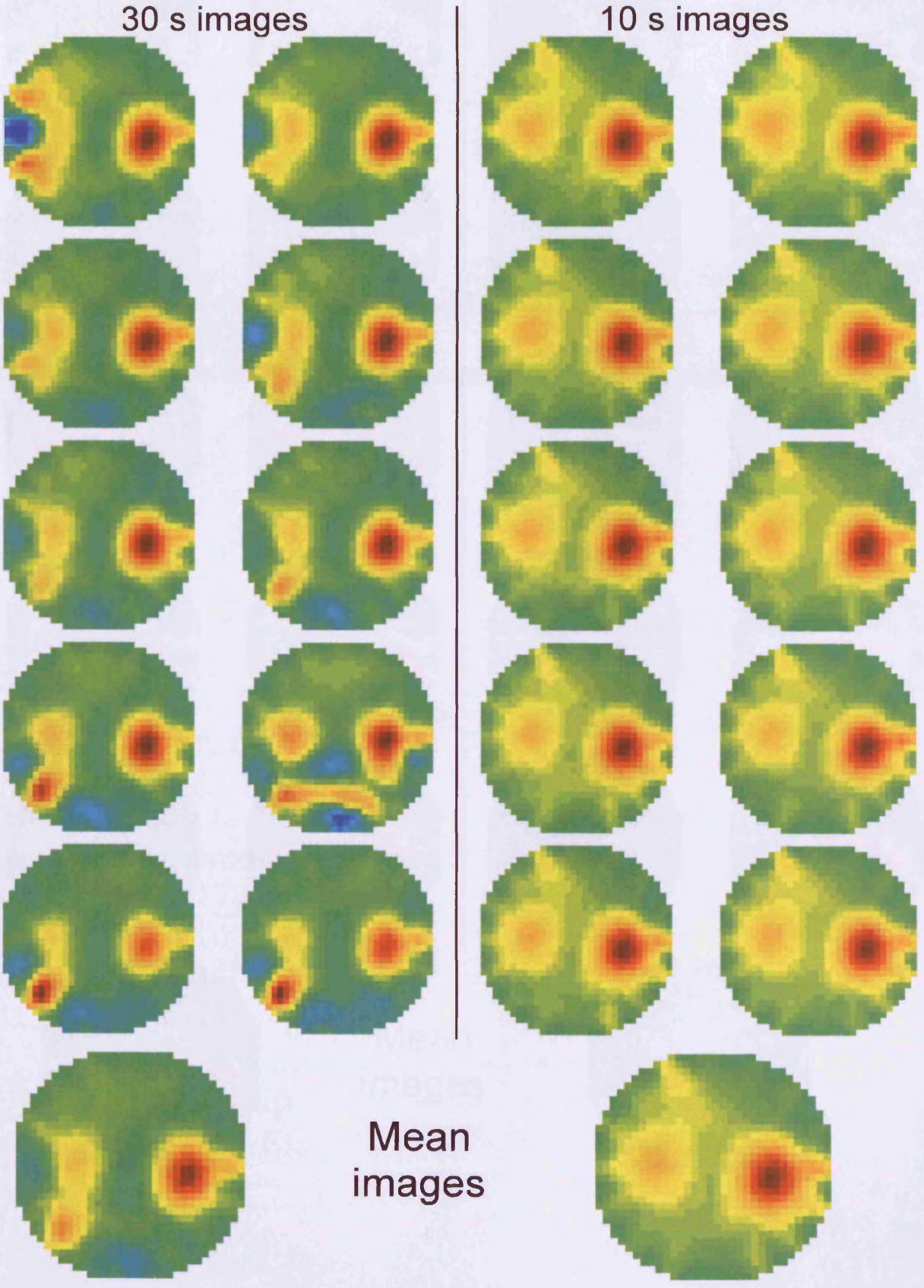

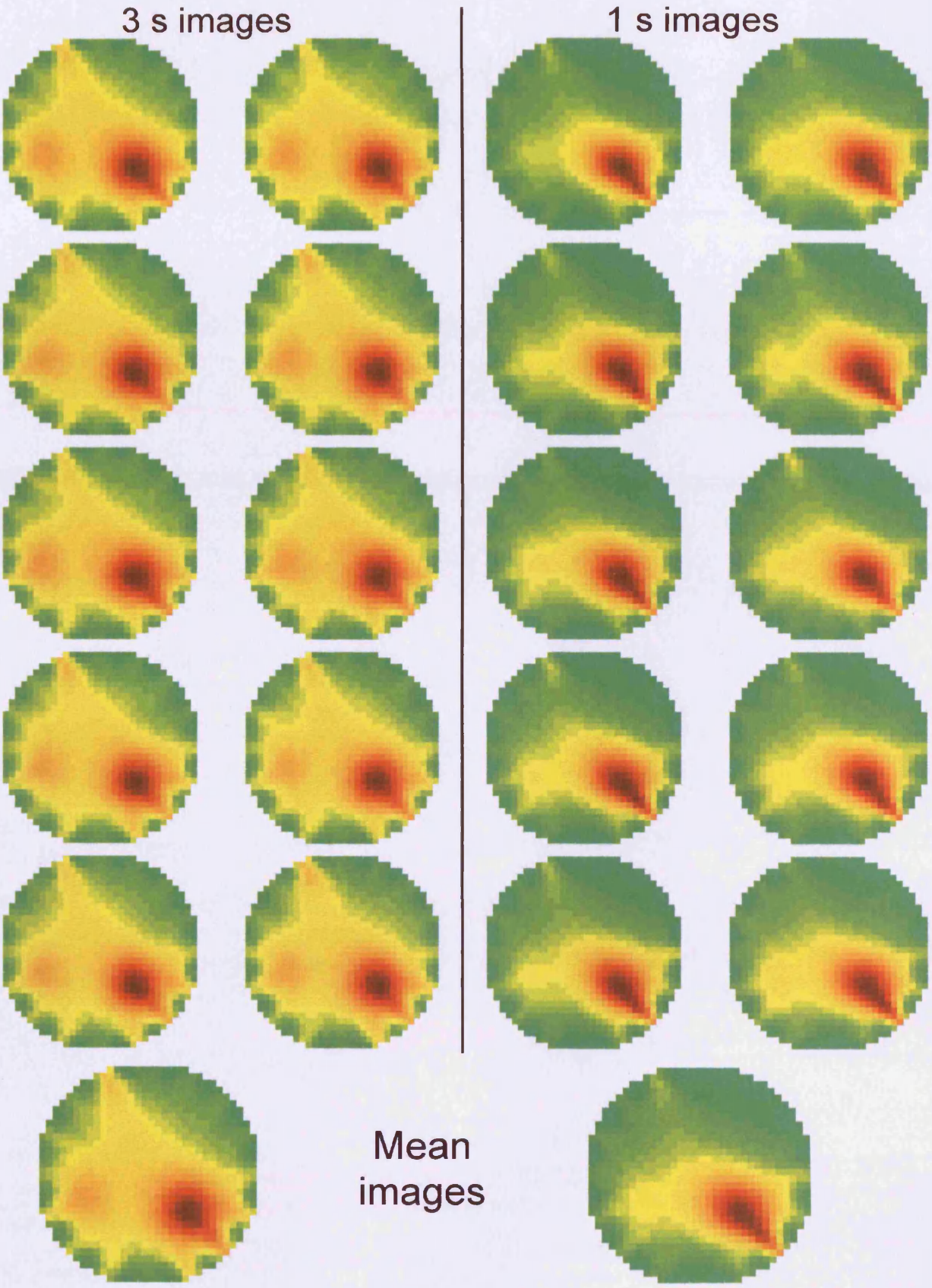
3 s images
1 s images
Mean images